

Université de Montréal

**Modification de films de graphène dans la post-décharge en flux
de plasmas micro-ondes d'azote à pression réduite**

Par

Germain Robert Bigras

Département de physique

Faculté des études supérieures et postdoctorales

Thèse présentée
en vue de l'obtention du grade de Philosophiae Doctor (Ph.D.)
en Physique

Août 2020

© Germain Robert Bigras, 2020

Université de Montréal
Département de Physique / Faculté Arts et Sciences

Cette thèse intitulée

**Modification de films de graphène dans la post-décharge en flux
de plasmas micro-ondes d'azote à pression réduite**

Présentée par
Germain Robert Bigras

A été évaluée par un jury composé des personnes suivantes

Michel Côté
Président-rapporteur

Luc Stafford
Directeur de recherche

Ahmad Hamdan
Membre du jury

Jocelyn Veilleux
Examinateur externe

Richard Martel
Représentant du doyen

Résumé

Ce projet de thèse porte sur le traitement de films de graphène dans la post-décharge en flux de plasmas micro-ondes d'azote à pression réduite. Différentes considérations de contamination de surface des échantillons se sont avérées cruciales pour ce travail. Par exemple, en présence d'hydrocarbures, les traitements dans les différentes régions de la post-décharge montrent des profils de production de dommages, d'incorporation d'azote et de fonctionnalisation de contaminants distincts. Le traitement agressif qu'offre la post-décharge proche résulte en la formation de complexes amorphes graphène-hydrocarbures responsables d'une forte hausse de la teneur en azote (jusqu'à 49%) pour des désordres modérés ($D:G = 1.3$). Pour les traitements dans la post-décharge lointaine, les hydrocarbures jouent un rôle de couche protectrice permettant une incorporation monotone (jusqu'à 18%) à très faible dommage ($D:G < 0.3$). Les espèces azotées sont néanmoins faiblement liées de sorte que le transfert vers un substrat de SiO_2 engendre une perte importante (> 80%) de la teneur en azote. Des considérations d'inhomogénéité de surface des films de graphène ont motivé le développement d'une nouvelle méthode d'analyse des cartographies Raman obtenues par un imageur hyperspectral. L'étude des spectres Raman au niveau des domaines versus aux joints de grains ont permis de mettre en évidence un mécanisme d'auto-réparation des joints de grains relié à l'anisotropie de la migration des adatomes de carbone en surface. L'accumulation de ceux-ci aux joints de grains mène à une émission d'adatomes responsable de l'annihilation de paires de Frenkel. Dans les plasmas azotés, il s'avère que ce mécanisme est également responsable d'une incorporation sélective d'azote aux domaines de croissance du graphène. Lorsque amorphisé, le dopage sélectif s'estompe puisque le transport des adatomes de carbone aux joints de grains, ainsi que l'accumulation essentielle au processus d'auto-réparation, deviennent entravés. Finalement, la recombinaison en surface d'atomes d'azote et la désexcitation de métastables $\text{N}_2(\text{A})$ sont identifiés comme principaux agents pour la production de dommages dans la post-décharge en flux d'azote. Un modèle d'incorporation impliquant la formation de dommages et l'adsorption d'atomes d'azote est proposé. En présence d'espèces oxydantes dans la post-décharge d'azote, la formation de dommages demeure limitée par les populations de N et de $\text{N}_2(\text{A})$.

Mots-clés : plasmas pression réduite, post-décharge en flux d'azote, diagnostics spectroscopiques des plasmas, graphène, caractérisation des matériaux

Abstract

This thesis project deals with the treatment of graphene films in the flowing afterglow of microwave nitrogen plasmas at reduced pressure. Various surface contamination considerations were found to be crucial for this work. For example, in the presence of hydrocarbons, the treatments in the different regions of the afterglow show distinct damage production, nitrogen incorporation and contaminant functionalization profiles. The aggressive treatment offered by the early afterglow results in the formation of amorphous graphene-hydrocarbon complexes responsible for a sharp increase in the nitrogen content (up to 49%) at moderate disorders ($D: G = 1.3$). For the treatments in the late afterglow, the hydrocarbons act as a protective layer, allowing a monotonic incorporation (up to 18%) with very low damage ($D: G < 0.3$). Nitrogenous species are found to be weakly bound so that transfer to an SiO_2 substrate generates a significant loss (>80%) of the nitrogen content. Considerations of surface inhomogeneity of graphene films have motivated the development of a new analysis method of Raman maps obtained by hyperspectral imager. The study of Raman spectra at growth domain versus grain boundary has revealed a self-healing mechanism of grain boundaries linked to the anisotropy of the migration of carbon adatoms at the surface. The accumulation of these at grain boundaries leads to an emission of atoms responsible for the annihilation of Frenkel pairs. In nitrogenous plasmas, this mechanism is also found to be responsible for the selective incorporation of nitrogen into the growth domains of the graphene. For amorphous graphene, selective doping fades as the transport of carbon adatoms to grain boundaries, and therefore the accumulation essential to the self-healing process, becomes impeded. Finally, the surface recombination of nitrogen atoms and the de-excitation of metastable $\text{N}_2(\text{A})$ are identified as the main agents defect generation in the nitrogen flowing afterglow. An incorporation model involving the formation of damage and adsorption of nitrogen atoms is proposed. In the presence of oxidizing species in the nitrogen afterglow, damage formation remains limited by populations of N and $\text{N}_2(\text{A})$.

Keywords: reduced pressure plasmas, nitrogen flowing afterglow, spectroscopic plasmas diagnostics, graphene, material characterisation

Table des matières

RÉSUMÉ	3
ABSTRACT	4
TABLE DES MATIÈRES	5
LISTE DES TABLEAUX	7
LISTE DES FIGURES	8
LISTE DES SIGLES ET ABRÉVIATIONS	11
REMERCIEMENTS	12
INTRODUCTION.....	13
CHAPITRE 1 – REVUE DE LA LITTÉRATURE	17
1.1 GRAPHÈNE : PROPRIÉTÉS, SYNTHÈSE ET TRAITEMENT	17
1.1.1 <i>Propriétés physico-chimiques du graphène</i>	17
Propriétés électroniques du graphène	18
Propriétés vibrationnelles du graphène	19
1.1.2 <i>Méthodes de synthèse du graphène</i>	22
Exfoliation mécanique	23
Dépôt chimique en phase vapeur.....	23
Dépôt chimique en phase vapeur assisté par plasma	25
1.1.3 <i>Méthodes de traitement post-synthèse du graphène</i>	25
Faisceau d'ions	26
Recuit thermique.....	30
Fonctionnalisation covalente de surface	32
Traitement par plasma	33
1.2 TRAITEMENT PAR PLASMA DU GRAPHÈNE	36
1.2.1 <i>Traitement du graphène par plasma d'argon</i>	37
1.2.2 <i>Traitement du graphène par plasma d'hydrogène</i>	39
1.2.3 <i>Traitement du graphène par plasma d'oxygène</i>	41
1.2.5 <i>Traitement du graphène par plasma d'azote</i>	43
Incorporation, bombardement et dopage.....	44
Amplification de potentiel catalytique du graphène	47
1.2.6 <i>Traitement du graphène par plasma d'ammoniac</i>	48
1.3 CONCLUSION	50

CHAPITRE 2 – CONSIDÉRATIONS EXPÉRIMENTALES.....	51
2.1 INTRODUCTION	51
2.2 COMPARAISON TRAITEMENT POST-DÉCHARGE PROCHE ET LOINTAINE	55
2.3 ÉTUDE DES PHÉNOMÈNES DE CONTAMINATION.....	80
CHAPITRE 3 – RÔLE DES INHOMOGÉNÉITÉS DE CROISSANCE	101
3.1 INTRODUCTION	101
3.2 NOUVELLE MÉTHODE D'ANALYSE PAR IMAGERIE RAMAN	104
3.3 AUTO-RÉPARATION PRÉFÉRENTIELLE DES JOINTS DE GRAINS.....	125
3.4 INCORPORATION SÉLECTIVE D'AZOTE	129
CHAPITRE 4 – RÔLES RESPECTIFS DES ESPÈCES ACTIVES DE LA POST-DÉCHARGE ET MODÈLE D'INCORPORATION DES ATOMES D'AZOTE	157
4.1 INTRODUCTION	157
4.2 RÔLE DES AZOTES ATOMIQUES ET DES AZOTES MOLÉCULAIRES MÉTASTABLES	159
4.3 RÔLE DES ESPÈCES OXYDANTES	178
CONCLUSION.....	186
RÉFÉRENCES BIBLIOGRAPHIQUES.....	191
ANNEXE.....	195
ANNEXE 1 : DONNÉES SUPPLÉMENTAIRES POUR L'ARTICLE PSST_2018	195
ANNEXE 2 : DONNÉES SUPPLÉMENTAIRES POUR L'ARTICLE CARBON_2019	198
ANNEXE 3 : EFFET DE RÉGÉNÉRÉSCENCE AUX JOINTS DE GRAINS.....	207
ANNEXE 4 : DONNÉES SUPPLÉMENTAIRES POUR L'ARTICLE RSI_2020	241
ANNEXE 5 : DONNÉES SUPPLÉMENTAIRES POUR L'ARTICLE NPJ.2D_2020.....	249
ANNEXE 6 : DONNÉES SUPPLÉMENTAIRES POUR L'ARTICLE NANOSCALE_2020.....	261

Liste des tableaux

TABLEAU 1 : DENSITÉS D'ESPÈCES DANS LA POST-DÉCHARGE EN FLUX POUR TROIS CONDITIONS DE PURETÉ DU GAZ PRINCIPAL. 180

Liste des figures

FIGURE 1 : A) DOUBLE-RÉSEAU TRIANGULAIRE DU GRAPHÈNE. B) STRUCTURE DE BANDE DU GRAPHÈNE [R2]. LES POINTS DE SYMÉTRIE M, K, K' ET Γ SONT IDENTIFIÉS.	19
FIGURE 2 : A) RELATION DE DISPERSION THÉORIQUE DES PHONONS DANS LE PLAN DU GRAPHÈNE B) SPECTRE RAMAN TYPIQUE DU GRAPHÈNE (ÉCHELLE LOGARITHMIQUE) [R2].....	20
FIGURE 3 : DÉCOUPLAGE DES EFFETS DE CONTRAINTE ET DU DOPAGE SUR LA POSITION DES BANDES 2D ET G. LES DIFFÉRENTS NUAGES DE POINTS SONT ASSOCIÉS À DES RECUTS SUBSÉQUENTS DE GRAPHÈNE SUR SiO ₂ (TEMPÉRATURE DE 100-400 °C) ET LA COURBE ROUGE PRÉSENTE LES VARIATION DES POSITIONS DE LA BANDE G ET 2D DE GRAPHÈNE INALTÉRÉ LORSQUE CELUI-CI EST SOUMIS À UN POTENTIEL DE GRILLE [R9]......	22
FIGURE 4 : ÉTAPES TYPIQUES DE CROISSANCE DE GRAPHÈNE PAR DÉPÔT CHIMIQUE EN PHASE VAPEUR [R12].	24
FIGURE 5 : PRODUCTION DE DÉFAUTS PAR BOMBARDEMENT IONIQUE POUR DIFFÉRENTS IONS INCIDENTS OBTENUE PAR DYNAMIQUE moléculaire avec potentiel analytique [R16]. Le dépôt d'énergie dans les niveaux électroniques n'est pas considéré dans les simulations d'approximation de collisions binaires.....	27
FIGURE 6 : A-E) REPRÉSENTATION PHÉNOMÉNOLOGIQUE DE LA VARIATION DE DÉFAUTS PRODUITS PAR FAISCEAU D'IONS [R17]. F) ÉVOLUTION DU SPECTRE RAMAN DU GRAPHÈNE EN FONCTION DE LA DOSE IONIQUE REÇUE D'IONS Ar ⁺ 90eV 45° G) ÉVOLUTION DU RATIO D/G EN FONCTION DE LA TAILLE DES CRYSTALLITES POUR PLUSIEURS ÉNERGIES DE RAYONNEMENT LASER. [R6]	28
FIGURE 7 : A) SPECTRE N1s de spectroscopie des photoélectrons induits par rayons X (XPS) pour un traitement de graphène par faisceau d'ions de N ⁺ de 25eV à 100eV. INCORPORATION GRAPHITIQUE (400.5eV) ET PYRIDINE (398.5eV). [R27] B) REPRÉSENTATION D'INCORPORATION D'AZOTE.	30
FIGURE 8 : A) ATTACHEMENT D'UN GROUPE ARYL PAR LA RÉDUCTION D'UN SEL DIAZONIUM. B) EXEMPLE DE RÉACTION DE CYCLOADDITION [R10].	32
FIGURE 9 : BOMBARDEMENT DE LA SURFACE PAR DIVERSES ESPÈCES DU PLASMA. A) NEUTRES B) IONS C) ÉTATS EXCITÉS D) PHOTONS. QUELQUES EXEMPLES DE RÉACTIONS DE GAIN DES ESPÈCES SONT PRÉSENTÉS À DROITE.	33
FIGURE 10 : DIAGRAMME DE POTENTIEL POUR A) L'ADSORPTION DISSOCIATIVE B) LA PHYSISORPTION ET C) L'ADSORPTION MOLÉCULAIRE. [R36]	34
FIGURE 11 : SCHÉMA D'UN TRAITEMENT (A) DIRECT ET (B) INDIRECT [R43]	37
FIGURE 12 : A) INTENSITÉS EN FONCTION DU TEMPS DES PRINCIPALES BANDES RAMAN, B) RATIO D:G ET D':D DU GRAPHÈNE TRAITÉ PAR PLASMA D'ARGON. TRACÉ À PARTIR DES DONNÉES PUBLIÉES DANS [R8].	38
FIGURE 13 : SPECTRE HAUTE RÉSOLUTION C1s XPS POUR LE GRAPHÈNE A) INALTÉRÉ ET C) TRAITÉ PAR PLASMA D'ARGON. B) COURBE COURANT-TENSION DE GFET [R3].	39
FIGURE 14 : SCHÉMA DE L'HYDROGÉNATION DU GRAPHÈNE DANS LES PLASMAS DE H ₂ [R34].	40
FIGURE 15 : A-B) TOMOGRAPHIE AFM D'UN TRAITEMENT INDIRECT EN PLASMA D'HYDROGÈNE À 500°C. 10MIN [R47] C) TOMOGRAPHIE AFM D'UN TRAITEMENT INDIRECT 500°C 20 [R48].	40

FIGURE 16 : MICROSCOPIE ÉLECTRONIQUE PAR EFFET TUNNEL (STM) DE TRAITEMENTS INDIRECTS PAR PLASMA D'OXYGÈNE. A) 0s B) 10 W/9 s c) 60 W/3 s d) 300 W/1.5 s e) AND 390 W/1.5 s. f) UN DÉFAUT TYPIQUE GÉNÉRÉ PAR LE TRAITEMENT. G) SPECTRE RAMAN ASSOCIÉ AUX TRAITEMENTS A)-e) [R42]	42
FIGURE 17 : TRAITEMENT POST-DÉCHARGE MICRO-ONDE AVEC POLARISATION DE SUBSTRAT ET PIÈGE À IONS. SPECTRES XPS N1s A) 1H PIÈGE ACTIVÉ. B) 35eV 10MIN PIÈGE DÉSACTIVÉ. C) 5eV 10MIN PIÈGE DÉSACTIVÉ. [R65].....	45
FIGURE 18 : EXEMPLES DE SPECTRE RAMAN POUR DES INCORPORATIONS DE N PAR TRAITEMENT PAR PLASMA DE N ₂ . A) GRAPHÈNE SOUS 2NM AL-OXYDE 150W N ₂ PLASMA [R69] b) 10W DIRECT RF N ₂ PLASMA [R70] c) 10W DIRECT RF N ₂ PLASMA [R71] d) 30-70W DIRECT N ₂ PLASMA [R63] e) TRAITEMENT INDIRECT EN PLASMA DE N ₂ AVEC PIÈGE À IONS ET SUBSTRAT POLARISÉ [R65]....	47
FIGURE 19 : A) SPECTRE RAMAN POUR UN TRAITEMENT INDIRECT DU PLASMA MICRO-ONDE NH ₃ . TRAITEMENT DE 0,3,6,9 MIN B) COURBE COURANT TENSION ET SPECTRE RAMAN ASSOCIÉ POUR DES TRAITEMENTS 0, 1, 2 MIN [R78].	50
FIGURE 20 : IMAGE DE LA POST-DÉCHARGE EN FLUX D'AZOTE. ON Y DISTINGUE SES QUATRE PRINCIPALES RÉGIONS.	52
FIGURE 21 : CARTOGRAPHIE (A) D:G, (B) 2D :G, (C) D:2D POUR L'ÉCHANTILLON NON TRAITÉ ET LE MÊME ÉCHANTILLON APRÈS 210 SECONDES DE TRAITEMENT PAR PLASMA.	126
FIGURE 22 : (A) LOCALISATION DES SPECTRES RAMAN IDENTIFIÉS COMME DES JOINTS DE GRAINS SUR LA RÉGION SONDÉE. (B) ÉVOLUTION DES DOMMAGES POUR LES DOMAINES DU GRAPHÈNE ET LES JOINTS DE GRAINS. LES COURBES VERTES ILLUSTRENT LES VARIATIONS ATTENDUES TEL QUE DÉCRITES PAR LE MODÈLE DÉVELOPPÉ PAR CANÇADO ET AL. POUR LES DÉFAUTS PUREMENT 0D ET 1D DANS [R91]	127
FIGURE 23 : SCHÉMA DE L'AUTO-RÉPARATION PRÉFÉRENTIELLE DES JOINTS DE GRAINS.: (1) FORMATION D'ADATOMES DE CARBONE ET DE LACUNES; (2) MIGRATION DES ADATOMES EN SURFACE; (3) TRANSPORT ANISOTROPIQUE LE LONG DES JOINTS DE GRAINS; (4) RÉPARATION DE DÉFAUTS AUX JOINTS DE GRAINS; (5) ÉMISSION DE CARBONE ET RÉPARATION DES DÉFAUTS À PROXIMITÉ DES JOINTS DE GRAINS. [R91]	128
FIGURE 24 : SPECTRES DES TROIS CONDITIONS ÉTUDIÉES POUR CIBLER LE RÔLE DES ESPÈCES OXYDANTES. ON DISTINGUE LE SECOND SYSTÈME POSITIF DE L'AZOTE (~316 NM) ET L'ÉMISSION DE LA NO _b À 320 NM.	180
FIGURE 25 : ÉVOLUTION DU RATIO D:A CORRIGÉ EN ÉNERGIE EN FONCTION DE LA LARGEUR À MI-HAUTEUR DE LA BANDE G. LES DEUX COURBES EN GRIS REPRÉSENTENT LE COMPORTEMENT ATTENDU POUR DES DÉFAUTS PUREMENT 0D OU 1D. LA LIGNE Verte EST POUR GUIDER L'ŒIL SEULEMENT.....	182
FIGURE 26 : ÉVOLUTION DU RATIO D:2D EN FONCTION DE LA FLUENCE TOTALE DE RECOMBINAISON DES N ET DE LA DÉSEXCITATION DES MÉTASTABLES N ₂ (A) EN SURFACE. LA LIGNE EST POUR GUIDER L'ŒIL UNIQUEMENT.	183
FIGURE 27 : RATIO XPS – N:C EN FONCTION DU RATIO RS – D:2D POUR TROIS CONDITIONS DE TRAITEMENT DANS LA POST-DÉCHARGE LOINTAINE AVEC PRÉSENCE D'ESPÈCES OXYDANTES. LES LIGNES SONT POUR GUIDER L'ŒIL ET POUR MATIÈRE À DISCUSSION SEULEMENT.....	185

Liste des sigles et abréviations

CVD	Dépôt chimique en phase vapeur (<i>Chemical Vapor Deposition</i>)
PECVD	Dépôt chimique en phase vapeur assisté par plasma (<i>Plasma-Enhanced Chemical Vapor Deposition</i>)
OES	Spectroscopie d'émission optique (<i>Optical Emission Spectroscopy</i>)
XPS	Spectroscopie des photo-photoélectrons X (<i>X-Ray photoelectron spectroscopy</i>)
RIMA	Raman IMAger™ - Photon ETC
SEM	Microscopie électronique à balayage (<i>Scanning Electron Microscopy</i>)
PCA	Analyse de composantes principales (<i>Principal Component Analysis</i>)
LA	Post-décharge lointaine (<i>Late Afterglow</i>)
EA	Post-décharge proche (<i>Early Afterglow</i>)
FPS	Premier système positif (<i>First positive system</i>)
SPS	Deuxième système positif (<i>Second positif system</i>)
FNS	Premier système négatif (<i>First negatif system</i>)

Remerciements

Je tiens tout d'abord à remercier mon directeur de thèse, Luc Stafford, qui m'a accordé sa confiance et son support alors que j'entamais mes débuts en recherche et qui m'a accompagné tout au long de mon développement dans le domaine.

J'aimerais également remercier les différents groupes avec lesquels j'ai collaboré lors de ma thèse et qui ont enrichi ma démarche au fur et à mesure de diverses rencontres. Un merci aux groupes de Michel Côté et de Richard Martel, et plus particulièrement aux étudiants Olivier Malenfant-Thuot, Carl Charpin et Charlotte Allard.

Un grand merci également à tous mes collègues du groupe de physique des plasmas de l'UdeM (*PPHARE* !) pour avoir rendu nos discussions, qu'elles soient formelles ou informelles, des plus intéressantes. Un merci particulier à Danielle, Leron, Xavier, Pierre et Antoine.

Je tiens à souligner aussi l'appui de mes amis de longue date avec lesquels j'ai pu profiter de moments significatifs essentiels pour me ressourcer. Merci à George, Guillaume, Jacqueline et Félix.

Un grand merci à toute ma famille qui m'a supporté tout au long de mon parcours. Votre support me tient à cœur. Merci à ma mère Monique, mon père Robert, mon frère Clément et ma sœur Juliette.

Et finalement, merci à mon amoureuse, Josiane, qui m'inspire à me dépasser et qui m'épaule dans toutes les circonstances !

Introduction

Dû à ses différentes hybridations possibles, le carbone peut composer un nombre important de structures, ses allotropes, comprenant notamment le graphite, le diamant, le graphène et les nanotubes de carbone. Le caractère distinct des propriétés de chacun de ces allotropes implique un nombre important de perspectives d'innovations dans le domaine des nanotechnologies. Depuis sa découverte expérimentale en 2004 [R1], le graphène ne cesse de susciter la fascination et de motiver un nombre considérable de recherches visant à exploiter ce matériau bidimensionnel novateur aux propriétés étonnantes dans une multitude de domaines d'applications.

Que ce soit à des fins de conception de systèmes miniatures à base de graphène ou de composition d'hétérostructure 2D, la nature monocouche du graphène représente un avantage considérable dans le fort engouement collectif de miniaturisation des dispositifs. Dans son état inaltéré, le graphène étonne par la force de ses liaisons intraplanaires, le confinement 2D de ses électrons de valence, sa forte conduction thermique, sa vitesse du son étonnante et sa forte transparence dans le visible. Les premières applications du graphène se sont ainsi focalisées sur ces propriétés. Toutefois, l'absence de bande d'énergie interdite de ce semi-métal entrave son utilisation pour certains dispositifs. La perspective de doper le graphène de porteurs de charge (négatifs ou positifs) étant centrale à son application en microélectronique et en optoélectronique, des efforts de recherche considérables sont maintenant dédiés au développement de techniques novatrices de modification du graphène.

L'enjeu industriel central à l'utilisation du graphène à grande échelle reste la synthèse de graphène de haute qualité tout en minimisant les coûts et la complexité du procédé. Doivent ensuite être développées des méthodes de traitement efficaces et adéquates selon l'application désirée. Ceci inclut des méthodes de dopage du graphène, par exemple par substitution d'un atome de carbone par un autre élément, ou encore des méthodes de fonctionnalisation, par exemple par greffage de groupements fonctionnels. Depuis sa découverte, le graphène est maintenant mis à l'épreuve, soumis à de nombreux traitements physiques et chimiques (et physico-chimiques), afin de mieux comprendre son comportement dans ces environnements.

Comme la réactivité du graphène est étroitement liée à la qualité de sa synthèse, à l'interaction avec son substrat et à sa structure (surface concave ou convexe, présence de joints de grains, monocouche ou multicouche, etc.), une pleine compréhension des processus physiques et chimiques mis en jeu dans le traitement post-synthèse du graphène est centrale à l'établissement de propriétés optimales du graphène modifié.

Parmi les méthodes de traitement du graphène, plusieurs procédés basés sur les plasmas, déjà bien établis en industrie, ont démontré leur fort potentiel. Ils se sont avérés une alternative sèche, rapide et écologique aux méthodes humides traditionnelles. Les plasmas sont également mieux adaptés à l'automatisation et leur grand éventail de conditions opératoires leur permet de favoriser une variété de processus physiques ou chimiques. C'est la grande diversité d'espèces actives mises en jeu (électrons, ions, anions, neutres, métastables, photons, radicaux, etc.) qui confère cette polyvalence aux procédés assistés par plasmas.

À ce jour, plusieurs milieux plasmagènes ont été explorés pour le traitement du graphène, incluant les plasmas d'argon, d'hydrogène, d'oxygène, d'azote et d'ammoniac. La physique des interactions plasmas-nanomatériaux reste toutefois à un niveau embryonnaire. Beaucoup d'inconnus demeurent au niveau de l'impact combiné des diverses espèces actives dans les traitements des matériaux de faibles dimensions comme le graphène. C'est pourquoi il est important de corrélérer exhaustivement les études des propriétés des matériaux traités par plasma aux études des caractéristiques du plasma. Ceci permettrait non seulement de faire des avancées majeures au niveau de la physique des divers processus mis en jeu mais aussi de judicieusement choisir les conditions opératoires du plasma favorables à l'obtention des propriétés désirées selon l'application envisagée.

Parmi l'éventail de sources à plasma couramment utilisées pour le traitement des matériaux et des nanomatériaux, on note les décharges capacitives et inductives produites par des champs électriques radiofréquences. Selon le choix des conditions opératoires, ces plasmas peuvent présenter de faibles (10^9 - 10^{10} cm $^{-3}$) ou de fortes (10^{11} - 10^{12} cm $^{-3}$) densités de particules chargées. Cependant, dans tous les cas, ces plasmas impliquent de fortes populations d'ions positifs accélérés dans une gaine au voisinage de la surface du graphène exposée au plasma. L'interaction

de ces ions avec le graphène peut induire des dommages importants, ce qui peut être problématique pour certaines applications. Pour contourner ce problème, plusieurs chercheurs ont proposé de recourir à des post-décharges spatiales ou temporelles. Ces milieux présentent l'avantage de fortes populations d'espèces neutres réactives mais souffrent de l'inconvénient qu'aucune espèce de plus haute énergie n'est présente pour initier certaines modifications physiques et chimiques.

Dans ce contexte, nous désirons explorer dans cette thèse de doctorat le potentiel de la post-décharge en flux de plasmas micro-ondes à pression réduite. Sous atmosphère d'azote, ces plasmas font apparaître une proche et une lointaine post-décharge avec des propriétés fondamentales intermédiaires entre le plasma principal et les post-décharges spatiales habituelles. Ainsi, les objectifs spécifiques de cette thèse sont: (1) *Réaliser une étude de pointe des propriétés fondamentales de la post-décharge en flux en fonction de ses conditions opératoires*. Pour ce faire, une nouvelle méthode de détermination de position dans la post-décharge (coefficients a ; $a = 0$ dans la proche post-décharge et $a = 1$ dans la post-décharge lointaine) est mise au point et utilisée pour évaluer des profils de densité des espèces les plus pertinentes pour l'interaction plasma-graphène ($N_2(A)$, $N(^4S)$, O). Des mesures de sonde de Langmuir permettent également d'obtenir les densités ionique et électronique. Les conditions de pureté du gaz d'azote sont aussi étudiées par l'ajout d'un purificateur de gaz. (2) *Explorer le potentiel de ces plasmas pour l'incorporation d'azote dans des films de graphène*. Différentes conditions expérimentales sont donc étudiées : position dans la post-décharge lointaine ou proche. L'étude de l'état de surface du graphène est réalisée par différentes méthodes de caractérisation des matériaux : spectroscopie des photoélectrons X (XPS), spectroscopie Raman (RS), microscopie électronique à balayage (MEB) et microscopie optique. (3) *Réaliser une étude fondamentale des interactions plasma-graphène en isolant les facteurs gouvernant la formation de dommages et l'incorporation des atomes d'azote dans le graphène traité par plasma*. Par le biais de conditions expérimentales judicieusement contrôlées, nous avons notamment pu étudier le rôle des espèces oxydantes, des atomes d'azote issus de la dissociation de $N_2(X)$, des métastables d'azote $N_2(A)$ sur la nature et l'amplitude des dommages, les effets de contrainte et le dopage. Un modèle d'incorporation des atomes d'azote est aussi proposé.

La thèse est divisée comme suit. Le premier chapitre porte sur les propriétés physico-chimiques du graphène, les méthodes de synthèse et les différentes approches de traitement de matériaux couramment utilisées afin de contrôler ses caractéristiques. Plus particulièrement, une revue des différents types de traitement basés sur les plasmas est détaillée afin de pouvoir mieux cibler le rôle des espèces actives dans divers milieux plasmagènes : argon, hydrogène, oxygène, azote et ammoniac. Le deuxième chapitre démontre l'importance d'un fin contrôle des conditions expérimentales sur le traitement par plasma du graphène. Les effets du vieillissement et des inhomogénéités spatiales d'échantillons sont d'abord discutés, puis les conditions expérimentales de traitement dans la post-décharge sont établies afin de favoriser la fonctionnalisation du graphène sans génération de dommages excessifs. Dans le chapitre 3, une nouvelle méthode d'analyse quantitative par spectroscopie Raman est mise au point afin de pallier les problématiques d'inhomogénéités de surface révélées au chapitre précédent. Cette méthode repose sur des mesures sur un nouvel appareil, le RIMA™ (Raman IMAge) développé par *Photon ETC*, et permet de suivre localement les évolutions de désordre, de contrainte et de dopage après traitement par plasma. Une auto-réparation préférentielle des joints de grains et un dopage préférentiel des domaines du graphène sont révélés. Finalement, au chapitre 4, selon un choix judicieux de conditions opératoires, les rôles de diverses espèces actives de la post-décharge en flux d'azote sont isolés. Enfin, une conclusion de ces recherches ainsi que quelques perspectives d'application pour l'avenir seront présentées.

Les mesures et analyses discutées dans ce travail sont surtout présentés sous la forme d'articles publiés ou récemment soumis pour publication dans des journaux scientifiques. La contribution spécifique de l'auteur à chacun de ces travaux est précisée avant chaque article.

Chapitre 1 – Revue de la littérature

Ce chapitre porte sur les propriétés fondamentales du graphène et l’altération de celles-ci lorsque l’échantillon est soumis à diverses méthodes de post-traitement. En premier lieu, les propriétés physico-chimiques du graphène sont présentées. Du fait de leur importance sur la structure du graphène et de leur effet sur les post-traitements, un survol des méthodes de croissance doit être réalisé. L’ensemble des méthodes les plus courantes de post-traitement sont ensuite revues et discutées, incluant celles basées sur des plasmas.

1.1 Graphène : propriétés, synthèse et traitement

Cette section présente les concepts fondamentaux desquels émerge l’intérêt porté au graphène depuis sa découverte. Les principales propriétés électroniques et vibrationnelles du graphène inaltéré sont détaillées en évoquant les fondements théoriques. Les propriétés du graphène ont été abondamment étudiées dans le passé et leur sensibilité aux défauts révèle que les contraintes expérimentales peuvent altérer de façon importante le graphène. Une liste non exhaustive des méthodes de synthèse et de traitement post-synthèse est exposée afin de pouvoir en établir les similitudes avec les traitements par plasma.

1.1.1 Propriétés physico-chimiques du graphène

Le graphène est une variété allotropique du carbone essentiellement bidimensionnelle composée de deux sous-réseaux triangulaires d’atomes de carbone (**Figure 1a**). L’existence même des différents allotropes du graphène provient de la capacité du carbone à s’organiser selon plusieurs hybridations. Ces hybridations consistent en un réarrangement des orbitales du carbone non lié ($2s, 2p_x, 2p_y, 2p_z$) afin de minimiser leur énergie. Ces hybridations confèrent au carbone des configurations géométriques définies qui permettent des agencements bien particuliers donnant lieu à des structures comme le diamant (tétraèdre régulier), le graphène (triangle) et le carbyne (linéaire). Dans le cas du graphène, chaque atome suit une hybridation de type sp^2 : l’atome non hybridé subit une transformation de son niveau $2s$ et deux de ses niveaux $2p$ (p_x et p_y où x et y sont dans la direction du plan) vers trois niveaux dégénérés. Ces trois orbitales forment des liaisons covalentes σ avec trois carbones adjacents dans le réseau graphénique. La troisième

orbitale 2p (p_z) de chaque atome est orientée hors du plan et forme une liaison π avec un carbone adjacent. L'ensemble des liens π forme un nuage d'électrons délocalisés en surface du graphène. Ce système peut être décrit comme un gaz bidimensionnel d'électrons d'une épaisseur de 3 Å, la distance interatomique des atomes de carbone étant typiquement de 1.42 Å [R2]. Les propriétés du graphène sont ici discutées en faisant la distinction entre ses propriétés électroniques et ses propriétés vibrationnelles.

Propriétés électroniques du graphène

Rappelons ici la dualité onde-particule des électrons essentielle à la compréhension des propriétés électroniques du graphène. On s'intéresse aux fonctions d'onde permises ainsi que leur énergie pour un électron dans un solide périodique infini. La structure de bande, ou relation de dispersion des électrons, est définie comme l'ensemble des valeurs possibles d'énergie d'un électron pour une impulsion donnée. Par le principe d'exclusion de Pauli, deux électrons ne peuvent occuper le même état de sorte que les électrons remplissent d'abord les bandes d'énergie inférieures.

La structure de bande particulière du graphène le distingue des métaux et des semi-conducteurs conventionnels. La configuration entre la bande de valence et de conduction permet de distinguer les matériaux métalliques des isolants et des semi-conducteurs. Si aucune bande d'énergie interdite n'est présente entre le dernier niveau occupé (niveau de Fermi) et la bande de conduction, alors le matériau est dit métallique. Par opposition aux métaux, si une bande d'énergie interdite est présente au niveau de Fermi, alors le matériau est dit isolant ou semi-conducteur. La **Figure 1b** illustre les bandes de conduction et de valence du graphène. Celles-ci ont la particularité de se rejoindre en un point dans l'espace d'impulsion ; le graphène est dit semi-métal. De plus, le comportement linéaire de la relation de dispersion aux points d'impulsion K et K' confère aux électrons une masse effective nulle [R2].

En présence d'un apport d'énergie externe, par exemple un photon d'énergie $E = hc/\lambda$, il est possible de faire passer un électron de la bande de valence (en y laissant un trou) vers la bande de conduction selon une transition purement verticale (en négligeant l'impulsion conférée par le photon). Cependant, l'efficacité d'absorption du graphène dans le visible est faible (2.3%). De

plus, les temps de vie de recombinaison des paires électron-trou sont très faibles (~ 1.5 ps) de sorte que les photodéTECTEURS à base de graphène possèdent typiquement de mauvaises photoréponses [R3].

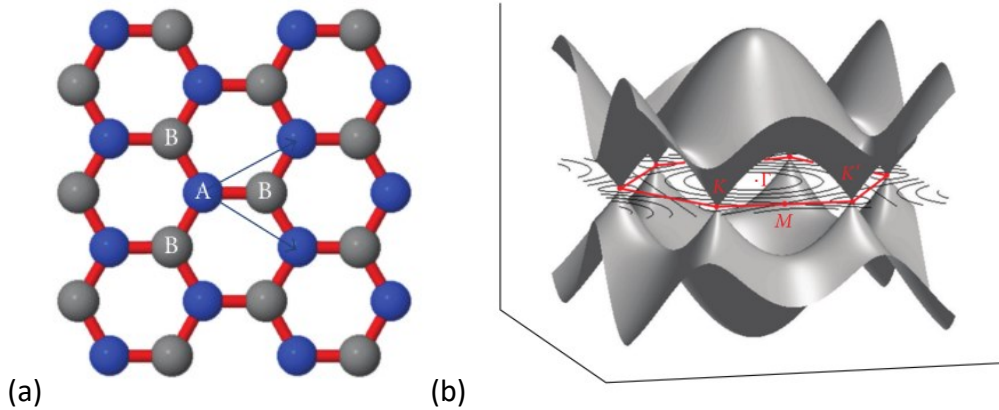


Figure 1 : a) Double-réseau triangulaire du graphène. b) Structure de bande du graphène [R2]. Les points de symétrie M, K, K' et Γ sont identifiés.

Propriétés vibrationnelles du graphène

Les propriétés électroniques fascinantes du graphène ne sont pas les seules raisons pour l'engouement de la recherche sur ce matériau de faible dimension. La force importante des liens entre les atomes aussi légers du plan du graphène (σ -bonds : 3.8eV) confère au son une vitesse remarquable (20 km/s) et une conductivité thermique record (5300 W/mK) [R2]. Cette forte conductivité lui permet ainsi de dissiper rapidement la chaleur, un enjeu important pour les dispositifs électroniques.

Étant donné la nature cristalline du graphène, seul certains modes de vibration des atomes du réseau (les phonons) sont permis. De façon analogue aux relations de dispersion des électrons, on peut établir une relation entre l'énergie et la quantité de mouvement des phonons. La relation de dispersion théorique des phonons du graphène est illustrée à la **Figure 2a**. On distingue six types de vibrations. Les phonons sont séparés en modes acoustiques A (d'énergie nulle au point d'impulsion nulle) et modes optiques O. Les modes peuvent être longitudinaux (LO et LA), orientés selon l'axe de liaison interatomique, ou traverses (TO et TA), contenus dans le plan graphénique mais perpendiculaires à la liaison interatomique. Certains modes sont également

hors-plan (ZO et ZA). La force des liens intraplanaires explique la plus grande vitesse des phonons LA (23.6m/s) par rapport aux modes TA (15.9m/s) [R4].

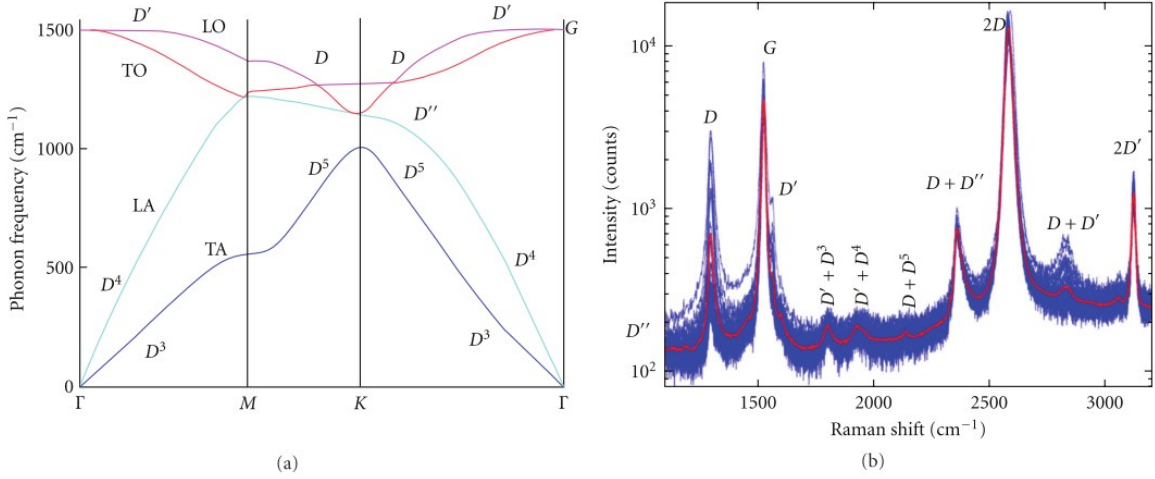


Figure 2 : a) Relation de dispersion théorique des phonons dans le plan du graphène b) Spectre Raman typique du graphène (échelle logarithmique) [R2].

L'absorption de photons par le graphène peut être exploitée comme méthode de caractérisation, par exemple la spectroscopie Raman utilisant un faisceau laser focalisé. Si l'électron excité par l'absorption du photon n'interagit avec rien, il se désexcitera en émettant un photon de même énergie. Si l'électron entre en collision avec un défaut ou émet/absorbe des phonons, alors le photon réémis par la désexcitation possèdera une longueur d'onde proche mais légèrement différente de celle de l'excitation. Cette différence d'énergie est caractéristique des types de défauts dans la zone caractérisée par le faisceau laser et les intensités relatives des différentes bandes obtenues renseignent alors sur l'état du graphène.

Par exemple, la présence de défauts structurels, d'hétéroatomes, d'espèces adsorbées ou même tout simplement d'un substrat peut venir modifier le libre parcours moyen des phonons (250 nm [R4] dans le graphène inaltéré) et ainsi induire de nouvelles transitions dans l'espace d'impulsion et d'énergie. Ces modifications se répercutent via les processus de diffusion photon-phonon et électron-phonon, c'est-à-dire sur les propriétés optiques et électroniques, respectivement.

Pour illustrer brièvement ce phénomène, un exemple de spectre Raman du graphène est présenté à la **Figure 2b**. Le graphène inaltéré présente deux signatures majeures: la bande G ($\sim 1580 \text{ cm}^{-1}$) et la bande 2D ($\sim 2700 \text{ cm}^{-1}$). La première est associée à un processus de diffusion électron-phonon de premier ordre dans les structures graphitiques alors que la deuxième repose sur l'interaction de deux phonons dans le graphène [R5]. En présence de dommages, l'électron excité par l'absorption du photon peut interagir avec un défaut pour modifier son impulsion. L'émission subséquente donne lieu à la bande D ($\sim 1350 \text{ cm}^{-1}$). Cette bande est donc directement reliée à la présence de défauts dans le graphène et augmente avec la densité de ceux-ci. Le ratio D:G est couramment utilisé pour quantifier les dommages dans les structures graphéniques. Ce ratio augmente avec les dommages, jusqu'à ce que la largeur à mi-hauteur des bandes D et G augmente. Au-delà de ce point, le ratio D:G diminue avec les dommages. [R6] Ce comportement est discuté plus en profondeur à la **Section 1.1.3** (Faisceau d'ions). La présence des défauts dans le graphène donne également lieu à une autre bande caractéristique: la bande D' ($\sim 1620 \text{ cm}^{-1}$) [R7]. Le ratio D:D' permet de distinguer si les défauts sont principalement de type sp^3 (D:D' ~ 13), lacune (D:D' ~ 7) ou bord de grains dans le graphite (D:D' ~ 3) [R8].

En plus des modifications sur l'intensité des bandes Raman, la modification du graphène peut entraîner des variations de la position des bandes. Par exemple, l'application de contraintes (de compression ou de traction) et la modulation de la densité de porteurs de charge peuvent modifier la position des bandes G et 2D [R9]. À titre d'exemple, la **Figure 3** présente les variations de position des bandes G et 2D en accentuant les axes permettant de découpler les effets des contraintes et du dopage. On remarque que la bande 2D est plus sensible aux contraintes alors que le dopage influence principalement la position de la bande G.

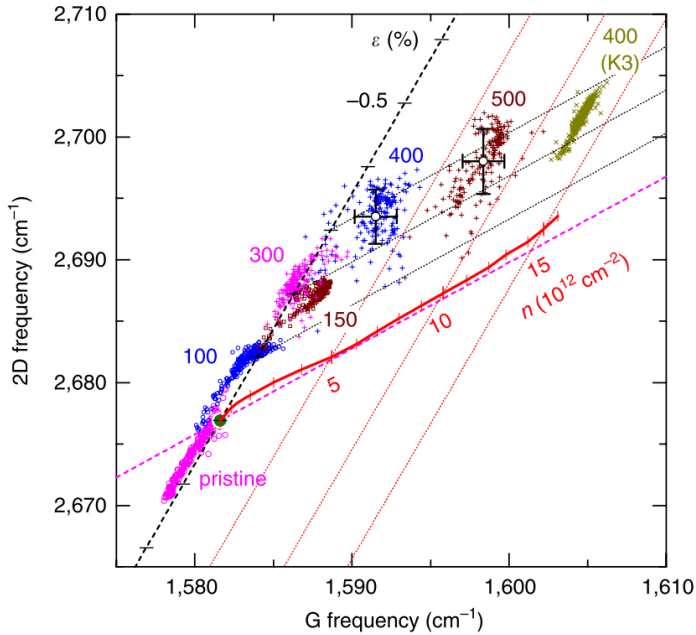


Figure 3 : Découplage des effets de contrainte et du dopage sur la position des bandes 2D et G. Les différents nuages de points sont associés à des recuits subséquents de graphène sur SiO_2 (température de 100-400 °C) et la courbe rouge présente les variations des positions de la bande G et 2D de graphène inaltéré lorsque celui-ci est soumis à un potentiel de grille [R9].

1.1.2 Méthodes de synthèse du graphène

Avec les années, une multitude de méthodes de synthèse du graphène ont été développées et optimisées. Les méthodes sont couramment classées en deux catégories : ascendantes (*bottom-up*) ou descendantes (*top-down*) [R10]. Dans le premier cas, la synthèse du graphène est effectuée avec des précurseurs à base de carbone. Il suffit de les assembler pour en obtenir ultimement une feuille de graphène. Dans le deuxième cas, le procédé utilise des composés à base de carbone arborant déjà une structure composée de graphène. On distingue un nombre important de méthode ascendante (dépôt chimique en phase vapeur, décomposition thermique du SiC) et descendantes (exfoliation mécanique, dépôt par faisceau moléculaire, ouverture de nanotubes de carbone, pyrolyse de sodium et d'éthanol, réduction d'oxyde de graphène, décharge d'arc du graphite, conversion de nano-diamants, synthèse solvothermique, méthode par flamme) [R2,11]. Afin de comparer les différentes méthodes, plusieurs paramètres sont pertinents : leur rapidité, leur simplicité, leur coût, leur impact écologique, la qualité du graphène

obtenu, les dimensions du graphène obtenu, le support du graphène (restriction quant à la nature du substrat, graphène en solution, poudre, etc.) et la souplesse de la méthode. Nous nous contenterons ici de ne détailler que trois de ces techniques, apparaissant, vu leur importance historique et leur potentiel industriel, appropriées à notre étude sur les films de graphène (par rapport au graphène en solution et en poudre).

Exfoliation mécanique

Historiquement, la toute première synthèse vérifiée de graphène fut réalisée par *Geim et Novoselov* [R1] par exfoliation mécanique du graphite. Cette méthode *top-down* utilise un échantillon de HOPG (*highly oriented pyrolytic graphite*) sur lequel sont gravées des structures de 5 µm de hauteur par plasma d'oxygène. Ces dernières sont ensuite fixées à un polymère photorésistant par chauffage. On applique alors une force pour détacher les structures du substrat. Une multitude de passages avec un film adhésif (*scotch tape*) permet de retirer des feuillets de graphène excédentaire jusqu'à ce qu'il ne reste qu'un nombre très faible de couches de graphène. Un nettoyage à l'acétone permet ensuite de dissoudre le polymère. Des feuillets de graphène d'un nombre variable de couches (1-10) peuvent être récupérés sur un autre substrat. La méthode permet d'obtenir des échantillons de bonne qualité (peu de défauts, bonne conduction thermique), mais de faible dimension (inférieur au mm² [R2]). De plus, le contrôle du nombre de couches est difficile. Il est nécessaire d'utiliser des méthodes de caractérisation pour s'assurer que le nombre de passages avec le film adhésif est suffisant, un même échantillon pouvant être composé d'îlots de graphène constitués de 1 à 10 couches. Pour ces raisons, l'exfoliation mécanique est surtout destinée à la recherche fondamentale et difficilement applicable en milieu industriel.

Dépôt chimique en phase vapeur

Le dépôt chimique en phase vapeur (CVD – *Chemical Vapor Deposition*) est une méthode *bottom-up* de croissance avec gaz précurseur. Avec un apport d'énergie approprié, un gaz précurseur (couramment le CH₄) subit des réactions chimiques (en phase gaz ou sur le substrat) qui permettent la formation d'une structure solide stable. Les réactions en phase gaz sont importantes lorsque le gaz précurseur est chauffé au-dessus de sa température de décomposition

(1200°C pour le CH₄) ou qu'un apport d'énergie externe (comme dans un plasma) permet la dissociation du précurseur. Celui-ci peut alors former d'autres composés plus complexes qui peuvent également réagir avec le substrat ou simplement se déposer.

Pour ces réactions en phase gaz, l'emploi d'un substrat (couramment le nickel et le cuivre) jouant le rôle de catalyseur à la décomposition thermique du précurseur permet de diminuer la température de décomposition (à ~1000°C pour le CH₄) et de favoriser des réactions chimiques limitées par la surface. Les mécanismes responsables de la croissance sont illustrés à la **Figure 4**. Brièvement, la principale différence entre les deux croissances illustrées provient du fait que le carbone possède un taux de dissolution beaucoup plus faible dans le cuivre que dans le nickel. Dans le cas du Ni, les atomes de carbone dissous dans le substrat à haute température réémergent par ségrégation lors du retour aux basses températures. En conséquence, des structures multicouches (1-2) sont typiquement obtenues contrairement au graphène le plus souvent monocouche sur Cu. [R12]

La présence de domaines cristallins ou de défauts sur le substrat augmente la densité de sites de nucléation et entraîne une baisse de la taille des domaines de graphène. De plus, la taille de ces domaines dépend de l'orientation cristalline du Cu puisque la migration en est dépendante [R13]. Les joints de grains du graphène, représentant des sites plus réactifs pour les réactions chimiques, diminuent les barrières de perméation et entraînent une diminution du libre parcours moyen des phonons et des paires électron-trou et [R14].

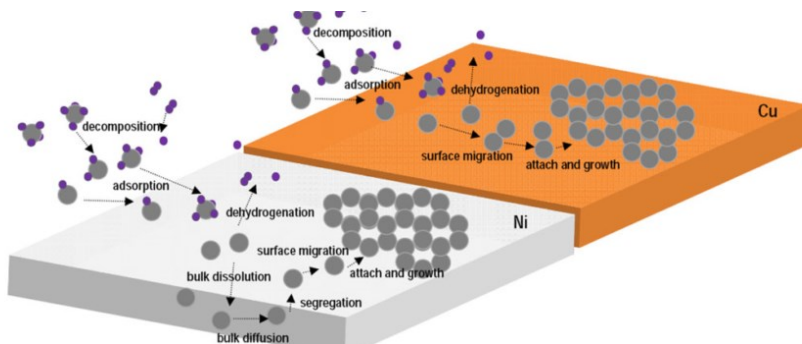


Figure 4 : Étapes typiques de croissance de graphène par dépôt chimique en phase vapeur [R12].

Grâce au bon contrôle du nombre de couches de graphène, à la grande surface de croissance et à la possibilité d'automatisation en milieu industriel, ces méthodes de synthèse CVD possèdent un fort potentiel d'applications, en particulier en microélectronique.

Dépôt chimique en phase vapeur assisté par plasma

Le dépôt chimique en phase vapeur assisté par plasma (PECVD – *Plasma Enhanced Chemical Vapor Deposition*) est une variante de la croissance par CVD. En particulier, ce processus repose sur des espèces énergétiques issues d'un plasma pour dissocier les molécules en phase gaz ; la décomposition thermique n'est donc plus requise et la croissance n'est plus limitée par les réactions en surface. Les structures obtenues peuvent être verticalement alignées et/ou déposées sur des substrats variés [R15]. Les méthodes de PECVD autorisent également l'introduction de différents gaz réactifs dans le plasma afin de venir incorporer d'autres atomes et ainsi modifier les propriétés physico-chimiques du graphène en cours de synthèse [R11].

1.1.3 Méthodes de traitement post-synthèse du graphène

Pour les applications où les propriétés intrinsèques du graphène inaltéré ne suffisent pas, un traitement post-synthèse du graphène est requis afin de modifier ses propriétés électroniques et vibrationnelles. Les méthodes de traitement peuvent viser plusieurs types de modifications des matériaux bidimensionnels comme le graphène: incorporation d'hétéroatomes, contrôle de la configuration chimique d'hétéroatomes, contrôle du type de bord du graphène, ingénierie de surface du graphène (découpe, gravure), production de défauts ponctuels ou étendus, restauration de défauts de croissance, greffage de groupes fonctionnels sur le plan ou les bords, etc.

Les impacts d'un traitement du graphène sur les propriétés de celui-ci peuvent être multiples. Parmi la panoplie de fonctionnalisation par traitements secs et humides développés au cours des années, on peut citer le dopage (d'électrons ou de trous pour modifier le niveau de Fermi), l'ouverture d'une bande d'énergie interdite dans la structure de bande du graphène, l'introduction de niveaux d'énergie de défauts dans la bande d'énergie interdite, la modification de sa réactivité de surface, l'augmentation de sa conductivité thermique ou électrique, etc. La

section qui suit fait état des principaux types de traitements post-croissance et de leur impact sur la structure ou la réactivité du graphène.

Faisceau d'ions

Lors de traitements de matériaux et de nanomatériaux par faisceaux d'ions, il est possible d'ajuster la nature, l'énergie et la dose des ions incidents sur le substrat. À basse énergie, les ions ne sont pas en mesure, en principe, de fournir l'énergie nécessaire au déplacement ou encore à l'éjection d'un seul carbone, alors qu'à plus haute énergie, l'ion risque d'entraîner des cascades collisionnelles complexes pouvant mener à la pulvérisation, l'implantation et des dommages plus étendus.

Historiquement, les modèles théoriques de bombardement de surface ont souvent été développés pour des matériaux pleins (*bulk materials*) où l'on peut considérer la cible comme un ensemble d'atomes de densité uniforme et le plus souvent répartis dans une structure amorphe. Il faut alors réaliser des expériences de dynamique moléculaire pour bien représenter le bombardement de structures cristallines où l'orientation peut jouer un rôle majeur, par exemple pour la canalisation des ions. La **Figure 5** présente différents types de défauts générés dans une monocouche de graphène à température ambiante par le bombardement de divers ions avec une énergie variant de quelques dizaines d'eV à 1 MeV. À basse énergie, les défauts sont principalement ponctuels (lacunes simples et doubles). Les défauts complexes deviennent importants à plus haute énergie, pour lesquelles les reculs dans le plan deviennent significatifs [R16].

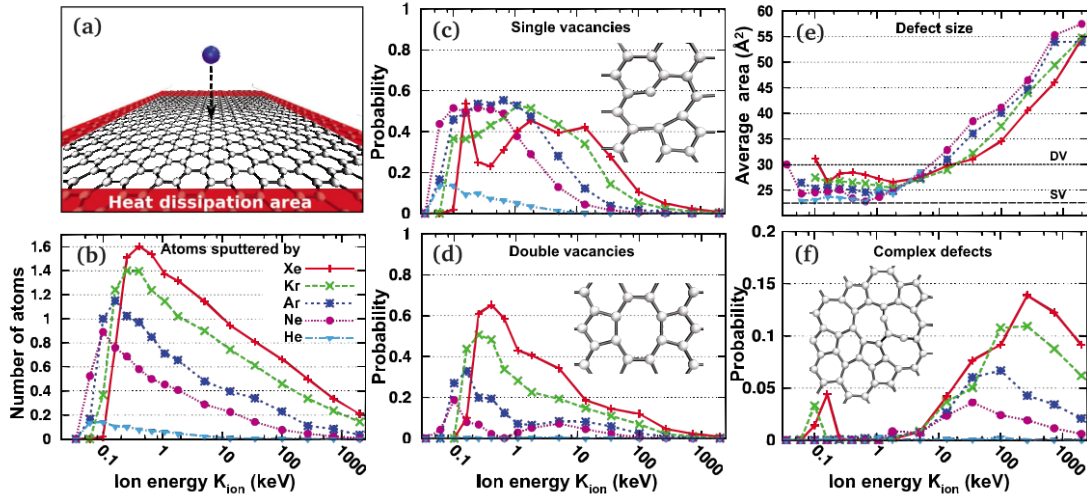


Figure 5 : Production de défauts par bombardement ionique pour différents ions incidents obtenue par dynamique moléculaire avec potentiel analytique [R16]. Le dépôt d'énergie dans les niveaux électroniques n'est pas considéré dans les simulations d'approximation de collisions binaires.

Pour expliquer les dommages d'irradiation dans le graphène, Lucchese *et al.* [R17] ont proposé un modèle phénoménologique du bombardement ionique en fonction de la dose. Selon leur modèle, les impacts ioniques donnent lieu à deux zones particulières de défauts : une zone de dommages structurels entourée d'une zone d'activation (**Figure 6a**). L'aire totale de ces deux régions croît initialement avec la dose jusqu'à ce que la densité de sites irradiés devienne si importante ($\sim 10^{13}\text{cm}^{-2}$) que les zones de défauts structurels détruisent des zones activées. Cette transition de structure de l'échantillon est analogue au modèle de Ferrari et Robertson [R18] qui propose une transition à partir de graphite inaltéré vers des structures amorphes en trois régimes distincts. Lors du régime 1, il y a une transformation des larges grains en nanocristallites (graphite polycristallin). Quant au régime 2, il est caractérisé par une formation graduelle de carbone amorphe composé de regroupements de carbone sp^2 . Finalement, lors du troisième régime, il y a formation de carbone tétraédrique amorphe par l'augmentation des liens sp^3 .

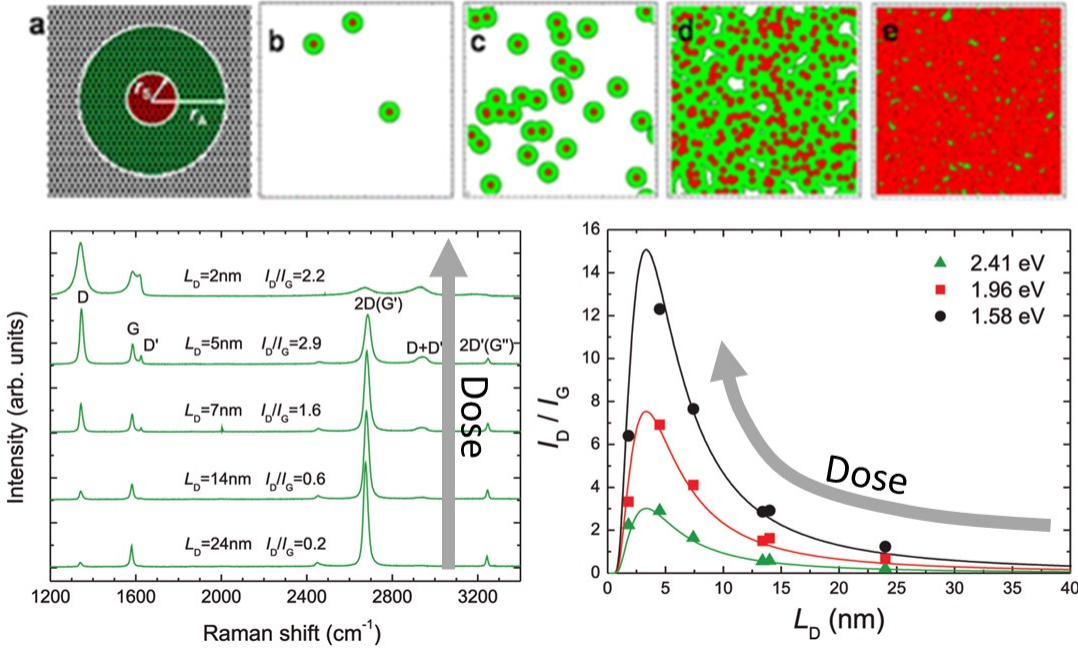


Figure 6 : a-e) Représentation phénoménologique de la variation de défauts produits par faisceau d’ions [R17]. f) Évolution du spectre Raman du graphène en fonction de la dose ionique reçue d’ions Ar⁺ 90eV 45° g) Évolution du ratio D/G en fonction de la taille des cristallites pour plusieurs énergies de rayonnement laser. [R6]

Tel que mentionné à la **Section 1.1.1**, la spectroscopie Raman peut renseigner sur les dommages structurels, notamment ceux causés par irradiation ionique. Les dommages peuvent modifier la valeur de la fréquence des bandes, leur élargissement et leur asymétrie [R19]. À titre d'exemple, la **Figure 6f** présente les spectres Raman pour un échantillon de graphène sur SiO₂ pour plusieurs doses ioniques entre 10^{11} Ar⁺ cm⁻² et 10^{15} Ar⁺ cm⁻² (90eV) [R6]. Pour des doses croissantes, le ratio D:G augmente, ce qui peut être corrélé à une variation de la taille des cristallites [R20]. En particulier, pour toutes les énergies du laser étudiées lors des mesures de spectroscopie Raman, la **Figure 6g** montre que le rapport D:G augmente tout d'abord avec la diminution de L_D suivant la relation de Tuinstra et Koenig ($I_D/I_G \propto 1/E_{\text{laser}}^4 L_a$) [R7,20]. Ce comportement est conforme au régime 1 de Ferrari et Robertson [R18] selon lequel l'irradiation du graphite conduit à la formation de nanocristallites (**Figure 6b-c**). L'augmentation du ratio D:G avec la dose d'irradiation est suivie d'une diminution assez abrupte reliée à de l'amorphisation (régime 2). Pour interpréter ce phénomène, Lucchese et al. [R17] ont proposé une expression analytique du rapport D:G.

Celle-ci comprend un premier terme associé aux dommages structurels, et un second, aux régions d'activation :

$$I_D/I_G(L_D) = C_S f_S(L_D, r_s) + C_A f_A(L_D, r_A, r_s) \quad (1.1)$$

où C_S et C_A sont les réponses Raman des régions structurellement endommagées et activées et f_S et f_A sont les fractions du plan occupées par chaque région. Ainsi, l'augmentation du rapport D:G avec les dommages d'irradiation s'explique par une augmentation de f_S et f_A (voir **Figure 6a-e**). Cependant, puisque $C_A > C_S$, on observe une diminution de D:G lorsque les dommages d'irradiation deviennent tels que la fraction du plan occupé par les zones activées commence à diminuer (conversion des zones activées en zones de défaut structurel). Notons que la transition entre le régime 1 et le régime 2 a lieu lorsque l'espacement entre les défauts devient plus faible que la distance moyenne parcourue par une paire électron-trou avant de diffuser avec un phonon [R6]. La **Figure 6f** montre également une décroissance importante de la bande 2D, un décalage de la bande G vers le bleu, ainsi qu'un élargissement des bandes G et 2D.

Les faisceaux d'ions peuvent également être utilisés pour « couper/façonner » le graphène; on parle alors de *nanopatterning* [R21,22]. Cette structuration du graphène peut être employée pour la conception de dispositifs électroniques, mais peut également lui conférer des propriétés optiques spécifiques. En effet, la coupure du graphène en petits îlots de tailles variables peut introduire un confinement quantique des électrons, procurant une photoluminescence dépendante de la taille de l'îlot dans le graphène [R23].

Au cours de traitements par faisceaux d'ions, le rôle du substrat est également à considérer. Par exemple, en présence de dommages importants, la nature des interactions entre le substrat et le graphène peut être altérée. En effet, le graphène, initialement lié par interactions *van der Waals*, peut former des liens covalents avec le substrat. Le simple changement de distance entre le graphène et le substrat peut également venir modifier la fonction de travail de graphène en décalant le niveau de Fermi. De faibles irradiations peuvent détacher le graphène du substrat alors que des fluences plus élevées peuvent lier le graphène au substrat. Ce comportement n'est pas observé pour des structures multicouches ; la couche en lien avec le substrat n'est pas

directement irradiée et les atomes déplacés des couches supérieures peuvent combler des lacunes des couches inférieures [R24].

L'utilisation d'ions réactifs permet d'allier création de dommages d'irradiation et incorporation d'hétéroatomes (exemple incorporation de N par faisceau N^+). Typiquement, les dommages engendrés par la dose d'ions sont si importants qu'un recuit (sous vide ou gaz inerte) peut alors être effectué pour restructurer le graphène. Pour de fortes énergies d'irradiation ($>100eV$), la formation de lacunes multiples facilite l'incorporation de site pyridine ou pyrrole (**Figure 7b**) [R25]. Pour des énergies plus faibles ($<100eV$), on observe une combinaison de liens graphitiques, pyridines et pyrroles [R26]. Les études en fonction de l'énergie des ions réalisées par *Zhao et al.* [R27], présentées à la **Figure 7a**, démontrent une contribution grandissante des pyridines avec l'énergie des ions. Des incorporations d'azote presqu'exclusivement graphitiques peuvent être obtenues avec des recuits à haute température (1300K) et de faibles doses [R28]. Dans l'ensemble, notons que les pourcentages d'incorporation par bombardement ionique sont assez faibles, soit entre 1 et 3%.

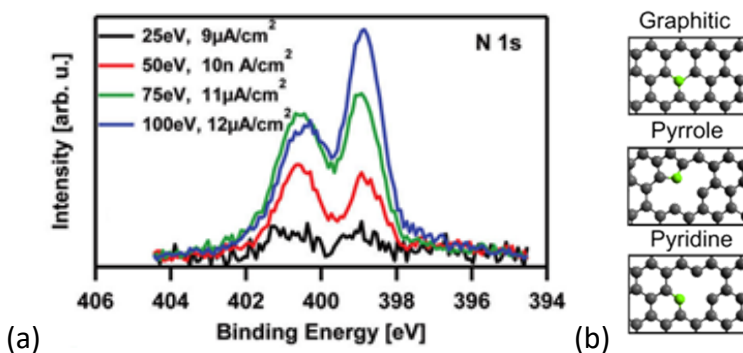


Figure 7 : a) Spectre N1s de spectroscopie des photoélectrons induits par rayons X (XPS) pour un traitement de graphène par faisceau d'ions de N^+ de 25eV à 100eV. Incorporation graphitique (400.5eV) et pyridine (398.5eV). [R27] b) Représentation d'incorporation d'azote.

Recuit thermique

Un traitement de recuit thermique consiste à chauffer le graphène directement (chauffage Joule) ou indirectement (chauffer un gaz ou le substrat). Les recuits peuvent être effectués sous vide, dans un gaz inerte ou dans un gaz réactif. Le chauffage peut permettre la migration et la

désorption des espèces adsorbées en surface. Tel que discuté dans la section de croissance par CVD (**Section 1.1.2**), la température peut également permettre des réactions en surface en présence d'un gaz réactif. Le chauffage peut aussi être une conséquence indésirable d'un type de traitement [R29].

Les processus chimiques sont beaucoup plus sensibles aux impuretés et aux défauts structurels sur l'échantillon que les processus physiques. Les changements de courbure prononcés et les bords du graphène représentent des sites préférentiels pour les réactions chimiques. À température ambiante, les groupes d'oxygène et d'hydrogène adsorbés procurent au graphène un dopage positif. Le chauffage permet de désorber ces impuretés et de rétablir le niveau de Fermi du graphène inaltéré [R30]. Un recuit subséquent en atmosphère d'ammoniac (NH_3) s'est révélé efficace pour produire des sites pyridiniques en bordure de nano-rubans de graphène pour effectuer un dopage négatif [R31]. De plus, une légère impureté d'oxygène dans le recuit au NH_3 semble favoriser la réaction d'incorporation des atomes d'azote.

Le recuit thermique en atmosphère d'oxygène permet la formation de lacunes sur le plan basal du graphène par gravure chimique. Des lacunes simples sont obtenues pour des recuits de 500K [R32] alors que des trous de dizaines de nanomètres sont obtenus pour des températures de plus de 700K. La densité de défauts obtenue pour un recuit à basse température (533K) atteint les 10^{12} cm^{-2} [R32]. Pour des températures plus élevées ($>1000\text{K}$), les hydrocarbures adsorbés en surface forment une couche de carbone amorphe. Pour des températures extrêmes ($>2000\text{K}$), le graphène se restructure de façon à obtenir une monocouche polycristalline [R33].

Les principaux intérêts des méthodes de recuit sont de stabiliser/restructurer le réseau graphénique afin d'obtenir des incorporations d'hétéroatomes purement substitutionnelles et de désorber les impuretés et en surface. Toutefois, la différence d'expansion thermique entre le graphène et son substrat induit des contraintes de compression ou de traction responsables de formation de défauts de type *ripple* dans le graphène [R9].

Fonctionnalisation covalente de surface

Les méthodes traditionnelles de fonctionnalisation covalente de surface consistent à mettre en contact le graphène avec une solution réactive afin que des produits réactifs viennent se fixer par la formation de liens covalents [R34]. Comme discuté dans la section sur le recuit thermique (**Section 1.1.3**, recuit thermique), les sites où il y a diminution de la délocalisation électronique (*ripples*, bords, défauts, déformations) sont des sites préférentiels pour les réactions chimiques. Deux exemples de fonctionnalisation covalente sont présentés : la réduction au sel diazonium et la cycloaddition.

Comme le montre la **Figure 8a**, la réduction au sel diazonium (groupe N_2^+ lié à un alkyle) sur le graphène permet l'incorporation de radicaux aryles (cycle aromatique lié à un alkyle). Le haut taux de fonctionnalisation dû à la haute réactivité des sels rend cette méthode difficilement limitable. Une forte dépendance du substrat est obtenue puisque la présence d'impuretés chargées ou d'adsorbants chargés dans le substrat induit des fluctuations dans le niveau de Fermi du graphène qui sont responsables d'une hausse de la réactivité chimique. [R10] La **Figure 8b** illustre une réaction de cycloaddition, i.e. liaison de deux (ou plus) composés afin de former un cycle aromatique. L'exemple présenté est une réaction de *Diels-Alder* liant un diène et un dienophile. Les deux carbones du plan changent d'hybridation de sp^2 vers sp^3 . Ce type de réaction permet l'ouverture d'une bande d'énergie interdite dans le graphène [R10]. Notons que le principal désavantage des méthodes par voies chimiques en milieux liquides de fonctionnalisation covalente de surface est leur difficulté d'automatisation en milieu industriel.

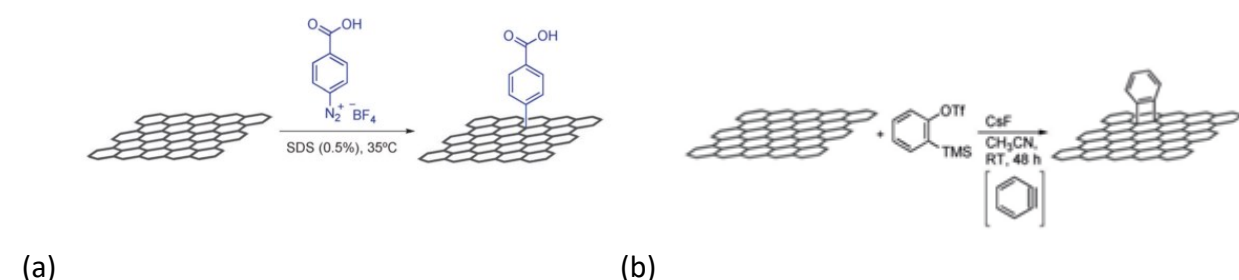


Figure 8 : a) Attachement d'un groupe aryl par la réduction d'un sel diazonium. b) Exemple de réaction de cycloaddition [R10].

Traitements par plasma

Le traitement par plasma exploite la phase plasma d'un gaz ou d'un mélange de gaz afin d'utiliser les espèces énergétiques présentes dans le plasma pour altérer directement ou indirectement l'échantillon exposé. Au cours des dernières années, ces traitements ont été appliqués à divers domaines (citons notamment l'activation de surfaces polymériques, la gravure pour des fins de micro-fabrication ou la stérilisation d'objets médicaux) en raison de leur nature paramétrable, leur rapidité et leur facilité d'adaptation aux procédés industriels. En effet, le contrôle de l'expérimentateur sur les conditions opératoires (pression, puissance d'alimentation, temps de traitement, nature et proportion des gaz, potentiel d'accélération des ions et bien plus) permet un ajustement fin des traitements. Les méthodes basées sur les plasmas se distinguent également des méthodes chimiques en milieux humides par leur plus faible impact environnemental.

La physique des interactions plasmas-nanomatériaux demeure cependant une discipline relativement jeune. Comme l'illustre la **Figure 9**, elle combine des effets de bombardement ionique, de fonctionnalisation de surface, de recuit thermique mais aussi d'autres contributions reliées à la présence de photons et d'espèces excitées caractérisées par de longues durées de vie (par exemple les métastables).

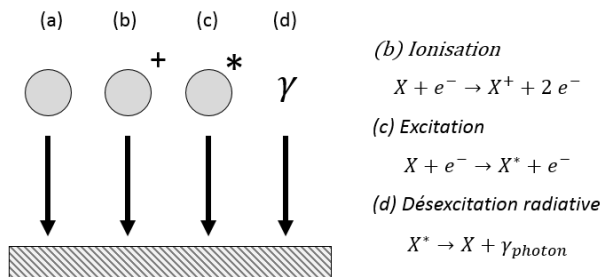


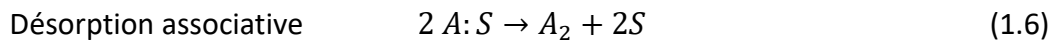
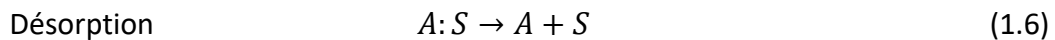
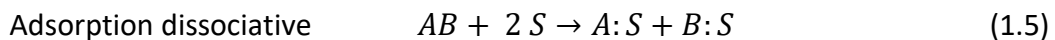
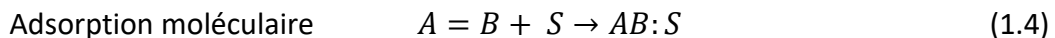
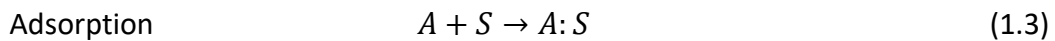
Figure 9 : Bombardement de la surface par diverses espèces du plasma. a) neutres b) ions c) états excités d) photons. Quelques exemples de réactions de gain des espèces sont présentés à droite.

Dans un plasma, les ions positifs sont naturellement accélérés vers une surface dans une région non-macroscopiquement neutre appelée la gaine ionique. Pour une gaine non-collisionnelle, le flux d'ions sur une surface est donné par :

$$\Gamma_{ions} = 0.6 n_{ions} v_B \quad (1.2)$$

où n_{ions} est la densité ionique en lisière de gaine et v_B est la vitesse de Bohm [R35]. Tel que mentionné précédemment pour les faisceaux d'ions, les dommages d'irradiation ionique dans le graphène peuvent être multiples et comprennent des modifications physiques (défauts ponctuels et étendus, amorphisation) mais aussi chimiques comme le dopage. L'ampleur de ces modifications relève de la nature, de l'énergie et de la dose des ions.

Le plasma peut aussi mener à la formation d'espèces réactives par dissociation d'un gaz réactif. La molécule mère ainsi que ses fragments peuvent ensuite donner lieu à divers processus d'adsorption et de désorption à la surface du substrat



Tout d'abord, l'adsorption est le processus décrit par l'attachement d'un atome ou d'une molécule en surface. Pour l'adsorption d'une molécule, cet attachement peut altérer le lien entre les atomes de la molécule, allant même jusqu'à favoriser sa dissociation. La **Figure 10** illustre les formes de potentiel typique pour quelques processus d'adsorption discutés ci-dessus.

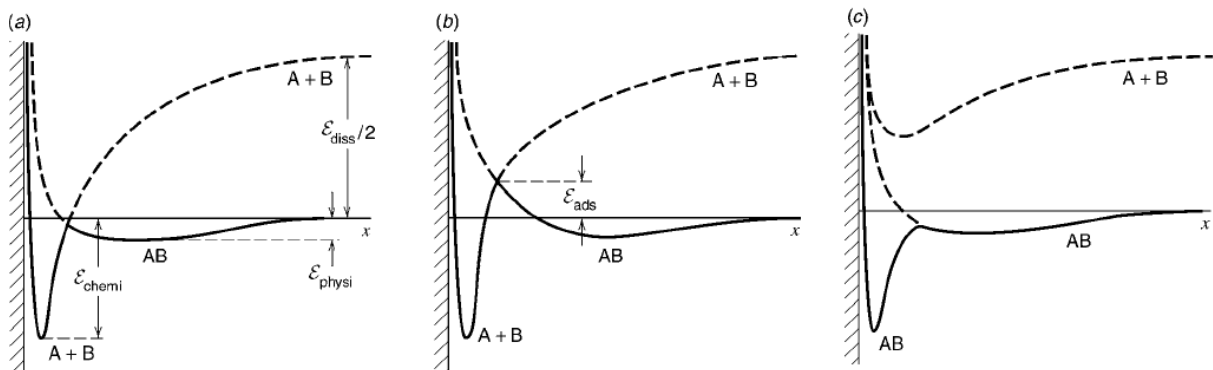


Figure 10 : Diagramme de potentiel pour a) l'adsorption dissociative b) la physisorption et c) l'adsorption moléculaire. [R36]

On distingue deux types d'adsorption. La première, la physisorption, est causée par des liens *van der Walls* avec la surface. L'énergie de physisorption est typiquement de 0.01-0.25 eV. Ces faibles énergies assurent une migration rapide des espèces adsorbées. Le deuxième type d'adsorption, appelé chimisorption, décrit le comportement d'une espèce formant des liens chimiques avec la surface. Pour des espèces atomiques adsorbées de H, C, N et O sur le graphène, les distances interatomiques sont de 1.5-1.6 Å et l'énergie de liaison pour la chimisorption est de 2-5 eV. Tout en étant liés sur la surface, les atomes adsorbés peuvent se déplacer d'un site voisin à l'autre. Ces énergies de migration en surface sont de 0.6 eV pour H et C et de 1 eV pour N et O [R37]. Notons que ces énergies sont faibles par rapport à l'apport énergétique des ions accélérés dans les gaines ioniques ou encore de celles associées aux processus de neutralisation des ions en surface [R36] ou de désexcitation en surface d'atomes dans un niveau excité [R38]. Notons aussi que les ions transfèrent directement leur énergie aux noyaux par collisions élastiques alors que le transfert d'énergie pour les processus de neutralisation et de désexcitation relève d'interactions électroniques et donc de transfert électron-phonon [R5,39,40].

Pour les réactions d'adsorption, le flux d'atomes neutres incidents sur la surface est donné par :

$$\Gamma_a = \frac{1}{4} n_a \langle v \rangle \quad (1.7)$$

où $\langle v \rangle$ est la vitesse moyenne (associée à l'agitation thermique) et n_a est la population de l'espèce a réactive dans le plasma. Cette cinétique d'adsorption est typiquement liée à une probabilité d'adsorption $S = S(\vartheta, T)$, où ϑ est le degré de recouvrement de la surface par les atomes adsorbés et T est la température de la surface [R41]. Le comportement de S avec ϑ et T dépend de la nature du processus d'adsorption (**Figure 10**) mais aussi de l'importance des processus de désorption. En effet, un fois adsorbées, ces espèces peuvent ensuite désorber (sous forme d'atomes ou de molécules) ou encore réagir avec les atomes du substrat pour donner lieu à diverses réactions comme la gravure. À titre d'exemple, l'adsorption d'un atome d'oxygène sur une surface de carbone peut donner lieu à de la gravure par désorption de produits de réactions volatiles CO et CO₂ [R42]. Ces réactions peuvent être spontanées à température ambiante ou encore assistées d'un apport d'énergie externe (ions, UV, métastables).

1.2 Traitement par plasma du graphène

Tel que discuté à la section précédente, les espèces actives du plasma peuvent être responsables de différentes interactions avec la surface, ce qui inclut le bombardement ionique, l'adsorption d'espèces réactives, la désexcitation en surface, etc. À l'évidence, l'importance de ces divers processus peut être ajustée selon un choix judicieux des conditions opératoires (pression, puissance, etc.), ce qui permet de varier l'énergie et la densité des différents ions, électrons, neutres et états excités au voisinage du substrat.

De manière générale, on dit des traitements basés sur les plasmas qu'ils sont soit *directs*, soit *indirects*. La **Figure 11** distingue deux schémas typiques de traitements. Dans le cas de traitements directs, l'échantillon est immergé dans le plasma de sorte qu'il est exposé à des flux importants d'espèces actives (ions, électrons, atomes, photons). Les fortes densités d'ions accélérés dans la gaine représentent toutefois des sources de dommages potentiellement indésirables. Dans le cas de traitements indirects, l'échantillon est positionné dans la post-décharge spatiale du plasma. L'échantillon est alors exposé à de fortes densités de neutres réactifs et à très peu d'ions. L'absence d'espèces énergétiques dans les traitements indirects diminue fortement la génération de dommages; cependant, elle empêche également les réactions de surface nécessitant un apport d'énergie externe.

Dans cette section, nous décrivons l'état des connaissances en physique des interactions plasma-graphène. Afin de couvrir adéquatement la littérature, la section est divisée selon les différents gaz. Les montages expérimentaux et les conditions typiques de traitement sont dépeints. Notons l'absence d'articles combinant la caractérisation du plasma et la caractérisation des matériaux ; combler cette lacune est l'un des principaux objectifs de notre projet de recherche. Notons également que les articles mettant l'accent sur la caractérisation des matériaux décrivent très peu leurs sources de plasma; l'identification exacte des conditions de traitement devient alors difficile, voire impossible.

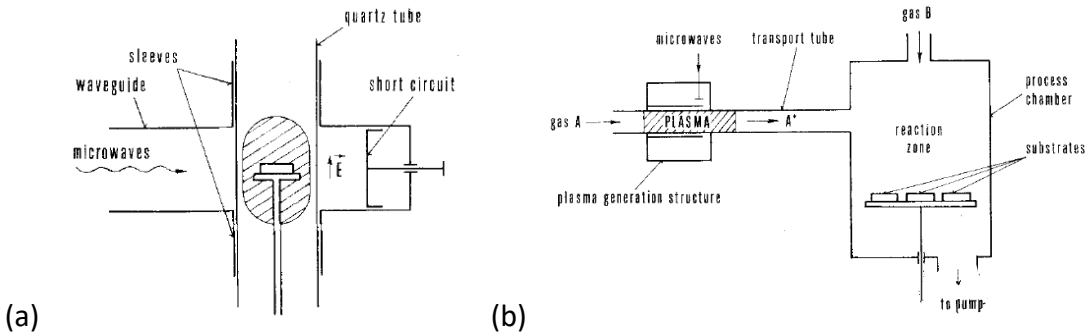


Figure 11 : Schéma d'un traitement (a) direct et (b) indirect [R43]

1.2.1 Traitement du graphène par plasma d'argon

En raison de la nature inerte de l'argon, plusieurs pourraient considérer les traitements par plasma d'argon très similaires au bombardement par faisceau d'ions. Cependant, la complexité des traitements par plasma provient de la présence et de l'interaction simultanée de plusieurs espèces énergétiques : au bombardement ionique se rajoutent la thermalisation par les neutres, l'irradiation par les photons et la désexcitation en surface d'espèces excitées.

La majorité des traitements par plasma en argon de matériaux graphéniques présentés dans la littérature sont effectués dans des réacteurs à très faible puissance ($\sim 1\text{-}100$ W). Dans ces systèmes, les modifications post-synthèse sont purement structurelles. À titre d'exemple, la **Figure 12** présente l'influence du temps d'exposition à un plasma d'argon sur les intensités des principales bandes Raman du graphène. À faible temps d'exposition, c'est-à-dire pour de faibles concentrations de défauts, la bande G demeure constante tandis que les bandes D et D' augmentent fortement. Pour un certain niveau de défauts, ici autour de 60 secondes, la bande D passe par un maximum et puis diminue. Ces résultats sont en accord avec les données et modèles d'irradiation ionique décrits à la **Section 1.1.3**. Ceci comprend un premier régime associé à une augmentation du rapport D:G due à une diminution de la taille des cristallites (faible temps de traitement) puis un second régime relié à l'amorphisation du graphène (temps de traitement élevé). Tout au long du régime 1, les auteurs notent également un rapport D:D' autour de 7, ce qui indique que les défauts produits par plasma d'argon sont principalement des lacunes [R8]. Bien que les auteurs attribuent l'ensemble de leurs observations à des dommages par irradiation

ionique, il est toutefois impossible de conclure si les ions sont les seules espèces actives mises en jeu.

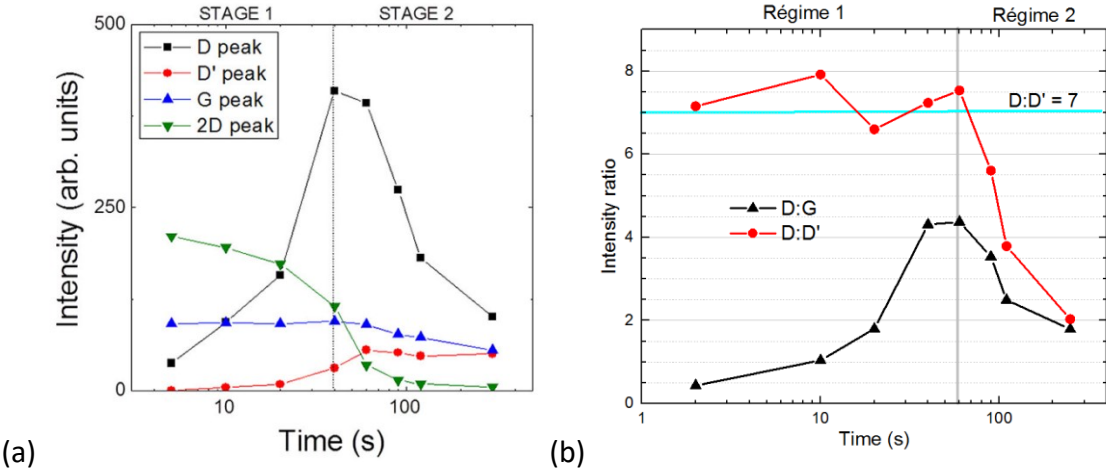


Figure 12 : a) Intensités en fonction du temps des principales bandes Raman, b) Ratio D:G et D':D du graphène traité par plasma d'argon. Tracé à partir des données publiées dans [R8].

Malgré le caractère “destructeur” des traitements par plasma d’argon, la production de défauts dans le graphène ouvre la voie à plusieurs applications. Les dommages engendrés agissent notamment comme sites de diffusion, ce qui favorise l’absorption de la lumière, diminue le temps de vie des porteurs de charge et augmente le photo-courant [R3]. Les lacunes introduites par les traitements par plasma d’argon peuvent aussi induire un dopage positif dans le graphène. Le graphène traité par plasma d’argon s’est en effet révélé prometteur comme transistor à effet de champs (GFET) [R3]. La **Figure 13** illustre les spectres XPS du graphène du GFET avant et après traitement par plasma ainsi que les courbes courant-tension révélant le dopage positif. Notons la présence des groupes oxygène sur les deux échantillons et l’augmentation des liens C-C sp^3 attribués aux dommages. De plus, la production de défauts favorise l’interaction du GFET avec des photons. Pour une irradiation dans le visible (405nm et 535nm), des paires électron-trou photo-induites confèrent un dopage p supplémentaire alors que l’irradiation UV (365nm) conduit à une désorption d’atomes d’oxygène chimisorbés et donc à un dopage négatif.

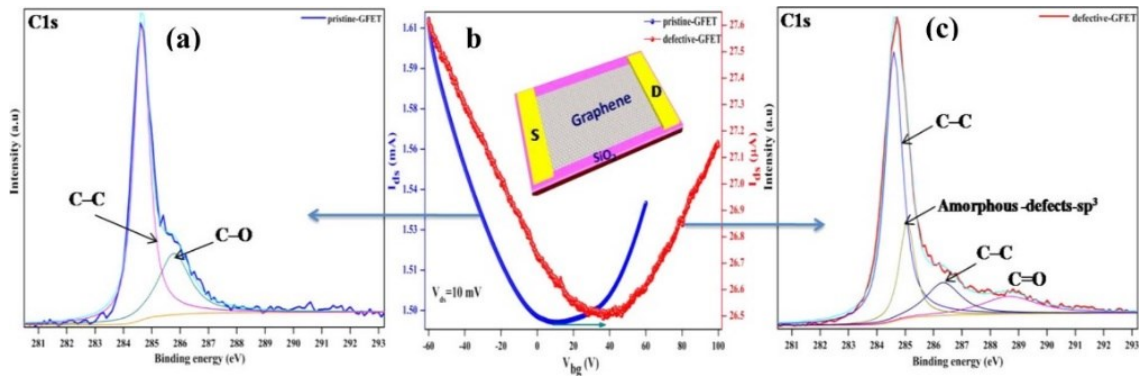


Figure 13 : Spectre Haute résolution C1s XPS pour le graphène a) inaltéré et c) traité par plasma d'argon. b) Courbe courant-tension de GFET [R3]

1.2.2 Traitement du graphène par plasma d'hydrogène

Dans les plasmas de H₂, la dissociation de la molécule mère conduit à des populations significatives d'atomes H qui peuvent induire une gravure chimique du graphène. Des études ont montré que celle-ci est fortement dépendante de la température de la surface et peut être assistée par bombardement ionique, par irradiation UV, etc. En effet, ces espèces énergétiques permettent la désorption d'hydrocarbures, même à basses températures.

Pour des traitements indirects sans chauffage, la gravure chimique dans les plasmas d'hydrogène est inhibée. Dans ce régime, les atomes de H peuvent néanmoins changer l'hybridation des atomes de carbone comme le montre la **Figure 14**. Une telle hydrogénéation du graphène diminue sa conductivité [R44], le rendant même isolant pour des recouvrements importants [R45]. Notons que ce processus est réversible : un recuit permet la désorption de l'hydrogène sans toutefois induire une gravure chimique [R45]. Notons aussi que l'hydrogénéation des structures monocouches dans les traitements indirects est différente de celle des multicoches. À cause de son plus fort lien avec le substrat, les barrières d'énergie pour l'hydrogénéation sont plus grandes pour le graphène (0.5 eV) que pour le graphite (0.2 eV) [R46]. Ainsi, la saturation en hydrogène du graphite est beaucoup plus rapide que celle des monocouches [R46]. Néanmoins, le graphène monocouche possède plus de plis (*ripples*) que les structures graphitiques de sorte que l'hydrogénéation sur ces sites devient spontanée. La formation de liaisons hydrogénées est donc beaucoup moins uniforme sur une monocouche.

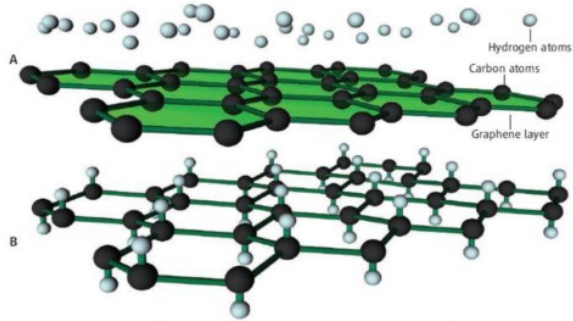


Figure 14 : schéma de l'hydrogénéation du graphène dans les plasmas de H_2 [R34].

Dans un traitement indirect, le chauffage du substrat permet de favoriser le processus de gravure chimique. Les vitesses de gravure sont généralement maximales pour des températures de 400-500°C. Cependant, même dans des conditions similaires de plasma, on peut noter des variations importantes de la vitesse de la gravure, mais aussi de son comportement (isotropie, uniformité) selon les différentes publications. En effet, dans des conditions similaires, *Diankov et al* [R47] ont obtenu des gravures rapides (40 nm/min) et isotropes alors que *Yang et al* [R48] ont obtenu des gravures plus lentes (8 nm/min) et anisotropes. La **Figure 15** présente la microscopie par force atomique (AFM) de ces deux traitements.

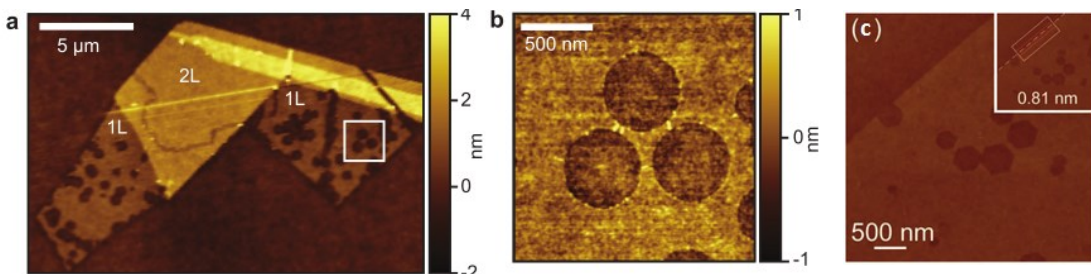


Figure 15 : a-b) Tomographie AFM d'un traitement indirect en plasma d'hydrogène à 500°C. 10min [R47] c) tomographie AFM d'un traitement indirect 500°C 20 [R48].

Dans le cas de *Diankov et al* [R47], le comportement de la gravure est différent pour les monocouches et les bicouches de graphène. De plus, le substrat montre un changement de contraste à la suite de traitement par plasma. Ces résultats indiquent que le substrat joue un rôle

important dans la distinction des deux types de gravure. Sur monocouche, les trous sont répartis non uniformément et montrent une vitesse de gravure similaire à celle observée sur les bords du graphène. Les impuretés du substrat offrent aussi un grand nombre de sites réactifs sur monocouche. Ceci explique la différence de deux ordres de grandeur entre la gravure sur monocouche (rapide) et celle sur bicouche (lente). De plus, la gravure du graphène multicouche est anisotrope et crée des trous hexagonaux. Ces mêmes types de structures ont été observées par *Yang et al* [R48] sur graphène monocouche. Cette anisotropie s'avère particulièrement utile car elle permet de révéler l'orientation du graphène et de concevoir différents dispositifs orientés avec le graphène (nanoruban, GFET, etc.). Les traitements à plus basse température et plus faibles densités d'atomes de H peuvent ensuite être utilisés pour graver principalement les bords de grains et ainsi ajuster la taille des nanorubans [R49].

En présence de bombardement ionique dans les plasmas d'hydrogène, il est possible de créer des sites privilégiés d'hydrogénéation ou encore de désorber des hydrocarbures formés dans le graphène. Par exemple, *Seifert et al.* [R50] ont proposé d'appliquer un potentiel négatif sur un échantillon traité dans la post-décharge en flux d'un plasma de H₂. Les auteurs ont noté la formation de sites de défauts uniformément espacés sur lesquels la gravure chimique était favorisée. Cependant, pour des temps élevés de traitement, l'échantillon devient sujet à un processus d'amorphisation [R50]. Notons que des traitements directs permettent également de favoriser la création de ces sites d'hydrogénéation [R51].

1.2.3 Traitement du graphène par plasma d'oxygène

Les traitements par plasma d'oxygène se sont montrés très efficaces dans les processus de microfabrication pour nettoyer, par gravure chimique, les résidus de polymères utilisés comme masque. Dans le cas du graphène, la gravure chimique conduit à la désorption de produits volatils de réaction, soit CO et CO₂ [R42]. Dans des conditions de traitement direct, on obtient généralement des gravures complètes en vertu des vitesses élevées de gravure. Ainsi, il devient possible, en contrôlant leur largeur, de modifier le confinement quasi-unidimensionnel de nanorubans en couplant photolithographie et gravure complète [R52].

Dans le cas de traitements indirects, comme la densité d'espèces actives est plus faible, la gravure en plasma d'oxygène est généralement incomplète (vitesse de gravure plus faible), ce qui augmente les processus de percolation en introduisant des lacunes [R53], principalement des lacunes simples [R42]. *Rozada et al.* [R42] ont démontré, comme l'illustre la **Figure 16**, qu'une sélection adéquate des conditions opératoires d'un traitement indirect par plasma d'oxygène permet de contrôler la densité de lacunes induites par le traitement. Ces générations de lacunes simples induisent un dopage de type p combiné à une diminution de la mobilité des porteurs de charge [R42,54].

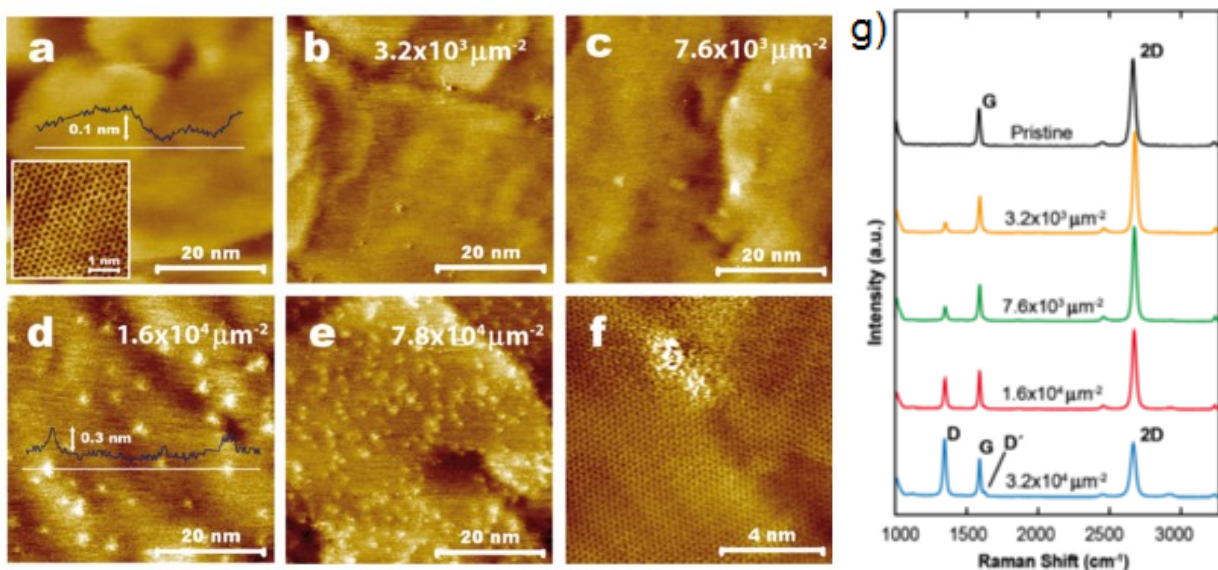


Figure 16 : Microscopie électronique par effet tunnel (STM) de traitements indirects par plasma d'oxygène. a) 0s b) 10 W/9 s c) 60 W/3 s d) 300 W/1.5 s e) and 390 W/1.5 s. f) un défaut typique généré par le traitement. g) spectre Raman associé aux traitements a)-e) [R42]

En plus des effets de gravure, les espèces oxydantes du plasma d'oxygène peuvent également s'adsorber à la surface du graphène. L'oxygène étant plus électronégatif que le carbone, il représente une perte d'électrons de la bande de valence et donc un dopage de type p [R53]. Le dipôle induit par cette différence d'électronégativité favorise l'adsorption de molécules pour les applications de détecteurs moléculaires [R55]. Ce changement de réactivité à la surface permet la création de ponts hydrogène, ce qui augmente la mouillabilité à l'eau de la surface (diminution de l'angle de contact de 90° à 20-30°) [R56].

Il est important de mentionner que, contrairement aux lacunes et aux défauts de type hydroxyle et époxyde qui modifient peu l'hybridation des carbones, les paires de liens carbonyles pouvant être obtenues dans les milieux oxydants, elles procurent une hybridation sp^3 et conduisent à une forte baisse de conductivité thermique (-83%) pour des densités de défauts très faibles (~0.1%) [R4]. Ce changement d'hybridation induit par l'adsorption d'oxygène en surface permet de rendre le graphène semi-conducteur en lui conférant une bande d'énergie interdite atteignant les 2 eV [R57]. Cependant, ce comportement n'est pas visible dans les structures multicouches puisque le découplage des couches diminue l'intensité du dipôle induit par les oxygènes adsorbés [R58].

Notons que les modifications induites au graphène par les plasmas d'oxygène sont, contrairement au traitement par plasmas direct d'hydrogène, partiellement réversibles [R59]. En effet, des recuits à haute température ($>800^\circ\text{C}$) peuvent libérer les groupes fonctionnels d'oxygène, mais laisseront la structure endommagée. Ces dommages peuvent toutefois être moins néfastes que les résidus de polymères pour certaines applications. Des méthodes de nettoyage par plasmas d'oxygène suivis de recuits permettent d'augmenter la conductivité du graphène. [R60]

1.2.5 Traitement du graphène par plasma d'azote

En raison de ses fortes similitudes avec le carbone, l'azote est un excellent candidat pour l'incorporation d'hétéroatomes dans le graphène. Sa masse ne diffère que de deux unités de masse atomique et il possède un électron de plus que le carbone. Dans ce contexte, plusieurs auteurs ont exploré le traitement du graphène par plasma de N_2 . Les espèces énergétiques du plasma permettent la dissociation du N_2 non-réactif en deux N fortement réactifs. La présence de sites d'incorporation (lacunes simples ou multiples, bords de grains) et/ou la présence d'espèces suffisamment énergétiques permet l'incorporation de ces atomes d'azote dans le graphène. La similitude entre les liens C-C (1.42 Å) et C-N (1.43 Å) permet à l'incorporation d'azote de faiblement déformer le graphène [R61]. Comme identifié à la **Figure 7b**, les principales incorporations aromatiques de l'azote sont de type pyridine, pyrrole et graphitique.

Incorporation, bombardement et dopage

L'intérêt de bien contrôler la nature des incorporations d'azote provient du fait que celles-ci n'ont pas le même impact sur le niveau de Fermi. En effet, seules les incorporations graphitiques entraînent un dopage négatif [R62]. Notons également que l'incorporation d'un azote dans un défaut de type *Stone-Wales* (rotation de 90° d'une paire de carbone) permet également un dopage négatif [R63]. Le dopage d'azote est responsable d'états électroniques localisés dans la bande de conduction [R64]. Cependant, les dommages d'irradiation obtenus dans les plasmas d'azote favorisent l'adsorption d'oxygène au contact avec l'air ambiant et ceci agit comme un dopage positif. La présence de ces atomes adsorbés entraîne alors une augmentation de la fonction de travail du graphène [R65]. Des étapes de recuit deviennent ainsi nécessaires pour observer la diminution de la fonction de travail attendue dans le cas d'incorporations de type graphitique seulement (sans les effets de l'adsorption d'oxygène) [R63].

La présence d'ions positifs dans les traitements du graphène par plasma influence également la distribution et la nature des incorporations azotées. Pour illustrer ce phénomène, *Lin et al.* [R65] ont eu recours à un piège à ions (plaques polarisées pour ne laisser passer que les espèces neutres) et un support polarisé pour étudier le bombardement de faible énergie (< 50eV) d'ions dans la post-décharge en flux d'un plasma de N₂. La **Figure 17** montre les spectres XPS N1s de trois conditions opératoires. Tout d'abord, l'échantillon a été exposé à 1h de traitement avec le piège à ions activé et sans polarisation (NG-2). L'incorporation obtenue est principalement de type pyridine. Les traitements avec le piège à ions éteint permettent à la fois des incorporations de type pyridine et graphitique, et ce, en proportions comparables. L'incorporation de type graphitique devient plus importante avec l'augmentation de l'énergie des ions de 5eV (NG-1a) à 35 eV (NG-1). La plus grande contribution des incorporations de type graphitique dans les traitements "agressifs" entraîne un dopage négatif (-0.4eV pour NG-1) plus important que ceux obtenus par traitement "doux" (-0.1eV pour NG-2).

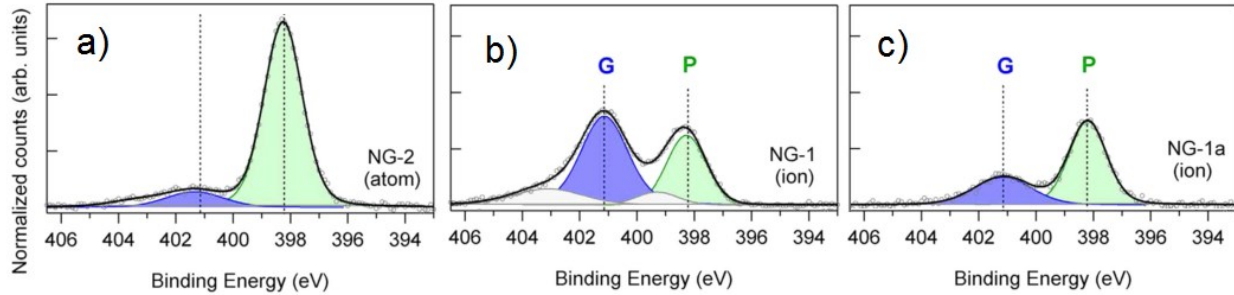


Figure 17: Traitement post-décharge micro-onde avec polarisation de substrat et piège à ions. Spectres XPS N1s a) 1h piège activé. b) 35eV 10min piège désactivé. c) 5eV 10min piège désactivé. [R65]

Notons que, contrairement aux traitements par faisceaux d'ions (**Section 1.1.3**), les traitements dans les plasmas composés de plus grandes populations d'espèces plus énergétiques ne favorisent pas les incorporations pyridines, mais plutôt les incorporations graphitiques. En effet, les énergies de bombardement dans le plasma ne semblent pas suffisantes pour entraîner la formation des lacunes multiples responsables de l'augmentation des incorporations de type pyridine [R66]. Le mécanisme exact menant aux incorporations de type graphitique pour des incorporations avec bombardement de faible énergie demeure néanmoins inconnu. Les sites de défaut produits par le bombardement ionique permettent toutefois l'adsorption préférentielle d'azote atomique, l'apport d'énergie externe pouvant ensuite activer une incorporation substitutionnelle. Puisque les sites de défauts de synthèse rendent possible l'adsorption, ce processus d'incorporation dépend également de la qualité cristalline initiale de l'échantillon [R66].

Une polarisation importante de l'échantillon permet d'explorer l'importance des défauts de synthèse du graphène traité dans les plasmas d'azote. *Bertóti et al.* [R67] ont étudié le traitement direct de graphène pour des énergies ioniques entre 25 eV et 200 eV. Pour des énergies importantes ($> 50\text{eV}$), on retrouve l'augmentation de pyridine associée aux lacunes multiples discutée dans la **Section 1.1.3** [R67]. Afin d'étudier le rôle des défauts de croissance, *Bertóti et al.* ont comparé les traitements d'un échantillon de graphène polycristallin et d'une structure extrêmement ordonnée, le HOPG (*Highly oriented pyrolytic graphite*). Pour de faibles énergies ($< 50\text{eV}$), le HOPG montre une incorporation inférieure (3.8%) à celle du graphène (6%). Pour les

énergies élevées (200eV), les deux structures montrent un taux d'incorporation d'azote similaire (9%). Contrairement au mécanisme discuté plus haut à faible énergie des ions, le mécanisme d'incorporation d'atomes d'azote à haute énergie est évidemment indépendant des défauts de synthèse (ceux-ci sont directement créées par l'irradiation ionique).

Notons que le rôle du substrat est particulièrement important pour déterminer le type d'incorporation d'azote. En effet, une intercalation d'oxygène entre le substrat d'iridium et la couche de graphène s'est montrée efficace pour favoriser l'incorporation de type graphitique [R68]. Les incorporations de type pyrrole et pyridine semblent quant à elles stabilisées par l'interaction graphène-substrat. L'incorporation graphitique est défavorisée dans les régions où le graphène est plus étroitement lié au substrat, comme dans les ondulations de Moiré [R68].

De la revue de littérature présentée dans cette section, on constate que les plasmas propices à l'incorporation aromatique d'azote sont également susceptibles d'endommager de façon importante le graphène par irradiation ionique. Le développement de nouvelles méthodes basées sur les plasmas, visant à diminuer ces dommages tout en permettant des taux élevés d'incorporation d'azote, est évidemment requis. Pour illustrer ces propos, la **Figure 18** présente les spectres Raman de quelques exemples de traitement par plasma de N₂ de graphène ainsi que les pourcentages correspondants d'incorporation. Dans la majorité des cas, l'extinction presque complète de la bande 2D indique une transition vers le régime 2 de *Ferrari et Robertson* [R18] et donc une forte amorphisation du graphène. Notons également qu'un nombre important d'articles révisés ne vérifient pas les dommages structurels par spectroscopie Raman ou alors ne s'informent pas de la nature des incorporations d'azote par XPS.

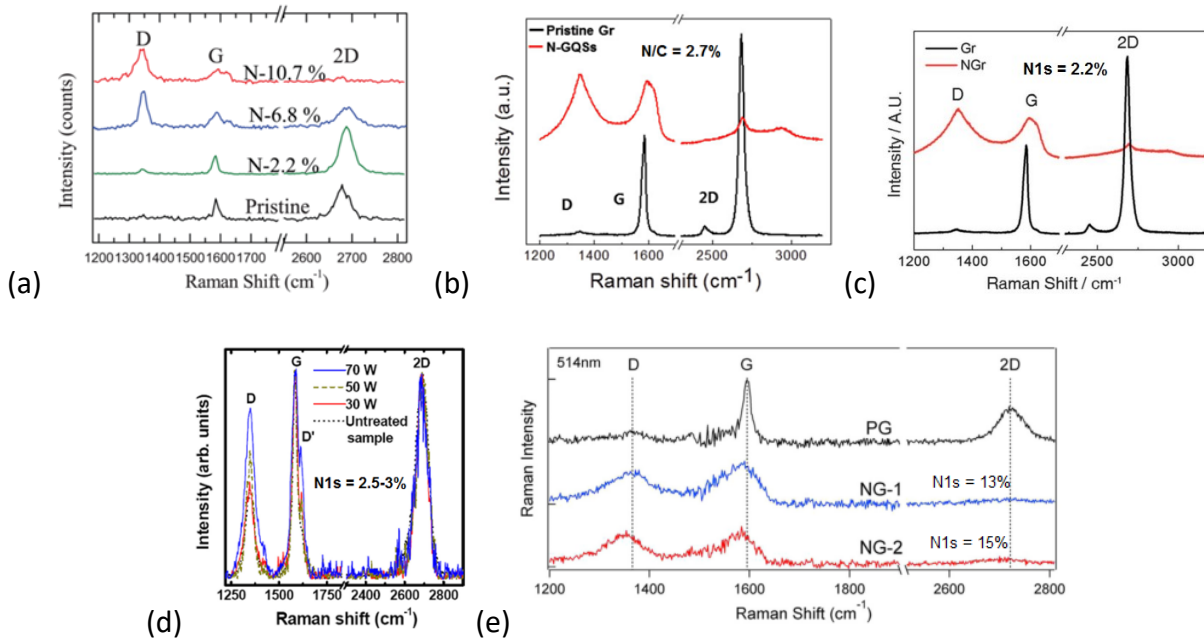


Figure 18 : Exemples de spectre Raman pour des incorporations de N par traitement par plasma de N₂. a) graphène sous 2nm Al-oxyde 150W N₂ plasma [R69] b) 10W direct RF N₂ plasma [R70] c) 10W direct RF N₂ plasma [R71] d) 30-70W direct N₂ plasma [R63] e) traitement indirect en plasma de N₂ avec piège à ions et substrat polarisé [R65]

Amplification de potentiel catalytique du graphène

En plus des effets de dopage, l'incorporation d'atomes d'azote permet également de proférer au graphène un comportement catalytique pour diverses réactions chimiques en surface. Les incorporations d'azote favorisent notamment la réduction en surface de O₂ et H₂O₂. En raison de la plus forte affinité électronique de l'azote, les carbones adjacents à ces hétéroatomes sont chargés positivement. Cette charge favorise l'adsorption d'oxygène (O₂ ou réactifs intermédiaires) en surface [R72]. La délocalisation des charges change le mode d'adsorption d'O₂. Sur le graphène inaltéré, le lien intraplanaire est perpendiculaire à la surface alors que l'azote affaiblit le lien O-O en facilitant l'adsorption où le lien intraplanaire est parallèle à la surface [R72]. Il est même admis que l'activité électrocatalytique du N-graphène est supérieure au platine conventionnellement utilisé.

Le graphène traité par plasma d'azote est également prometteur pour la production écologique d'hydrogène. Les photocathodes de Si-graphène azotées présentent une meilleure activité

catalytique pour la production d'hydrogène. Le graphène, en plus d'empêcher l'oxydation du Si, offre des sites de réactivité accrue lorsque traité à l'azote. Cette hausse de l'efficacité de conversion, le faible coût du graphène, et sa stabilité en font un candidat idéal pour ces applications [R71].

Les incorporations d'azote dans l'oxyde de graphène réduit par plasma d'azote haussent également la capacitance de supercondensateurs d'un facteur 4 (de 70 F/électrode à 280 F/électrode) par rapport au graphène inaltéré [R73]. De plus, la bonne conductivité du graphène et sa grande aire de surface le rendent idéal pour entreposer et libérer l'énergie électrique des liens électrostatiques entre les ions et l'électrolyte. Le cycle de vie des ultracondensateurs à base de graphène est de l'ordre de 2×10^5 cycles, soit 10 fois plus long que les pseudocondensateurs développés pour pallier aux trop faibles capacités des condensateurs conventionnels [R73]. Les incorporations sont principalement sous forme pyridine et contribuent favorablement au processus de charge et décharge. Les pyrroles favorisent également l'augmentation de la capacité, mais une trop grande densité de pyrrole rend la rétention ionique trop élevée pour que la charge et la décharge soient réversibles [R73].

1.2.6 Traitement du graphène par plasma d'ammoniac

L'intérêt du plasma d'ammoniac (NH_3) est multiple. En effet, la dissociation de l'ammoniac dans le plasma fournit une multitude d'atomes réactifs neutres (N , NH , NH_2 , H) qui peuvent mener à plusieurs effets discutés dans les précédentes sections. Tout comme pour les plasmas d'hydrogène, (**Section 1.2.2**), certaines conditions opératoires peuvent favoriser la gravure chimique par les atomes de H . Les processus d'incorporation de N et leur dépendance avec l'énergie des ions incidents discutés pour les plasmas de N_2 (**Section 1.2.5**) demeurent valides. De plus, les espèces réactives peuvent également se lier à la surface et engendrer une multitude de réactions et de déformations du réseau graphénique.

Par exemple, les traitements par plasma d'ammoniac se sont montrés efficaces pour simultanément réduire le graphène et y incorporer des atomes d'azote. Contrairement aux méthodes de réduction humide d'oxyde de graphène, les méthodes basées sur les plasmas, de par leur nature sèche, possèdent l'avantage de minimiser la réagrégation des îlots de graphène

lors de la réduction [R74]. En plus de la diminution du ratio D:G qui corrobore la libération des groupes fonctionnels d'oxygène, la liaison aux azotes dans les cycles aromatiques rétablit les hybridations sp^2 des carbones avoisinants. Du fait de l'élimination des courbures entraînées par les liens sp^3 , la réduction diminue aussi la rugosité de la surface. La réduction des groupes époxydes est assurée par le N_2H_4 formé dans la décharge. Toutefois, le traitement induit des dommages structuraux visibles par la composante amorphe en spectroscopie Raman. Suite à l'extinction majeure du signal D:G, une réaugmentation des dommages est obtenue par l'amorphisation et le bombardement ionique [R75].

La capacité réductrice du plasma d'ammoniac permet également de nettoyer et de doper le graphène après que celui-ci ait reçu un traitement en plasma d'oxygène [R56]. Les lacunes créées par la gravure en plasma d'oxygène peuvent alors permettre l'incorporation d'azote dissocié dans le plasma. En effet, pour des traitements indirects, les effets de traitement NH_3 sont extrêmement dépendants des lacunes préexistantes. De plus, pour des températures suffisamment basses, l'hydrogène dissocié dans le plasma ne sera pas responsable de gravure chimique. Sans usage de prétraitement, l'incorporation devient limitée par les défauts de croissance et le traitement par plasma d'ammoniac permet le dopage négatif (0.2 eV) par l'incorporation d'azote (3% N1s) dans la structure graphénique [R76]. La création des liens C-C sp^3 est alors reliée à la liaison de groupes organiques aux sites de défauts et aux bords de grains. Les barrières d'adsorption de N, NH ou NH_2 sont très faibles (< 0.2 eV) et l'incorporation (2-3 eV) peut facilement être activée par la désexcitation ou la recombinaison d'espèces actives du plasma [R77].

Le traitement indirect d'un plasma micro-onde d'ammoniac permet une mise en présence importante de radicaux sans trop endommager l'échantillon. Les spectres Raman montrent une saturation dans le temps du pic D, suivie d'une diminution du pic 2D (**Figure 19a**). [R78] L'augmentation du pic D est reliée à la déformation de la structure par l'adsorption de radicaux. Un recuit subséquent (400-800°C) permet de désorber les espèces adsorbées pour restaurer partiellement le graphène. Les courbes courant-tension (**Figure 19b**) montrent notamment le dopage positif intrinsèque dû au substrat et aux impuretés. Les traitements subséquents entraînent un dopage négatif associé à des incorporations de type graphitique.

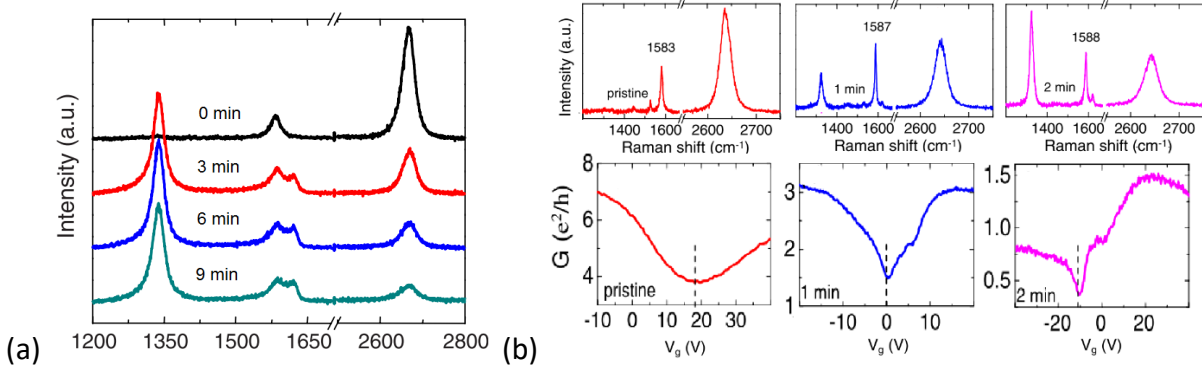


Figure 19 : a) Spectre Raman pour un traitement indirect du plasma micro-onde NH_3 . Traitement de 0,3,6,9 min b) courbe courant tension et spectre Raman associé pour des traitements 0, 1, 2 min [R78].

1.3 Conclusion

Dans ce chapitre, nous avons exposé les principales propriétés électroniques et vibrationnelles du graphène, ses méthodes de synthèse et de traitement post-synthèse. En dépit de la littérature sur les traitements dans des plasmas d'argon, d'hydrogène, d'oxygène, d'azote et d'ammoniac, on constate que plusieurs défis scientifiques et technologiques demeurent. En particulier, très peu de recherches ont été réalisées afin de corrélérer les propriétés du plasma avec les modifications des propriétés du graphène de sorte que l'état des connaissances sur la physique des procédés basés sur les plasmas reste qualitatif. Des études paramétriques complètes paraissent nécessaires pour maîtriser la physique des traitements par plasma des matériaux de faibles dimensions comme le graphène afin d'ajuster leurs propriétés selon l'application envisagée.

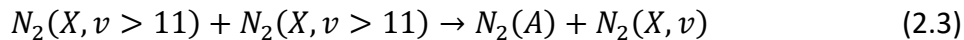
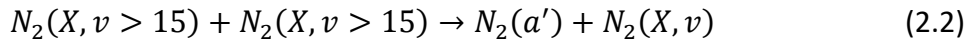
Chapitre 2 – Considérations expérimentales

2.1 Introduction

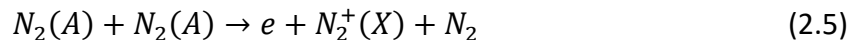
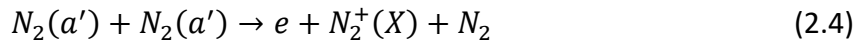
Afin de répondre à certains défis scientifiques et technologiques abordés dans le chapitre précédent, nous avons choisi d'utiliser la post-décharge en flux de plasmas micro-ondes dans l'azote à pression réduite. Cet environnement a déjà démontré son potentiel dans le traitement des nanomatériaux. En effet, il a été montré qu'il est possible de restaurer des sites de défauts de croissance non radiatifs dans des nanofils de InGaN/GaN et même de modifier leurs spectres de photoluminescence par l'introduction d'oxygène [R79]. Pour des flux gazeux suffisamment élevés (100 – 1000 sccm) et des pressions suffisamment hautes (3-20 Torr), une zone lumineuse apparaît alors au-delà du plasma principal [R80]. Cette zone lumineuse additionnelle est une conséquence d'un pompage vibrationnel (*V-V pumping*) par collisions dans la phase gazeuse :



Il s'en suit un transfert de cette énergie vibrationnelle vers des niveaux électroniques excités. Ceci cause la hausse locale des densités de niveaux métastables de l'azote, $N_2(A)$ et $N_2(a')$:



Ces niveaux excités sont ensuite à l'origine de l'ionisation *Penning* (ionisation par transfert d'énergie interne) au-delà de la décharge principale :

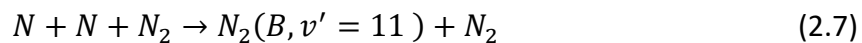


On observe ainsi une décharge (et donc une émission lumineuse) loin de la décharge principale sans l'application d'un champs électrique additionnel. On distingue deux régions composant la post-décharge en flux : la post-décharge proche (*Early afterglow – EA*) et la post-décharge lointaine (*Late afterglow - LA*). La transition entre ces deux régions le long de l'écoulement gazeux est causée par l'appauvrissement graduel des espèces électroniquement excitées alors qu'aucun autre apport d'énergie externe n'est fourni au système. Cette transition est couramment décrite par un coefficient “ a ” qui exprime la distribution vibrationnelle du premier système positif de

l'azote ($N_2(B) \rightarrow N_2(A)$) comme une combinaison linéaire d'une distribution de la post-décharge proche ($\alpha = 0$) et de la post-décharge lointaine ($\alpha = 1$) [R81] :

$$R_{B,v} = (1 - \alpha) R_{B,v'}(\text{early}) + \alpha R_{B,v'}(\text{late}) \quad (2.6)$$

La distribution vibrationnelle de la post-décharge proche suit, comme la décharge principale, une distribution de Boltzmann caractérisée par une température vibrationnelle T_{vib} , avec $T_e > T_{\text{vib}} > T_n$, où T_e est la température des électrons et T_n la température des neutres. Quant à la post-décharge lointaine, elle subit une inversion de population autour de $v = 11$ dû à la recombinaison à trois corps de l'azote atomique [R81]:



À titre d'illustration, la **Figure 20** présente une image de la post-décharge en flux du plasma micro-onde dans l'azote à pression réduite sur laquelle sont identifiées les différentes régions d'intérêt. Après la décharge principale, caractérisée par une forte émission lumineuse, on observe une région sombre dans laquelle s'effectue le pompage V-V (Équation 1.8) et où s'amorcent les réactions d'excitation (Équations 1.9 et 1.10) et d'ionisation (Équations 1.11-1.12). On observe ensuite la post-décharge proche puis la post-décharge lointaine. L'espacement entre le plasma et la post-décharge est régi par la cinétique collisionnelle (Équations 1.8-1.12) et dépend donc de la pression et de la vitesse de l'écoulement (ou du débit de gaz dans un réacteur de dimensions données).



Figure 20 : Image de la post-décharge en flux d'azote. On y distingue ses quatre principales régions.

Dans ce chapitre, nous présenterons d'abord, à la **Section 2.2**, une caractérisation par spectroscope d'émissions optique et par sonde de Langmuir des propriétés fondamentales de la post-décharge en flux de plasmas micro-ondes dans l'azote à pression réduite. En particulier, nous avons analysé le profil spatial des atomes d'azote, des ions N_2^+ , des électrons et des métastables

d'azote le long de l'écoulement gazeux, i.e. pour divers temps après la fin de la décharge principale. Tel qu'attendu, ces travaux révèlent l'apparition d'une post-décharge proche autour de 10 ms suivie d'une post-décharge lointaine pour des temps supérieurs.

Afin d'identifier la nature et l'amplitude du désordre engendré par le traitement par plasma, nous avons recours à deux principales méthodes de caractérisation : la spectroscopie Raman (RS) et la spectroscopie de photoélectrons X (XPS). Pour les mesures de RS, nous utilisons un montage de Raman confocal couramment utilisé pour la caractérisation de matériaux (inVia Renishaw). À l'aide d'un microscope optique, une région est sélectionnée et les acquisitions sont intégrées sur une zone circulaire d'environ 1 µm de diamètre. Il est alors possible de cartographier le traitement en déplaçant le laser sur différentes zones identifiables en microscopie optique. Contrairement aux mesures Raman, le montage XPS utilisé dans ce travail fournit des mesures beaucoup plus macroscopiques (ESCALAB 3 MKII); la région sondée est d'environ 2 mm x 3 mm. On obtient alors une vision beaucoup plus globale de l'échantillon avec un signal prédominant des régions représentant le plus de recouvrement de l'échantillon (les domaines du graphène). Ce niveau de caractérisation est standard dans la caractérisation de traitements par plasma du graphène de sorte qu'elle a été favorisée pour aborder les analyses réalisées durant cette thèse.

Nos travaux montrent que la post-décharge proche est beaucoup trop agressive et induit un nombre considérable de dommages, incluant l'amorphisation. Au contraire, la post-décharge lointaine révèle un comportement assez monotone d'incorporation avec peu de dommages. Cet environnement sera donc considéré comme plus adéquat pour le reste des travaux de cette thèse. Cette première partie est présentée sous la forme d'un article publié dans *Plasma Source Science and Technology* en décembre 2018. Contribution des auteurs : G. Robert Bigras – mesures et traitements expérimentaux, caractérisation et rédaction. X. Glad – mesures Raman et rédaction. R. Martel, A. Sarkissian et L. Stafford – supervision. Ensemble des auteurs – discussion et interprétation des résultats.

Nos premiers traitements par plasma du graphène ont soulevé plusieurs enjeux reliés à la préparation, à l'entreposage et à l'exposition à l'air ambiant des échantillons de graphène. Ainsi, la **Section 2.3** détaille l'importance de l'état des échantillons pour le traitement par plasma. Par

le vieillissement des échantillons et l'exposition de ceux-ci aux conditions ambiantes nous discutons de l'effet des contaminants de surface et de l'oxydation du substrat. On note que la présence d'oxyde de cuivre sous le graphène contribue à un découplage du graphène avec le substrat et altère significativement la cinétique de formation des dommages. L'influence de contaminants de surface sur l'incorporation d'azote est également discutée et suggère l'utilisation de plus de considérations pour l'entreposage des échantillons. Ces résultats sont présentés sous la forme d'un article publié dans *Carbon* en avril 2019. Contribution des auteurs : G. Robert – mesures et traitements expérimentaux, caractérisation et rédaction. X. Glad – mesures Raman et rédaction. R. Martel, et L. Stafford – supervision. Ensemble des auteurs – discussion et interprétation des résultats.

2.2 Comparaison traitement post-décharge proche et lointaine

Treatment of graphene films in the early and late afterglows of N₂ plasmas: comparison of the defect generation and N-incorporation dynamics

Germain Robert Bigras¹, Xavier Glad¹, Richard Martel², Andranik Sarkissian³, Luc Stafford¹

¹ Département de Physique, Université de Montréal, Montréal, Québec, CANADA

² Département de Chimie, Université de Montréal, Montréal, Québec, CANADA

³ Plasmionique Inc., Varennes, Québec, CANADA

Abstract

Graphene films grown on copper substrate by chemical vapor deposition were exposed to the flowing afterglow of a reduced-pressure N₂ plasma sustained by microwave electromagnetic fields (surface-wave plasma). Two set of conditions were examined by controlling the gas flow rate: the late afterglow (LA) characterized by high number densities of reactive N atoms and the early afterglow (EA) in which significant populations of metastable N₂(A) states and positive ions (N₂⁺ and N₄⁺) coexist with plasma-generated N atoms. LA treatments of graphene films show monotonous and steady incorporation of nitrogen atoms along with very low damage. However, given the very mild LA treatment conditions, a large part of the N atoms remains weakly bonded to the graphene surface; a feature ascribed to the plasma-induced functionalization of airborne hydrocarbon contaminants. In such conditions, graphitic inclusion of plasma-generated N atoms is limited to native defect sites. On the other hand, the presence of highly energetic species in the EA induces significant damage combined with much higher N-incorporation. Detailed Raman analysis of EA-treated samples further reveals a transition from vacancy-type defects to much larger multi-vacancies with increasing treatment time. This complete set of data indicates that through a judicious control of the populations of reactive N atoms, metastable N₂(A) states, and positive ions (N₂⁺ and N₄⁺), the flowing afterglow of microwave N₂ plasmas represents a highly promising tool for precise, post-growth tuning of the defect generation and N-incorporation dynamics in graphene films.

Keywords – Microwave plasmas, Flowing afterglows, Plasma-induced modification of materials and nanomaterials, Plasma-graphene interactions

1. Introduction

Over the past decade, numerous studies have been conducted to discover efficient and reliable methods to modify the physical and chemical properties of graphene films for a wide range of technological applications [1–5]. Whether it has been for fine tuning of the film conductivity by defect generation [6,7] or for enhancing its oxygen reduction capabilities by incorporation of nitrogen species [8,9], the fine control of the physical and chemical properties of graphene films has remained the central point of many researches on this highly promising nanomaterial. Indeed, most of the applications of graphene films require modification of the 2D honeycomb carbon lattice. In recent years, the popularity of plasma-based approaches for post-growth modification of graphene films has significantly risen due to their highly parameterizable nature, low cost, and ecological advantages.

Remote plasma treatment [10–18] is often used as a source of low-energy reactive neutrals in materials and nanomaterials processing. In most cases, the low-energy reactive neutrals cannot initiate thermally-activated surface reactions such that surface functionalization is limited to native defects and grain boundaries [17]. On the other hand, direct immersion of nanomaterials into a plasma can result in substantial damage generation, and even amorphisation; a feature mostly due to positive ions accelerated in the plasma sheath surrounding the substrate surface [19–21]. The drawbacks of such indirect and direct plasma-based approaches are hard to circumvent in a single-step treatment. More specifically, in the case of nitrogen incorporation, plasma-based treatments that result in high N-incorporation are known to significantly damage the graphene lattice [3,22].

This article deals with a versatile, post-growth treatment of graphene films by using the flowing afterglow of a microwave N₂ plasma. The very-low ion number density and high concentration of reactive neutrals and metastable species in this plasma-based medium is a radical departure from what is currently the state of the art in surface functionalization of materials and nanomaterials, mainly because the energy reservoir of metastable N₂(A) species (6 eV) can provide activation

energy for surface processes that would not occur spontaneously, while leaving the translational or kinetic energy of both the impinging species and the materials undisturbed. For example, this flowing afterglow was recently used for the modification of InGaN/GaN dot-in-a-wire nanostructures with the objective of tuning their emission properties [23]. By changing the N₂ gas flow rate, it was possible to expose the nanostructures to either the early afterglow (EA) or the late afterglow (LA) of the microwave N₂ plasma. While the band-edge emission from the GaN matrix of InGaN/GaN nanowires decreased due to the creation of non-radiative recombination centers in the near-surface region, the emission from the InGaN dots strongly increased. Such increase could not be explained by a plasma-induced shift of the GaN absorption edge; it was rather attributed to the passivation of grown-in defects and dynamic annealing induced by the plasma-generated N atoms and N₂(A) metastable states without excessive introduction of ion-induced damage. Inspired by this study, we compare in this work the treatment of graphene films in the early and late afterglows of microwave N₂ plasmas. After a detailed characterization of the flowing afterglow by Langmuir probe and optical emission spectroscopy, a combination of X-ray Photoelectron Spectroscopy (XPS), Scanning Electron Microscopy (SEM) and Raman Spectroscopy (RS) is used to examine the defect generation and N-incorporation dynamics in graphene films grown by chemical vapor deposition.

2. Experimental details

The experimental setup is shown in **Fig. 1** and thoroughly detailed in a previous paper [24]. A 2.45 GHz surface wave propagates along an 8-mm diameter (6-mm inner diameter) fused silica tube. The wave is excited by a gap-type wave launcher, namely a surfatron [25]. The injected power is set at 30 W, the working pressure at 6 Torr and the gas flow rate is adjusted in order to expose the sample to two different conditions in this nominally pure nitrogen flowing afterglow, namely the early and late afterglows (**Fig. 1**). Both afterglow regions are linked to the N₂ vibrational-vibrational pumping mechanism, which creates highly energetic N₂ vibrational states that are pushed downstream of the plasma zone by relatively high gas flow rates. These highly energetic N₂ vibrational states can collide to form metastable states, namely, N₂(A) and N₂(a') (at 6 eV and 8.1 eV above ground N₂(X), respectively) and subsequent ion-electron pairs by associative ionization reactions [26]. Both regions appear as bright areas downstream of the main surface-

wave plasma region and are separated from the latter by a non-radiative area called the dark zone [24]. To minimize the presence of impurities in the gas phase, the experiments were conducted with a base pressure of 1.7×10^{-7} Torr, an ultra-high-purity N₂ gas (99.999%) and a gas purifier (SAES Pure Gas Inc Nitrogen MC1-920F).

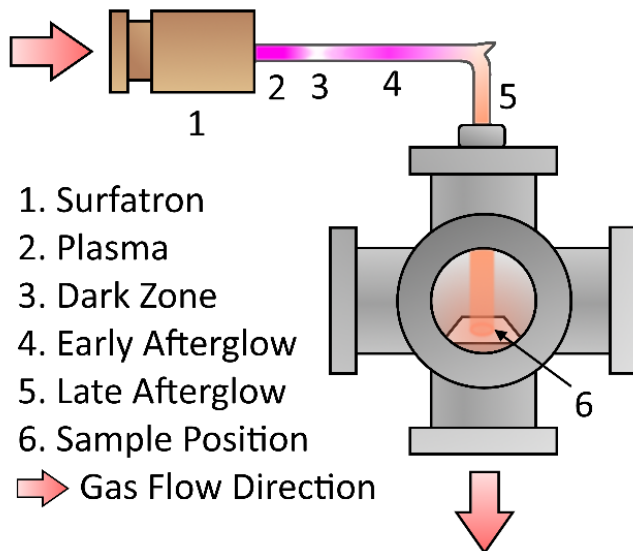


Fig. 1 - Treatment of graphene films in the flowing afterglow of microwave N₂ plasmas created by the propagation of an electromagnetic surface wave. Schematic of the plasma system, where 1-4 show the location of the different zones of the discharge and afterglow regions and 5 is the position of the graphene sample in the downstream flow. When the N₂ flow rate is increased, the early afterglow is shifted towards the sample.

The experiments were conducted on graphene films grown by chemical vapor deposition on polycrystalline copper foils (Alfa Aesar item No. 13382). Growth conditions are detailed elsewhere [27]. Briefly, the foil is treated with acetic acid and then annealed at 1000°C for 30 min under 50 mTorr of H₂ before introducing CH₄ until a pressure of 500 mTorr is reached. After a growth phase of 10 min, the sample received a cooling phase in H₂. The 5×10 mm² samples were then exposed to five subsequent 30-second treatments to the flowing afterglow between which X-Ray photoelectron spectroscopy (XPS) and Raman spectroscopy (RS) were carried out. Selected samples were also observed by Scanning Electron Microscopy (SEM).

XPS was performed on an ESCALAB 3 MKII device using the 300 W Al K α source, the beam size being 2×3 mm². Survey and high-resolution spectra were taken with 100 eV and 20 eV pass energy and a step of 1 eV and 0.05 eV, respectively. For the deconvolution, peaks full width at half maximum (FWHM) were set to 1.6 eV for C1s, 1.8 eV for O1s and 1.7 eV for N1s, except for the main C1s main peak sp² C-C (284.6 eV) and the associated pi-pi* shake-up (291.3 eV). The sp² C-C peak is fitted using a Doniach-Sunjic [28] (asymmetry factor alpha = 0.06 [29]) convoluted with a Lorentzian-Gaussian product (1:1) to represent its metallic properties. A smaller FWHM is used for this band since the carbon lattice is highly ordered. Other bands are fitted with a Lorentzian-Gaussian product (1:1). The sp² C-C shake-up is allowed a larger FWHM due to its satellite nature.

Under excitation from visible light, copper emits a broad background photoluminescence associated to its surface plasmon emission [30,31]. Hence, RS on graphene is usually performed after transfer on SiO₂/Si substrates. This is commonly done by using Poly(methyl methacrylate) (PMMA) which leaves PMMA residue, adsorbed O₂ and trapped H₂O [32] on the sample. These impurities may desorb during subsequent plasma treatment and induce unwanted chemical etching [33]. Besides, their removal is tricky and can create irremediable defects in the graphene film [34]. In this study, the transfer has been avoided in favor of the use of a 488-nm laser wavelength (2.54 eV) enabling easy baseline subtraction (see supplementary data S1) while keeping good signal-to-noise ratio. The measurements were done using a ×50 objective (numerical aperture 0.60) leading to a spot size of about 1.5 μm (around 2.7×10⁸ carbon atoms) with a laser power fixed at 0.7 mW and an acquisition time of 30 s. Repetitive measurements confirmed that the sample was not damaged by the laser exposition.

Scanning electron microscopy (SEM) was also performed to assess microscopic damage to the graphene and substrate. The same area was probed before and after the first 30 s treatment using a JEOL JSM-7600F at an acceleration voltage of 1 kV in the secondary electron mode (gentle-beam). The observed area being located close to the edge of the sample, possible damage arising from the electron irradiation would not be probed by XPS or RS measurements.

3. Experimental results

3.1 Characterization of the flowing afterglow

The species contained in the early and late afterglow regions of microwave N₂ plasmas (namely N(⁴S) atoms, N₂(A) metastable states, positive ions and electrons) can be carefully characterized by Langmuir probe and optical emission spectroscopy measurements [24]. The important results are summarized in **Fig. 2** as a function of the afterglow time. This parameter is a partially de-dimensionalized spatial coordinate combining sample position with respect to the end of the surface-wave plasma column, gas velocity and operating pressure. It allows for rather direct comparison of the populations of plasma-generated species over a wide range of operating conditions. The rise in all quantities at 10 ms corresponds to the early afterglow [35,36], while longer times can be ascribed to the late afterglow. The two dashed lines in **Fig. 2** identify the experimental conditions investigated for the treatment of graphene films: the early afterglow (9 ms) and the late afterglow (35 ms). Over the range of experimental conditions examined in this work, the EA and LA regions were obtained at a gas flow rate of 300 and 100 sccm (standard cubic centimeters per minute), respectively.

In **Fig. 2**, the concentration of charged particles is obtained from Langmuir probe measurements. The ion number density is estimated from the ion saturation current using Orbital Motion Limited (OML) theory [37]. For the two treatment conditions selected, the early afterglow shows a much higher ion density ($n_i = 6 \times 10^8 \text{ cm}^{-3}$) than the late afterglow ($n_i = 6 \times 10^6 \text{ cm}^{-3}$). As for the electron density, it is estimated from the probe current at the discharge potential VP. The latter is obtained from the point where the second derivative of the current-voltage characteristics goes through zero [37]. At this point, there is no electric field (neglecting space-charge electric fields) such that the electron thermal velocity dictates the measured current,

$$I_e = 1/4 n_e e v_e A_p , \quad (1)$$

where n_e is the electron number density at the Langmuir probe position, e is the absolute value of the electron charge, and A_p is the probe area. Thermal velocities are calculated from the electron energy distribution function (EEDF) that were found to be close to a Maxwellian for all conditions investigated [24]. The resulting electron and ion number density profiles reveal the

same behavior: a characteristic rise of both densities at the transition between the dark zone and the EA followed by a smooth decrease for the gradual transition between EA and LA. As for n_e , it decreases from $9 \times 10^6 \text{ cm}^{-3}$ to $7 \times 10^4 \text{ cm}^{-3}$ between the EA and LA. The electron density is therefore 10 to 100 times lower than the ion density. Due to the large increase of the number densities of charged particles (ions and electrons) in the EA, the graphene samples are expected to sustain much greater damage from EA treatments.

The $N(^4S)$ number densities displayed in **Fig. 2** were obtained using NO titration as described in Ref. [38]. Optical emission spectroscopy measurements were performed transverse to the gas flow, 1 cm from the substrate position through a quartz window. The population of $N(^4S)$ is several orders of magnitude (7) larger than the ion number density. It ranges from $2 \times 10^{15} \text{ cm}^{-3}$ to $4 \times 10^{14} \text{ cm}^{-3}$ between the EA and LA regions. Actinometry on the first and second positive system of N2 was also used to determine the population of $N_2(A)$ metastable states [39]. As shown in **Fig. 2**, the number density of $N_2(A)$ metastable species decreases from $3 \times 10^{11} \text{ cm}^{-3}$ to $2 \times 10^{10} \text{ cm}^{-3}$ between the EA and LA regions.

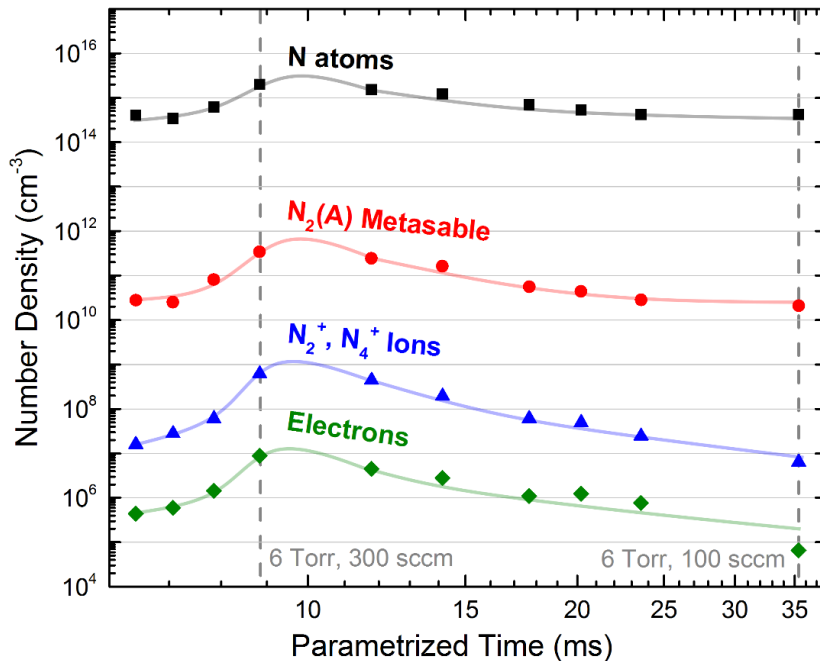


Fig. 2 – Influence of the parametrized time on the ions (N_2^+ and N_4^+), electrons, $N(^4S)$ and metastable $N_2(A)$ populations in pure N₂.

The complete set of data presented in **Fig. 2** confirms that by adjusting the parametrized time, or the gas flow rate for a constant pressure and fixed distance between the end of the surface-wave plasma column and the substrate, significant changes in the populations of plasma-generated N(⁴S) atoms, N₂(A) metastable states, positive ions and electrons can be achieved at the substrate surface. In this context, the LA region (mostly characterized by a high number densities of N(⁴S) atoms) should yield to relatively “mild” treatments of graphene films. In contrast, the EA region (characterized by a significant amount of highly energetic species, in particular N₂(A) metastable species and positive ions (N₂⁺ and N₄⁺), in addition to N(⁴S) atoms) should represent a much “harsher” environment for the treatment of nanomaterials.

3.2 X-Ray Photoelectron Spectroscopy of plasma-treated graphene films

XPS is a powerful tool to assess the incorporation of heteroatoms in graphene films [29]. Typical survey spectra are presented in Supplementary Data (S2) for reference. **Fig. 3** shows the XPS high-resolution C1s scans performed on graphene films for various LA and EA treatment times. It is worth recalling that the time in **Fig. 3** represents subsequent treatment times on the same substrate. For example, 150 s consists of 5 times 30 s, not a continuous 150 s treatment.

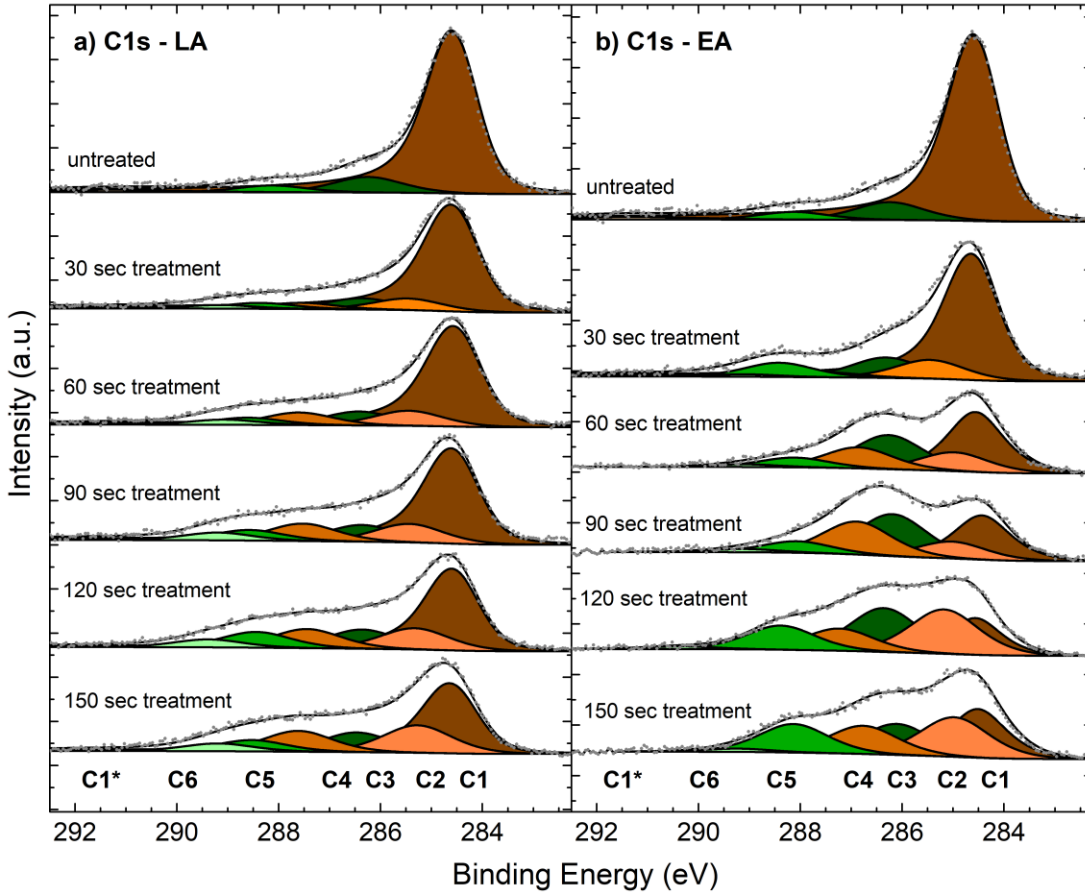


Fig. 3 – XPS high-resolution C1s scans for late (a) and early (b) afterglow at 0, 30, 60, 90, 120 and 150 seconds of total treatment times.

The C 1s band peaks at a binding energy of 286.4 eV and shows a tail up to 290 eV. These higher energy contributions are linked to various carbon, nitrogen and oxygen bonds. The main C1 (sp² C-C) contribution for graphene is found at 284.6 eV [29,40–44] and its satellite C1* (π - π^* shake-up) at 291.3 eV [40–42]. Carbon-nitrogen moieties are identified by the two sub-peaks C2 (sp² C=N) and C4 (sp³ C-N) respectively at 285.45 ± 0.1 eV [29,45,46] and 287.4 ± 0.1 eV [46–48]. Oxygen contributions are linked to multiple bands: C3 (C-OH) at 286.3 ± 0.1 eV [42–44,48], C5 (C=O and/or O=C-O) at 288.4 ± 0.2 eV [40,43,46,47,49] and C6 (O=C-OH) at 289.0 ± 0.2 eV [48]. EA treatments show a strong C1 decrease, significantly greater than for LA treatments; this implies higher damage generation. Overall, the ratios C2/C1 and C4/C1 are higher for EA than for LA, suggesting a more important N-incorporation after treatment in EA than in LA. In addition, the ratios C3/C1, C5/C1 and C6/C1 significantly increase for the EA treatments. This rise in the

oxygen-to-carbon proportion reveals stronger damage; a feature linked not only to multiple exposures to the harsher EA environment but also to multiple exposures to ambient air conditions between each plasma-based treatment. We will come back to this point in the discussion section.

XPS high-resolution N1s bands for several subsequent treatment times in the LA and the EA are presented in **Fig. 4**. Nitrogen seems to be present in many adsorbed, aromatic and edge configurations. More specifically, both treatments yield at least 3 nitrogen moieties in graphene: N1 (pyridine) at 398.5 ± 0.1 eV [29,45,50,51], N2 (amine, nitroso and or pyrrole) at 399.7 ± 0.1 eV [29,51–54] and N3 (graphitic) at 401.1 ± 0.1 eV [29,45,50,51,54]. The graphitic moiety is a simple substitution of one carbon atom by one nitrogen atom in the honeycomb graphene lattice. This incorporation is generally desirable for applications requiring negative doping [55]. As shown in **Fig. 4**, the N1s band on the EA-treated graphene sample is centered at a lower binding energy due to the presence of another nitrogen moiety generally identified as adsorbed nitrogen (N0) around 398 ± 0.1 eV [56,57]. As previously mentioned, the EA-treated sample shows greater damage and therefore may allow higher nitrogen incorporation in graphene films, in particular in adsorbed and edge configurations [10]. This result is not only consistent with the presence of an additional N0 moiety in the N1s spectra but also with the significant increase of the C2/C1 and C4/C1 ratios observed in Fig. 3 for the C1s band. Another nitrogen configuration is found for EA-treated graphene at about 404 ± 0.1 eV; this band is generally identified as trapped N2 and/or adsorbed NO [29,40,50].

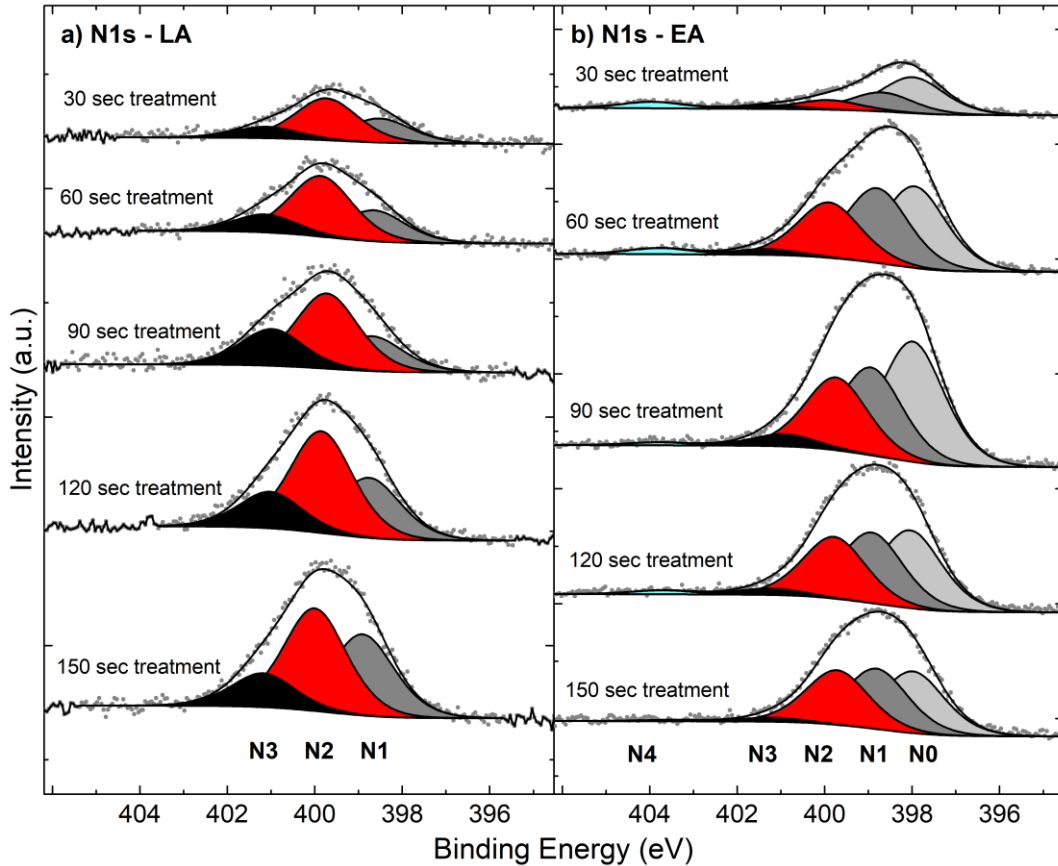


Fig. 4 – XPS high-resolution N1s scans for late (a) and early (b) afterglows at 0, 30, 60, 90, 120 and 150 seconds of total treatment times. No N1s signal was observed in untreated graphene samples.

Fig. 5 summarizes the influence of subsequent early and late afterglow treatment times of the same sample on the concentration fraction of all nitrogen moieties. LA treatments show a smooth and steady rise of nitrogen incorporation with increasing total treatment time. More specifically, most nitrogen moieties increase quasi-linearly with time, except the graphitic (N3) contribution that saturates around 2.5%. In addition, N2 is always superior to N1 which is always superior to N3. This suggests that the formation of aromatic nitrogen or graphitic nitrogen is preceded by N adsorption. Nevertheless, it is worth mentioning that density functional theory calculations have revealed that the activation energy for substitutional incorporation of nitrogen atoms in pristine graphene films is very large (22 eV) [58,59]. On the other hand, the energy barrier decreases drastically (<0.5 eV) [60,61] in presence of vacancy-type defects. Since the energy reservoir of plasma-generated species in the LA is insufficient for both the direct substitutional incorporation

of nitrogen atoms and the creation of vacancy-type defects in pristine graphene (>7.5 eV) [62], the formation dynamics of graphitic nitrogen in the LA thus seems to be limited to native defect sites.

Fig. 5 further reveals that the N-incorporation is much higher after treatment in the EA than the one achieved after the same exposure to the LA. This can be explained by the formation of additional defects in the EA, and thus to a defect concentration larger than the one driving the N-incorporation dynamics in LA treatments. Indeed, in the EA, the presence of highly energetic species, especially N₂(A) metastable states and positive ions (N₂⁺ and N₄⁺), can induce the formation of significant damage. This includes punctual, vacancy-type defects, but also extended defects such as large multivacancies that ultimately shrink the graphene nanodomains [63]. Such mechanism certainly explains the radical change in the sample composition observed by XPS. At short treatment times, EA treatments of graphene films first induce a very fast increase in the N-incorporation (up to $[N_{1s}/(C_{1s}+N_{1s}+O_{1s})] = 49\%$). However, at higher doses of highly-energetic, plasma-generated species, this increase is followed by a significant decrease of the N-incorporation (27%). Such behavior can be ascribed to excessive damage formation (in particular large multivacancies), leaving fewer sites for incorporated and trapped N-bearing species. This aspect is further discussed in **Section 4**.

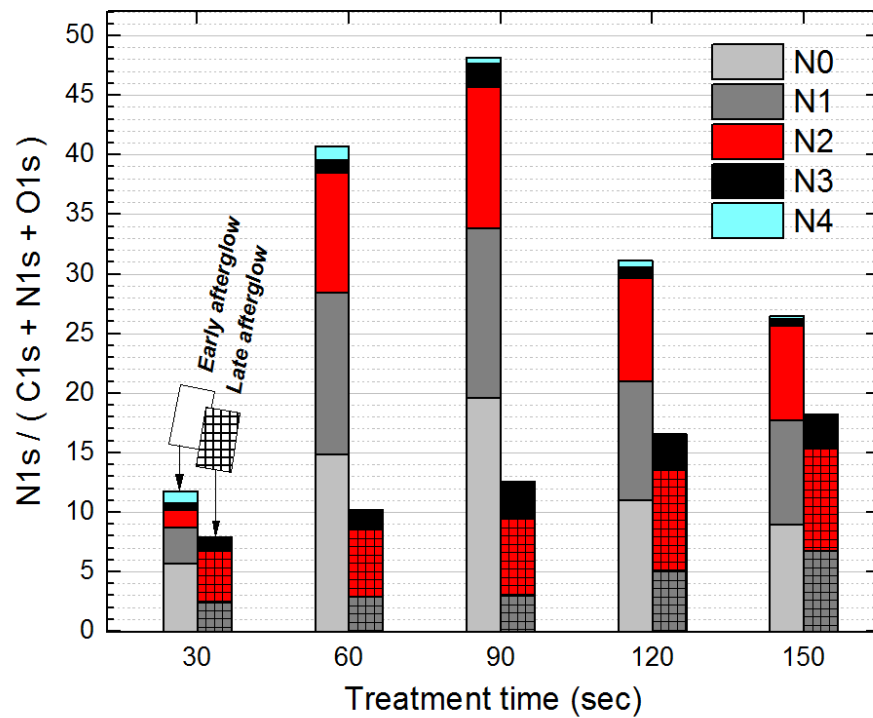


Fig. 5 – N1s relative percent incorporation for EA and LA treatments as a function of subsequent treatment times.

3.3 Scanning Electron Microscopy of plasma-treated graphene films

Fig. 6 shows SEM images for LA (**Fig. 6a-c**) and EA treatments (**Fig. 6d-f**) for 0 s (**Fig. 6a,d**), 30 s (**Fig. 6b,e**) and 150 s (**Fig. 6c,f**) subsequent treatment times on the same sample. Due to the numerous plasma treatments, we were unable to find the same zone after the final 30-second treatment and thus, another area, typical of the graphene surface, was chosen. Note that, in order to find the same location on the sample (a, b and d, e), regions near obvious defects where chosen and probed. These are not representative of the whole substrate.

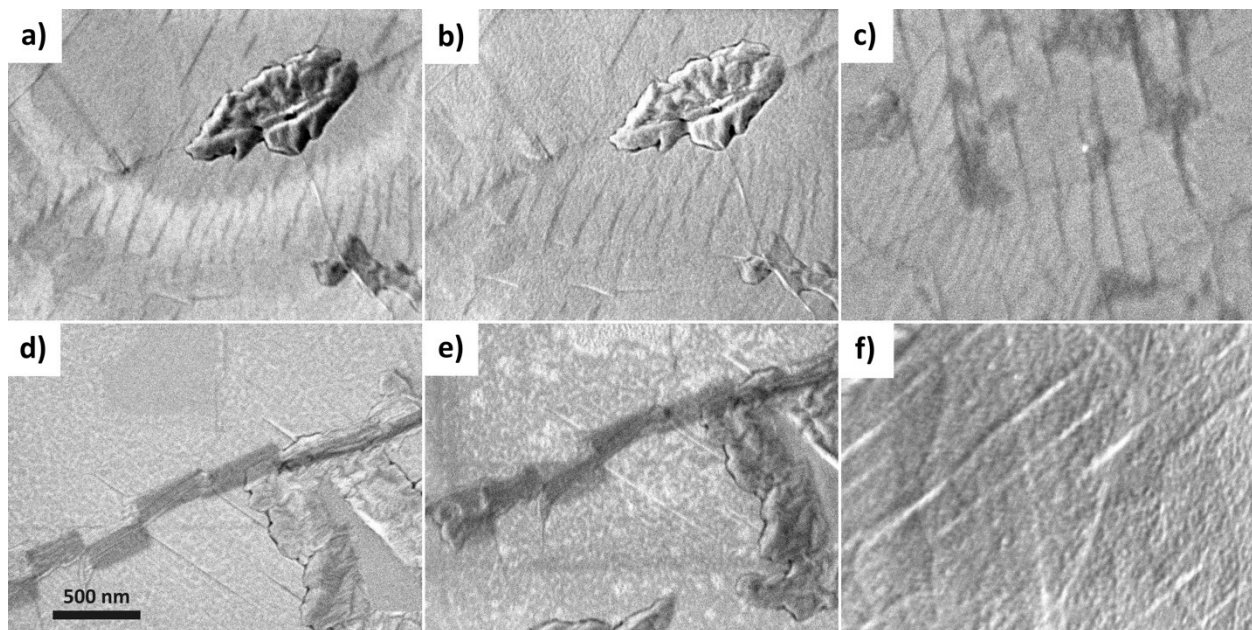


Fig. 6 – Scanning electron microscope image of LA (a-c) and EA (d-f) treated samples for 0 s (a,d), 30 s (b,e) and 150 s (c,f) treatment times. a) and b) as well as d) and e) show the same area for LA and EA-treated samples, respectively. Each image presents the same magnification. Strong white patterning is visible for both images of EA treated sample (e-f). This morphology change is not present in the LA-treated sample.

As shown in **Fig. 6**, LA treatments induce the formation of very few defects only noticeable as light contrasted regions on the graphene surface. Despite the presence of dark areas at $t = 150$ s (**Fig. 6c**), the graphene seems mostly unaltered. On the other hand, EA treatments of graphene films present strong white patterning on the surface and, subsequently, show a very strong surface morphology change. After the last treatment, the roughness of the graphene film has noticeably changed. This is consistent with the damage formation dynamics deduced from XPS analysis for EA-treated graphene films; a feature ascribed to the presence of highly energetic species, mostly N₂(A) metastable species and positive ions (N²⁺ and N⁴⁺).

3.4 Raman Spectroscopy of plasma-treated graphene films

Raman spectroscopy allows in-depth characterization of graphene films. It has been extensively used to identify notably the doping [64,65], structural disorder [19,66–69], tensile or compressive strain [70–72] or the nature of defects [20,21] in pristine or modified graphene films. Raman

spectra of defect-free single-layer graphene films possess several distinctive features, mainly the G (~ 1580 cm $^{-1}$) and 2D (~ 2700 cm $^{-1}$ at a laser wavelength of 488 nm, also called G') peaks. In the presence of grown-in or post-growth-process-induced defects in the lattice, the so-called D band arises around 1350 cm $^{-1}$. The D:G peak ratio is thus directly linked to the damage formation or the so-called crystallite size La [68,73] (determined by edges, vacancies, grain boundaries, in-plane substitution heteroatoms, etc. [74]). However, the Fermi level [65] and the laser wavelength [75] also influence the D peak intensity. On copper, the interaction with the underlying substrate makes the determination of La tricky [76–78]. Thus, RS studies of graphene films on copper mainly focus on the value of the D over G band intensity ratio to assess the damage sustained by the graphene lattice.

Fig. 7 presents the evolution of the average spectra for EA and LA as a function of the total treatment time. Spectra are systematically taken on 4 fixed locations on the graphene sample (with a 1- μm precision) between each 30-s afterglow treatment for both LA and EA. For each spectrum presented in **Fig. 7**, a normalization has been applied with respect to their 2D band intensity. To avoid unwanted broadening of the bands, the 2D and G peaks were shifted to their average value before the averaging process. This method was chosen over a standard average procedure to obtain consistent peak shapes, intensities and FWHMs in **Fig. 7** [79]. For the growth conditions used in this study, graphene was fully grown and was mainly monolayer. This is confirmed by Raman 2D:G ratio of 2 for untreated sample and the presence of only one component in the deconvolution of the 2D band (as opposed to 4 components in bilayer graphene) [80].

Results presented in **Fig. 7** show that the LA treatments induce very low damage as the 2D band remains the dominant feature even after 150 s [21]. The D band stays weak compared to the G peak, yielding D:G ratios up to 0.3. The overall behavior of the Raman spectra for EA-treated samples is drastically different. After only 30-s, the D band reaches very high values (D:G ratio ~ 1). Two other contributions could also be distinguished: around 1450 cm $^{-1}$ (Gaussian peak) identified as amorphous carbon (a-C) [81,82] and around 1620 cm $^{-1}$ (Fano line shape) known as the D' band [74,83]. As expected, the EA treatments lead to significantly more damage than the

LA treatments and, for 60 s and after, seem to initiate the formation of amorphous carbon. We will come back to this point later in the text.

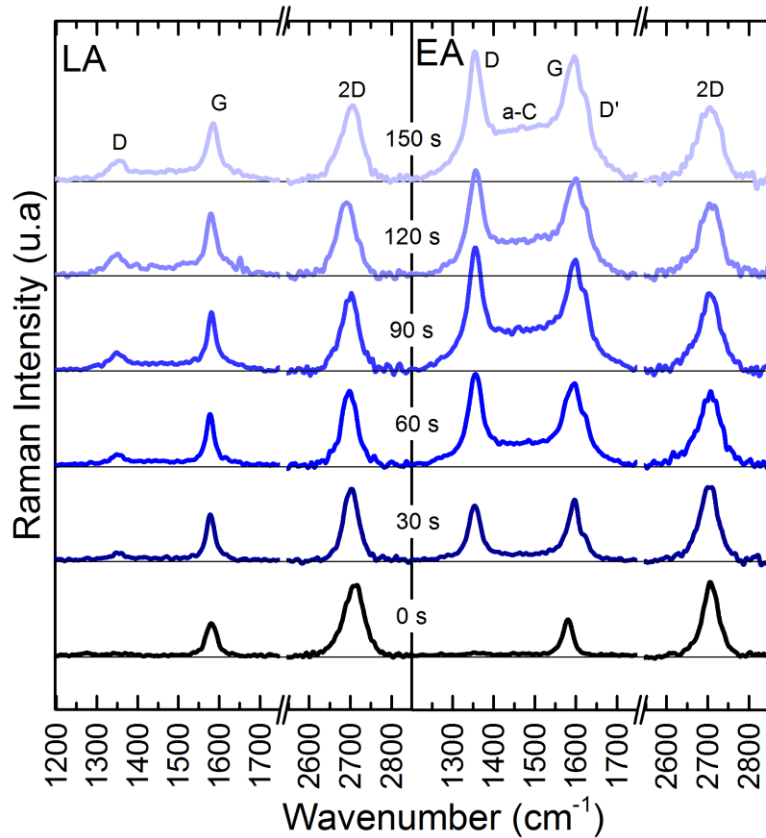


Fig. 7 – Raman spectra obtained as a function of the total exposure time for a graphene film exposed to LA (left) and EA (right) treatments. A 2.54-eV (488-nm) laser is used and each spectrum is normalized according to its 2D band intensity.

Fig. 8a shows the D:G intensity ratio as a function of treatment time for both LA and EA conditions. As previously stated, this ratio can be used to assess the damage generation dynamics in graphene films. For the LA-treated sample, the D:G ratio steadily increases and reaches a maximum value around 0.3 (very low damage). Such trend roughly scales with the N-incorporation observed in **Fig. 5**. On the other hand, for the EA-treated sample, the D:G ratio first sharply rise up to a maximum value of 1.6 at 90 s and then decreases down to 1.15 after 150 s. Again, such behavior roughly scales with the N-incorporation dynamics observed in **Fig. 5**. However, for comparable N-incorporation values, much higher D:G ratios are observed for EA-

treated samples. This is consistent with the formation of damage due to the presence of highly energetic species in the EA. As mentioned above, EA-induced damage in graphene films includes punctual, vacancy-type defects, but also extended defects such as large multivacancies that shrink the graphene nanodomains [63].

As shown in **Fig. 7** and **8a**, the high D:G ratios for EA-treated samples is accompanied by a significant rise in the Raman signal ascribed to amorphous carbon. For increasing defect site density, the graphene is expected to follow the well-documented transition towards amorphous carbon [19–21,84]. However, the D:G ratios generally observed for carbon amorphisation are between 2 and 3 (for a laser energy of 2.54 eV) [19–21]. In addition, the 2D:G ratios reported in **Fig. 8b** only falls from 2.3 to 1 with increasing total treatment time to the EA; this ratio is expected to fall under 1 at the beginning of carbon amorphisation [21,71]. Finally, the FWHMs of the D and G bands are not as broad as those commonly observed in the literature for amorphous or polycrystalline graphene. It is therefore believed that the last treatment steps of the EA-treated sample bring the state of the graphene films near the transition towards amorphous graphene. Overall, it is worth noting that the N-incorporation, obtained by XPS in both EA and LA treated samples, is very high for such low D:G ratios. We will come back to this point in the discussion section.

From all the previous observations, it is clear that the presence of highly energetic species in the EA induces significant damage in graphene films. Nevertheless, the identification of the nature of the plasma-generated damage defects is one of the key challenges paving the way of understanding the state of the graphene surface as it is being treated. Previous studies [20,21] elaborated on the correlation between the nature of defects and the D:D' ratio obtained by RS. Prior to the transition towards amorphisation of the graphene film, the D:D' ratio should be constant for a given damage type. For example, vacancy-type defects in graphene films produce a D:D' ratio of 7, while edge-type defects yield a D:D' ratio of 3.5 [20,21]. **Fig. 8c** presents the D:D' ratio for EA treatments as a function of the total treatment time. Due to the absence of significant damage (and thus significant D and D' peaks) for the untreated sample and the LA-treated sample, the D:D' ratio is only depicted for EA-treated sample after 30 s. As shown in **Fig. 8c**, the ratio decreases from a value of 6.8 at 30 s towards 3.5 at 150 s. Since the transition towards

amorphisation is assumed to only occur passed the final treatment time, this decrease indicates a modification in the damage type, going from vacancy-type defects at low treatments times to more extended edge-type defects beyond 90 s. Such change in the damage type around 90 s is consistent with the observed changes in the trends for the N-incorporation dynamics observed for EA-treated samples in **Fig. 5**.

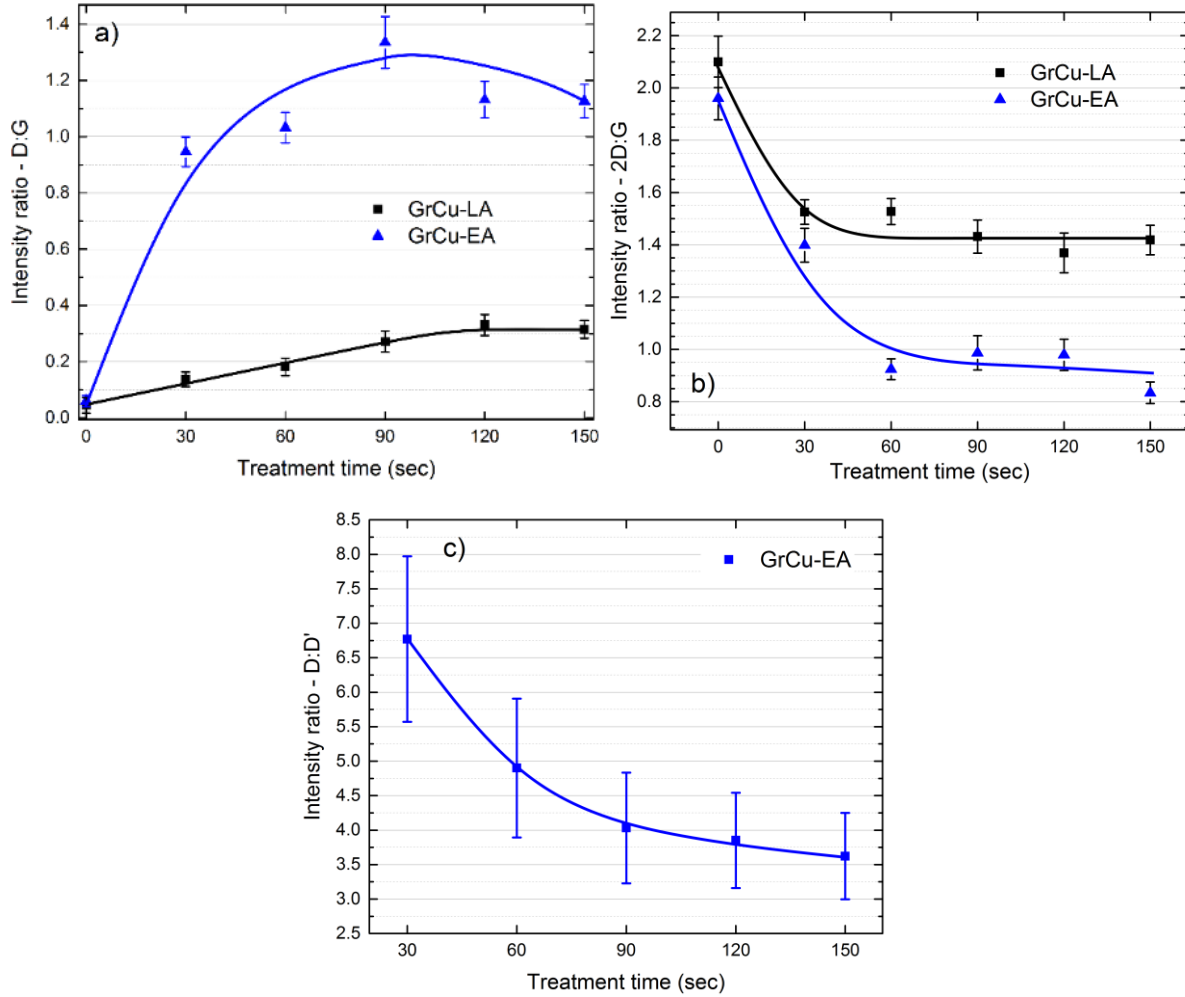


Fig. 8 –D:G (a), 2D:G (b) and D:D' (c) band ratios obtained by Raman spectroscopy as a function of total treatment time for graphene samples exposed to the LA or the EA. Lines are guides to the eye only.

4. Discussion

XPS measurements reveal high nitrogen incorporation for both LA and EA. However, in previous studies, transfer of LA-treated graphene samples on copper substrate towards SiO₂ substrate revealed that an important fraction (80%) of N-incorporated atoms disappeared [79]. This is because most of these moieties are weakly-bonded, carbon-nitrogen groups; a feature ascribed to the plasma-induced functionalization of airborne hydrocarbon contaminants [79]. As reported by Li et al.[85], deposition of hydrocarbon compounds unavoidably occurs on graphene films kept under uncontrolled, atmospheric-pressure conditions. For the subsequent LA treatments carried out in this study, multiple exposures to both the LA and uncontrolled, atmospheric-pressure conditions allows easy N incorporation into the hydrocarbon film, yielding significant number of carbon-nitrogen groups. Since the underlying graphene remains mostly undamaged, this mechanism also leads to very low D:G ratios, as obtained by RS (0.3; see **Fig. 8a**). The resulting sample is thus believed to be weakly nitrogen-doped graphene beneath a thin nitrogen and oxygen functionalized hydrocarbon film. In such mild LA treatments, despite the contribution of airborne contaminants, it can still be concluded that the graphitic (N3) incorporation is limited by the number of grown-in defects in graphene films.

For EA-treated samples, the presence of airborne contaminants also significantly enhances the N-incorporation dynamics. However, in contrast to the mild LA treatments, the presence of highly energetic species in the EA can result in numerous additional effects. First, with an appropriate source of energy, the weakly-bonded hydrocarbon contaminants become subject to amorphisation [86]. This mechanism could contribute to the increase of the amorphous carbon feature revealed by RS (**Fig. 7**). Second, in presence of irradiation effects by positive ions and metastable species in the EA, the weakly-bonded hydrocarbon film could bind with the underlying graphene film. This would yield to a broadening of the D, 2D and G bands, as seen in the experiments (**Fig. 7**). Finally, dissimilarly to the steady nitrogen incorporation behavior observed for the LA treatments, the rather destructive nature of EA treatments results in a decrease of the nitrogen incorporation at higher treatment times. Through Raman analysis, the harsher EA environment was found to create multi-vacancies in the graphene lattice. This would necessarily reduce the number of available incorporation sites and thus the nitrogen content at higher N

atoms doses (higher treatment times). Ion-assisted reticulation and subsequent formation of hydrocarbon-graphene structures could also be responsible for the decrease of the nitrogen content probed by XPS. This analysis is further supported by the evolution of the Cu2p XPS peak (see Fig. S3) that reveals a strong increase of the copper oxide contribution with treatment time for EA. The presence of large multi-vacancies sites would obviously promote O bonding to the copper sample and increase the XPS response of the now uncovered copper oxide. Such behavior highlighting the presence of a maximum at 90 s can also be seen in the evolution of the C1s signal (see Fig. 3).

Overall, both treatments present their share of perks and drawbacks. Based on the results presented in this work, it seems that the LA conditions are too gentle to induce a strong aromatic incorporation of N species while the EA conditions are harsher and would ultimately lead to an amorphisation of the graphene film. However, the main advantage of the flowing afterglow of microwave N₂ plasmas is that one may easily adjust the flux to increase or decrease the populations of positive ions and N₂(A) metastable states in order to finely control the damage generation, and possibly the N aromatic incorporation content. Such hybrid plasma-based treatments would combine the advantages that both regions of the flowing afterglow provide; defect-limited incorporation of plasma-generated atoms without strong airborne contaminant amorphisation and controlled damage generation.

5. Conclusion

Graphene films grown on copper substrate by chemical vapor deposition were exposed to the flowing afterglow of a reduced-pressure N₂ plasma sustained by microwave electromagnetic fields (surface-wave plasma). Two different environments were selected by controlling the gas flow rate: the late afterglow (LA) characterized by high number densities of reactive N atoms and the early afterglow (EA) in which significant populations of metastable N₂(A) states and positive ions (N₂⁺ and N₄⁺) coexist with plasma-generated N atoms.

LA treatments show monotonous and steady incorporation of nitrogen and damage generation. The incorporation is assessed by XPS and reaches values of (N1s/(C1s+N1s+O1s)) of 18% while the Raman D:G ratio stays very low (0.3). High N incorporation combined with very low damage

is ascribed to the plasma-induced functionalization of airborne hydrocarbon contaminants. Given the very mild LA treatment conditions, a large part of the N atoms remains weakly bonded to the graphene surface without strongly damaging the underlying graphene. The graphitic aromatic incorporation is found to be defect-limited and the principal nitrogen incorporation mechanism result from airborne hydrocarbons functionalization.

The EA treatments are significantly more damaging to the graphene lattice. This damage generation allows an increase in the nitrogen content assessed by XPS (reaching 49% at 90 s treatment time). Additionally, the presence of these highly energetic species lead to the formation of an amorphous carbon film on top of the graphene film that is linked to the irradiation-induced modification of surface hydrocarbons. This phenomenon is supported by the relatively small D:G ratios of 1.3 provided by RS for such high nitrogen incorporation. In addition, the transition of the D:D' ratio from 6.7 to 3.6 indicates a defect type transition from vacancy to edges explained by the formation of increasingly large multivacancies.

These results show the viability of the flowing afterglow technique as a promising tool for precise post-growth tuning of the defect density and damage type for graphene films. Indeed, even though only two conditions were studied, the flowing afterglow of microwave N₂ plasmas consists in a continuous transition between the two damage generation mechanisms presented in this paper. Therefore, tuning the gas flow rate enables judicious control of the populations of reactive N atoms, metastable N₂(A) states, and positive ions (N₂⁺ and N₄⁺) interacting with graphene films. This flowing afterglow approach opens the path to one-step processes allowing controlled defect generation with a high N-incorporation. Subsequent post-treatment, like reconstructive annealing for example, could give even more control on the relative percent of nitrogen moieties.

6. Acknowledgments

This work was financially supported by the National Science and Engineering Research Council (NSERC), PRIMA-Québec, Plasmionique inc., Photon Etc., and the Fonds de Recherche du Québec – Nature et Technologies (FRQNT).

7. References

- [1] A. Zurutuza, C. Marinelli, *Nat. Nanotechnol.* 9 (2014) 730–734.
- [2] A. Ney, P. Papakonstantinou, A. Kumar, N.-G. Shang, N. Peng, *Appl. Phys. Lett.* 99 (2011) 102504.
- [3] M. Fan, Z. Feng, C. Zhu, X. Chen, C. Chen, J. Yang, D. Sun, *J. Mater. Sci.* 51 (2016) 10323–10349.
- [4] V. Georgakilas, M. Otyepka, A.B. Bourlinos, V. Chandra, N. Kim, K.C. Kemp, P. Hobza, R. Zboril, K.S. Kim, *Chem. Rev.* 112 (2012) 6156–6214.
- [5] N.G. Shang, P. Papakonstantinou, M. McMullan, M. Chu, A. Stamboulis, A. Potenza, S.S. Dhesi, H. Marchetto, *Adv. Funct. Mater.* 18 (2008) 3506–3514.
- [6] W. Zhao, Y. Wang, Z. Wu, W. Wang, K. Bi, Z. Liang, J. Yang, Y. Chen, Z. Xu, Z. Ni, *Sci. Rep.* 5 (2015) 11962.
- [7] A. Nourbakhsh, M. Cantoro, T. Vosch, G. Pourtois, F. Clemente, M.H. van der Veen, J. Hofkens, M.M. Heyns, S. De Gendt, B.F. Sels, *Nanotechnology* 21 (2010) 435203.
- [8] Y. Wang, Y. Shao, D.W. Matson, J. Li, Y. Lin, *ACS Nano* 4 (2010) 1790–1798.
- [9] Y. Shao, S. Zhang, M.H. Engelhard, G. Li, G. Shao, Y. Wang, J. Liu, I.A. Aksay, Y. Lin, *J. Mater. Chem.* 20 (2010) 7491.
- [10] J.B. McManus, A. Hennessy, C.P. Cullen, T. Hallam, N. McEvoy, G.S. Duesberg, *Phys. Status Solidi* 1700214 (2017) 1700214.
- [11] F. Joucken, Y. Tison, J. Lagoute, J. Dumont, D. Cabosart, B. Zheng, V. Repain, C. Chacon, Y. Girard, A.R. Botello-Méndez, S. Rousset, R. Sporken, J.C. Charlier, L. Henrard, *Phys. Rev. B - Condens. Matter Mater. Phys.* 85 (2012) 1–5.
- [12] A. Dias, N. Bundaleski, E. Tatarova, F.M. Dias, M. Abrashev, U. Cvelbar, O.M.N.D. Teodoro, J. Henriques, *J. Phys. D. Appl. Phys.* 49 (2016) 055307.
- [13] R. Yang, L. Zhang, Y. Wang, Z. Shi, D. Shi, H. Gao, E. Wang, G. Zhang, *Adv. Mater.* 22 (2010) 4014–4019.
- [14] N. McEvoy, H. Nolan, N. Ashok Kumar, T. Hallam, G.S. Duesberg, *Carbon N. Y.* 54 (2013) 283–290.
- [15] N.A. Kumar, H. Nolan, N. McEvoy, E. Rezvani, R.L. Doyle, M.E.G. Lyons, G.S. Duesberg, *J. Mater. Chem. A* 1 (2013) 4431.
- [16] V.M. Pereira, J. Nilsson, A.H.C. Neto, *Carbon N. Y.* 50 (2007) 395–403.
- [17] M. Seifert, J.E.B. Vargas, M. Bobinger, M. Sachsenhauser, A.W. Cummings, S. Roche, J.A. Garrido, *2D Mater.* 2 (2015) 024008.
- [18] G. Diankov, M. Neumann, D. Goldhaber-Gordon, *ACS Nano* 7 (2013) 1324–1332.
- [19] A. Ferrari, J. Robertson, *Phys. Rev. B* 61 (2000) 14095–14107.
- [20] A. Eckmann, A. Felten, I. Verzhbitskiy, R. Davey, C. Casiraghi, *Phys. Rev. B* 88 (2013) 035426.
- [21] A. Eckmann, A. Felten, A. Mishchenko, L. Britnell, R. Krupke, K.S. Novoselov, C. Casiraghi, *Nano Lett.* 12 (2012) 3925–3930.
- [22] A. Dey, A. Chroneos, N.S.J. Braithwaite, R.P. Gandhiraman, S. Krishnamurthy, *Appl. Phys. Rev.* 3 (2016) 021301.
- [23] J.A. Ferreira, H.P.T. Nguyen, Z. Mi, R. Leonelli, L. Stafford, *Nanotechnology* 25 (2014) 435606.
- [24] J. Afonso Ferreira, L. Stafford, R. Leonelli, A. Ricard, *J. Appl. Phys.* 115 (2014) 163303.

- [25] M. Moisan, Z. Zakrzewski, R. Pantel, *J. Phys. D. Appl. Phys.* 12 (1979) 219–237.
- [26] M.K. Boudam, B. Saoudi, M. Moisan, A. Ricard, *J. Phys. D. Appl. Phys.* 40 (2007) 1694–1711.
- [27] S. Choubak, M. Biron, P.L. Levesque, R. Martel, P. Desjardins, *J. Phys. Lett.* 4 (2013) 1100–1103.
- [28] S. Doniach, M. Sunjic, *J. Phys. C Solid State Phys.* 3 (1970) 285–291.
- [29] T. Susi, T. Pichler, P. Ayala, *Beilstein J. Nanotechnol.* 6 (2015) 177–192.
- [30] S.D. Costa, A. Righi, C. Fantini, Y. Hao, C. Magnuson, L. Colombo, R.S. Ruoff, M.A. Pimenta, *Solid State Commun.* 152 (2012) 1317–1320.
- [31] A. Mooradian, *Phys. Rev. Lett.* 22 (1969) 185–187.
- [32] A. Pirkle, J. Chan, A. Venugopal, D. Hinojos, C.W. Magnuson, S. McDonnell, L. Colombo, E.M. Vogel, R.S. Ruoff, R.M. Wallace, *Appl. Phys. Lett.* 99 (2011) 2–5.
- [33] X. Glad, L. de Poucques, J. Bougdira, *J. Phys. D. Appl. Phys.* 48 (2015) 495304.
- [34] Y.-C. Lin, C.-C. Lu, C.-H. Yeh, C. Jin, K. Suenaga, P.-W. Chiu, (2011).
- [35] V. Guerra, E. Tatarova, F.M. Dias, C.M. Ferreira, *J. Appl. Phys.* 91 (2002) 2648–2661.
- [36] V. Guerra, P.A. Sá, J. Loureiro, *J. Phys. Conf. Ser.* 63 (2007).
- [37] F.F. Chen, *Plasma Sources Sci. Technol.* 18 (2009).
- [38] S. Bockel, A.M. Diamy, A. Ricard, *Surf. Coatings Technol.* 74–75 (1995) 474–478.
- [39] A. Ricard, S. Oh, V. Guerra, *Plasma Sources Sci. Technol.* 22 (2013) 035009.
- [40] A. Achour, S. Vizireanu, G. Dinescu, L. Le Brizoual, M.A. Djouadi, M. Boujtita, *Appl. Surf. Sci.* 273 (2013) 49–57.
- [41] H. Estrade-Szwarcopf, *Carbon N. Y.* 42 (2004) 1713–1721.
- [42] M.. b Koinuma, H.. b Tateishi, K.. b Hatakeyama, S.. b Miyamoto, C.. b Ogata, A.. b Funatsu, T.. b Taniguchi, Y.. b Matsumoto, *Chem. Lett.* 42 (2013) 924–926.
- [43] A. Siokou, F. Ravani, S. Karakalos, O. Frank, M. Kalbac, C. Galiotis, *Appl. Surf. Sci.* 257 (2011) 9785–9790.
- [44] D. Yang, A. Velamakanni, G. Bozoklu, S. Park, M. Stoller, R.D. Piner, S. Stankovich, I. Jung, D.A. Field, C.A. Ventrice, R.S. Ruoff, *Carbon N. Y.* 47 (2009) 145–152.
- [45] N. Hellgren, R.T. Haasch, S. Schmidt, L. Hultman, I. Petrov, *Carbon N. Y.* 108 (2016) 242–252.
- [46] S.C. Hernández, F.J. Bezares, J.T. Robinson, J.D. Caldwell, S.G. Walton, *Carbon N. Y.* 60 (2013) 84–93.
- [47] I. Bertóti, M. Mohai, K. László, *Carbon N. Y.* 84 (2015) 185–196.
- [48] S. Kaciulis, *Surf. Interface Anal.* 44 (2012) 1155–1161.
- [49] V. Datsyuk, M. Kalyva, K. Papagelis, J. Parthenios, D. Tasis, A. Siokou, I. Kallitsis, C. Galiotis, *Carbon N. Y.* 46 (2008) 833–840.
- [50] W. Ding, Z. Wei, S. Chen, X. Qi, T. Yang, J. Hu, D. Wang, L.J. Wan, S.F. Alvi, L. Li, *Angew. Chemie - Int. Ed.* 52 (2013) 11755–11759.
- [51] M. Scardamaglia, B. Aleman, M. Amati, C. Ewels, P. Pochet, N. Reckinger, J.F. Colomer, T. Skaltsas, N. Tagmatarchis, R. Snyders, L. Gregoratti, C. Bittencourt, *Carbon N. Y.* 73 (2014) 371–381.
- [52] C. Batich, D. Donald, *J. Am. Chem. Soc.* 106 (1984) 2758–2761.
- [53] J.R. Pels, F. Kapteijn, J.A. Moulijn, Q. Zhu, K.M. Thomas, *Carbon N. Y.* 33 (1995) 1641–1653.
- [54] X. Wang, X. Li, L. Zhang, Y. Yoon, P.K. Weber, H. Wang, J. Guo, H. Dai, *Science* (80-.). 324 (2009) 768–771.

- [55] T. Schiros, D. Nordlund, L. Pálová, D. Prezzi, L. Zhao, K.S. Kim, U. Wurstbauer, C. Gutiérrez, D. Delongchamp, C. Jaye, D. Fischer, H. Ogasawara, L.G.M. Pettersson, D.R. Reichman, P. Kim, M.S. Hybertsen, A.N. Pasupathy, *Nano Lett.* 12 (2012) 4025–4031.
- [56] M. Scardamaglia, C. Struzzi, S. Osella, N. Reckinger, J.-F. Colomer, L. Petaccia, R. Snyders, D. Beljonne, C. Bittencourt, *2D Mater.* 3 (2016).
- [57] M. Scardamaglia, T. Susi, C. Struzzi, R. Snyders, G. Di Santo, L. Petaccia, C. Bittencourt, *Sci. Rep.* 7 (2017) 7960.
- [58] J. Kotakoski, C.H. Jin, O. Lehtinen, K. Suenaga, A. V. Krasheninnikov, *Phys. Rev. B - Condens. Matter Mater. Phys.* 82 (2010) 1–4.
- [59] E.H. Åhlgren, J. Kotakoski, A. V. Krasheninnikov, *Phys. Rev. B* 83 (2011) 115424.
- [60] O. Malenfant-Thuot, G. Robert Bigras, L. Stafford, M. Cote, *Bull. Am. Phys. Soc.* (2018) F35.00005.
- [61] C.P. Ewels, D. Erbajar, P. Wagner, X. Rocquefelte, R. Arenal, P. Pochet, M. Rayson, M. Scardamaglia, C. Bittencourt, P. Briddon, *Faraday Discuss.* 173 (2014) 215–232.
- [62] F. Banhart, J. Kotakoski, A. V. Krasheninnikov, *ACS Nano* 5 (2011) 26–41.
- [63] R. Narayanan, H. Yamada, M. Karakaya, R. Podila, A.M. Rao, P.R. Bandaru, *Nano Lett.* 15 (2015) 3067–3072.
- [64] A. Das, S. Pisana, B. Chakraborty, S. Piscanec, S.K. Saha, U. V Waghmare, K.S. Novoselov, H.R. Krishnamurthy, a K. Geim, A.C. Ferrari, A.K. Sood, *Nat. Nanotechnol.* 3 (2008) 210–215.
- [65] M. Bruna, A.K. Ott, M. Ijas, D. Yoon, U. Sassi, A.C. Ferrari, *ACS Nano* 8 (2014) 7432–7441.
- [66] Y.-B.B. Zhou, Z.-M.M. Liao, Y.-F.F. Wang, G.S. Duesberg, J. Xu, Q. Fu, X.-S.S. Wu, D.-P.P. Yu, *J. Chem. Phys.* 133 (2010) 234703.
- [67] O. Lehtinen, J. Kotakoski, A. V. Krasheninnikov, A. Tolvanen, K. Nordlund, J. Keinonen, *Phys. Rev. B - Condens. Matter Mater. Phys.* 81 (2010) 1–4.
- [68] L.G. Cançado, A. Jorio, E.H.M. Ferreira, F. Stavale, C. a. Achete, R.B. Capaz, M.V.O. Moutinho, A. Lombardo, T.S. Kulmala, a. C. Ferrari, *Nano Lett.* 11 (2011) 3190–3196.
- [69] M.M. Lucchese, F. Stavale, E.H.M. Ferreira, C. Vilani, M.V.O. Moutinho, R.B. Capaz, C. a. Achete, A. Jorio, *Carbon N. Y.* 48 (2010) 1592–1597.
- [70] J.E. Lee, G. Ahn, J. Shim, Y.S. Lee, S. Ryu, *Nat. Commun.* 3 (2012) 1024.
- [71] K. Jia, Y. Su, Y. Chen, J. Luo, J. Yang, P. Lv, Z. Zhang, H. Zhu, C. Zhao, T. Ye, *Vacuum* 116 (2015) 90–95.
- [72] J. Zabel, R.R. Nair, A. Ott, T. Georgiou, A.K. Geim, K.S. Novoselov, C. Casiraghi, *Nano Lett.* 12 (2012) 617–621.
- [73] F. Tuinstra, L. Koenig, *J. Chem. Phys.* 53 (1970) 1126–1130.
- [74] L.M. Malard, M. a. Pimenta, G. Dresselhaus, M.S. Dresselhaus, *Phys. Rep.* 473 (2009) 51–87.
- [75] L.G. Cançado, K. Takai, T. Enoki, M. Endo, Y.A. Kim, H. Mizusaki, A. Jorio, L.N. Coelho, R. Magalhães-Paniago, M.A. Pimenta, *Appl. Phys. Lett.* 88 (2006).
- [76] G. Giovannetti, P.A. Khomyakov, G. Brocks, V.M. Karpan, J. Van Den Brink, P.J. Kelly, *Phys. Rev. Lett.* 101 (2008) 4–7.
- [77] O. Frank, J. Vejpravova, V. Holy, L. Kavan, M. Kalbac, *Carbon N. Y.* 68 (2014) 440–451.
- [78] J. Cermak, T. Yamada, K. Ganzerova, B. Rezek, *Adv. Mater. Interfaces* 3 (2016) 1–7.
- [79] G. Robert Bigras, X. Glad, C. Charpin, D. Cardinal, P. Levesque, R. Martel, L. Stafford, *Carbon N. Y.* (2018).

- [80] A.C. Ferrari, J.C. Meyer, V. Scardaci, C. Casiraghi, M. Lazzeri, F. Mauri, S. Piscanec, D. Jiang, K.S. Novoselov, S. Roth, A.K. Geim, Phys. Rev. Lett. 97 (2006) 1–4.
- [81] A. Sadezky, H. Muckenhuber, H. Grothe, R. Niessner, U. P??schl, Carbon N. Y. 43 (2005) 1731–1742.
- [82] M. Pawlyta, J.N. Rouzaud, S. Duber, Carbon N. Y. 84 (2015) 479–490.
- [83] R. Beams, L.G. Cançado, L. Novotny, J. Phys. Condens. Matter 27 (2015) 083002.
- [84] L.G. Cançado, M. Gomes de Silva, E.H.M. Ferreira, F. Hof, 2D Mater. 4 (2017) 025039.
- [85] Z. Li, Y. Wang, A. Kozbial, G. Shenoy, F. Zhou, R. McGinley, P. Ireland, B. Morganstein, A. Kunkel, S.P. Surwade, L. Li, H. Liu, Nat. Mater. 12 (2013) 925–931.
- [86] J. Hong, M.K. Park, E.J. Lee, D. Lee, D.S. Hwang, S. Ryu, Sci. Rep. 3 (2013) 2700.

8. Supplementary data

Additional data on Raman baselines, XPS surveys, spectra and XPS high-resolution Cu2p spectra are presented in **Annexe 1** of this thesis.

2.3 Étude des phénomènes de contamination

Low-damage nitrogen incorporation in graphene films

by nitrogen plasma treatment: effect of airborne contaminants

Germain Robert Bigras¹, Xavier Glad¹, Leron Vandsburger¹, Carl Charpin²,

Pierre Levesque², Richard Martel², Luc Stafford¹

¹ Département de Physique, Université de Montréal, Montréal, Québec, CANADA

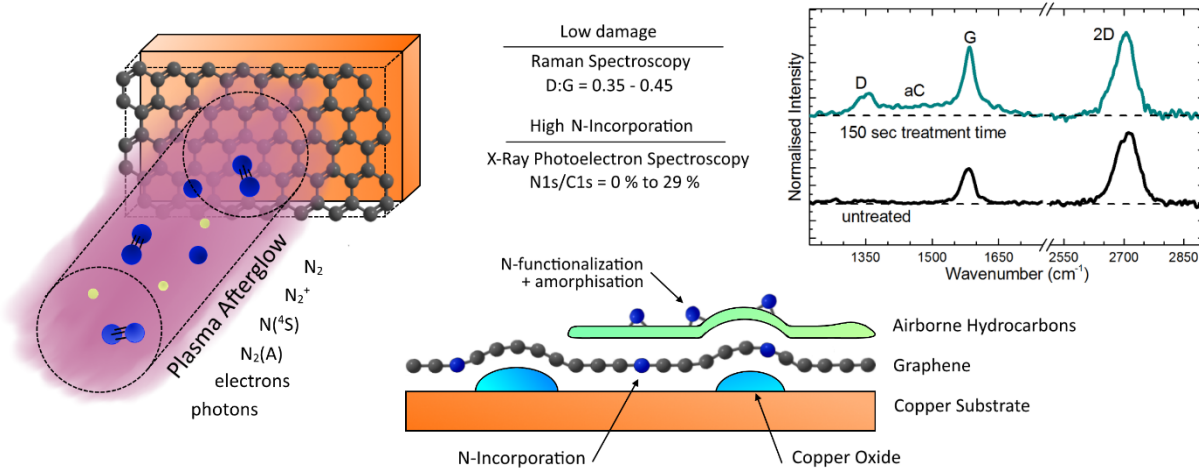
² Département de Chimie, Université de Montréal, Montréal, Québec, CANADA

ABSTRACT

Graphene films grown on copper by chemical vapor deposition were exposed to the late afterglow of a reduced-pressure N₂ plasma sustained by microwave electromagnetic fields. X-ray photoelectron and Raman spectroscopies reveal extremely high incorporation of plasma-generated N atoms into the graphene film (N/C = 29%) while maintaining an unprecedentedly low-damage generation (D:G = 0.35-0.45) compared to the literature (0.5 to 2.5). The incorporation dynamics between graphene on copper and graphene on copper oxide are also compared and discussed. After transfer on SiO₂/Si substrate, the N/C content decrease to only 6%. This reveals that a large part of the N atoms are weakly bonded to the graphene surface. Most of the nitrogen incorporation seems linked to the functionalization of weakly bonded hydrocarbons initially adsorbed from air exposure or carbon-nitrogen structures arising from plasma-surface interactions.

Keywords – graphene, N-incorporation, downstream plasma treatment, X-Ray photoelectron spectroscopy, Raman spectroscopy

Graphical Abstract



1. Introduction

Graphene has been extensively studied due to its promising potential for the next generation of electronic and optoelectronic devices [1,2]. These applications require graphene to operate as a semiconductor [3]. Therefore, the availability of versatile post-growth processing techniques is primordial to implement graphene in technologies where strong doping, band gap engineering or magnetic response is necessary, especially in the domain of large-area films grown by chemical vapor deposition (CVD). In recent years, various methods have been explored to tune the doping with nitrogen atoms of graphene films as a means of either increasing the electron density or inducing a band gap by direct incorporation of heteroatoms [4]. On one hand, an optimized nitrogen doping would maximize the n-type doping characteristics while retaining a minimal defect density in the graphene films. X-Ray photoelectron spectroscopy (XPS) is commonly used to probe the N/C ratio. Overall the incorporation reported in the literature ranges from 1% to 16% [3–7]. Confirmation on the aromatic nature of the incorporated N atoms is not always assessed and experimentally very difficult to determine. Yet, a significant proportion of the incorporation may not actively participate in n-type doping. On the other hand, Raman spectroscopy (RS) has proven to be a powerful tool to assess the lattice defect density using the intensity ratio of the D over the G band. D:G ratios reported in the literature usually vary from 0.5 to 2.5 [8–10]. Studies often aim blindly at increasing the nitrogen content while minimizing defect generation even

though further confirmation should be obtained on the effective doping of the graphene lattice itself.

This article exploits an innovative post-growth treatment method of graphene films in the late-afterglow of microwave N₂ plasmas at reduced pressure in order to shed light on crucial contamination-related considerations regarding the N-incorporation. This rather unique plasma-based environment offers a very-low ion number density while providing a high concentration of reactive neutral atoms N(⁴S) and metastable N₂(A) species [11]. The coexistence of these two species is a radical departure from what is currently the state of the art in surface functionalization of materials and nanomaterials, mainly because the energy reservoir of metastable N₂(A) species (6 eV) can provide activation energy for surfaces processes that would not occur spontaneously, while leaving the translational or kinetic energy of both the impinging species and the materials undisturbed. Another interest of this N₂ flowing afterglow technique comes from the possibility to easily adjust the populations of active species by varying the gas flow rate [11]. Inspired by previous studies reporting significant improvement of the emission properties from InGaN/GaN dot-in-a-wire nanostructures with minimal ion irradiation damage [11,12], this late afterglow of microwave N₂ plasmas appears as a highly promising candidate for efficient and low-damage nitrogen incorporation in graphene films. This singular plasma environment is more likely to enhance chemically driven surface reactions over purely physical ion bombardment. Even for freshly grown graphene, Li et al. [13] showed that the graphene receive a strong variation of its hydrophobicity within days due to the deposition of hydrocarbons on the surface. The plasma environment in use here has the potential to enhance functionalization at the surface (i.e. reaction between nitrogen and the hydrocarbons) without strong damage generation. In this work, a combination of XPS and RS measurements is used to investigate the N-atom incorporation dynamics and plasma-induced damage on Cu-grown graphene films (with a clear distinction between graphene on copper and graphene on copper oxide) and after transfer to SiO₂/Si substrates.

2. Experimental details

The experimental setup is shown in **Fig. 1** and thoroughly detailed in a previous paper [11]. A gap-type wave launcher (namely surfatron [14]) maintains a 2.45 GHz surface wave on a 8-mm diameter (6-mm inner diameter) fused silica tube. The injected power is set to 30 W. For a working pressure of 6 Torr, this results in a microwave N₂ plasma with a length of about 2-3 cm. Besides the main plasma zone, two other bright regions appear in the flowing afterglow of nominally pure N₂ plasmas: the early afterglow and the late afterglow [15]. The afterglow expands first into the bent fused silica tube and then into the stainless-steel processing chamber. Depending on the N₂ gas flow rate, the graphene film placed at a fixed distance from the wave launcher may be exposed to the early (high gas flow rate) or the late afterglow (low gas flow rate) [11,12]. The densities of plasma-generated N atoms, N₂(A) metastable species and positive ions in the downstream region were determined in a previous paper by optical emission spectroscopy and Langmuir probe measurements [11]. To ensure a minimal presence of impurities, the experiment was conducted with a base pressure of 1.7x10⁻⁷ Torr, an ultra-high-purity N₂ gas (99.999%) and a gas purifier (SAES Pure Gas Inc Nitrogen MC1-920F). Further discussion on oxygen contamination sources is presented in Supplementary data (S1).

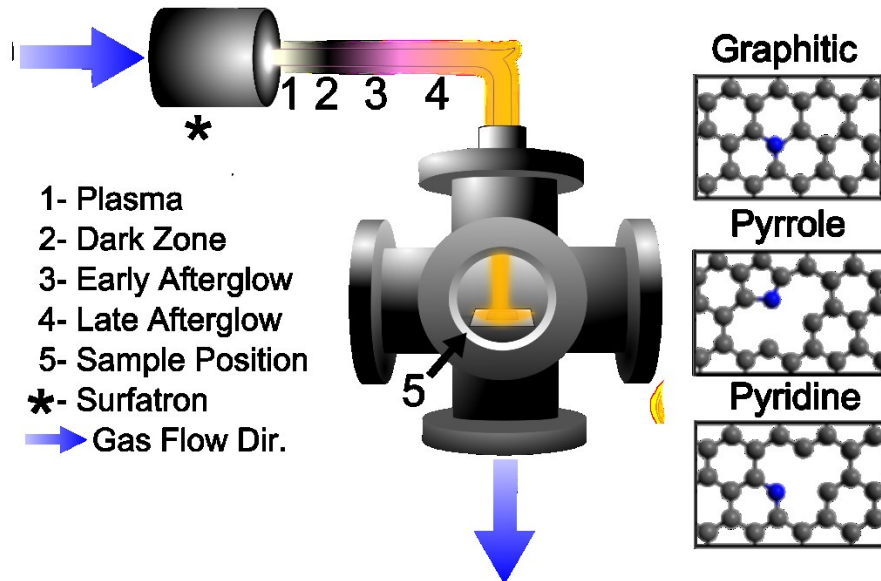


Fig. 1 - Treatment of graphene films in the late afterglow of microwave N₂ plasma. Schematic of the plasma system, where 1-4 is the location of the different zones of the discharge and 5 is the position of the graphene sample in the downstream flow. The right panel also shows various N-incorporation sites: graphitic, pyrrole and pyridine.

For all experiments reported in this work, the system was operated at 6 Torr with a N₂ gas flow rate of 100 sccm (standard cubic centimeters per minute) so that the sample is immersed in the late afterglow. In such conditions, the populations of atomic nitrogen N(⁴S) and metastable N₂(A) species are respectively 10¹⁴ cm⁻³ and 10¹⁰ cm⁻³. Positive ion densities in this region are less than 10⁷ cm⁻³; this is much lower than the values observed in the main plasma region (>10¹¹ cm⁻³) and in the early afterglow (~10⁹ cm⁻³). As shown by Kang *et al.* [16], the heavy species temperature is close to 300K in the late afterglow of N₂ plasmas at reduced pressure, which further eliminates flux-induced heating of the sample by neutrals impinging onto the substrate surface. This aspect was confirmed in a previous publication [12].

The graphene sample was synthesized by CVD process on a 25 μm copper foil (Alfa Aesar item No. 13382). Growth conditions are detailed elsewhere [17]. Briefly, the foil is treated with acetic acid then annealed at 1000°C for 30 min under 50 mTorr of H₂ before introducing CH₄ until a pressure of 500 mTorr is reached. After a growth phase of 10 min, the sample is cooled in H₂. The 5×10 mm² graphene sample then received five subsequent late-afterglow treatments of 30

seconds each (up to a total of 150 seconds) between which XPS and RS were carried out. Graphene samples have been stored in atmospheric conditions for a month before treatment. As such, the defective grain boundaries (GBs) of the CVD-grown graphene allowed the permeation of O₂ leading the formation of numerous oxidized Cu islands [18] which have been confirmed by RS [19–21] (**Fig. S2**) and XPS [22,23] (**Fig. S3**). This procedure was chosen to ensure reproducibility since the whole duration of our experiment campaign is about two weeks. Indeed, both substrate oxidation [18] and graphene hydrophobicity [13] receive strong changes within the first month. Static contact angle of graphene on copper was calculated using 5 µL droplets of water. The obtained value of 93 ± 7 ° (**Fig. S4**) reveals the expected transition towards hydrophobicity of graphene related to the deposition of hydrocarbon airborne contaminants [13]. Note that that exposure to atmospheric conditions may also have other effects on graphene and N-doped graphene, such as surface energy [24].

XPS was performed on an ESCALAB 3 MKII device using the 300 W Al K α source (300 W Mg K α for samples on SiO₂/Si). Since the N1s band fall in the region of the Cu LVV Auger bands for magnesium sources (317 eV to 486 eV), an aluminum source was used for graphene on copper. In the case of graphene on SiO₂, magnesium is chosen for its increased absolute intensity and its slightly smaller line width on the setup used. The beam size was set at 2x3 mm². The survey and high-resolution spectra were taken with respectively 100 eV and 20 eV pass energy and a step of 1 eV and 0.05 eV. The resolution of the high resolution spectra is around 0.8 eV. Full width at half maximum (FWHM) and shape of the peaks were carefully considered following a calibration experiment on the XPS setup. With the exception of the C1s main peak sp² C-C (284.6 eV) and the associated pi-pi* shake-up (291.3 eV), FWHM were set to 1.6 eV for C1s, 1.8 eV for O1s and 1.7 eV for N1s. The sp² C-C peak is fitted using a smaller FWHM since it is highly ordered while a larger FWHM is permitted for the shake-up due to its satellite nature. To account for the metallic properties of the graphene lattice, an asymmetric Doniach-Sunjic [25] peak (asymmetry factor alpha = 0.06 [26]) convoluted with a Lorentzian-Gaussian product (1:1) is used for the sp² C-C band. All other bands are fitted with a Lorentzian-Gaussian product (1:1).

RS of CVD-grown graphene on Cu foil is usually performed after transfer on SiO₂/Si since copper presents a broad background photoluminescence associated to its surface plasmon emission

[27,28]. However, the transfer to SiO₂/Si is commonly performed using Poly(methyl methacrylate) (PMMA) and leaves PMMA residue, adsorbed O₂ and trapped H₂O [29] that may desorb during plasma treatment and lead to unwanted chemical etching[30]. Moreover, the removal of these residues requires thermal treatment under vacuum that induces irremediable defects to the graphene film [31]. Since the present study focuses on plasma-induced defects and knowing that the D:G band ratio (related to the disorder or defects) does not depend on the substrate [32], the transfer has been avoided before the final plasma treatment in favor of the use of a 488-nm laser wavelength (2.54 eV) promoting easy baseline subtraction (especially between 1100 and 1700 cm⁻¹) and good signal-to-noise ratio. The measurements were done using a ×50 objective (numerical aperture 0.60) leading to a spot size of about 1.5 μm (or about 2.7×10⁸ carbon atoms). The spot size has been verified by scanning electron microscopy (SEM) after irradiating amorphous carbon (**Fig. S5**). In order to avoid heating of the substrate, the power was set to 0.7 mW and the acquisition time to 30 s. Repetitive measurements confirmed that the sample was not damaged by the laser exposure.

Graphene growth differs greatly with the crystal orientation of the copper substrate [18,20,32–34]. This leads to a higher number density of GBs for graphene grown on Cu (100) than on Cu (111) [33]. Therefore, the copper oxidation (seeded at GBs) reveals the polycrystalline nature of the substrate. To balance the inhomogeneity of the samples, RS was carried out at the same exact position (with a spatial resolution of 0.2 μm) on seven locations of the sample to cover multiple (3) copper crystal orientations (detailed in **Fig. S6**). Since, the spatial resolution of the XPS is millimetric, both graphene on copper and defective graphene (GBs, on oxidized copper, etc.) are probed. Thus, for each 30-second treatment, both graphene on copper (4 spectra) and on copper oxide (3 spectra) were examined in RS as a way to establish links between the two characterization methods.

Further insight on the n- or p-doping of graphene films can be obtained at the end of the plasma experiment by transferring graphene films on SiO₂/Si [35,36]. Such study is not within the scope of this article. Nonetheless, transfer to SiO₂/Si substrate has been performed to assist our interpretation regarding the N-incorporation. Details on the transfer method can be found elsewhere [37]. Briefly, the graphene film is coated with 100 nm of PPMA and copper is etched

with ammonium persulfate. The graphene and PMMA are applied on the Si/SiO₂ substrate before dissolving PMMA with acetone. Finally, the sample is rinsed out three times with isopropanol. After transfer, Raman mappings (200 points) have been carried out at a wavelength of 514 nm (0.5 mW) with a ×50 objective.

3. Experimental results and discussion

3.1 Plasma treatment of graphene films on copper

Fig. 2 shows the XPS survey and high-resolution scans performed on graphene films as a function of the total (late afterglow) plasma treatment time. Carbon C1s band arises around 284.6 eV with a tail up to 290 eV, nitrogen N1s band is found at 400 ± 2 eV and oxygen O1s presents an asymmetric peak around 532 ± 3 eV. Inspired by various studies reported in literature, C1s spectra are fitted with seven sub-peaks. The main feature C1 (sp₂ C-C) contribution for graphene is found at 284.6 eV [26,38–42] and its satellite C1* (π - π^* shake-up) at 291.3 eV [38–40]. Carbon-nitrogen moieties are identified by the two sub peaks C2 (sp₂ C=N) and C4 (sp₃ C-N) respectively at 285.45 ± 0.1 eV [26,43,44] and 287.4 ± 0.1 eV [44–46]. Oxygen contributions are linked to multiple bands: C3 (C-OH) at 286.3 ± 0.1 eV [40–42,46], C5 (C=O and/or O=C-O) at 288.4 ± 0.2 eV [38,41,44,45,47] and C6 (O=C-OH) at 289.0 ± 0.2 eV [46]. Nitrogen is present in both aromatic and edge configurations. Three nitrogen moieties are found: N1 (pyridine) at 398.5 ± 0.1 eV [26,43,48,49] , N2 (amine, nitroso and or pyrrole) at 399.7 ± 0.1 eV [26,49–52] and N3 (graphitic) at 401.1 ± 0.1 eV [26,43,48,49,52]. The associated peaks for oxygen-carbon and oxygen-nitrogen bindings have been studied in O1s to avoid any inconsistencies in the interpretation. The O1s bands were fitted following: O1 (O*=C-OH and Cu₂O) at 530.5 ± 0.2 eV [38,42,47,53], O2 (C-OH,C-O-C and/or C=O) at 532.0 ± 0.2 eV [45,47] and O3 (O=C=O* and nitroso) at 533.2 ± 0.2 eV [45,50]. Element ratio presented in this work were corrected using Wagner sensitivity factors (C1s:0.250, N1s:0.420, O1s:0.660, Cu2p:6.300)

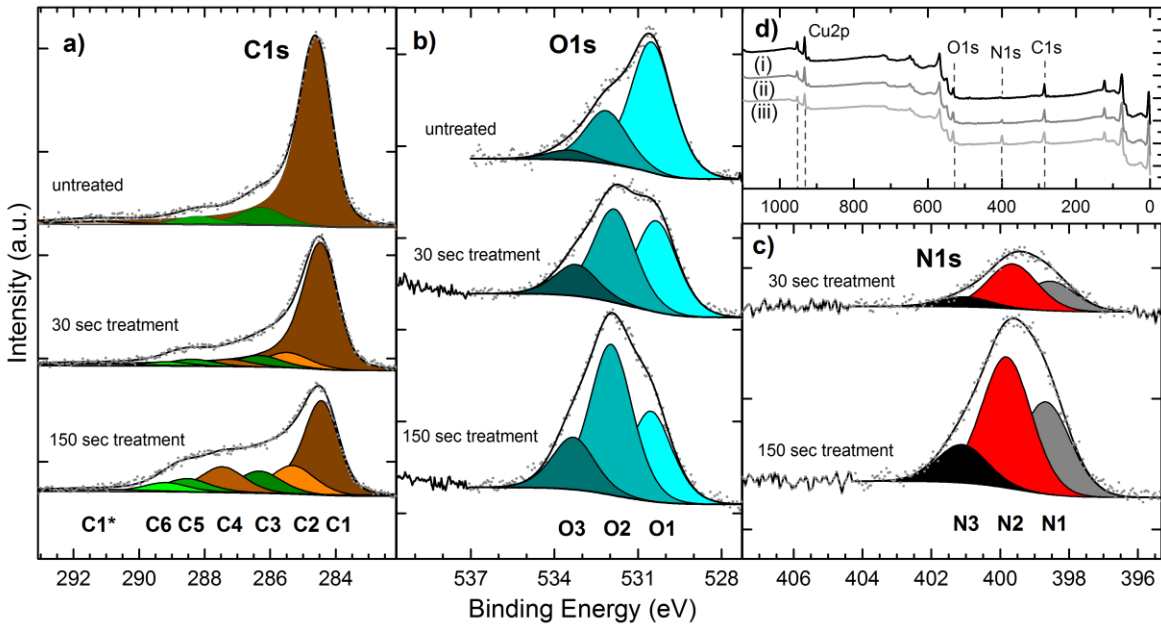


Fig. 2 – XPS survey and high-resolution scans (C1s, O1s and N1s) for the graphene films treated by the late afterglow for 0 (untreated), 30 and 150 s (total treatment time). No N1s contribution is found at 0 s.

The atomic percent obtained from the survey spectra are reported in **Fig. 3a** (various atomic ratios are also presented in **Fig. S7**). A slight but unavoidable increase of the oxygen concentration is observed due to the subsequent manipulations of the sample in ambient conditions. As detailed in Supplementary data (S1), oxygen content is not believed to grow due to oxidation occurring during the plasma treatment (due to presence of impurities coming from residual vacuum and impurities in the feed gas) but rather because of the successive exposures of increasingly damaged graphene to uncontrolled, atmospheric-pressure conditions. However, it is worth highlighting from the data presented in **Fig. 2** that a large fraction of the O1s signal is linked to copper oxidation and therefore not directly related to the functionalization of the graphene films. As for the N1s signal, **Fig. 3a** shows a steady increase incorporation of nitrogen with treatment time. The relative atomic percent of each nitrogen incorporation are reported in **Fig. 3b** as a function of the total treatment time. Overall, the N-incorporation monotonically increases, reaching a N/C ratio of 29.4% ($N1s/(C1s+N1s+O1s) = 18.18\%$) for a 150-s plasma treatment. The

graphitic incorporation (N3) increases towards a saturation beyond 90-s plasma treatment (N/C = 4.3%).

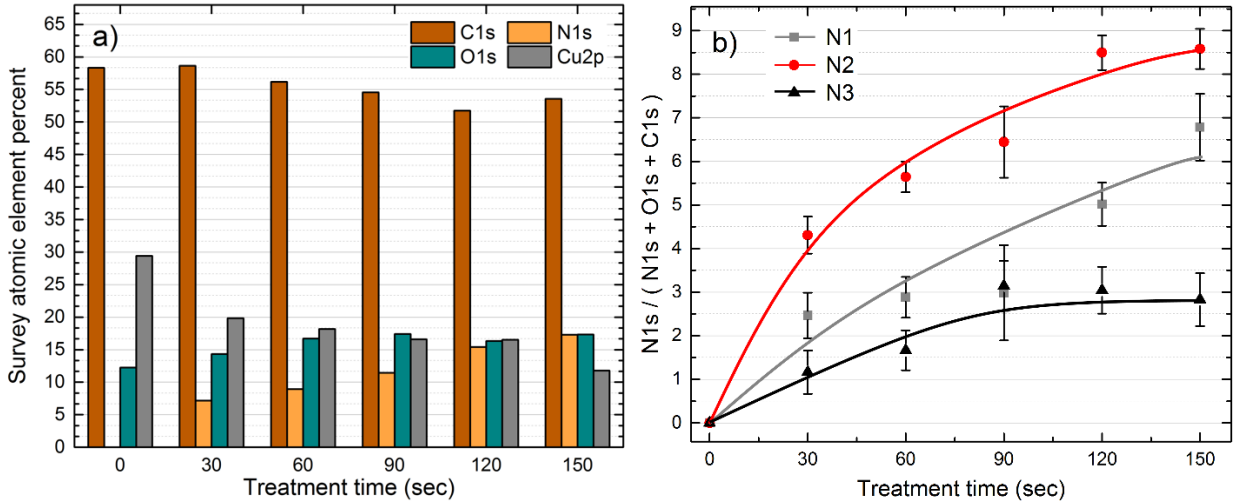


Fig. 3 – a) Survey atomic element percent (sensitivity corrected) of graphene films as a function of treatment time to the late afterglow. N1s:C1s ratio reaches an incorporation ratio of 33% after 150 s. b) Relative atomic percentage (C1s+O1s+N1s) of N1, N2 and N3 as a function of the total treatment time. Lines are guides to the eye only.

RS is a powerful tool to investigate carbon materials and nanomaterials [54,55], especially graphene [56]. Raman spectra of defect-free single-layer graphene possess several distinctive features, mainly the peaks G ($\sim 1580 \text{ cm}^{-1}$) and 2D ($\sim 2700 \text{ cm}^{-1}$ at a laser wavelength of 488 nm, also called G'). The former is a first-order scattering process assigned to the doubly-degenerated, in-plane vibrational mode while the latter is a two-phonon Raman (second order) process involving zone-boundary phonons. Such phonons also lead to the D peak ($\sim 1350 \text{ cm}^{-1}$) in disordered graphene and, thus, the defect density throughout the graphene lattice may be assessed by the value of the ratio of D over G peak intensities [57–59]. The latter is indeed directly linked with the crystallite size [57,60]. However, the D band intensity is related to the defect concentration (edge, vacancies, grain boundaries, in-plane substitution heteroatoms) [61] but also to the laser wavelength [62] and the graphene Fermi level [35]. It results that the estimation of the crystallite size can be tricky, especially on Cu-grown graphene since its Fermi level is shifted by the interactions with the underlying substrate [18,20,63], notably copper and copper oxide

[20,64,65]. Thus, this RS study of graphene films on polycrystalline Cu foils mainly focuses on the value of the D over G band intensity ratio to assess the damage undergone by the graphene lattice after late afterglow treatment.

Fig. 4 presents the evolution of the averaged Raman spectra of graphene on copper on 4 locations (GrCu) and graphene on oxidized copper on 3 locations (GrO_x) for subsequent 30-s (late afterglow) plasma treatments. Spectra have been centered on the G and 2D bands (separately) to avoid any increase of the FWHM due to the averaging process. This method has been chosen over standard averaging in order to show spectra with FWHM, intensity ratio and overall line shapes to be as close as possible to the original spectra while minimizing the noise. To determine line intensity, deconvolutions are performed on each individual spectrum and final line ratio errors are calculated to match a 95% confidence interval in the deconvolution. For each averaged spectrum, the normalization has been applied with respect to their maximum, i.e. the 2D band intensity. All raw spectra can be found in Supplementary data **Fig. S8**. It is worth noting that the modification induced by the treatment is different for GrCu and GrCuO_x. On CuO_x, the 2D and G bands both show an important blue-shift (+15 and +7 cm⁻¹, respectively) that may be explained by the relaxation of tensile strain [20,36]. Indeed, bumps caused by the growth of copper oxide under the graphene induce tensile strain in this region [20]. The plasma treatment most likely releases that strain when generating defects. Note that a tensile strain implies an increase of the covalent bond length and, thus, a decrease of the bond stability. Such regions are therefore expected to be more sensitive to the plasma irradiation. Regarding the G band position, it is also known to be affected by the size of the crystallites (blue-shift when the latter decreases) and the doping (blue-shift for n- or p-doping) [66]. On GrCu, the position of G is rather constant up to 60 s before a blue-shift appears (+4 cm⁻¹). Moreover, at 90 s and after, an additional contribution is noticeable around 1500 cm⁻¹, between the D and G bands. The later may be attributed to amorphous carbon [31,67] and/or oxidized graphene [68],[69].

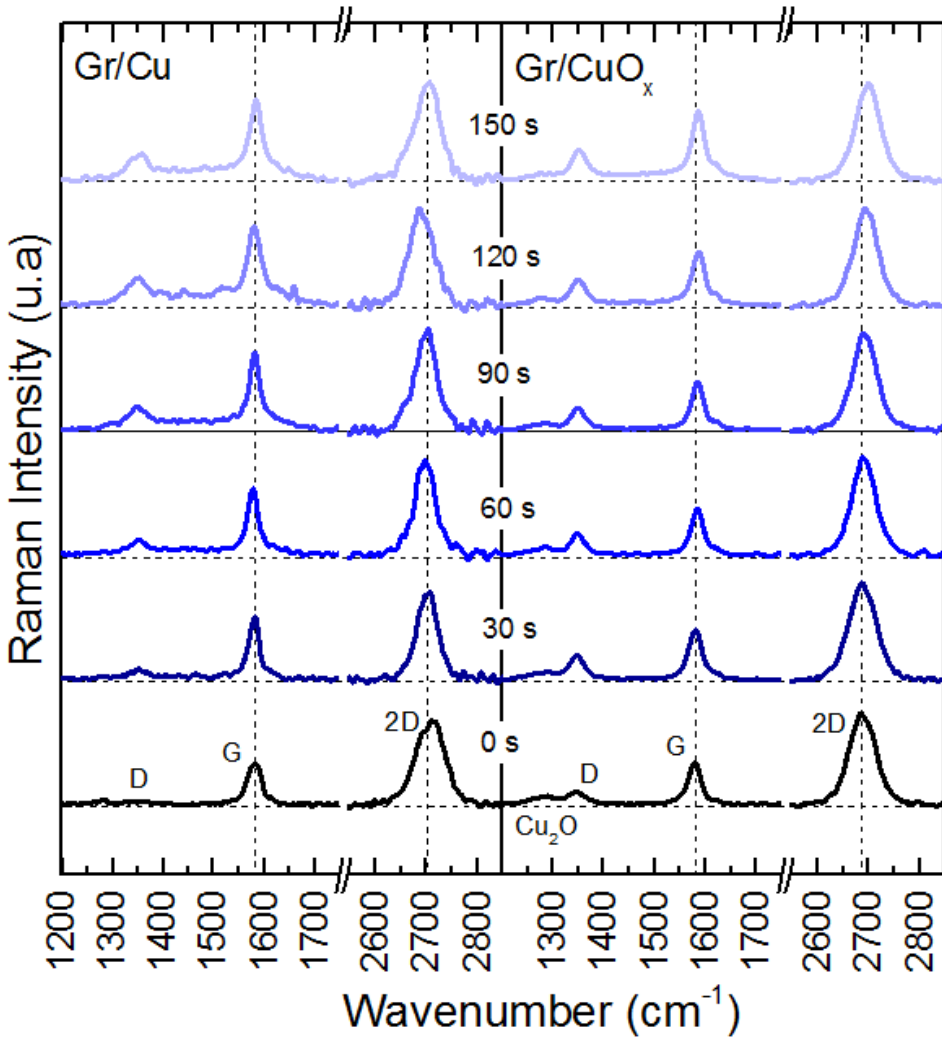


Fig. 4 – Raman spectra obtained as a function of treatment time for graphene on Cu and CuO_x. A 2.54-eV laser is used; followed by a baseline subtraction. Spectra are normalized according to their respective 2D band.

The D:G ratios for both GrCu and GrCuO_x are shown in Fig. 5. The defect density steadily increases for graphene on copper while graphene on oxide suffers a rapid increase of D:G ratio followed by a rather constant value. The former supports the steady N-atom incorporation measured by XPS. The difference in contact doping effect [20] and the additional strain-induced doping [20] (corroborated by the large 2D band shift) for graphene on CuO_x is what most probably leads to the different behavior observed. Note that n- or p-doping is known to induce a decrease in the Raman D band intensity [35].

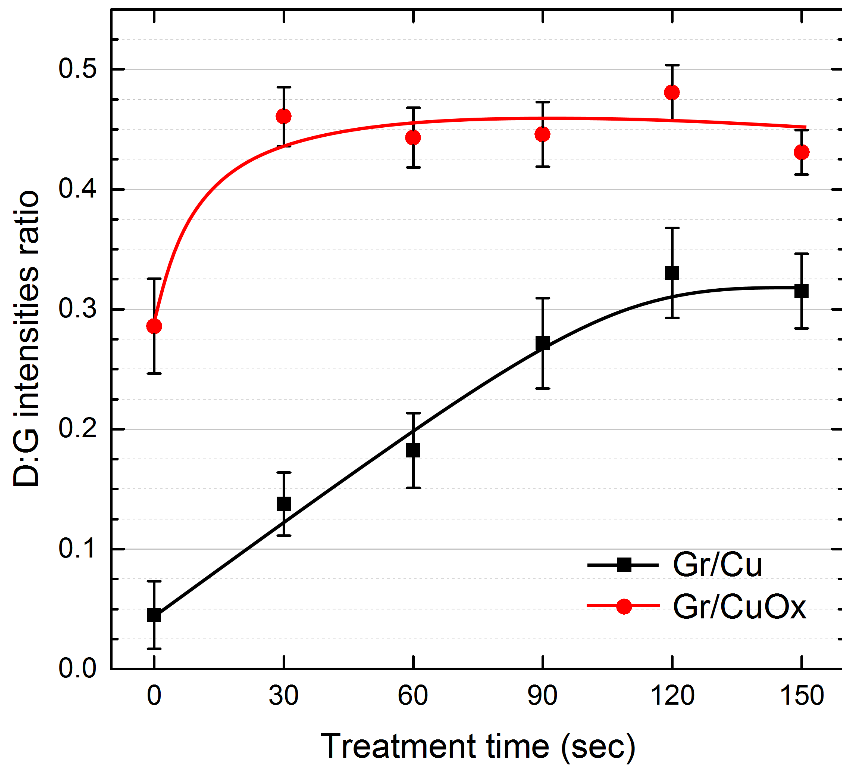


Fig. 5 - Ratios of Raman D over G peaks as a function of treatment time for both graphene on copper and graphene on copper oxide. Lines are guides to the eye only.

3.2 Graphene transfer to SiO₂

Following transfer of graphene films onto Si/SiO₂ substrate, additional XPS survey and high-resolution spectra have been performed. The results are presented in **Fig. 6**. An important decrease of the N/C content (from 29.4 % to 6 %) is observed; this corroborates the assumption that an important part of the N1s feature was associated with out-of-plane contributions. Indeed, the transfer process and the cleaning step required to remove the protecting polymer is likely to remove a large part of the functionalized hydrocarbons. No particular trend is observed in the decrease of nitrogen moieties. This would either imply that the N-incorporation is only localized within the hydrocarbon film or that the chemical environment of N atoms within the graphene lattice is comparable to the one within the airborne contaminant film. However, the C4/C1 (sp^3 C-N/ sp^2 C-C) contribution decreases from 20% to 3%. To establish if the decrease in N1s signal is caused by screening due to polymer residues, XPS characterization is performed on graphene on

copper before and after PMMA deposition and cleaning (without changing substrate) (see Supplementary data (S9)). No significant decrease in the sp^2 C-C is present and only a slight increase of O1s is observed.

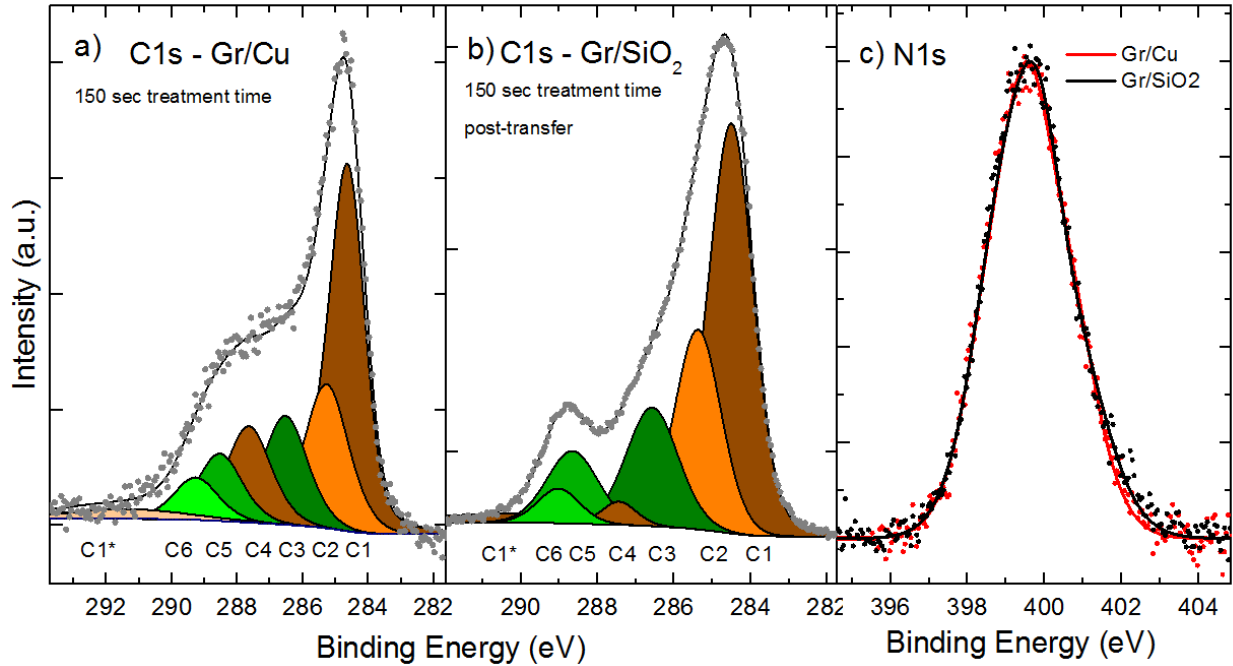


Fig. 6 – XPS high resolution spectra before and after transfer to Si/SiO₂ substrate. C1s spectrum before (a) show a much more dominant C4 band then high resolution C1s spectrum after transfer (b). The normalized high resolution N1s spectra (c) does not present any particular trend in term of the proportions of sub-bands.

Raman analysis has been performed on the Si/SiO₂-transferred graphene film at a laser wavelength of 514 nm. This wavelength has been selected because it provides a stronger Raman response than 488 nm. Being unable to trace back the exact points used for RS of graphene films on copper foils, 200 points of measurements have been recorded and averaged (surface mapping) for the transferred sample. The comparison of the D:G ratios before and after graphene transfer requires a laser energy dependent correction factor ($\lambda_{l,\text{SiO}_2}^4/\lambda_{l,Cu}^4$) to balance the different Raman responses of the activated graphene [44]. In this context, the D:G ratios obtained at 514 nm should be divided by $514^4/488^4 = 1.23$ to be compared with the ones recorded at 488 nm. Note that the D:G ratios should not change significantly with the transfer [32]. The Raman spectra

and the corrected D:G_{488nm} ratio is reported in **Fig. 7**. In untreated samples, D:G is 0.05 for Gr/Cu and Gr/SiO₂ and 0.28 for Gr/CuO_x. On the 150-s sample, this ratio decreases from 0.3 for Gr/Cu (0.45 for Gr/CuO_x) to 0.15 for Gr/SiO₂. This decrease of the D:G ratio after transfer is also accompanied by a decrease of the broad signal between the D and G bands linked to amorphous carbon [31,67] and/or oxidized graphene [68],[69]. This implies that the graphene has not been altered by the transfer and that a significant part of the D feature has another origin than the alteration of the graphene lattice itself. Therefore, the feature responsible for the D:G pre-transfer is related to interactions between surface contaminants and graphene that would explain both the amorphous content and the dispersion of phonons.

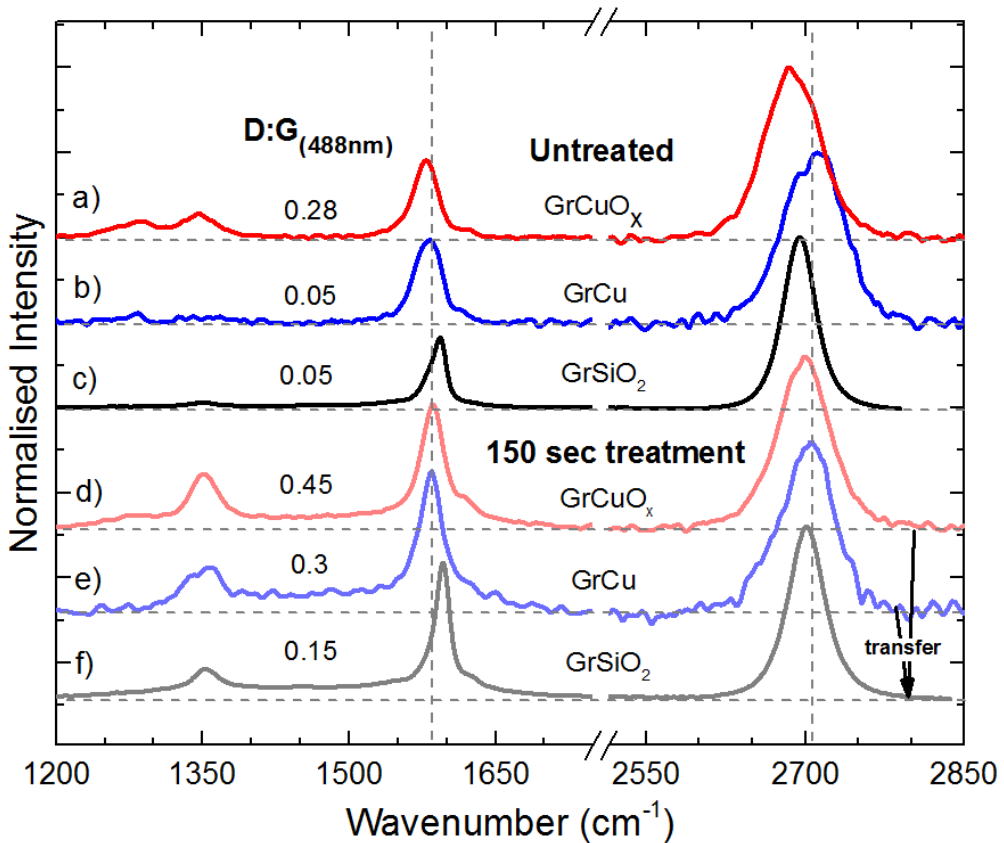


Fig. 7 - Raman spectra obtained for untreated (a-c) and 150 s plasma treated (d-f) graphene before (a,b,d,e) and after (c,f) transfer to SiO₂ substrate. A 2.54-eV (488 nm) laser is used samples on copper while a 2.41 (514 nm) laser is used for the transferred sample; followed by a baseline subtraction. Spectra are normalized according to their respective 2D band.

4. Discussion

XPS measurements show strong N incorporation with moieties having binding energies often identified in the literature as stable, aromatic inclusions. However, transfer towards SiO₂ substrate revealed that an important fraction (80%) of N atoms disappeared since most of these moieties are weakly-bonded, carbon-nitrogen groups. The exact nature of these adsorbates and the mechanism responsible for such unusually high N incorporation remains open. Nevertheless, the increase of the XPS C:Cu ratio (**Fig. S7**) reveal a surface deposition of carbon. A fraction of this contribution could be explained by a mild carbon etching (2-step etching mechanism[30,70] or adatom substitution [71] via Stone-Wales defects creation [10,72]) and subsequent surface diffusion and association reactions of carbon and oxygen species during the (late afterglow) plasma treatment. Such surface reactions are likely to be facilitated by the presence of N₂(A) metastable species and UV photons in the late afterglow region that represent a significant energy reservoir for plasma-surface interactions [12]. This mechanism would result in the creation of graphitic carbon nitride or similar triazine structures on the topmost surface of graphene films [45]. These structures have already been identified to allow high N-incorporation [45]. In such conditions, the authors have also reported weakly-damaged graphene, which is consistent with the very low D:G ratios obtained by RS after treatment in the late afterglow (0.35-0.45; see **Fig. 5**).

Since the C:Cu ratio obtained by XPS significantly increases between 0 and 150 s, some other mechanism also needs to be considered. Indeed, the creation of graphitic carbon nitride and triazine structures due to carbon etching, surface diffusion and association reactions cannot lead to a net gain of carbon atoms, and thus to an important increase of the C:Cu ratio. The increase of the ratio is rather explained by the screening of the copper as additional O and N species bond to the surface; artificially inducing a decrease in the copper content. Li et al. [13] have shown the strong impact of the unavoidable hydrocarbon deposition on graphene films kept under uncontrolled, atmospheric-pressure conditions. Over the range of experimental conditions examined in this work, this would allow easy N incorporation into the hydrocarbon film, yielding significant amount of carbon-nitrogen groups. In such situation, N-bearing species become trapped by the amorphous matter on the surface of the graphene film. Since the underlying

graphene remains mostly undamaged, this mechanism also leads to very low D:G ratios, as obtained by RS after plasma treatment (0.35-0.45; see **Fig. 5**).

Based on this framework, the majority of the nitrogen atoms observed by XPS after treatment in the late afterglow of microwave N₂ plasmas are weakly bonded and linked to the presence of carbon nitride, triazine, and nitrogenated hydrocarbon film on the surface of graphene films. The exact nature of the chemicals bonds of nitrogen moieties remain undetermined due to presence of N₂ peak both linked to weakly bonded nitrogen present on the hydrocarbon and aromatic inclusions in the underlying graphene lattice. On the other hand, XPS and RS analysis performed after transfer to the SiO₂ substrate indicates aromatic inclusion for a reasonable proportion of the remaining nitrogen atoms. This is supported by a number of findings: (i) the nearly complete loss of sp³ C-N (C4) observed in **Fig. 6**, (ii) the decrease of the D:G ratio observed in **Fig. 7** and (iii) the decrease of the broad signal between the D and G bands linked to amorphous carbon[31,67] and/or oxidized graphene[68],[69] displayed in **Fig. 7**. The decrease of nitrogen content following the transfer cannot solely be described by signal screening due to hydrocarbon film deposition after the transfer. Indeed, the contaminant film deposition occur rapidly in ambient conditions (in less than an hour [13]) and is thus present in every characterizations performed during this work. Overall, the sample is thus believed to be high-quality nitrogen-doped graphene underneath a thin nitrogenated and oxygenated hydrocarbon film.

5. Conclusion

CVD-grown graphene on copper foils were exposed to the late afterglow of a microwave N₂ plasma at reduced pressure. XPS measurements reveal both N-incorporation in aromatic and out-of plane configurations with an N/C ratio reaching 29.4%. N-incorporation on copper foils was found to be unstable after transfer to SiO₂/Si substrates and advocates in favor of a more cautious interpretation of the N1s feature. Indeed, bands that are commonly associated with aromatic incorporations (pyrrolic, pyridinic, and graphitic) without further sample characterization may not always be aromatic inclusions into the graphene lattice itself. Moreover, Raman spectroscopy reveals the change in the treatment dynamics for graphene on copper and graphene on copper oxide. Despite the very high percent of incorporated N, both regions reveal very low D:G ratios

(0.45 for GrCuOx, 0.35 for GrCu). Subsequent transfer to SiO₂/Si substrate shows a significant loss (80%) of nitrogen species; a feature linked to the liberation of weakly bonded N-species, including graphitic carbon nitride, triazine structures and/or oxygenated and nitrogenated hydrocarbon film on the topmost surface of the weakly-damaged graphene film.

6. Acknowledgments

This work was financially supported by the National Science and Engineering Research Council (NSERC), PRIMA-Québec, Plasmionique inc., Photon Etc., and the Fonds de Recherche du Québec – Nature et Technologies (FRQNT).

7. REFERENCES

- [1] D. Jariwala, V.K. Sangwan, L.J. Lauhon, T.J. Marks, M.C. Hersam, *Chem. Soc. Rev.* 42 (2013) 2824–60.
- [2] S.K. Vashist, J.H.T. Luong, *Carbon N. Y.* 84 (2015) 519–550.
- [3] A. Dey, A. Chroneos, N.S.J. Braithwaite, R.P. Gandhiraman, S. Krishnamurthy, *Appl. Phys. Rev.* 3 (2016) 021301.
- [4] M. Fan, Z. Feng, C. Zhu, X. Chen, C. Chen, J. Yang, D. Sun, *J. Mater. Sci.* 51 (2016) 10323–10349.
- [5] C.N.R. Rao, K. Gopalakrishnan, A. Govindaraj, *Nano Today* 9 (2014) 324–343.
- [6] H. Wang, T. Maiyalagan, X. Wang, *ACS Catal.* 2 (2012) 781–794.
- [7] X. Wang, G. Sun, P. Routh, D.-H. Kim, W. Huang, P. Chen, *Chem. Soc. Rev.* 43 (2014) 7067–7098.
- [8] B.-J. Lee, S.-C. Cho, G.-H. Jeong, *Curr. Appl. Phys.* 15 (2015) 563–568.
- [9] S.H. Park, J. Chae, M.-H. Cho, J.W.J.H. Kim, K.-H. Yoo, S.W. Cho, T.G. Kim, J.W.J.H. Kim, *J. Mater. Chem. C* 2 (2014) 933–939.
- [10] J.J. Zeng, Y.J. Lin, *Appl. Phys. Lett.* 104 (2014).
- [11] J. Afonso Ferreira, L. Stafford, R. Leonelli, A. Ricard, *J. Appl. Phys.* 115 (2014) 163303.
- [12] J.A. Ferreira, H.P.T. Nguyen, Z. Mi, R. Leonelli, L. Stafford, *Nanotechnology* 25 (2014) 435606.
- [13] Z. Li, Y. Wang, A. Kozbial, G. Shenoy, F. Zhou, R. McGinley, P. Ireland, B. Morganstein, A. Kunkel, S.P. Surwade, L. Li, H. Liu, *Nat. Mater.* 12 (2013) 925–931.
- [14] M. Moisan, Z. Zakrzewski, R. Pantel, *J. Phys. D. Appl. Phys.* 12 (1979) 219–237.
- [15] V. Guerra, E. Tatarova, F.M. Dias, C.M. Ferreira, *J. Appl. Phys.* 91 (2002) 2648–2661.
- [16] N. Kang, M. Lee, A. Ricard, S. Oh, *Curr. Appl. Phys.* 12 (2012) 1448–1453.
- [17] S. Choubak, M. Biron, P.L. Levesque, R. Martel, P. Desjardins, *J. Phys. Lett.* 4 (2013) 1100–1103.
- [18] O. Frank, J. Vejpravova, V. Holy, L. Kavan, M. Kalbac, *Carbon N. Y.* 68 (2014) 440–451.

- [19] S. Chen, L. Brown, M. Levendorf, W. Cai, S.Y. Ju, J. Edgeworth, X. Li, C.W. Magnuson, A. Velamakanni, R.D. Piner, J. Kang, J. Park, R.S. Ruoff, *ACS Nano* 5 (2011) 1321–1327.
- [20] J. Cermak, T. Yamada, K. Ganzerova, B. Rezek, *Adv. Mater. Interfaces* 3 (2016) 1–7.
- [21] R. Hawaldar, P. Merino, M.R. Correia, I. Bdikin, J. Grácio, J. Méndez, J.A. Martín-Gago, M.K. Singh, *Sci. Rep.* 2 (2012) 682.
- [22] M.C. Biesinger, L.W.M. Lau, A.R. Gerson, R.S.C. Smart, *Appl. Surf. Sci.* 257 (2010) 887–898.
- [23] F. Yang, Y. Liu, W. Wu, W. Chen, L. Gao, J. Sun, *Nanotechnology* 23 (2012) 475705.
- [24] M. Kumar, A. Javid, J.G. Han, *Langmuir* 33 (2017) 2514–2522.
- [25] S. Doniach, M. Sunjic, *J. Phys. C Solid State Phys.* 3 (1970) 285–291.
- [26] T. Susi, T. Pichler, P. Ayala, *Beilstein J. Nanotechnol.* 6 (2015) 177–192.
- [27] S.D. Costa, A. Righi, C. Fantini, Y. Hao, C. Magnuson, L. Colombo, R.S. Ruoff, M.A. Pimenta, *Solid State Commun.* 152 (2012) 1317–1320.
- [28] A. Mooradian, *Phys. Rev. Lett.* 22 (1969) 185–187.
- [29] A. Pirkle, J. Chan, A. Venugopal, D. Hinojos, C.W. Magnuson, S. McDonnell, L. Colombo, E.M. Vogel, R.S. Ruoff, R.M. Wallace, *Appl. Phys. Lett.* 99 (2011) 2–5.
- [30] X. Glad, L. de Poucques, J. Bougdira, *J. Phys. D. Appl. Phys.* 48 (2015) 495304.
- [31] Y.-C. Lin, C.-C. Lu, C.-H. Yeh, C. Jin, K. Suenaga, P.-W. Chiu, (2011).
- [32] L. Zhao, R. He, K. Taeg Rim, T. Schiros, K.S. Kim, H. Zhou, C. Gutiérrez, S.P. Chockalingam, C.J. Arguello, L. Palova, D. Nordlund, M.S. Hypertsen, D.R. Reichman, T.F. Heinz, P. Kim, A. Pinczuk, G.W. Flynn, A.N. Pasupathy, *Science* (80-.). 333 (2011) 999–1004.
- [33] Joshua D. Wood, *Nano Lett.* (2011) 4547–4554.
- [34] S. Nie, J.M. Wofford, N.C. Bartelt, O.D. Dubon, K.F. McCarty, *Phys. Rev. B - Condens. Matter Mater. Phys.* 84 (2011) 1–7.
- [35] M. Bruna, A.K. Ott, M. Ijas, D. Yoon, U. Sassi, A.C. Ferrari, *ACS Nano* 8 (2014) 7432–7441.
- [36] A. Das, S. Pisana, B. Chakraborty, S. Piscanec, S.K. Saha, U. V Waghmare, K.S. Novoselov, H.R. Krishnamurthy, a K. Geim, A.C. Ferrari, A.K. Sood, *Nat. Nanotechnol.* 3 (2008) 210–215.
- [37] J.W. Suk, A. Kitt, C.W. Magnuson, Y. Hao, S. Ahmed, J. An, A.K. Swan, B.B. Goldberg, R.S. Ruoff, *ACS Nano* 5 (2011) 6916–6924.
- [38] A. Achour, S. Vizireanu, G. Dinescu, L. Le Brizoual, M.A. Djouadi, M. Boujtita, *Appl. Surf. Sci.* 273 (2013) 49–57.
- [39] H. Estrade-Szwarcopf, *Carbon N. Y.* 42 (2004) 1713–1721.
- [40] M.. b Koinuma, H.. b Tateishi, K.. b Hatakeyama, S.. b Miyamoto, C.. b Ogata, A.. b Funatsu, T.. b Taniguchi, Y.. b Matsumoto, *Chem. Lett.* 42 (2013) 924–926.
- [41] A. Siokou, F. Ravani, S. Karakalos, O. Frank, M. Kalbac, C. Galiotis, *Appl. Surf. Sci.* 257 (2011) 9785–9790.
- [42] D. Yang, A. Velamakanni, G. Bozoklu, S. Park, M. Stoller, R.D. Piner, S. Stankovich, I. Jung, D.A. Field, C.A. Ventrice, R.S. Ruoff, *Carbon N. Y.* 47 (2009) 145–152.
- [43] N. Hellgren, R.T. Haasch, S. Schmidt, L. Hultman, I. Petrov, *Carbon N. Y.* 108 (2016) 242–252.
- [44] S.C. Hernández, F.J. Bezares, J.T. Robinson, J.D. Caldwell, S.G. Walton, *Carbon N. Y.* 60 (2013) 84–93.
- [45] I. Bertóti, M. Mohai, K. László, *Carbon N. Y.* 84 (2015) 185–196.
- [46] S. Kaciulis, *Surf. Interface Anal.* 44 (2012) 1155–1161.
- [47] V. Datsyuk, M. Kalyva, K. Papagelis, J. Parthenios, D. Tasis, A. Siokou, I. Kallitsis, C. Galiotis, *Carbon N. Y.* 46 (2008) 833–840.

- [48] W. Ding, Z. Wei, S. Chen, X. Qi, T. Yang, J. Hu, D. Wang, L.J. Wan, S.F. Alvi, L. Li, *Angew. Chemie - Int. Ed.* 52 (2013) 11755–11759.
- [49] M. Scardamaglia, B. Aleman, M. Amati, C. Ewels, P. Pochet, N. Reckinger, J.F. Colomer, T. Skaltsas, N. Tagmatarchis, R. Snyders, L. Gregoratti, C. Bittencourt, *Carbon N. Y.* 73 (2014) 371–381.
- [50] C. Batich, D. Donald, *J. Am. Chem. Soc.* 106 (1984) 2758–2761.
- [51] J.R. Pels, F. Kapteijn, J.A. Moulijn, Q. Zhu, K.M. Thomas, *Carbon N. Y.* 33 (1995) 1641–1653.
- [52] X. Wang, X. Li, L. Zhang, Y. Yoon, P.K. Weber, H. Wang, J. Guo, H. Dai, *Science* (80-.). 324 (2009) 768–771.
- [53] K.X. Yao, X.M. Yin, T.H. Wang, H.C. Zeng, *J. Am. Chem. Soc.* 132 (2010) 6131–6144.
- [54] A.C. Ferrari, J. Robertson, *Philosophical Trans. Math. Phys. Eng. Sci.* 363 (2004) 2477–2512.
- [55] M.S. Dresselhaus, G. Dresselhaus, R. Saito, A. Jorio, *Phys. Rep.* 409 (2005) 47–99.
- [56] A.C. Ferrari, J.C. Meyer, V. Scardaci, C. Casiraghi, M. Lazzeri, F. Mauri, S. Piscanec, D. Jiang, K.S. Novoselov, S. Roth, A.K. Geim, *Phys. Rev. Lett.* 97 (2006) 1–4.
- [57] L.G. Cançado, A. Jorio, E.H.M. Ferreira, F. Stavale, C. a. Achete, R.B. Capaz, M.V.O. Moutinho, A. Lombardo, T.S. Kulmala, a. C. Ferrari, *Nano Lett.* 11 (2011) 3190–3196.
- [58] M.M. Lucchese, F. Stavale, E.H.M. Ferreira, C. Vilani, M.V.O. Moutinho, R.B. Capaz, C. a. Achete, A. Jorio, *Carbon N. Y.* 48 (2010) 1592–1597.
- [59] L.G. Cançado, M. Gomes de Silva, E.H.M. Ferreira, F. Hof, *2D Mater.* 4 (2017) 025039.
- [60] F. Tuinstra, L. Koenig, *J. Chem. Phys.* 53 (1970) 1126–1130.
- [61] L.M. Malard, M. a. Pimenta, G. Dresselhaus, M.S. Dresselhaus, *Phys. Rep.* 473 (2009) 51–87.
- [62] L.G. Cançado, K. Takai, T. Enoki, M. Endo, Y.A. Kim, H. Mizusaki, A. Jorio, L.N. Coelho, R. Magalhães-Paniago, M.A. Pimenta, *Appl. Phys. Lett.* 88 (2006).
- [63] G. Giovannetti, P.A. Khomyakov, G. Brocks, V.M. Karpan, J. Van Den Brink, P.J. Kelly, *Phys. Rev. Lett.* 101 (2008) 4–7.
- [64] R. Blume, P.R. Kidambi, B.C. Bayer, R.S. Weatherup, Z.-J. Wang, G. Weinberg, M.-G. Willinger, M. Greiner, S. Hofmann, A. Knop-Gericke, R. Schlögl, *Phys. Chem. Chem. Phys.* 16 (2014) 25989–26003.
- [65] R. Wu, L. Gan, X. Ou, Q. Zhang, Z. Luo, *Carbon N. Y.* 98 (2016) 138–143.
- [66] K. Jia, Y. Su, Y. Chen, J. Luo, J. Yang, P. Lv, Z. Zhang, H. Zhu, C. Zhao, T. Ye, *Vacuum* 116 (2015) 90–95.
- [67] A. Sadezky, H. Muckenhuber, H. Grothe, R. Niessner, U. P??schl, *Carbon N. Y.* 43 (2005) 1731–1742.
- [68] J.S. Mehta, A.C. Fauchett, A. Sharma, J.M. Mativetsky, *J. Phys. Chem. C* 121 (2017) 16584–16591.
- [69] A.A.K.K. King, B.R. Davies, N. Noorbehesht, P. Newman, T.L. Church, A.T. Harris, J.M. Razal, A.I. Minett, *Sci. Rep.* 6 (2016) 1–6.
- [70] A. V. Krasheninnikov, K. Nordlund, *J. Appl. Phys.* 107 (2010).
- [71] C.P. Ewels, M.I. Heggie, P.R. Briddon, *Chem. Phys. Lett.* 351 (2002) 178–182.
- [72] F. Banhart, J. Kotakoski, A. V. Krasheninnikov, *ACS Nano* 5 (2011) 26–41.

8. Supplementary data

Additional data on the sources of oxygen impurities, Raman spectroscopy and copper oxide, XPS and copper oxide, static water contact angle, are provided in **Annexe 2** of this thesis.

Chapitre 3 – Rôle des inhomogénéités de croissance

3.1 Introduction

Tel que discuté brièvement au **Chapitre 2**, les inhomogénéités de surface présentes sur l'échantillon de graphène sont responsables de fortes variations de ses propriétés une fois traité par plasma. En effet, les points sondés au-dessus d'oxyde présents sur le substrat de cuivre révélaient des spectres Raman et des cinétiques de production de dommages tout à fait distincts. L'origine de ces types d'inhomogénéités de surface reliés à la préparation des échantillons, que nous appellerons dans cette thèse *inhomogénéités de croissance*, est multiple. On note tout d'abord l'effet du substrat. Le cuivre, par exemple, peut être oxydé. Cette oxydation peut avoir lieu avant ou après la croissance. L'oxydation post-croissance peut avoir lieu par migration sous le graphène mais également par perméation aux joints de grains [R82]. Des liens avec le substrat peuvent se former, ou un découplage du substrat peut survenir [R83,84]. Cette même baisse d'interactions avec le substrat est notamment présente lorsque le graphène est transféré sur SiO₂. D'autres effets dis de Moiré (*Moirés Patterns*) peuvent exister et jouer sur l'interaction avec le substrat et les profils de tension de surface [R85]. Outre le substrat, les joints de grains formés lors de la croissance représentent des sites attendus de réactivité accrue. On y décerne un changement de topologie, de dopage avec le substrat, et de conduction thermique [R86,87]. Ces sites sont particulièrement intéressants à étudier pour cibler des mécanismes se produisant à la surface du graphène lors d'un post-traitement. On note également des contaminants résultant de produits utilisés pour le transfert de substrat du graphène, ou même déjà présents dans le montage utilisé pour la croissance. Ceux-ci peuvent apparaître comme des particules de tailles et densités variables en surface [R88,89]. On comprend ainsi que selon la nature de la croissance du graphène, la présence de ces inhomogénéités varie. En effet, pour des échantillons exfoliés, les inhomogénéités reliées au transfert et aux domaines sont pratiquement absentes.

On rappelle ici que dans le cadre de ce projet de thèse, les échantillons sont obtenus par CVD et, sont donc caractérisés par des domaines de tailles variables (30-80 µm) sur l'ensemble de l'échantillon. De plus, selon les conditions opératoires de la chambre de croissance, la présence de contaminants de surface varie. À noter également qu'à la lumière des préoccupations

abordées au **Chapitre 2**, chaque série de mesures (et donc chaque article présenté plus bas) est réalisée sur plusieurs échantillons issus de la même croissance et du même transfert. De plus, les échantillons sont gardés dès que possible sous une cloche à vide pour limiter les effets de contaminations par les hydrocarbures [R90].

Pour combler le manque de résolution spatiale des méthodes conventionnelles de RS utilisées au **Chapitre 2**, et pour s'affranchir des délais dérisoires que peuvent prendre des imageries Raman standards en mode *point-par-point*, une nouvelle méthode est explorée. En effet, une grille de 100 x 100 à haute résolution (1 µm) spatiale avec des zones de 1 µm peut prendre plus de 7h de temps d'acquisition afin d'obtenir un bon signal sur bruit. Ainsi, un travail de collaboration a été débuté entre notre groupe de recherche, le groupe de recherche du professeur Richard Martel – Université de Montréal et la compagnie Photon ETC. Un appareil prometteur, le RIMA™ (Raman IMAGING) a été utilisé pour enregistrer des spectres Raman de 130 µm x 130 µm sur le graphène avec une résolution spatiale de 130 nm en cellules 1x1 (ou 490 nm en cellules 3x3). Une méthode de traitement des données a ainsi été mise au point afin de permettre d'extraire le plus d'informations possibles des 10^5 – 10^6 spectres obtenus pour chaque mesure.

La **Section 3.2** établit la base de cette nouvelle méthode de traitement des données RIMA. On y démontre le potentiel de la méthode pour extraire un nombre important de relations entre l'état initial et final de chaque traitement par plasma. Cette section est présentée sous la forme d'un article publié dans *Review of Scientific Instruments* en mai 2020. Le potentiel de la méthode est montré pour le traitement de graphène obtenu par CVD sur cuivre puis transféré sur SiO₂, et finalement traité par plasma d'argon. Le choix du plasma d'argon plutôt que du plasma d'azote comme traitement "typique" est motivé par une littérature plus abondante. Je partage dans cet article le titre de premier auteur avec Pierre Vinchon. Les contributions pour l'article vont comme suit : G. Robert Bigras – méthode de filtrage de bruit, de traitement des données, de déconvolution et d'alignement des mesures, rédaction P. Vinchon – traitement par plasma, mesures, rédaction. C. Allard – support pour l'utilisation du montage RIMA™. R Martel et L. Stafford – supervision. Ensemble des auteurs – discussion et interprétation des résultats.

La **Section 3.3** résume brièvement des résultats issus des travaux de la thèse de P. Vinchon qui sont essentiels à la compréhension de la suite de cette thèse. Cette contribution, dans laquelle G. Robert Bigras est co-auteur, mise sur le potentiel d'innovation de la méthode d'analyse que nous avons mise au point dans la **Section 3.2**. Plus précisément, on montre qu'il existe un mécanisme d'auto-réparation préférentielle des dommages à proximité de joints de grains du graphène lors de traitements dans un plasma d'argon. Cet article récemment publié dans *Nature Materials* est fourni à l'Annexe 3. Les contributions sont comme suit : P. Vinchon – rédaction, traitements expérimentaux. X. Glad – rédaction. G. Robert Bigras – traitement des données. R Martel et L. Stafford – supervision. Ensemble des auteurs – discussion et interprétation des résultats.

Dans la **Section 3.4** est présenté une version revisitée de la méthode présentée à la **Section 3.2**. Celle-ci permet l'identification de multiples zones présentant des comportements distincts lorsque soumises aux traitements dans la post-décharge en flux de plasmas d'azote. La méthode de soustraction d'artefact, la méthode de filtrage de bruit et une nouvelle méthode de regroupement (*clustering*) de spectres, toutes basées en partie sur la décomposition des spectres en composantes principales (PCA, *Principal Component Analysis*), ont permis de quantifier l'évolution des dommages sur l'ensemble des inhomogénéités de surface de l'échantillon. Des mesures complémentaires de microscopie électronique à balayage (MEB) ont permis d'identifier la présence et l'impact d'impuretés de nature SiO_x en surface, de joints de grains, et des domaines sur la dynamique d'incorporation des atomes d'azote. Le découplage optique des contraintes et du dopage et des mesures complémentaires de XPS ont permis de conclure sur un dopage négatif de manière préférentielle dans les domaines du graphène. Ces mesures sont présentées sous la forme d'un article publié dans *Nature Partner Journal : 2D Materials*. Les contributions sont comme suit : G. Robert Bigras – traitements expérimentaux, traitement des données et rédaction. X. Glad – rédaction. R Martel et L. Stafford – supervision. Ensemble des auteurs – discussion et interprétation des résultats.

3.2 Nouvelle méthode d'analyse par imagerie Raman

Probing plasma-treated graphene using hyperspectral Raman

G. Robert Bigras ^{*1}, P. Vinchon ^{*1}, C. Allard ², X. Glad ¹, R. Martel ², L. Stafford ^{1**}

^{*} Equally credited authors ^{**} Corresponding author: luc.stafford@umontreal.ca

¹ Département de Physique, Université de Montréal, 1375 Avenue Thérèse-Lavoie-Roux,
Montréal, Québec, H2V 0B3, CANADA

² Département de Chimie, Université de Montréal, 5155 Chemin de la Rampe, Montréal, Québec,
H3T 1J4, CANADA

ABSTRACT

Raman spectroscopy provides rich optical signals that can be used, after data analysis, to assess if a graphene layer is pristine, doped, damaged, functionalized, or stressed. The area being probed by a conventional Raman spectrometer is, however, limited to the size of the laser beam ($\sim 1 \mu\text{m}$); hence, detailed mapping of inhomogeneities in a graphene sample requires slow and sequential acquisition of a Raman spectrum at each pixel. Studies of physical and chemical processes on polycrystalline and heterogeneous graphene films require more advanced hyperspectral Raman capable of fast imaging at high spatial resolution over hundreds of microns. Here, we compare the capacity of two different Raman imaging schemes (scanning and global) to probe graphene films modified by a low-pressure plasma treatment and present an analysis method providing assessments of the surface properties at local defects, grain boundaries and other heterogeneities. By comparing statistically initial and plasma-treated regions of graphene, we highlight the presence of inhomogeneities after plasma treatment linked to the initial state of the graphene surface. These results provided statistical results on the correlation between graphene initial state and the corresponding graphene-plasma interaction. This work further demonstrates the potential use of global hyperspectral Raman imaging with advanced Raman spectra analysis to study graphene physics and chemistry on a scale of hundreds of microns.

Keywords: Hyperspectral Raman imaging, graphene treatment, graphene-plasma interaction, principal component analysis filtering

1. INTRODUCTION

Raman spectroscopy of graphene provides access to quantitative assessments of local defect density, doping state and strain levels, and, hence, represents a powerful tool for probing the quality and the chemistry of a graphene sample [1-3]. Acquiring Raman maps over macroscopic scales generates a wealth of additional information about the sample, including local heterogeneities of defects, differences in doping or stress, and helps further understand complex transformations linked to these differences. As an example, the complexity of the graphene-plasma interaction was recently highlighted by Raman mapping of polycrystalline graphene films after low-pressure argon plasma treatments [2].

The current standard Raman methods of mapping are based on scanning schemes in which the laser beam (or line) is moved pixel by pixel (or line by line). Conventional Raman are poorly adapted for macroscopic scales because the spatial resolution is limited by the beam shape and size, which is typically of around 1 μm . Generating maps with both acceptable signal-to-noise ratio and high spatial resolution are therefore time-consuming [1]. Hyperspectral Raman Imaging (RIMA) is a global imaging scheme that has demonstrated itself to be a highly promising alternative to conventional Raman imaging schemes [1]. The instrument acquires millions of Raman spectra in a reasonable time (hours), which provides enough data for statistical analysis while allowing spatial correlation. With these advances, difficulties arise, however, when trying to evaluate quantitative values from hyperspectral Raman maps due to artefacts intrinsic to the setup and to the low density of power imposed with global illumination, which maximum value is set so as to prevent graphene damage.

Here, we present a refined data processing method for RIMA images based on Principal Component Analysis (PCA) filtering to extract the most information possible on the physics and chemistry of polycrystalline graphene films grown on copper substrates by Chemical Vapor Deposition (CVD) and then transferred on SiO_2 substrates using conventional transfer methods. Through fast data handling, the method provides two-dimensional histograms of registered

datasets that allow to spatially compare the Raman results of pristine graphene films with that of the same sample after a low-pressure argon plasma treatment. Thanks to the RIMA method, the characterization is facilitated by a wide field of view (hundreds of micrometers) and a good spatial resolution (tens of micrometers for a field of view of hundreds of micrometers). As demonstrated by results on graphene plasma treatments, the method reveals itself as a promising alternative to investigate novel graphene-plasma interactions and mechanisms.

2. EXPERIMENTAL DETAILS

The RIMA instrument (described in details in [3], Photon Etc) relies on volumetric Bragg tunable filters (BTF) to acquire hyperspectral Raman images. Briefly, a 532 nm laser is focused at the focal length of a 100x objective, providing a field of view of $130 \mu\text{m} \times 130 \mu\text{m}$ to the sample. The authors' custom shaping module provides the laser a flat top intensity profile, which ensures homogeneity of the laser exposition at the graphene surface. Scattered light emitted from the graphene surface is collected via the same objective and redirected towards the BTF. Gradient images are collected at a 1024×1024 pixels charged couple device (CCD, 1024×1024 PIXIS, Princeton Instruments) for various angular position of the BTF. The final spectra are reconstructed via a wavelength rectification digital process [3]. The instrument provides spectra with a spectral resolution of 8 cm^{-1} but measurements are typically performed with 3 cm^{-1} acquisition steps. Each image contains a mapping with 1048576 points (1024×1024). The laser power is set to 3.5 W (power density of $2.1 \times 10^8 \text{ W/m}^2$), which is low enough to ensure no damage generated to the graphene sample during measurements [4].

The area probed depends on the objective used; the 100x and 50x objective provides images of $130 \times 130 \mu\text{m}^2$ and $260 \times 260 \mu\text{m}^2$, respectively. Due to the high number of pixel (1024×1024), a maximum spatial resolution of 130 nm is achieved with the 100x objective. This value coincide with the diffraction limit of the setup [3]. Through binning of few pixels on the CCD camera, one can decrease the exposure time for good signal-to-noise ratio, but at the cost of a decrease of the spatial resolution. In this work, the first measurements were carried out using 1x1 binning and 100 sec of exposure time. The same region was probed after exposure of the sample to a planar-type Inductively Coupled Plasma (ICP) operated in nominally pure argon (details elsewhere [2]

and experimental conditions presented in Supplementary Data I). Due to time constraints, RIMA measurements of plasma-treated graphene samples were acquired using 3x3 binning ($0.39\text{ }\mu\text{m} \times 0.39\text{ }\mu\text{m}$) and 20 sec exposure time.

For the purpose of making a comparison with conventional Raman, we present additional Raman spectra acquired using a confocal Raman spectroscopy setup (Renishaw inVia). A 514 nm argon laser was used as the source and the power at the sample position was set at 0.7 mW. The spectral resolution is 1 cm^{-1} . The 100x objective of inVia provides a laser diameter of about $1\text{ }\mu\text{m}$ on the sample. The power density ($2.2 \times 10^8\text{ W/m}^2$) of the laser was kept below the onset of laser-induced damage in graphene films [4]. Baseline subtractions were performed using a polynomial baseline function and peak fitting was performed right afterward using a Lorentzian line shape. For sake of comparison with RIMA images of plasma-treated graphene samples, 36x36 point-by-point area mappings are recorded with a step of $4\text{ }\mu\text{m}$ to probe the uniformity of the surface. Both Raman mappings with the Renishaw and with RIMA (3x3 binning and 20 sec time exposure) took 1h30-2 hours to execute.

Principal component analysis (PCA) filtering was performed to reduce signal noise and to ease the fitting process [5,6]. **Fig. 1** presents typical Raman spectra before (grey) and after (red) PCA filtering for both untreated (a) and plasma-treated (b) graphene samples. Each spectrum is taken as an observation by considering each wavenumber values as a dimension for the analysis. Following the respective subtraction of the mean value of each observation, a linear combination of the initial dimension is found to minimize the variance of the data. The obtained dimension is subtracted, and the calculation is done iteratively as many times as there are dimensions. The resulting dimensions are therefore sorted according to the contribution of the observations. The first components represent dominants features of the signal while low variance's components arise from noise in the observations. Thus, by reducing dimension numbers, one can essentially filter the data noise. In this case, the number of components chosen for the reconstruction are determined by a threshold of contribution to the cumulative signal. Components considered for the reconstruction are selected until the next component provides less than 0.05% of the cumulative signal. Additional details on the filtering process are presented in Supplementary Data

II. Mean spectra of each acquisition cube, criteria on the number of PCA components to consider and additional typical spectra are also presented.

Overall, an excellent matching is obtained in **Fig. 1** between initial Raman spectra and reconstructed Raman signal after PCA filtering. Indeed, the sufficient number of components considered ensures that no information is lost. Some important features arise using PCA filtering. The small peak around 1550 cm^{-1} was hidden in the noise for most spectra and is linked to an intrinsic artefact present in the RIMA setup [3,7]. This will be further discussed later.

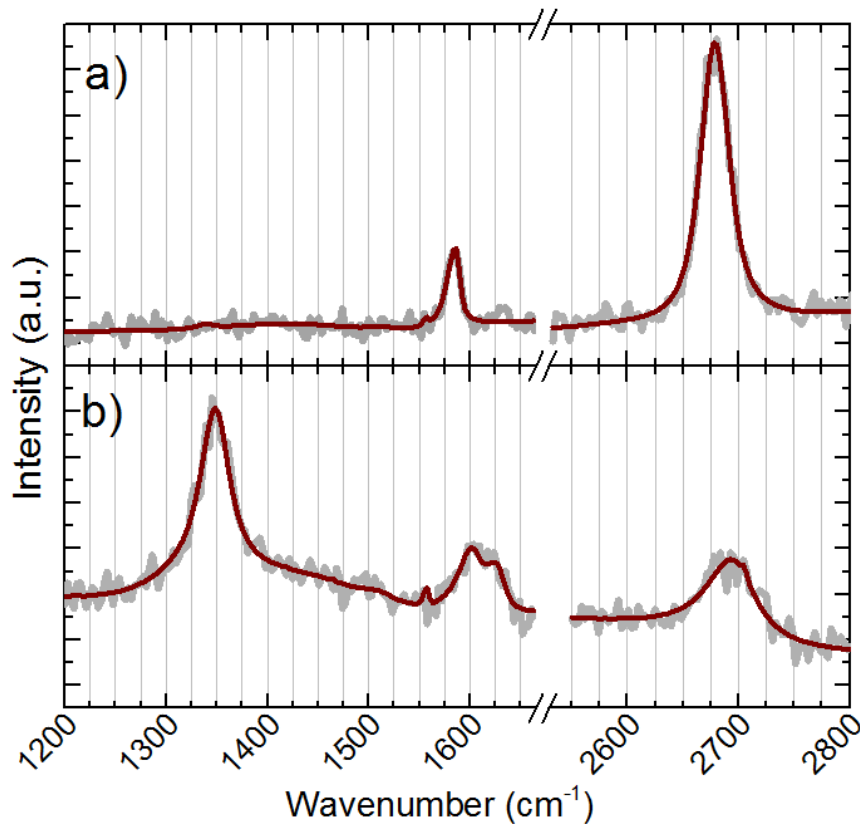
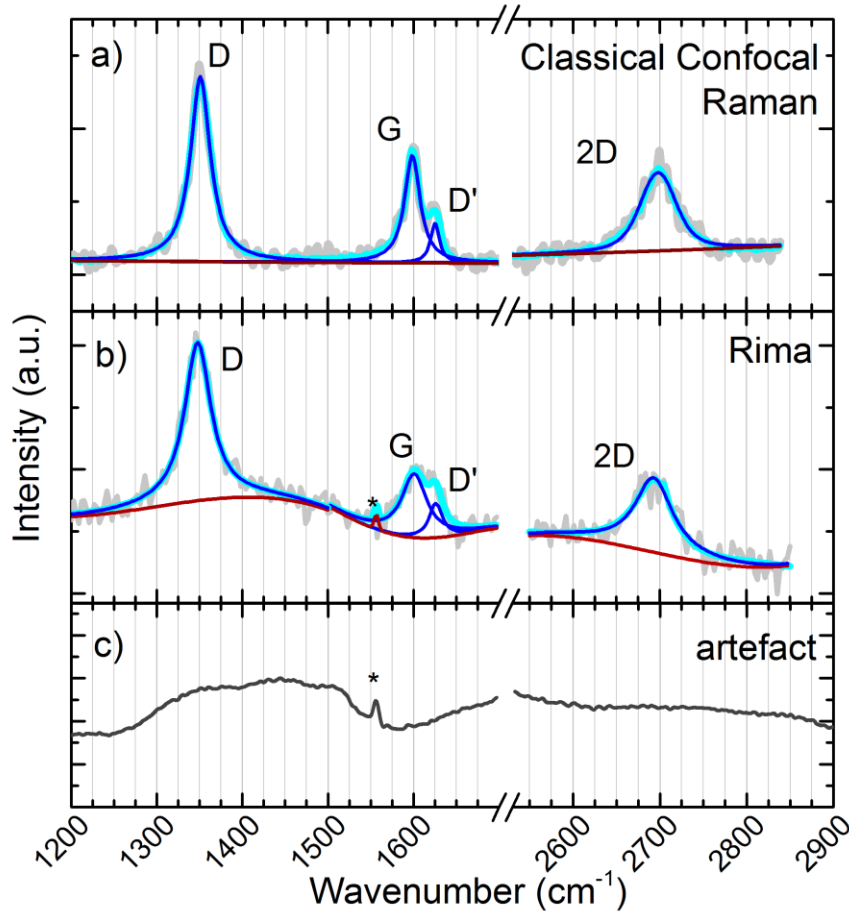


Fig.1 - Comparison raw data and PCA filtered data for untreated (a) and plasma-treated (b) graphene.

After PCA filtering, Raman spectra are fitted using a nonlinear least square fitting method with normalization and centering. Each spectrum is separated in three regions (D, G&D' and 2D regions of graphene). A precise baseline subtraction is mandatory to obtain quantitative analysis of the Raman measurements and to remove residual contributions, such as fluorescence from the

substrate and other intrinsic artefacts (e.g. beam inhomogeneities, fluorescence from optical components). The shape of the RIMA artefact changes over the surface of the camera. This explains the variation of the curvature's amplitude of the baseline between points recorded at different position (see **Fig.1** for example). Additionally, an increase of exposure time naturally increases the ratio between the Raman signal and this baseline. Polynomial curves are used for baseline fitting with an order chosen to be the smallest possible while keeping good fitting results. The method ensures a good baseline subtraction as long as the line shape of each bands is chosen wisely so that no bands are neglected. For each acquisition cube, fitting of the three regions is performed for a large number of orders for the polynomial baseline subtraction. Order that are clearly too low are automatically discarded. From the remaining orders, one is selected as the optimal for the fit. It is chosen low enough to make sure there is no overfitting, but also high enough to allow the baseline to have the necessary curvature to best follow the profile of the artefact. Overall, the error on the band emission intensity, band position and band width introduced by the choice of the order is very small (see additional details in Supplementary Data III). Figs. 2 a-b present a comparison between typical Raman spectra obtained at a given position using both RIMA and Renishaw inVia. Overall, the spectra are alike in terms of linewidths and intensity ratios (see Section 3.2 for additional discussion).



*Fig.2 – Comparison of Raman spectra obtained either from a conventional confocal (Renishaw inVia) mapping (a) or from the RIMA instrument (Photon etc) (b). (c) Typical spectra of the broad signal form artefacts in RIMA giving a singular line shape. Fits to the spectra and polynomial fit to the baseline are also shown. The sharp feature marked with * is an instrument's artefact.*

Fig 2c presents a Raman spectrum of bare cleaned SiO₂ (cleaned during 30 min in acetone at 60°C followed by three rinses in IPA for 10 min). Since SiO₂ has no Raman peak in this spectral range, the resulting spectrum is only composed of parasitic lights (fluorescence and artefacts). It is worth highlighting that the data displayed in **Fig. 2c** were recorded at the same position on the CCD as that of the RIMA spectrum in **Fig. 2b**. A similar profile was actually obtained, which supports the conclusion that the baseline in the G&D' region on **Fig. 2b** is extrinsic to the graphene signal. Since graphene is present on only one of the samples, this comparison indicates, however, that the absolute intensity and shape of background signals vary from pixel to pixel, which makes baseline

subtractions arduous. The nature of the artefacts is still under investigation, but it is currently believed to arise from fluorescence in the objectives.

Fitting parameters for the spectra (band intensity, band position, band width) can easily be presented either as maps or histograms. Already, these results are of interest for doping, strain and defect assessments [3,10]. Furthermore, the huge dataset provided by the RIMA cube gives access to extremely detailed statistical distributions and allows for a precise registration of the measurements taken on the same region before and after plasma treatments. To proceed, an image of logical value is extracted via a criterion on band parameters chosen for each measurement. Typically, a threshold on the absolute G-band intensity is used because it highlights distinguishable features from CVD-grown polycrystalline graphene films such as cracks and defects. Then an alignment using only rotation and translation of these two logical masks (0 or 1) are used to define a transformation process that can be applied to all band parameters to establish point-by-point behavior. Typical mean images are extracted as a confirmation (Supplementary Data IV). As discussed in Section 3.3, results show that the method allows a direct correlation of graphene initial properties with that of the resulting plasma-treated sample.

3. DATA PROCESSING

3.1 UNIFORMITY OF UNTREATED SAMPLES

At first, RIMA was used to study untreated graphene films. The large field of view enables a quantitative evaluation of the graphene uniformity. Two areas were chosen alongside each other with a clear crack overlapping in the two selected regions. This is done to access the ability to extract band parameters from the raw data without any distortion on the output, but also to demonstrate the ability of the RIMA system to probe area larger than the actual field of view of the setup. Systematic variations of intensity ratios due to an incorrect data processing would be made visible when aligning the two images. Measuring two zones also enables to probe variations of the signal that range over a single field of view. This crack and others small defects facilitate the alignment of the two sets of data after processing. Hence, it is possible to obtain an image of all parameters used to fit graphene peaks. For examples, **Fig. 3** presents images of intensity peak

ratio of the D over G bands (D:G), 2D over G bands (2D:G) as well as the position and FWHM of the 2D band for the two stitched areas.

Overall the sample reveal an average D:G value of 0-0.1 with some small spots where the local signal rises up to 0.3. These damaged areas of around 500 nm wide are spread on the regions. These are also aligned on well-defined lines. Looking at the overlapping area between the two regions, a fairly good stitching is obtained. The values of the point defects and the background of graphene with low defect density have a good match. The 2D:G mapping shows a much larger variation; its values are contained between 1 and 4, with a mean value of around 2.5. There are clear disparities between several areas on the same region. These distinct areas are absent of the D:G mapping and thus 2D:G ratio can provide additional meaningful information. The last two mappings show 2D bands features. Peak positions show variations of strain around defect points identified in the D:G mappings. In the case of the 2D bandwidth, a maximum value below

45 cm⁻¹ is observed while the mean value is around 32 cm⁻¹. Consequently, it rules out possible bilayer presence on the pristine graphene. Furthermore, lines can be noticed that seem to define domains between graphene grains [9]. It is interesting to note that such domains are not observed when imaging band intensities ratio. This will be further discussed in Section 3.2. The values of the overall parameters of the fits are latter presented in Section 3.2 Tab. 1. All those values are expected for CVD-grown polycrystalline graphene films [1].

Ultimately, the overall good stitching of the two images underlines the coherence of the RIMA method over the whole surface probed by the measurements. Still, some discrepancies are noted and might originated from the non-flat laser irradiation of the probed area. Although the beam-shaping module enable a laser profile as flat as possible, some variations of the intensity are still present of the side (~15% variation across the field view [3]). This change in the ratio between the Raman bands and the singularly shaped background alters the polynomial baseline subtraction leading to slight variation at the edges. Yet, these variations are very small. Consequently, the level of details enabled by the high spatial resolution combined with the large field view opens the way to better understanding of graphene properties and processing.

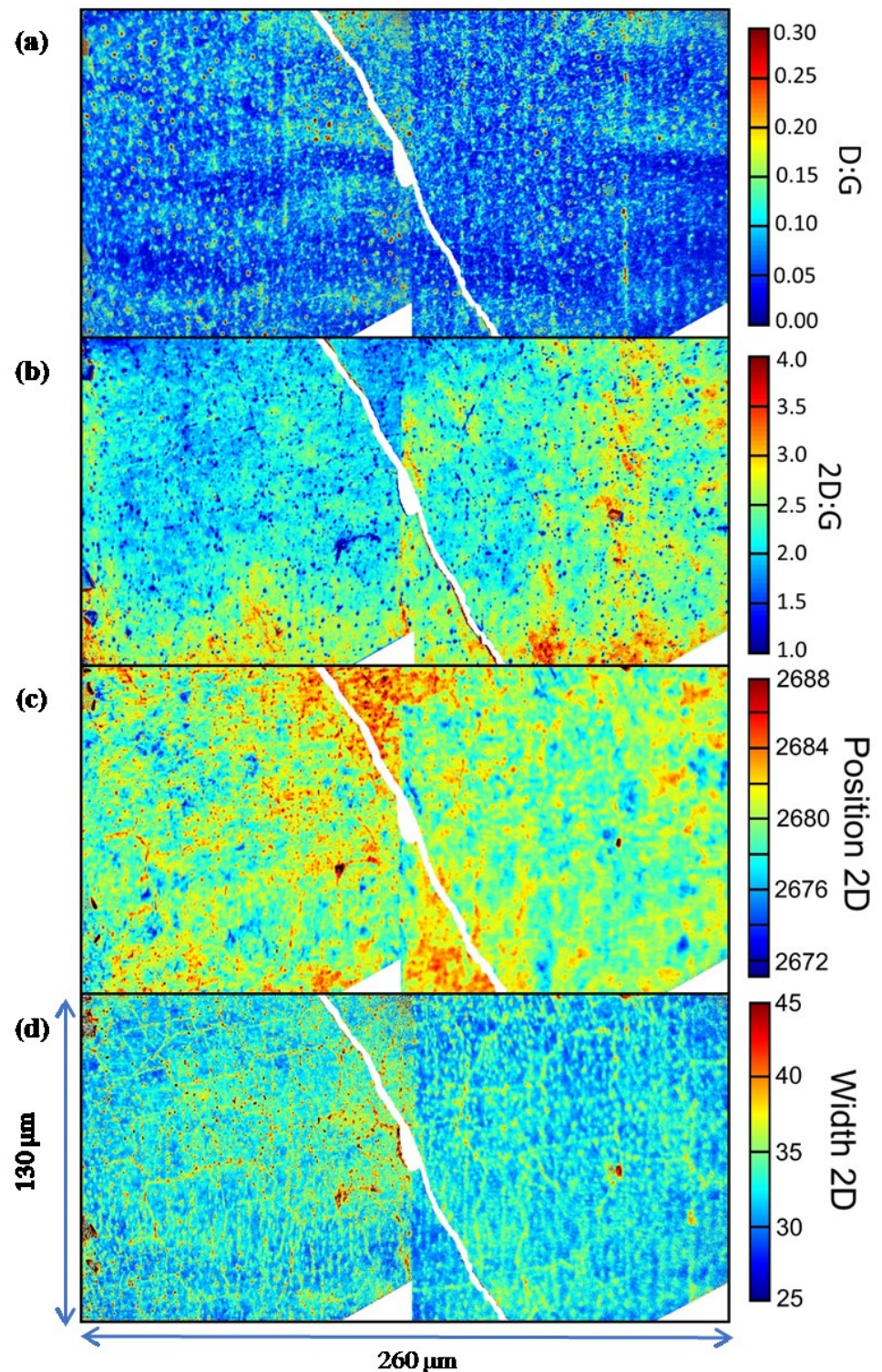


Fig.3 – Juxtaposition of two zones of untreated graphene. (a) 2D:G ratio, (b) D:G ratio, (c) 2D position and (d) 2D width are presented.

3.2. PLASMA TREATMENTS OF GRAPHENE: COMPARISON BETWEEN CONVENTIONAL (CONFOCAL) RAMAN AND RIMA

The same sample presented in Section 3.1 was exposed to the argon ICP plasma and the same region was then measured in order to follow its evolution following the low-pressure plasma treatment (graphene-plasma interaction is dominated by very-low-energy ion irradiation [2]). For simplicity, only the left most region displayed in **Fig. 3** was characterized. In order to consolidate measurements made by RIMA, the region was analyzed with a conventional confocal Raman system (Renishaw inVia). A high-resolution mapping of 1296 points was completed with a step of 4 μm to evaluate local states of the graphene in a processing time comparable to the one of RIMA measurements.

Fig. 4 presents D:G, 2D:G and D:D' ratios images of the same region evaluated by RIMA and by conventional confocal Raman. Compared to the untreated spectra, there is a clear increase of D:G ratio evaluated by both methods from 0.2 up to 3.5. Both methods further present a gradient of the peak ratio on the whole region from 3.5 down to 1. With RIMA images, some domains can be observed delimited by thin lines with low values of D:G around 1 with higher values in the center from 1.5 to 3. Such patterns can hardly be observed with classical Raman mapping. In the case of the 2D:G ratio, both approaches display a low value below 1.4 down to 0.2 with a gradient across the region. The shape, orientation and intensity of the gradient are in good agreements and therefore confirms the fitting methods of the acquired datasets with RIMA. The 2D:G ratio map also shows the same domains obtained with D:G ratio. This time, they are delimited by higher value of 2D:G. Finally, the D:D' ratio values vary between 3 and 7. However, the gradient determined with the two techniques are quite different. Values from the upper part of RIMA image are higher (>6) than those with low-resolution Raman (~3). This discrepancy might arise from the difficulty to fit the D' peak, given its low value and its proximity with the G peak. The singular shape of the artifact in this spectral range is also cumbersome (see additional details in Supplementary Data III).

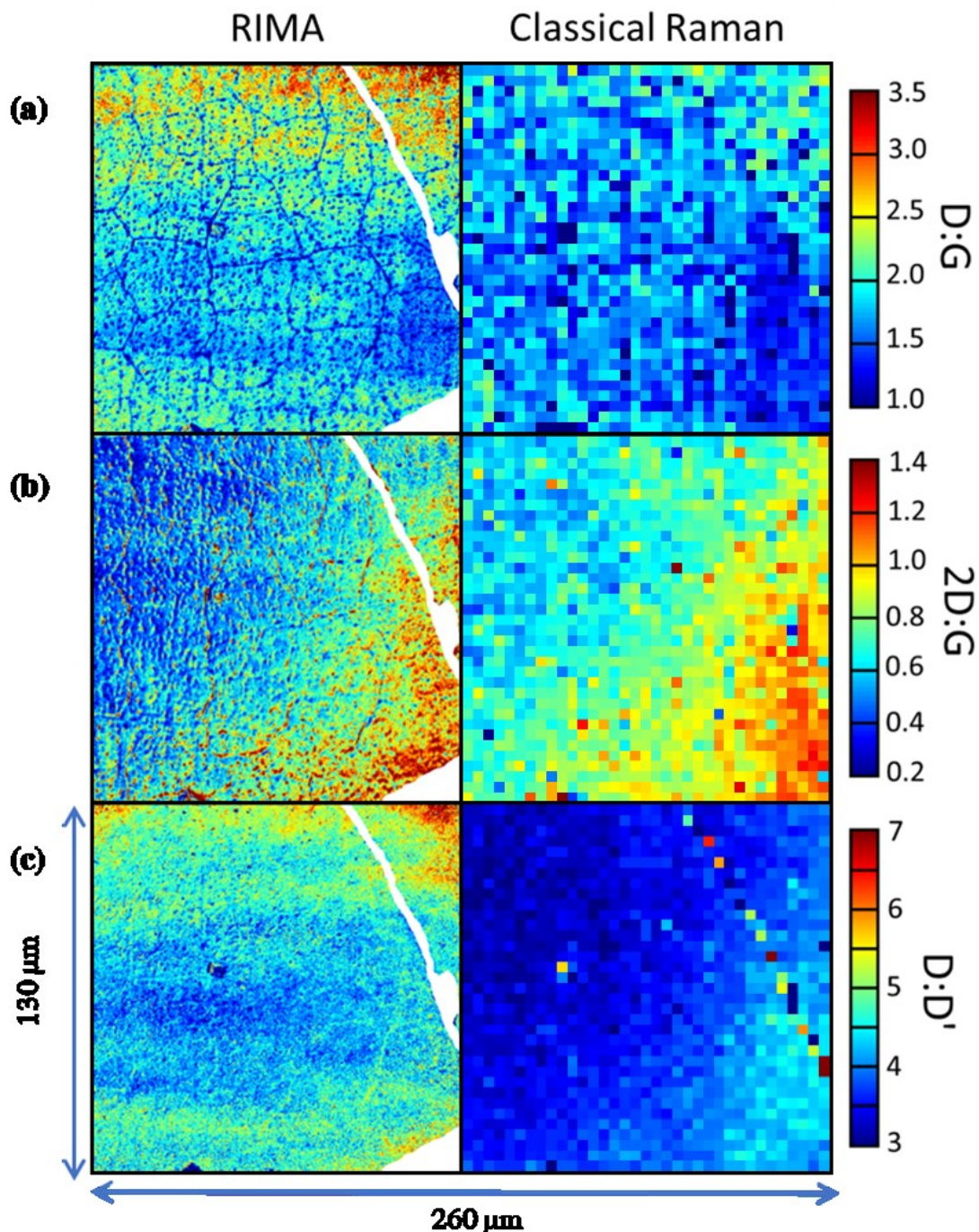


Fig.4 – Comparison of (a) D:G, (b) 2D:G and (c) D:D' ratios for mapping taken with RIMA (left column) and conventional confocal Raman (inVia) (right column).

It is interesting to note that domains highlighted by the 2D linewidth of the untreated graphene (**Fig. 3**) clearly appear on maps of the D:G and 2D:G peak ratios after plasma exposure. The

delimitation of domain growth given by a low value of D:G and a high value of 2D:G suggests that this domain lines are affected differently by the plasma treatment than the rest of graphene. Domain boundaries are typically interpreted as dislocations and hence, these defect lines are a priori more resistant to plasma irradiation. Giving larger 2D:G and lower D:G, the apparent resistance of these boundaries requires more testing by, for example, varying the approach angle of the bombarding ions to compensate the curvature around those dislocations [9].

While RIMA and InVia measurements on the same area of the plasma-treated sample reveal similar spatial behaviors (**Fig. 4**), some variations can be seen in the absolute values of selected band parameters. This aspect is examined in more details in Table 1 that summarizes mean values of different band parameters of interest along with the standard deviations obtained across the whole region probed by RIMA and InVia. When possible, corrections are applied on the band parameters obtained with the confocal setup to account for the different excitation energy of the RIMA and InVia systems (Supplementary Data VI). As can be seen, most band parameters show comparable values for plasma-treated graphene. However, small differences occur, for example for the D:G ratio. Geometric concerns seem to explain such variations. Indeed, the 1 μm diameter laser spot (surface area $\sim 3 \mu\text{m}^2$) used in the standard confocal system is of the same order of magnitude than the average distance between graphene boundaries and other regions with increased disorder ($\sim 2\text{-}5 \mu\text{m}$) (regions characterized by low D:G ratios in **Fig. 4.a**). In addition, these regions present much stronger Raman intensities (2-3 times the signal of graphene domains). This implies that random inVia measurements over the whole graphene sample will be strongly affected by these damaged regions. On the other hand, RIMA measurements using a 3x3 binning ($0.39 \mu\text{m} \times 0.39 \mu\text{m}$) can probe zones in the $\sim 0.15 \mu\text{m}^2$ range. Such dissimilarities in the surface areas necessarily involve distinct proportions of graphene domains, graphene boundaries, and disorders in each individual zone of InVia and RIMA measurements such that “local” and spatially-averaged values of Raman band parameters provided by the two methods can differ.

The rather destructive effect of the low-pressure plasma treatment examined in this study is observed by a decrease of 2D:G ratio with the simultaneous increase of the D:G ratio and D:2D. 2D:G values below 1 indicates that the graphene is starting to undergo a transition towards amorphization [10,11]. The D:D' peak ratio of 4.4 indicates that the nature of the defects is a

combination of vacancy and boundaries defects [10]. This is only true if the graphene is at the beginning of the amorphous stage, which is believed to be the case since the 2D:G ratio is still high enough. For both RIMA and conventional Raman, spectra show no sign of a broad Raman band between the D and the G band characteristic of amorphous carbons [12]. Furthermore, the broadening of the peaks width of all bands further supports high damage generated by the plasma treatment [13]. The increase of the 2D and D mean positions suggests the presence of a variation of strain and/or doping of the graphene sample [14]. However, the increase of the G band position being much larger than the increase of the 2D band position implies significant p-doping levels probably due to the creations of holes by ion bombardment. One must nonetheless be cautious when extracting values of doping and strain. Indeed, the dependence of bands energy on the doping level and the strain is strongly dependent on the graphene state. Damaged [15] and pristine [14,16] graphene reveal different G and 2D band shifts as a function of charge carrier modification. Additionally, graphene from CVD grown [17] and graphene exfoliated [14,16] also reveal different line-shift behaviors when subjected to doping and strain. Further investigation on a per sample basis are needed to extract strain and doping mapping from RIMA measurements.

Expression	inVia not corrected		inVia corrected		RIMA Treated		RIMA Untreated	
	Mean	STD	Mean	STD	Mean	STD	Mean	STD
2D:G	0.79	0.18	-		0.66	0.19	2.3	0.4
D:G	1.7	0.3	1.9	0.4	2.1	0.5	0.089	0.047
D:D'	3.8	4.0	-	-	4.4	0.4	-	-
D:2D	2.2	0.7	-	-	3.4	1.3	0.04	0.02
Γ_G	23.7	3.3	23.7	3.3	26.9	3.5	12.9	1.7
Γ_{2D}	50.2	4.6	50.2	4.6	61.6	6.3	31.4	1.5
Γ_D	30.3	3.4	30.3	3.4	34.7	1.2	22.8	2.5
ω_G	1595.9	2.1	1596.4	2.1	1600.3	1.2	1587.2	1.3
ω_{2D}	2697.5	2.4	2705.8	2.4	2688.0	3.2	2679.8	1.5
ω_D	1350.8	1.3	1355.0	1.3	1348.5	0.3	1343.6	2.5

Table 1 - Comparison for various Raman parameters between untreated and plasma-treated monolayer graphene samples. The mean and standard deviations are also presented. A threshold on the G band intensity is used to remove points with no graphene (e.g. the crack and where the image is cropped on the side)

3.3. COMPARISON BETWEEN INITIAL AND FINAL STATES OF GRAPHENE

The comparison between untreated and plasma-treated states of the graphene sample goes beyond the mere analysis of the mean values and standard deviations. As discussed in Section 2.1, the high number of points and good spatial resolution in RIMA maps allow easy registration of the same zone for subsequent measurements. By following the process described above, one can easily link the final state of a sample to the graphene properties taken before plasma treatment at the exact same position. Achieving the same registration precision with a conventional confocal Raman setup would require excessively long acquisition (very high spatial resolution) and RIMA is therefore clearly distinct for that purpose.

The method of characterization presented above is, to our knowledge, absent in the literature, even though the unique correlations this method can provide are numerous. Using the dataset of both states of the same graphene sample, one can present the results of the plasma treatment

as a double-histogram of two functions of the Raman parameters. The number of available output distribution is enormous. On one hand, we would like to focus on D:G, 2D:G, D:D' or Γ_G parameters to highlight the effect of plasma-induced damage. On the other hand, it seems interesting to explore the variation of the G band position versus the initial position of the 2D band to study strain effect on doping. Clearly, a whole new analysis platform for the study of graphene physics and chemistry is enabled by this method, but we will rather focus on a subset of parameters with the associated interpretation so as to demonstrate the usefulness of the method.

As an example, **Fig. 5** presents the statistical distribution of the variation of 2D:G ratio ($2D:G_{final} - 2D:G_{initial}$) as a function of the initial 2D:G ratio (pristine graphene film). This plot highlights a specific behavior in these histograms through a normalization along one axis to allow the visualization of the change in distribution of a first parameter (here a variation of 2D:G) as a function of another parameters (here 2D:G ratio). A straight tendency is obtained; the diminution of the 2D:G ratio is much larger for points with higher initial 2D:G ratios (i.e. higher quality graphene). This is expected since the decrease of 2D:G ratio is smaller when the state of the graphene is brought towards amorphization [10].

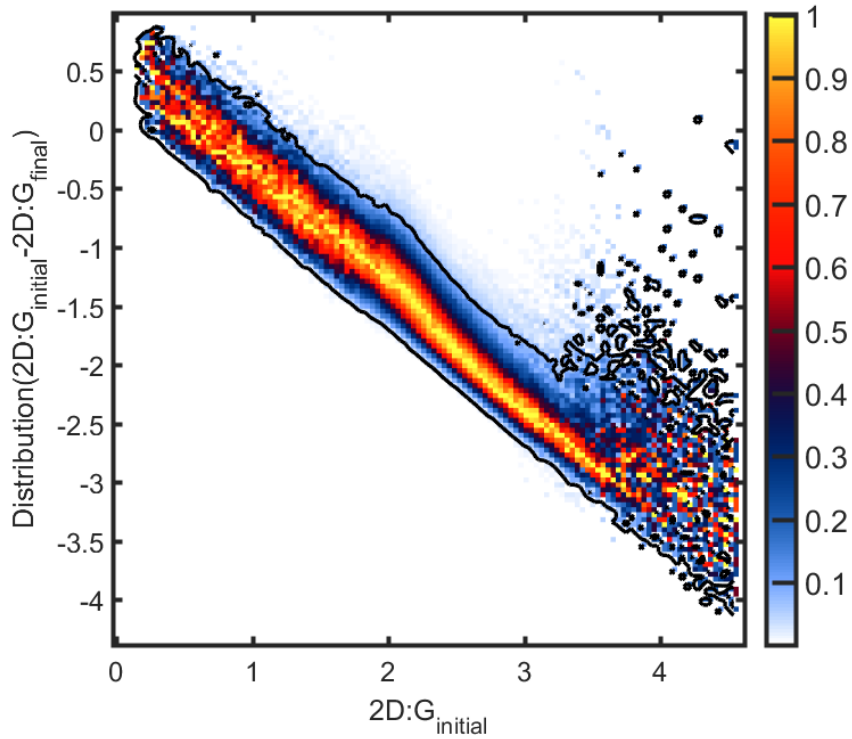


Fig.5 – Distribution of the variation of 2D:G ratio as a function of the initial 2D:G ratio. High quality graphene undergoes a larger decrease than what is seen in regions of low quality graphene.

The same kind of analysis is possible using the D:G ratio and D:2D ratio. D:G is widely used in the literature, but its value is susceptible to change with doping. In contrast, D:2D is independent of doping [15,16] and increases with disorder. Figure 6 presents the distribution of the variation of D:G ratio as a function of the initial D:G ratio. The distribution is much broader and the disparity between the variation of the D:G ratio for high quality (low initial D:G) and poor quality (high initial D:G) is much smaller. The same method is used for D:2D in Fig.7. A similar trend is observed. Initially, low-damaged graphene undergoes a stronger increase of the D:2D ratio. Both results support the fact that initially-damaged graphene regions can withstand higher plasma treatment. The distribution of the D:2D increase of initially low damaged graphene is much wider than the one of for the ratio D:G. Further works are needed to extract additional information from those distributions, which is outside the scope of this paper.

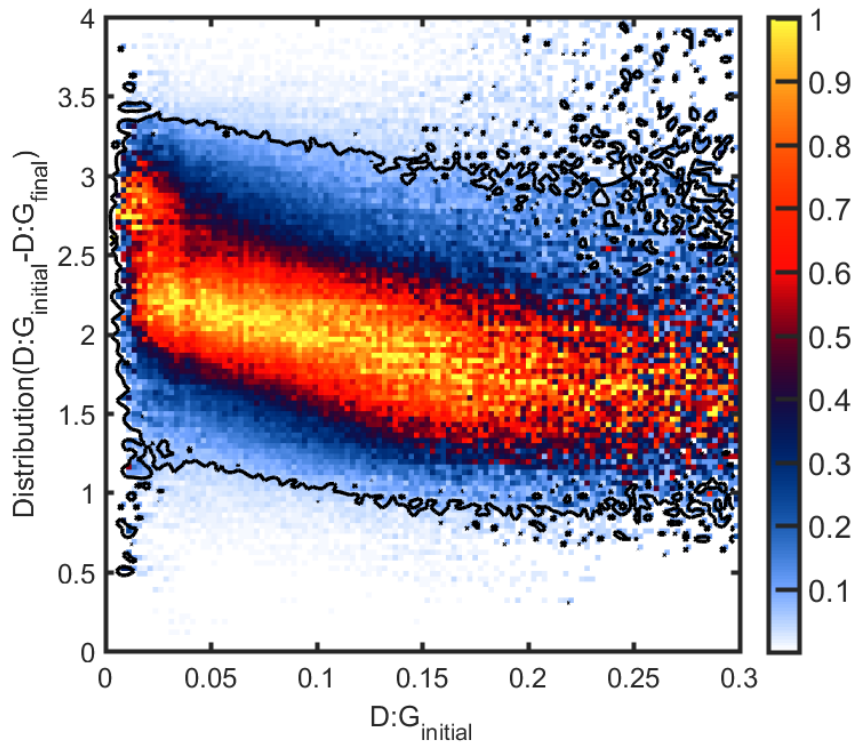


Fig.6 – Distribution of the variation of D:G ratio as a function of the initial D:G ratio. Higher quality graphene undergoes a larger increase of D:G values compared to lower quality graphene. The distribution of the D:G ratio is wider for initially larger D:G ratio

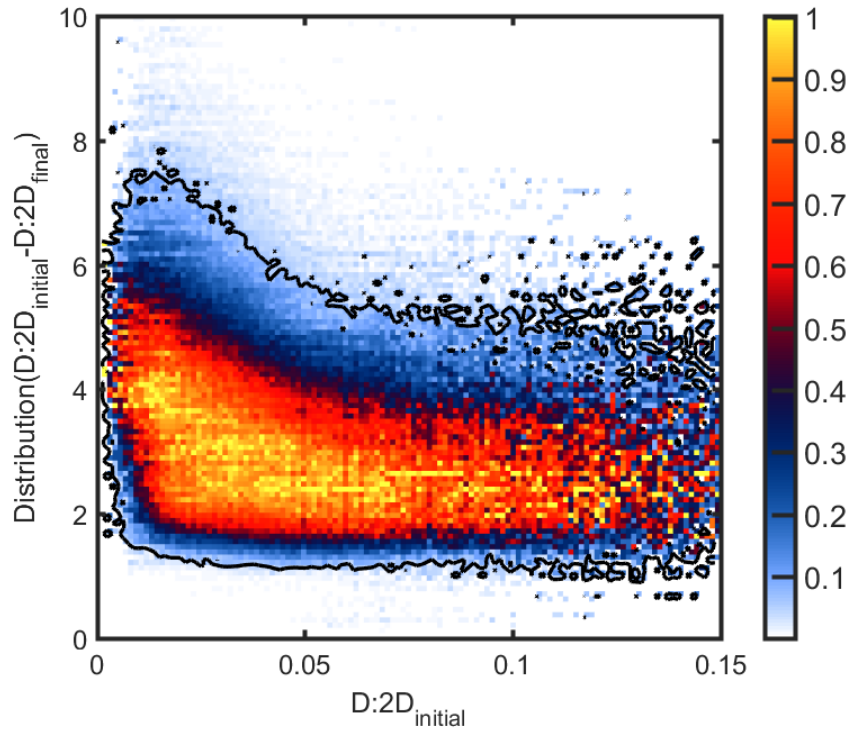


Fig. 7 – Distribution of the variation of D:2D ratio as a function of the initial D:2D ratio. Higher quality graphene undergoes a larger increase of D:2D values compared to lower quality graphene. The distribution of the D:2D ratio is wider for initially low D:2D ratio.

4. CONCLUSION

While the promises of Raman spectroscopy in the study of graphene properties are undeniable, the quantitative information it provides on damage, strain and doping remains local. By taking advantage of the high-throughput Hyperspectral Raman Imaging (RIMA) instrument recently highlighted in the literature [3], we have developed a refined method to characterize graphene on a macroscopic scale. Through careful baseline subtraction and noise filtering, high-quality distributions of band parameters became obtainable. With proper “stitching” of the Raman maps, the results show that the method adds several benefits to conventional Raman analysis by comparing registered information before and after structural or chemical modifications. Here, results with the method show how small heterogeneities (local defects, grain boundaries, etc.) in pristine graphene materials influence the outcomes of low-pressure plasma treatments. Graphene grain boundaries are clearly visible in the maps using the width of the 2D band for the

untreated sample. After low-energy ion irradiation in a low-pressure argon plasma, these linear domains become more distinct using maps of the D:G and 2D:G ratios. Further registration grants access to the distributions and indicates that the Raman spectra of initially-damaged graphene regions (boundaries) evolves more slowly than that of undamaged regions under plasma treatments. This new method is bound to evolve with the development of new tools capable of extracting meaningful information on graphene physics and chemistry.

5. ACKNOWLEDGMENTS

This work was financially supported by the National Science and Engineering Research Council (NSERC), PRIMA-Québec, Plasmionique inc., Photon Etc., the Canada Research Chair and the Fonds de Recherche du Québec – Nature et Technologies (FRQNT).

6. DATA AVAILABILITY

The data that support the findings of this study are available from the corresponding author upon reasonable request.

7. REFERENCES

- [1] A.C. Ferrari, D.M. Basko, *Nat. Nanotechnol.* 8 (2013) 235–246.
- [2] P. Vinchon, X. Glad, G. Robert-Bigras, A. Sarkissian, R. Martel, L. Stafford, *J. Vac. Sci. Technol. A* (2019).
- [3] E. Gaufrès, S. Marcet, V. Aymong, N.Y.W. Tang, A. Favron, F. Thouin, C. Allard, D. Rioux, N. Cottenye, M. Verhaegen, R. Martel, *J. Raman Spectrosc.* 49 (2018) 174–182.
- [4] A. Roberts, D. Cormode, C. Reynolds, T. Newhouse-Illige, B.J. LeRoy, A.S. Sandhu, *Appl. Phys. Lett.* 99 (2011) 051912.
- [5] F. Castells, P. Laguna, L. Sörnmo, A. Bollmann, J.M. Roig, *EURASIP J. Adv. Signal Process.* 2007 (2007) 074580.
- [6] E. De la Hoz, E. De La Hoz, A. Ortiz, J. Ortega, B. Prieto, *Neurocomputing* 164 (2015) 71–81.
- [7] S. Choubak, P.L. Levesque, E. Gaufres, M. Biron, P. Desjardins, R. Martel, *J. Phys. Chem. C* 118 (2014) 21532–21540.
- [8] L.G. Cançado, M. Gomes de Silva, E.H.M. Ferreira, F. Hof, *2D Mater.* 4 (2017) 025039.
- [9] T. Lee, F.A. Mas'ud, M.J. Kim, H. Rho, *Sci. Rep.* 7 (2017) 16681.
- [10] A. Eckmann, A. Felten, A. Mishchenko, L. Britnell, R. Krupke, K.S. Novoselov, C. Casiraghi, *Nano Lett.* 12 (2012) 3925–3930.
- [11] A. Eckmann, A. Felten, I. Verzhbitskiy, R. Davey, C. Casiraghi, *Phys. Rev. B* 88 (2013) 035426.
- [12] A. Sadezky, H. Muckenhuber, H. Grothe, R. Niessner, U. P??schl, *Carbon N. Y.* 43 (2005) 1731–1742.

- [13] Y.-B.B. Zhou, Z.-M.M. Liao, Y.-F.F. Wang, G.S. Duesberg, J. Xu, Q. Fu, X.-S.S. Wu, D.-P.P. Yu, *J. Chem. Phys.* 133 (2010) 234703.
- [14] J.E. Lee, G. Ahn, J. Shim, Y.S. Lee, S. Ryu, *Nat. Commun.* 3 (2012) 1024.
- [15] M. Bruna, A.K. Ott, M. Ijas, D. Yoon, U. Sassi, A.C. Ferrari, *ACS Nano* 8 (2014) 7432–7441.
- [16] A. Das, S. Pisana, B. Chakraborty, S. Piscanec, S.K. Saha, U. V Waghmare, K.S. Novoselov, H.R. Krishnamurthy, a K. Geim, A.C. Ferrari, A.K. Sood, *Nat. Nanotechnol.* 3 (2008) 210–215.
- [17] M.A. Bissett, W. Izumida, R. Saito, H. Ago, *ACS Nano* 6 (2012) 10229–10238.

8. Supplementary Data

Additional data on plasma treatment conditions, PCA-assisted data noise filtering, polynomial baseline subtraction, cube registration and excitation energy correction are provided in **Annexe 4** of this thesis.

3.3 Auto-réparation préférentielle des joints de grains

La **Section 3.2** révèle l'importance de considérer l'état initial de l'échantillon lors de l'analyse des traitements par plasma. En effet, les régions de plus haut désordre démontrent une "résistance" à la production de dommages additionnels par le plasma. Cette conclusion s'avère vraie lorsque l'on regarde l'état global de l'échantillon mais la méthode discutée ne permet toutefois pas de révéler le comportement de certaines régions de l'échantillon comportant un nombre de spectres beaucoup plus faible. C'est le cas notamment des joints de grains et de dommages ponctuels qui peuvent être présents dans les échantillons obtenus par CVD. Avant d'étudier les dynamiques de production de dommages dans la post-décharge en flux de plasmas micro-ondes dans l'azote à pression réduite, nous nous sommes intéressés aux dommages produits dans un environnement inerte des plasmas d'argon.

Les travaux discutés ici sont tirés de la série de mesures présentées dans l'article « PREFERENTIAL SELF-HEALING AT GRAIN BOUNDARIES IN PLASMA-TREATED GRAPHENE » publié dans *Nature Materials* en juillet 2020 [R91]; l'article intégral est fourni à l'**Annexe 3**.

La

Figure 21 présente différentes cartographies des paramètres de déconvolution Raman d'intérêt pour l'échantillon non traité ainsi que le même échantillon après 210 sec de traitement au plasma d'argon. Pour l'échantillon non traité, les joints de grains du graphène sont absents des cartographies des rapports D:G et D:2D. On devine la présence potentielle de bicouches et/ou de joints de grains par la présence de régions avec un ratio 2D:G plus faible. Le traitement par plasma confirme l'apparition des joints de grains qui présentent alors des ratios D:G et D:2D plus faibles caractéristiques de régions moins endommagées. À noter toutefois qu'il y a bel et bien désordre dans les domaines et les joints de grains (D:G et D:2D augmentent partout par rapport à l'échantillon non traité), mais l'augmentation est moins marquée aux joints de grains. Suivant la méthode proposée dans l'article de *Cancado et al.* [R92], on peut suivre l'évolution des dommages dans les domaines versus aux joints de grains (**Figure 22**).

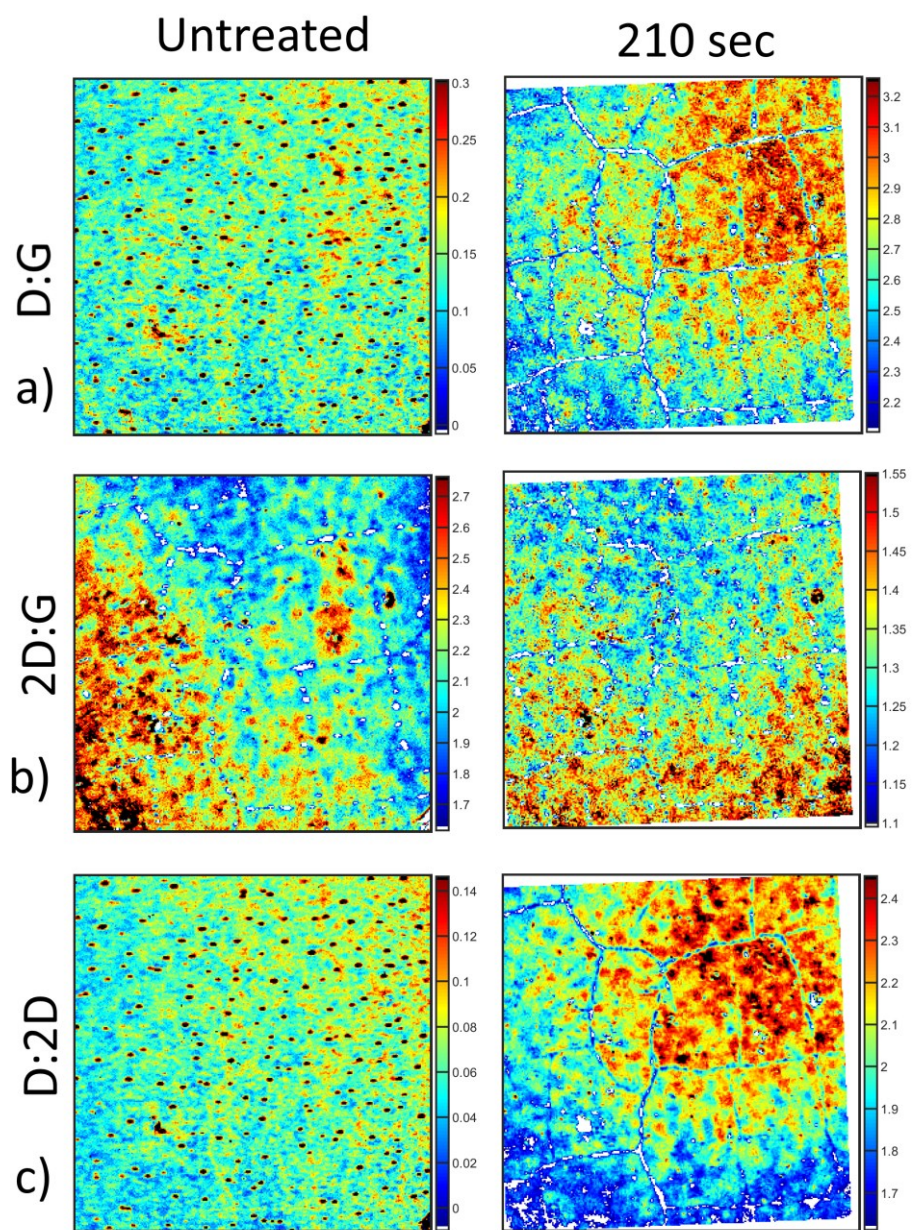


Figure 21 : Cartographie (a) D:G, (b) 2D :G, (c) D:2D pour l'échantillon non traité et le même échantillon après 210 secondes de traitement par plasma.

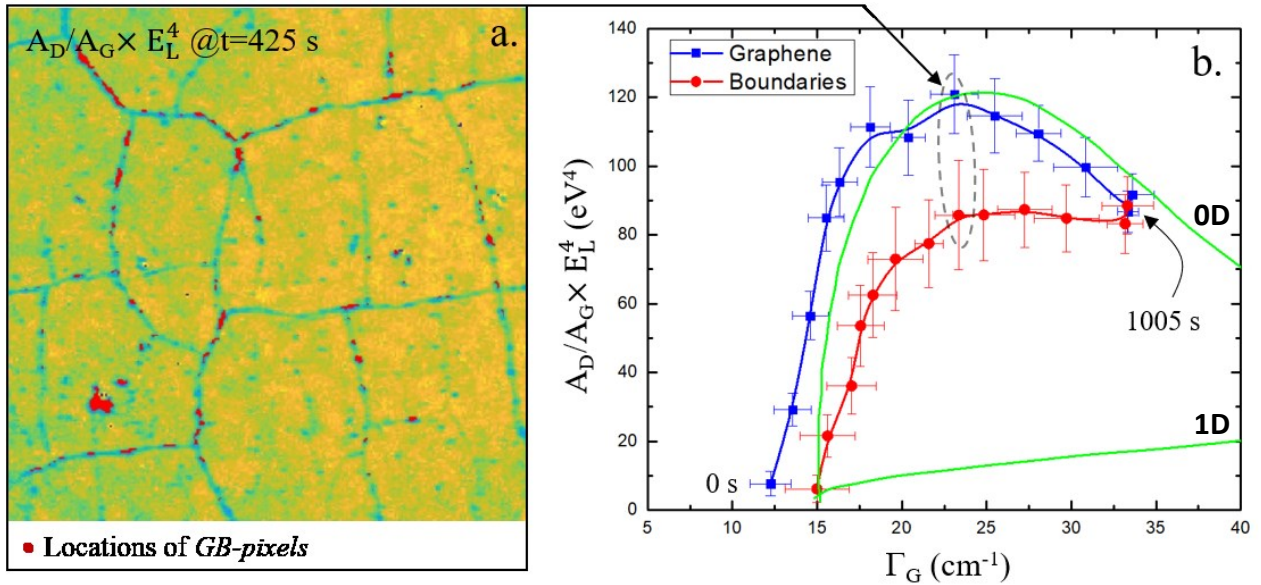


Figure 22 : (a) Localisation des spectres Raman identifiés comme des joints de grains sur la région sondée. (b) Évolution des dommages pour les domaines du graphène et les joints de grains. Les courbes vertes illustrent les variations attendues tel que décrites par le modèle développé par Cançado et al. pour les défauts purement 0D et 1D dans [R91]

Dans l'ensemble, on note un comportement propre aux joints de grains à s'opposer à la formation de dommages. Ceci peut à prime abord paraître contre-intuitif. En effet, ces régions sont typiquement caractérisées par des réactivités chimiques accrues et de plus faibles liaisons interatomiques responsables d'une diminution de l'énergie requise pour le déplacement des atomes et/ou l'éjection de matière. Ce comportement s'explique plutôt par une auto-réparation préférentielle des joints de grains dont les détails sont résumés à la **Figure 23**. Les énergies mises en jeu dans les traitements par plasma couverts dans l'article (11-13 eV) sont nettement sous le seuil typiquement nécessaire pour la formation de dommages dans le graphène (18-20 eV) [R93]. La formation de dommages par irradiation ionique à d'aussi faible énergie est encore sujet à investigation, mais serait favorisée par un apport d'énergie supplémentaire associé à la désexcitation en surface de niveaux excités et la recombinaison en surface des ions [R91]. En dépit des faibles valeurs d'énergie des ions, on obtiendrait aussi une concentration importante d'atomes de carbone et de lacunes. Grâce à leur plus faible énergie de migration (0.4 eV versus 1.5 eV [R93]), les adatomes de carbone sont en mesure de migrer plus facilement vers les joints

de grains. Une accumulation des atomes de carbone aux joints de grain a lieu dû à la migration préférentielle le long de ceux-ci [R87,94]. Par un mécanisme similaire à celui observé dans les matériaux 3D, l'émission d'adatomes des joints de grains peut ensuite réparer des défauts à proximité. Il en résulte une baisse apparente des dommages sondés aux alentours des joints de grains, ce qui est cohérent avec les mesures expérimentales.

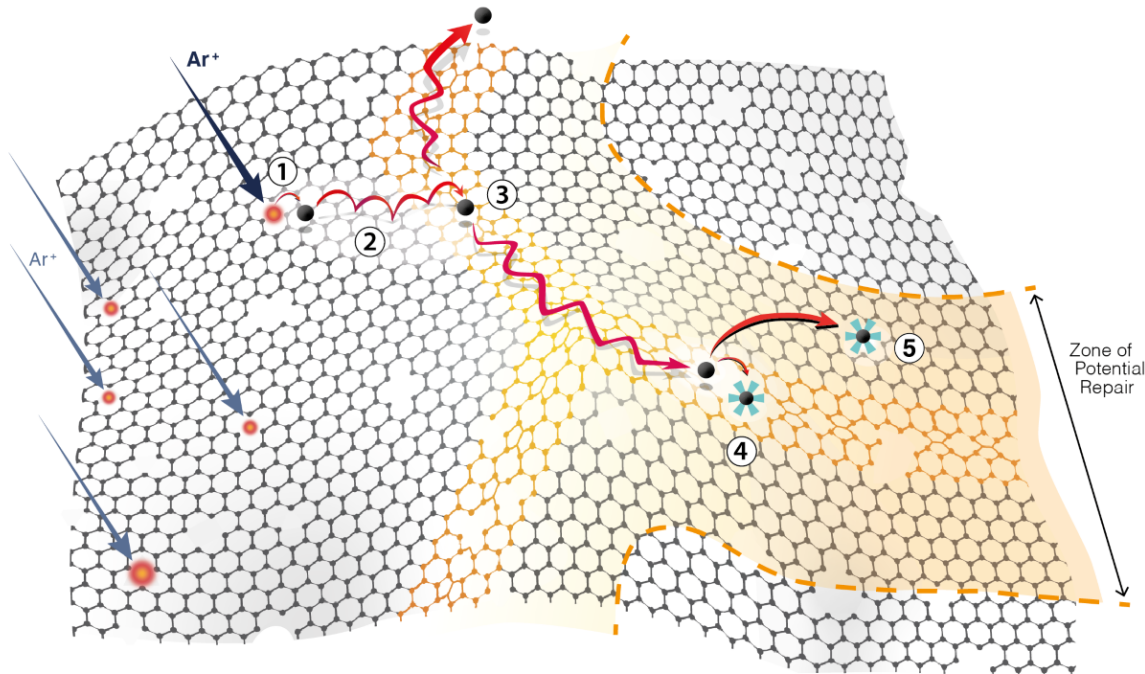


Figure 23 : Schéma de l'auto-réparation préférentielle des joints de grains.: (1) Formation d'adatomes de carbone et de lacunes; (2) Migration des adatomes en surface; (3) Transport anisotrope le long des joints de grains; (4) Réparation de défauts aux joints de grains; (5) Émission de carbone et réparation des défauts à proximité des joints de grains. [R91]

3.4 Incorporation sélective d'azote

Selective nitrogen doping of graphene domains due to preferential healing of plasma-generated defects near grain boundaries

G. Robert Bigras¹, X. Glad¹, P. Vinchon¹, R. Martel², L. Stafford¹

¹Département de Physique, Université de Montréal, Montréal, Québec, CANADA.

²Département de Chimie, Université de Montréal, Montréal, Québec, CANADA.

Abstract

Hyperspectral Raman IMAGING (RIMA) is used to study spatially-inhomogeneous polycrystalline monolayer graphene films grown by chemical vapor deposition. Based on Principal Component Analysis (PCA) clustering, distinct regions are differentiated and probed after subsequent exposures to the late afterglow of a microwave nitrogen plasma at a reduced pressure of 6 Torr (800 Pa). The 90×90 μm² RIMA mapping shows differentiation between graphene domains (GDs), grain boundaries (GBs), as well as contaminants adsorbed over and under the graphene layer. Through an analysis of few relevant band parameters, the mapping further provides a statistical assessment of damage, strain and doping levels in plasma-treated graphene. It is found that GBs exhibit lower levels of damage and N-incorporation than GDs. The selectivity at GBs is ascribed to (i) a low migration barrier of C-adatoms compared to N-adatoms and vacancies and (ii) an anisotropic transport of C-adatoms along GBs, which enhances adatom-vacancy recombination at GBs. This preferential self-healing at GBs of plasma-induced damage ensures a selective incorporation of N-dopants at plasma-generated defect sites within GDs. This surprising selectivity vanishes, however, as the graphene approaches an amorphous state.

1. Introduction

Numerous industrial applications of graphene rely on large-area synthesis, which is commonly achieved by chemical vapour deposition (CVD) [1]. This method leads to the formation of numerous grain boundaries (GBs) between graphene domains (GDs). The former have been extensively studied since they are extremely different from GDs with respect to their electronic

[2–4], mechanical [5], magnetic [6] and chemical [7,8] properties. GBs also have shown both etching enhancement [9,10] or self-healing [11] depending on the irradiation conditions. The understanding of extended defect topology [12] at GBs is limited and quickly vanishes when various growth condition are considered during irradiation of graphene. [13,14]. As pointed out by Malola et al. [7]: “Grain boundaries [...] are like snowflakes—there is no flake like another”; this clearly highlights their inherent complexity due to a sheer number of different possible GB configurations, each exhibiting its own intrinsic properties [7,15–17]. This thus makes difficult the study of damage formation by ion or plasma irradiation of polycrystalline graphene films in presence of GBs.

Recently, new advances in a non-intrusive spectroscopic technique called hyperspectral Raman imaging (RIMATM – Photon ETC.) has been applied to study the inhomogeneity of plasma-induced disorders in the graphene lattice [18,19]. This method has been able to detect strong areal differences in polycrystalline monolayer graphene samples grown by CVD that were supposedly highly uniform. Being able to study spatial discrepancies is fundamental since it is well-known that functionalization of graphene differs according to local defects initially present in the pristine lattice, be it GBs, dislocations or impurities such as PMMA residues.

Inspired by reference [18], the present study capitalizes on RIMA capacities to examine the respective Raman signatures of GDs and GBs following the exposure of polycrystalline monolayer graphene to the late-afterglow of a microwave nitrogen plasma at reduced pressure. More precisely, a method based on Principal Component Analysis (PCA) filtering of hyperspectral Raman mappings [19] is developed and used to analyze behaviors observed in different regions of the CVD-grown graphene samples. The method is able to differentiate clusters that present instances of similar Raman signature. Thus, it can probe the late-afterglow nitrogen plasma treatment effect on these regions [20,21]. Coupled with X-ray photoelectron spectroscopy, the doping level of the plasma-treated sample is assessed. By monitoring local variations in the initial pristine state and in the resulting plasma-treated state of the same graphene film, the study sheds light on dynamical behaviors of N and C adatoms during plasma treatment. Using recent literature, this analysis brings a deeper understanding of a doping selectivity in nitrogen plasma treatments.

2. Experimental Setup

Graphene samples (grown on copper foil by CVD [22] and then transferred on SiO₂/Si substrates using a standard PMMA procedure [23]) were exposed to the late-afterglow region of a reduced-pressure plasma sustained by microwave electromagnetic fields [20,21]. A schematic of the plasma reactor is presented in **Supplementary information S-I**. In this study, the sample undergoes subsequent plasma treatment steps between which the sample is probed over a 90 x 90 μm² area using a Raman Imager (RIMA™) from Photon ETC [19]. The spatial resolution of Raman measurements is 390 nm. The RIMA allows the acquisition of a high number of spectra (here 116 281) from which parameters of the different bands are extracted. The G (\sim 1580 cm⁻¹) and 2D (\sim 2700 cm⁻¹) bands are prominent features of the untreated sample, while the D (\sim 1350 cm⁻¹) and D' (\sim 1600 cm⁻¹) bands rise with the generation of plasma-induced disorders [24]. Typical RIMA measurements as well as examples of data preparation and processing are presented in **Supplementary information S-II** and **Supplementary information S-III**, respectively.

In order to highlight the differences between the regions probed inside the selected area of polycrystalline monolayer graphene films, a new processing method was developed. All spectra from the Raman map are first centered using their mean values and normalized according to their standard deviations. Principal component analysis (PCA) is performed using all spectral values as dimensions and after subtraction of the mean values of the spectra. The first 30 components are then separated into 10 clusters using Gaussian unmixing. The number of clusters is arbitrary and is taken high enough to make sure that most distinguishable regions over the polycrystalline monolayer graphene films are separated into different clusters. The number of components taken for noise filtering is typically lower than 30 [18] and thus the number of considered PCA components is high enough to ensure adequate distinction of the relevant areas. Since the number of components is arbitrary, some clusters are combined by comparing various band parameters (mainly D over G band intensity ratio as well as width and position of the G band). This allows for the definition of final clusters that highlight regions of distinct Raman signatures.

To investigate the evolution of each cluster as the plasma treatment steps are performed, an image registration (allowing only translation and rotation) is carried out to align every plasma-

treated measurement relative to the initial region of the untreated graphene sample. This enables a precise study of the evolution of different graphene areas as a function of their initial pristine state (grain boundary, local defects, contaminants, etc.) [18].

Scanning electron microscopy (SEM) is carried out after the last plasma treatment to assess the topographical state of the different clusters over the polycrystalline monolayer graphene film. We deliberately chose not to use SEM in between the different steps of plasma irradiation due to the possible electron beam-induced contamination effects [25]. Moreover, the increasingly damaged state of the film after plasma treatment might cause important surface charging effects as the sample gets more amorphous and thus perturbs subsequent Raman analysis. The SEM analysis was performed using a JEOL JSM-7600F in secondary emission mode at 3.0 kV; this allows for a good spatial resolution while ensuring a relatively small electron penetration depth.

Finally, X-Ray photoelectron spectroscopy (XPS) is performed to assess the doping level of the polycrystalline monolayer graphene films. The setup is a Thermo Scientific K-Alpha (CAE detector, 180° double focusing hemispherical analyzer, 128 channel detector) operating with pass energies of 200 eV and 50 eV for survey and high-resolution scans, respectively. The step energy is 1 eV for the surveys and 0.1 eV for the high-resolution spectra. A flood gun is used to ensure minimal shifts due to charging. The spot size of 400 microns is centered on the area probed by the RIMA system.

3. Results

Figure 1a,c presents SEM images at different magnifications over specific regions of the graphene sample after the final plasma treatment. The clusters identified by PCA analysis over the same regions are shown in **Figure 1b,d**. We notice the dominance of the green cluster (72%) matching the graphene domains (GDs). The red (2%) and black (7%) clusters appear to be prevalent at linear defects, seemingly grain boundaries (GBs) and defects in their vicinity. Magenta (5%) and blue (15%) regions are mostly local defective graphene spots (GSs) at the center of the graphene domains. Such comparison thus demonstrates the capability of Raman spectroscopy with RIMA when coupled with a clustering method to highlight the local variation of supposedly uniform monolayer graphene films. Since some of the GSs appear to be undistinguishable from GDs in the

SEM images, the clustering technique permits not only to reveal these defective regions, but also allows their detailed characterization before and after plasma irradiation. Similar features can be seen by optical imaging over the whole area probed by RIMA analysis. In order to avoid content duplication, the results are presented in **Supplementary information S-IV**.

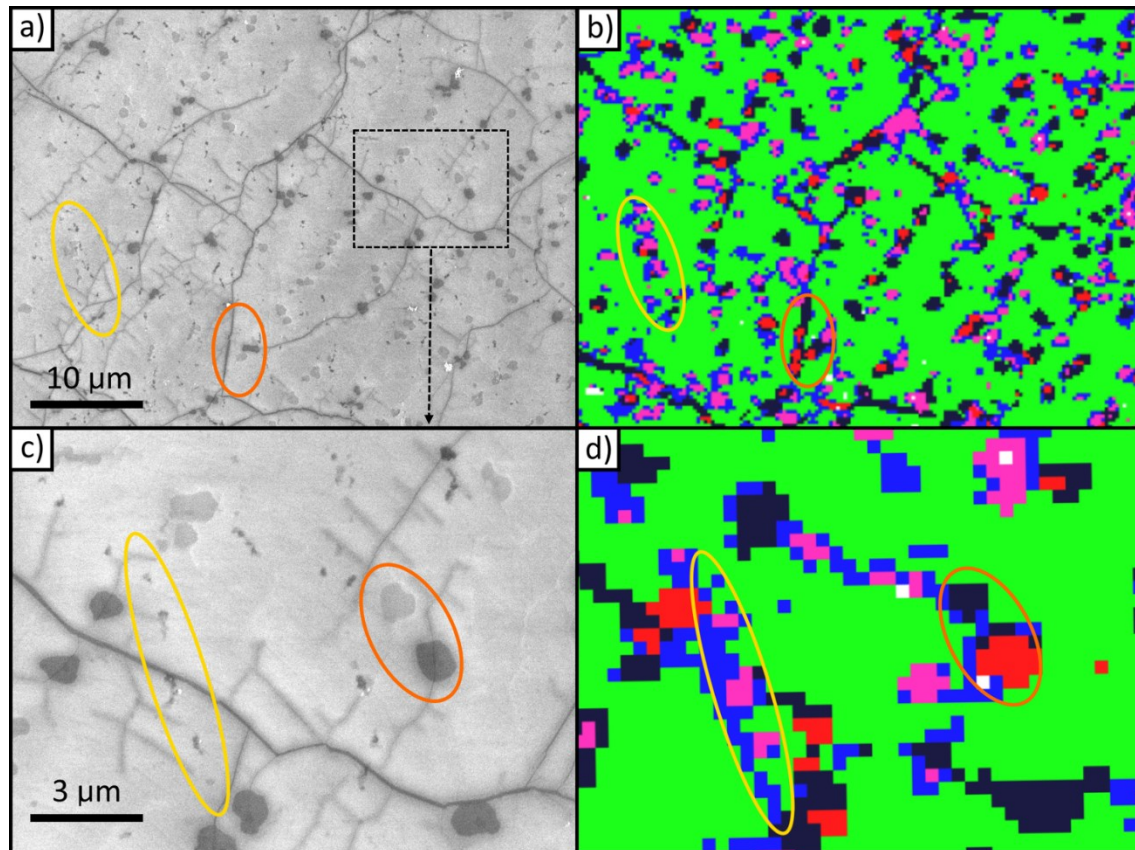


Figure 1. (a,c) SEM images of the zone analyzed by Hyperspectral Raman (b,d) after the last treatment step. Clusters are colored similarly as in the optical images of **Figure S1** presented in supplementary data. Surface contaminants (yellow circles) are linked to the GSs (blue and purple clusters). GBs and defect spots (orange circle) are a good match with the red and black clusters.

SEM images presented in **Figures 1a-d** reveal several topographical features often coinciding with the Raman mapping, in particular the presence of darker lines linked to the boundaries of the various growth domains in polycrystalline graphene films. These lines linked to GBs can also be seen in the comparison between optical image and RIMA cluster mapping presented in **Supplementary information S-IV**. Note that, due to the width discrepancy between the Raman

pixels ($390\text{ nm} \times 390\text{ nm}$) and the GBs (typically 2-3 nm wide [26]), details seen with SEM (electron beam diameter $\sim 1\text{ nm}$) may not always be observed in the Raman mapping. Another interesting feature of the SEM images displayed in **Figure 1a,c** is the presence of darker circular areas (circled in orange) throughout the whole graphene surface. Typically organized following straight lines, these have a consistent size of about $1\text{ }\mu\text{m}$ in diameter. They also exist in two distinct shades: dark or light gray. As can be seen in **Figure 1c**, these regions tend to be crossed by crack-like fractal linear defects emanating from GBs. While they resemble holes in SEM images, their Raman signature (red and black clusters, see all details below) is similar to GBs. These circular features were also examined by Energy-Dispersive X-ray Spectroscopy; the results are shown in **Supplementary information S-V**. On these darker circular areas, a rise of carbon by about a factor of two with respect to GDs was observed. No significant change of the other elements was seen. This indicates that these dark and light gray spots represent bilayer graphene domains.

Another distinct feature is the presence of numerous isolated dots (highlighted in a yellow circle) spread in a rather uniform way throughout the graphene surface. Considering the surface sensitivity of SEM at 3 kV acceleration voltage (electron penetration depth of about 150 nm in SiO_2 [27]), this could correspond to contaminants introduced either during the growth by CVD and/or through transfer process of the graphene sample onto SiO_2/Si substrate. Most likely, these dots are mostly contaminants commonly seen in CVD-graphene grown on copper in quartz furnace due to a devitrification of the quartz tube [28]. When untreated, these carbon-coated SiOx -based particles appear as small white dots uniformly spread on the untreated surface of the graphene. This aspect was confirmed by Energy-Dispersive X-ray Spectroscopy; the results are also shown in **Supplementary information S-V**. After plasma treatments and laser exposure (from Raman imaging) of the region of the monolayer graphene film that becomes increasingly amorphous, we noted a change in the morphology of these contaminants (white dots become darker). Graphene surrounding these defects should exhibit modified strain and/or doping, which signals are different in Raman with respect to GDs. Here, these contaminants are linked to the GSs component of the Raman mapping (blue and magenta clusters).

To easily assess relevant properties of CVD-grown graphene films before and after plasma treatment, Raman band parameters can be plotted using normalized 2-D histograms such as in

Figure 2a. A maximum count normalization is made and the observed contours are set at 10% of the maximum for each cluster. This allows to easily highlight how the properties of the graphene differ from a region to another. The red and black clusters present lower G band frequency (ω_G) and higher compressive strain (i.e. higher 2D frequency; ω_{2D}) than the green regions. This is typical of CVD-grown GBs [29] and strengthens the aforementioned observation deduced from **Figure 1**. The GSs (blue and magenta clusters) and GDs (green) present similar ω_G and ω_{2D} behaviors with a tail at slightly lower values for the former. However, multiple factors can influence band frequency, including doping [30] and/or damage [31]. As discussed below, further investigation is required to identify the nature of these clusters. For comparison purpose, **Figure 2b** presents a similar 2-D histogram for the full region probed without any cluster differentiation (standard method). In such case, the data does not permit the study of low-count regions. While Raman mappings could help distinguish two regions for a given peak parameter, it cannot do so without parametrization along two different band parameters. Mean values of Raman band parameters for each cluster are provided in **Supplementary information S-VI**.

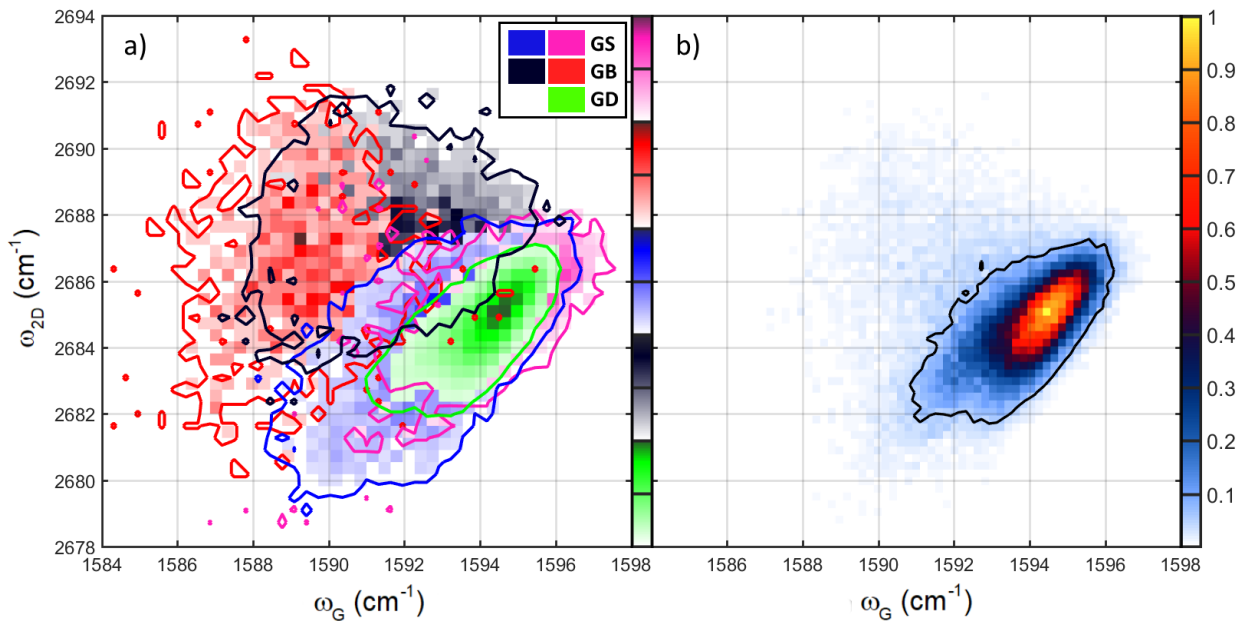


Figure 2. a) Frequency of the 2D band as a function of the frequency of the G band for pristine graphene. Each cluster is depicted as a 2-D normalized histogram. b) Same data as in a, but plotted without cluster differentiation.

A well-established method of characterization of damage generation and damage type in graphene is to plot the ratio of the area of the D and G bands ($A_D:A_G$) as a function of the bandwidth of the G band (Γ_G) [32]. **Figure 3** presents such analysis for different successive plasma treatment times of the same graphene sample: $t = 0$ (a), 60 s (b), 120 s = 2×60 s (c), 180 s = 3×60 s (d) and 240 s = 4×60 s (e). The top orange curve is related to pure 0D defect generation (point defects) while the bottom one corresponds to pure 1D defect generation (line defects and reduction of the crystallite sizes) [32]. Due to the change in the coverage ratio of structurally-damaged area and activated area, both damage generation pattern (0D or 1D) reveal different Raman signal evolution as the disorder increases. For 0D defects, a sharp rise is followed by a decrease of $A_D:A_G$ as a function of Γ_G as structurally-damaged areas start covering activated areas of nearby defects. This occurs for low inter-defect distances (LD). The 1D defects show a slower and monotonous increase of $A_D:A_G$ as a function of Γ_G as the size of nonacristaline (La) domains decreases.

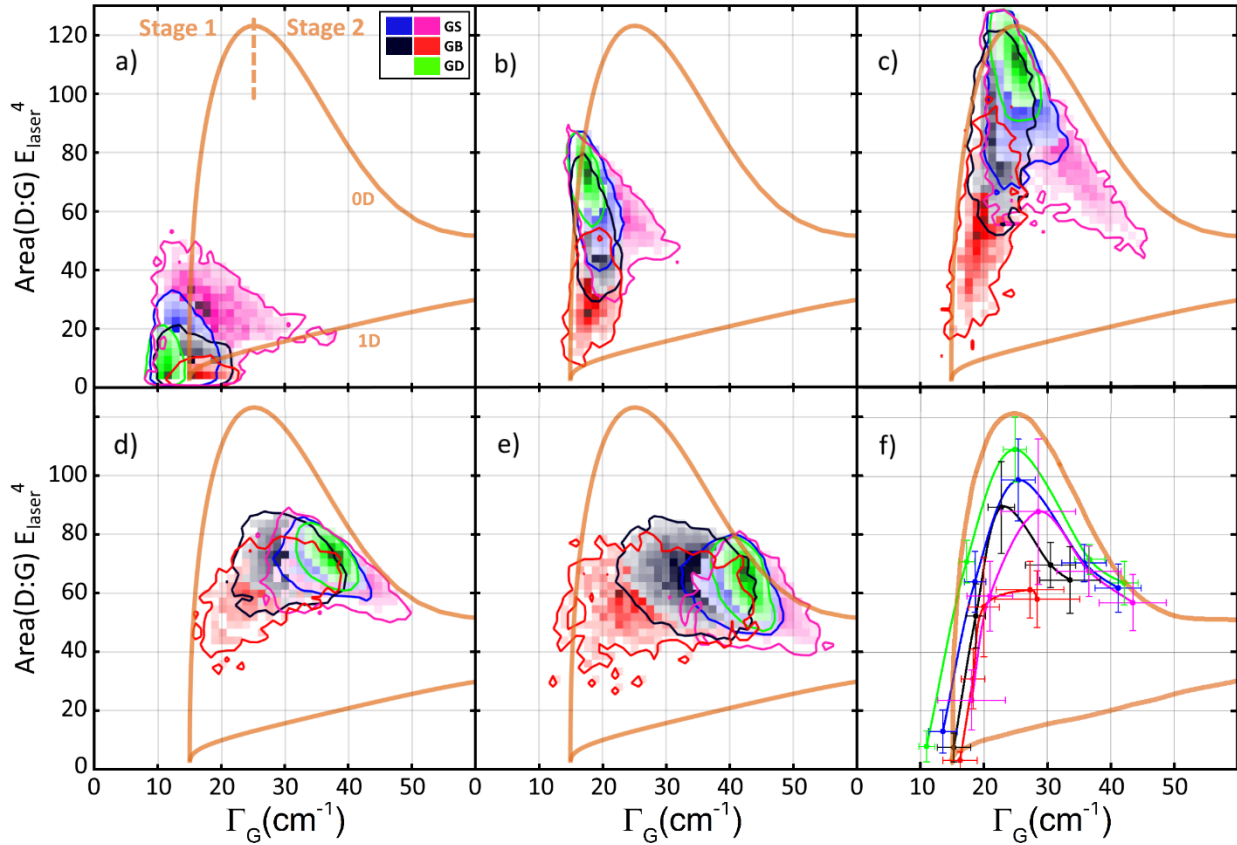


Figure 3. Areal ratio of the D over G bands corrected by laser energy as a function of line width of G for $t = 0$ (a), 60 (b), 120 (c), 180 (d) and 240 s (e) of subsequent treatment times on the same zone of the same sample. Top and bottom orange solid lines represent the OD and 1D type defect generation trajectories, respectively. Average values and error margins for all clusters and all treatment times are shown in (f). Colored lines in (f) are guides to the eye.

In Figure 3a, it can be seen that the GDs (green) of the untreated graphene sample present a very narrow distribution at low Γ_G and $A_D:A_G$, whereas GBs (red and black) show much larger Γ_G while keeping a low $A_D:A_G$. The GS (magenta and blue) data exhibit a rather large $A_D:A_G$ ratio with a rather high and broadly-distributed Γ_G . After the first plasma treatment, Figure 3b reveals a strong increase of $A_D:A_G$ for the GDs, while Γ_G is rather constant. This corresponds to a strong OD damage generation to reach about halfway of the OD-type defect curve. Regarding the GSs, they show a lower $A_D:A_G$ with a slightly higher Γ_G . Most notably, the GBs seem to present a strong sturdiness to the plasma treatment as the AD:AG values of the red and black clusters are much lower than the ones of the GDs. This conclusion cannot necessarily be extrapolated to any type of sample as

growth condition can alter the properties of GBs [12]. Since each pixel probes an area far greater than the actual width of GBs ($390 \times 390 \text{ nm}^2$ versus about 2-3 nm [26]), the black and red clusters correspond to areas containing various densities and/or types of GBs [7].

After two subsequent 60-s treatments (**Figure 3c**), the $A_D:A_G$ ratio from GDs reaches the maximum of the empirical 0D defect generation curve ($y \sim 110 \text{ eV}^4$, $x \sim 25 \text{ cm}^{-1}$). At this point, the sample has reached the end of the first stage of damage generation (stage 1 [31–33]). Further damage progressively causes the amorphization of the graphene (stage 2 [31–33]), which is characterized by global disorder with increasing amount of sp^3 C-C bonds. At the end of stage 1, GBs still show good resistance to the plasma-induced damage, exhibiting both smaller values of Γ_G and $A_D:A_G$ ratios. The last two plasma treatments (**Figure 3d** and **Figure 3e**) reveal very similar results. As the sample is brought closer to an amorphous state, additional plasma treatments have seemingly less effect on the Raman band parameters [31,33]. The GDs and GSs show similar signal even though a slight decrease in their $A_D:A_G$ ratios and an increase in their Γ_G (up to 45 cm^{-1}) are observed. On the other hand, GBs show a lower increase in their Γ_G , which is particularly noticeable in the red cluster data.

Figure 3f presents a summary of the clusters' damage generation over all the treatment steps where the mean value for each step and cluster type is plotted (error bars correspond to the standard deviation). The maximum $A_D:A_G$ value for GBs is much lower than for GDs, whose damaging behavior is close to the empirical 0D damage generation curve (top green curve). This highlights the differences in the damage generation: for GBs, a change in both crystalline sizes (La) and inter-defect length (LD) is present, while GDs essentially see a change in LD [32].

The assessment of damage with the D:G band ratio for monolayer graphene can be misleading due to its simultaneous dependence on charge carrier density. Indeed, values derived from D:G plots decrease for increasing doping (both positive or negative) [34,35]. In contrast to the D:G ratio, the D:2D ratio steadily increases with rising lattice disorder [36], and its value remains independent upon increasing strain and doping [35,37]. This explains the recent use of this marker in damage assessment studies in graphene. In this work, the band ratio D:2D is therefore used as a direct indicator of the disordered state of the graphene lattice. Furthermore, the 2D:G ratio is

known to be very sensitive to perturbation of the pristine graphene lattice; its value sharply decreases with increasing disorders of any types [38,39], including GBs [40]. The 2D:G ratio also decreases for bi- and multi-layer graphene [41]. While 2D:G is also known to be influenced by the doping level [35], this ratio (unlike D:G) decreases monotonously with increasing damage and thus facilitates the interpretation of the results. In this framework, **Figure 4** presents the evolution of the 2D:G ratio as a function of the corresponding D:2D ratio.

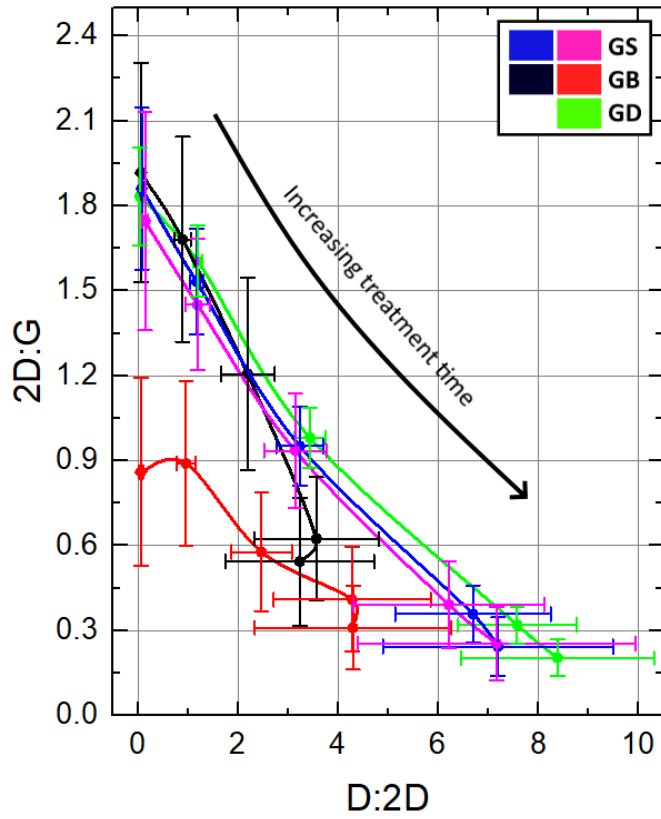


Figure 4. 2D:G as a function of D:2D for each cluster and different total treatment times. Each point is set at the mean value of its respective cluster data with an error bar corresponding to a standard deviation.

As can be seen in **Figure 4**, almost all clusters present large 2D:G for the untreated sample. This implies growth of good quality graphene. As expected, a decrease of 2D:G of similar amplitude is found all over the sample after the plasma treatment, but the increase in D:2D is larger for clusters linked to GD and GS regions. This difference of behavior hints towards inhomogeneities in the

variation of strain and or doping. Thus GBs seems to undergo a much less aggressive disorder generation: the increase of D:2D from GB-related spectra is two times lower than the one of GDs. Regarding 2D:G, each cluster presents a sharp drop with increasing plasma treatment time with black and red clusters linked to GBs experiencing lower decreases.

The band frequency variations of G (ω_G) and 2D (ω_{2D}) can provide significant insights on the doping and strain levels of the graphene film. Indeed, the 2D band shows a large shift with change in lattice strain while its counterpart varies strongly with the graphene doping level [30,35]. However, the method as proposed by *Lee et al.* for separating strain and doping [30] does not necessarily translates to damaged samples such as those investigated here since ω_G is also related to defect density for amorphous, nanostructured and diamond-like carbon sp² materials [31]. Based on the work of *Bruna et al.* [35], it is possible, however, to extract the behavior of ω_G and ω_{2D} as a function of charge carrier density for damaged graphene (**Supplementary information S-VII**). The linear behavior of ω_{2D} and ω_G highlighted by *Lee et al.* [30] is lost for p-doped damaged graphene. A complete characterization of the band frequency shifts would therefore be required to decouple strain from doping for graphene undergoing increasing disorder. In the current work, the correlation extracted from *Bruna et al.* [35] is used instead since plasma-induced disorder is relatively important. In such conditions, for n-doped graphene, ω_{2D} becomes proportional to ω_G (**Supplementary information S-VII**). Since we expect the nitrogen plasma to induce n-type doping, this modified method is better adapted, as discussed below. Moreover, *Bisset et al.* [29] revealed the importance of the crystallinity of the sample in the analysis of the ω_G and ω_{2D} variations in response to strain. Indeed, highly polycrystalline CVD-grown samples (crystallite size $L_a \sim 1 \mu\text{m}$) show an increase of ω_G for compressive strain at GBs, as opposed to the decrease observed in exfoliated graphene ($L_a \sim 20 \mu\text{m}$). Since their laser beam diameters are of the order of the CVD-grown graphene domain size, this implies that the x-scale proposed by Lee et al. should be reversed for GB-related data, i.e. for red and black clusters.

In line with these studies, **Figure 5a** presents the variation of ω_{2D} and ω_G mean values for all the regions and between the subsequent plasma treatment steps. For ω_G , all regions initially show a small redshift followed by a large blueshift. For ω_{2D} , two distinct behaviors are observed: GBs

show a monotonous increase while all other regions undergo a redshift followed by a large blueshift. **Figure 5b-c** present the change in doping and strain of each cluster as a function of the plasma treatment time. Such values are obtained by projecting the values of **Figure 5a** along the charge carrier density axis introduced by *Bruna et al.* [35] and the strain axis introduced by *Bissett et al.* [29]. Only the shifts of the mean values are considered (to best distinguish the clusters) and the error bars result from the propagation of the errors of the linear fits performed on the relation between strain or charge carrier concentration on Raman band positions (as extracted from the literature [30,34,35]). In order for any discussion about variations in doping and strain to be relevant, one must first remove the expected effect of damage generation for these conditions. As demonstrated by *Eckmann et al.* [42], no clear change in ω_G and ω_{2D} should be observed for damaged graphene before the amorphization stage. Entering stage 2 of the amorphization trajectory, the 2D and G bands show large redshifts and blueshifts, respectively. In addition, the effect is much stronger for the 2D band and thus the projection may bias the calculation of the strain from **Figure 5b**, but only for the last two treatments and for the heavily-damaged clusters (GDs and GSs).

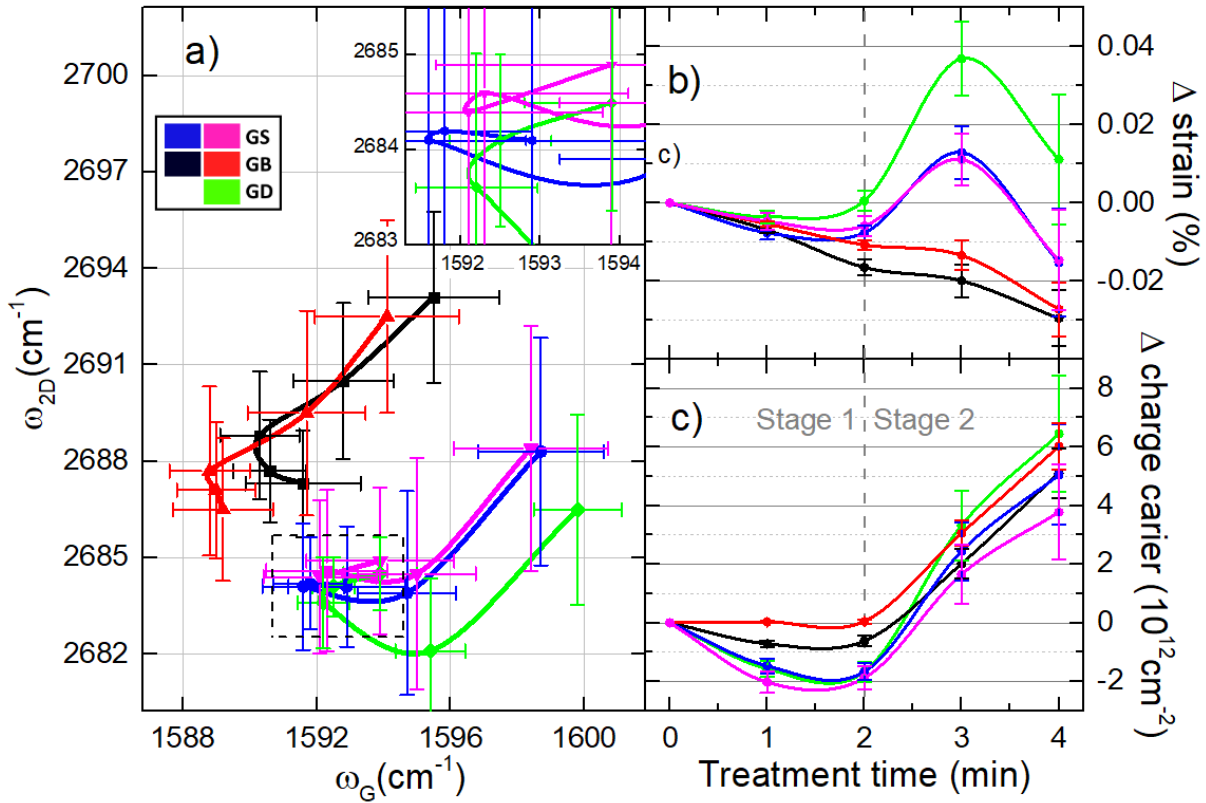


Figure 5. a) 2D band frequency as a function of G band frequency for all clusters and plasma treatment steps. Each point is set at the mean value of its respective cluster, the standard deviation is taken as the error bar and lines are guides to the eye only. Relative variation in strain (b) and charge carrier density (c) for each cluster with respect to their pristine state as a function of treatment time. Error bars for (b-c) show the propagation error of the linear fits (doping and strain) and their projections along the axes defined by Lee et al. [30] (corrected for GB clusters).

Based on this analysis, the strain and doping behaviors presented in **Figure 5b** and **Figure 5c** reveal two distinct regimes. The first stage corresponds to a transition from graphene to nanocrystalline graphene (stage 1) and the second to the transition towards amorphous carbon (stage 2) [31,33,42]. The same transition was highlighted in **Figure 3** (transition towards amorphous carbon is responsible for a decrease of D:G at high disorder levels [32]). More specifically, the first three graphene states along the amorphization trajectory (plasma treatment times: 0, 1 and 2 min) fall into stage 1, in which doping and strain behaviors differ among the different clusters. Most

noticeably, the doping of GBs remains constant, while the concentration of charge carriers decreases for the other regions of the sample. This feature provides a first hint of a more selective nitrogen incorporation at GDs (a so-called segregation of nitrogen dopants at GDs [43]). In addition, since both p- and n-type dopings increase ω_{2D} and ω_G , a decrease along the axis used for the so-called strain-doping decoupling is related to either a decrease of p- or n-type doping. In **Figure 5c**, this doping reduction for GDs and GSs reaches a maximum between 1 and 2 min of plasma treatment. It is usually expected that untreated graphene films grown by CVD show impurity-based (unintentional) p-type doping [44,45]. Therefore, it can readily be expected that such initial p-type doping first disappears before n-type doping from nitrogen incorporation can appear.

As for the strain evolution during stage 1, it can be seen in **Figure 5b** that all clusters sustain a compressive strain with GBs suffering most of that strain. It is worth mentioning that nitrogen incorporation is expected to induce a mild compressive strain to the graphene due to its inferior bond length (C-C: 1.42 Å versus C-N: 1.37 Å [46]). Thus, a doping-related strain is expected to be relatively small for low to medium nitrogen incorporation levels [47]. Therefore, the strain features observed in **Figure 5b** are most likely due to plasma-induced disorder than to plasma-induced doping in monolayer graphene films.

As discussed above, during the transition towards amorphization (stage 2), ω_{2D} and ω_G are expected to redshift and blueshift, respectively [42]. This effect is not considered for the optical separation of strain and doping as it would require criteria to access the transition towards amorphization. As detailed previously and according to [11,35], D:2D is independent of doping, and thus it represents an ideal candidate to discuss qualitatively the effects of an increase of damage on the expected change of the calculated strain (*Lee et al.*'s model [30]). According to *Eckmann et al.* [42], a rise in lattice disorder (in stage 2) leads to a decrease of ω_{2D} and an increase of ω_G with a slope of around $\Delta\omega_{2D}/\Delta\omega_G \sim -1.5$. This would translate in an overall rise of tensile strain (see *Figure 3b* of [30]), which is consistent with the presence of defects (such as vacancies) allowing strain relaxation. In our case, **Figure 5b** does reveal a rise in tensile strain prior to the amorphization between $t = 1$ and 3 min. In addition, such increase is not present for the GB-derived clusters (red and black): only a reduction of the decreasing slope is observed. This may

be explained by their lower degree of disorder (lower D:2D ratios, **Figure 4**), allowing for less strain relaxation than GDs and GSs. Moreover, such increase of compressive strain might arise due to numerous adatom incorporations leading to inverse Stone-Wales defects [48]. As for the doping in stage 2, it can be seen that the estimated doping level for all clusters follows a similar rise. This rather spatially-uniform change in doping over the entire graphene surface is linked to the transition towards amorphization. More details are provided below.

X-Ray Photoelectron spectroscopy (XPS) is performed to further support the incorporation dynamics of nitrogen atoms extracted from the decoupling of strain and doping. For each plasma treatment step, XPS is used to extract the N:C ratio and the various components of the N1s high-resolution spectrum. Survey spectra reveal moderate amount of nitrogen incorporation following subsequent exposure of the graphene films to the late-afterglow of microwave N₂ plasmas (N1s/(N1s+C1s) = 3.7%, 5.7% and 7.6% at 1 min, 2 min and 3 min of plasma treatment, respectively). XPS surveys are provided in **Supplementary information S-VIII**. High resolution spectra of C1s and N1s are presented at **Figure 6a-b**. The C1s region presents the main sp² C-C bond typical of graphene at 284.6 eV [49–54] as well as additional features at higher binding energies related to N bonding (*e.g.* sp² C=N at 285.5 ± 0.1 eV [54–56] and sp³ C-N at 287.5 ± 0.1 eV [56–58]) or O (C-OH at 286.5 ± 0.2 eV [51–53,58], C=O and/or O=C-O at 288.5 ± 0.2 eV [49,52,56,57,59] and O=C-OH at 289.4 ± 0.2 eV [58]). The N1s region reveals a strong contribution of the pyrrole-nitroso type of inclusions at 400.1 eV [54,60–63] with reasonable amount of pyridine (399.2 eV [54,55,63,64]) and graphitic incorporations (401.3 eV [54,55,62–64]). Oxygen inclusion arise due to the exposition to atmospheric conditions of the plasma -reated sample between each measurement. Its presence is limited for the untreated sample and is most likely caused by surface contamination [21]. Plasma-induced disorder creates dangling bonds responsible for oxygen inclusion after the treatment and further exposition to ambient air. This contamination is not believed to play a major role in the change in charge carrier concentration or its homogeneities across the graphene surface.

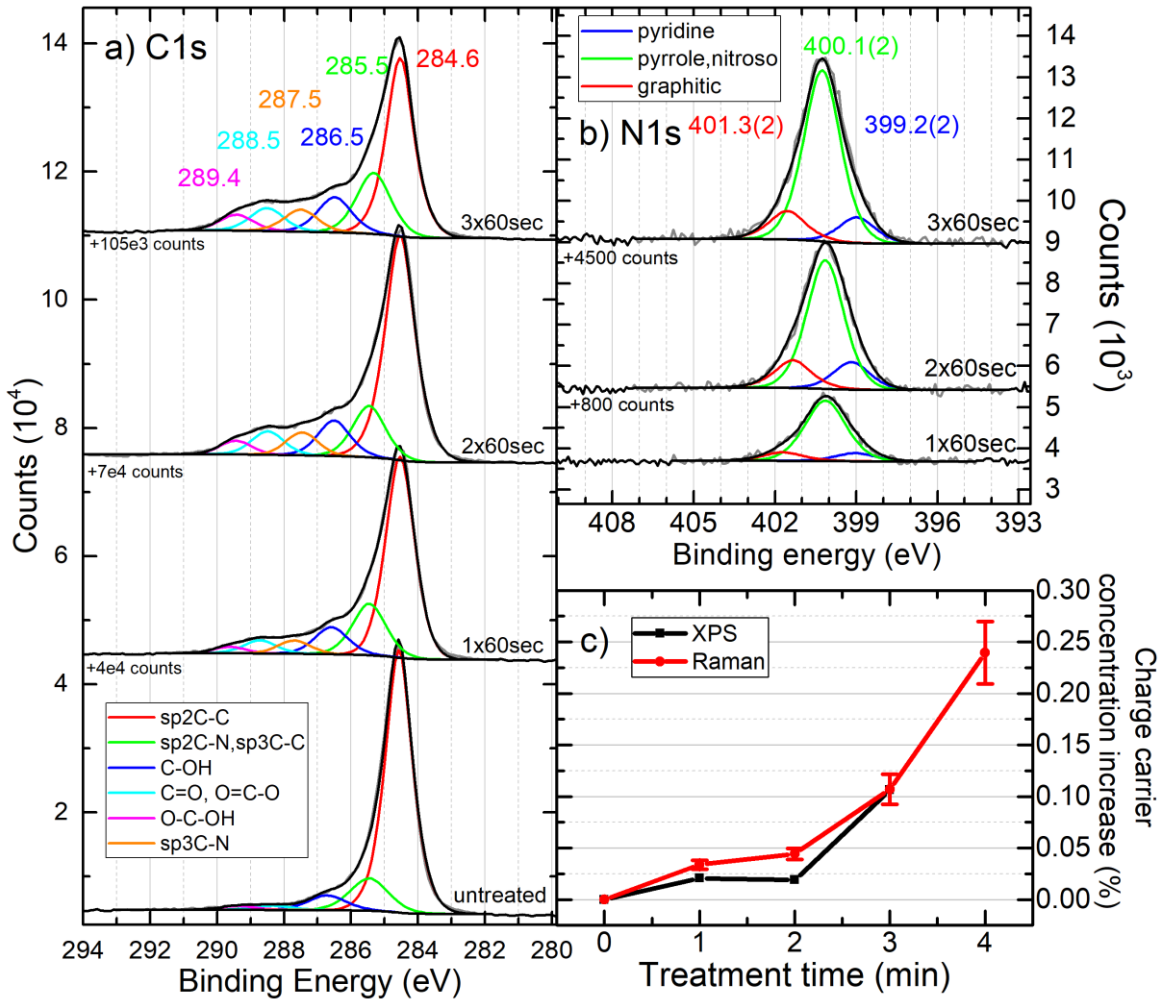


Figure 6. High resolution XPS spectra in the regions of C1s (a) and N1s (b) for all sample states. Nitrogen and oxygen bondings to carbon cause the asymmetry of the C1s band. Charge carrier concentration increase (c) as a function of treatment time extracted from Raman data treatments of graphene domains (green cluster) by optical decoupling of strain and doping (red) and XPS graphitic-pyridine inclusion (black).

Each nitrogen inclusion is expected to contribute differently to the modification of the Fermi level in monolayer graphene films. While graphitic inclusions induce n-type doping (0.54 e/N), pyridine provides p-type doping (0.45 p/N) [65]. Pyrrole inclusions are less discussed in the literature, but one expects their effects to be limited for low to medium nitrogen contents [66]. The product of the nitrogen atomic fraction ($\text{N1s}/(\text{N1s}+\text{C1s})$) from the survey scans by the respective percent contribution of each nitrogen component from the high-resolution N1s scans is used to estimate the corresponding charge carrier concentration for each plasma treatment step. These results are

compared in **Figure 6c** to those extracted from Raman optical decoupling of strain and doping, for GDs only. Here, the absolute change in charge carrier density obtained from Raman analysis and presented in **Figure 5c** were divided by the atomic density of carbon atoms in graphene domains ($3.85 \times 10^{15} \text{ cm}^{-2}$) to obtain percent variations. (i) Because XPS measurements are spatially-averaged, it is impossible to distinguish in XPS the different regions or clusters (as in RIMA), and (ii) GDs represent more than 70% of the graphene surface (see **Figure 1** and **Figure S5** of the **Supplementary information S-IV**), it is therefore expected that XPS data are mostly due to GDs. As can be seen in **Figure 6c**, similar trends and values are obtained from both XPS and RIMA. However, it is worth highlighting that due to the similar nitrogen content of both graphitic and pyridinic inclusions and their relatively low percent contribution in the overall N1s signals, the corresponding errors in XPS data analysis can be large.

4. Discussion

Further analysis of the Raman band parameters displayed in the previous section can be used to better understand how each region of the graphene film is altered by the plasma treatment. Despite the use of a reactive plasma source, the analysis proposed by *Cancado et al.* [32] still holds and reveals the creation of 0D defects at the GDs (**Figure 3**). In most plasma irradiation studies, such defects are linked to ion bombardment of the graphene sample. In the late afterglow region of the microwave nitrogen plasma, however, the kinetic energy of positive ions interacting with the graphene sample (of around 0.5 eV, **Supplementary information S-VIX**) is too low to cause any relevant damage. Since pure knock-on collisions can be ruled out in such conditions, other damage formation mechanisms involving local potential energy transfers must be involved [67], including the surface neutralization of N_2^+ - 16 eV, the surface deexcitation of $\text{N}_2(\text{A})$ metastable species – 6 eV, and the surface recombination of nitrogen atoms - 10 eV [68]. Similar energy exchange processes were proposed to reduce the energy barrier by a factor of 4 (from 9 eV to 2.3 eV) for Frenkel pair formation in graphene-like structures under a carbon adatom flux [69]. Note that, over the range of experimental conditions examined in this study, high-energy photons emanating from the main microwave plasma zone cannot reach the late-afterglow region due to the use of an adequately-shaped knee in the discharge tube (**Supplementary information S-I**).

In addition to energy transfer processes, residual oxygen species present in the microwave plasma and flowing afterglow (as a result of base pressure impurities and outgassing of plasma reactor walls) could also induce mild chemical etching of carbon atoms in monolayer graphene films. Such phenomenon is expected to be mostly specific to GBs, as previously observed in O- and H-bearing plasmas [9,70–72]. Surprisingly, GBs reveal less damage generation than all other regions: this is evidenced by a much weaker D:2D ratio at GBs than in GDs. In addition, D:D' ratios are constant for all clusters (**Supplementary information S-X**), suggesting that there is no preferential defect type generation [33]. Thus, damage formation must either be slower at GBs due to their intrinsic organization or there is a preferential self-healing of plasma-induced damage in these regions. In plasma irradiation conditions leading to a large density of carbon adatoms, *Vinchon et al.* [11] recently revealed that the GBs were more resilient than GDs due to a more efficient Frenkel pair recombination in their vicinity. Briefly, such preferential healing of plasma-generated defects near grain boundaries results from (i) the difference between the migration energy of carbon adatoms (0.4 eV) and vacancies (1.6-3.0 eV) [73] and (ii) the anisotropic transport of these 0D defects along the axis of GBs [17,74]. This induces an accumulation of carbon adatoms at the GBs, which enhances the probability for adatom-vacancy recombination in the vicinities of GBs. Such mechanism would obviously result in a net loss of vacancies close to the defect sites of black and red clusters, which explains the low D:2D ratios observed for the latter. This mechanism is expected to vanish as the sample gets more damaged due to limited transport of C-adatoms towards GBs (carbon adatoms now become mostly trapped by disorders in the GDs). Anisotropic transport of carbon adatoms along GBs is also strongly reduced as the graphene approaches the amorphous state. In such conditions, carbon adatoms coverage is expected to become much more uniform. Due to the limited amount of data, however, this transition towards the amorphous state cannot be studied in detail.

As mentioned above, the change in doping extracted from the method presented by *Lee et al.* [30] (updated with measurements of *Bissett et al.* [29] and *Bruna et al.* [35]) reveals a much larger doping at GDs than at GBs (**Figure 5c**). Such dopant segregation at GDs is revealed while fewer disorder is induced at GBs. This selective incorporation of nitrogen atoms at GDs only occurs for the first two plasma treatments, i.e. when graphene is still in stage 1 along the amorphization

path. The explanation is two-fold. First, as evidenced by the observed variations in D:2D ratios (**Figure 4**), GDs sustain more damage overall than GBs, the latter being subject to a preferential self-healing phenomenon [11]. This results in a larger population of vacancies at GDs, which are favored sites for N-atoms incorporation. Second, a crucial aspect to dopant selectivity is the large difference between the migration barrier of carbon and nitrogen adatoms on the graphene surface: 0.4 eV for C [73] and 1.1 eV for N [75]. This means that C-adatoms are highly mobile on monolayer graphene films over the range of experimental conditions investigated here (~ room temperature [76]), while N-adatoms are much less mobile. Thus, considering the C-adatoms and vacancies behaviors in the study of *Vinchon et al.* [11], a strong population imbalance is expected to arise throughout the sample between C- and N-adatoms with a greater density of carbon adatoms at the GBs. Eventually, as the sample engages its transition towards amorphization (stage 2), the incorporation becomes more homogeneous throughout the whole graphene surface and affects all clusters in a very similar way (**Figure 5c**). This inhibits the preferential self-healing mechanism such that the N-incorporation dynamics in the stage 2 becomes less selective.

It is worth highlighting that the amplitude of the nitrogen content (3-8%) is similar to what is typically observed for other treatments of CVD-grown monolayer graphene films (1-16%) [77-79]. The assessment of the electronic doping is not always performed, specially its spatial distribution and its behavior for increasingly disordered graphene. *Zhao et al.* [43] have shown the synthesis of N-doped graphene by CVD and have revealed localization of nitrogen incorporation at graphene domains, where a much lower 0.4% graphitic content is shown responsible for n-type doping. Here, plasma-generated nitrogen atoms are found in many more inclusion configurations, but specific incorporation in the domains is still present even for the much larger nitrogen content.

5. Conclusion

A combination of Hyperspectral Raman IMager (RIMA) and Principal Component Analysis (PCA) clustering was used to distinct different regions of a polycrystalline graphene film grown by CVD and exposed to the late afterglow of a microwave N₂ plasma at low pressure. The precision of the

technique, verified by optical microscopy and scanning electron microscopy, is effective in highlighting the evolution of different regions of the sample: graphene domains (GDs), over- and sub-graphene contaminants (GSs) as well as grain boundaries (GBs). Through careful decoupling of strain and doping effects in Raman spectroscopy, a selective doping by plasma-generated nitrogen species is revealed at the GDs for the first two plasma treatments. Such dopant segregation is believed to be made possible by a combination of two phenomena. First, a preferential self-healing mechanism occurring at GBs leads to a decrease of the population of vacancies in their vicinity, the latter being a favored site for N-atoms incorporation. Second, an imbalance is expected to occur resulting in a greater density of carbon and nitrogen adatoms at the GBs and GDs, respectively. After the third plasma treatment, the higher defect density throughout the entire graphene surface reduces the mobility of C-adatoms towards the GBs, which stop the preferential self-healing mechanism, giving more homogenous N-incorporation across the different regions. Over the range of experimental conditions investigated, n-type doping is evaluated at 0.24%, a result confirmed by X-ray photoelectron spectroscopy. This powerful technique demonstrated the importance of the migration barrier of each plasma-generated defects; accumulating and incorporating more mobile defects in the vicinity of the GBs while defects with higher migration barriers segregate within GDs. These results and the characterization method presented in this study are of particular relevance for the understanding of surface processes in 2D materials and paves the way toward a complete tailoring of the doping levels in graphene films.

6. Methods

Experimental Setup

A gap-type wave launcher (surfatron) maintains a 2.45 GHz surface wave along an 8-mm external (6-mm internal) diameter fused silica discharge tube. The whole apparatus is extensively described in previous publications [20,21,80]. In this study, the pressure is set to 6 Torr (800 Pa), the gas flow to 100 standard cube centimeter per minute (sccm) and the injected power to 32 W. The resulting plasma length is about 2 cm. From the surfatron gap, the early afterglow peaks at 4 cm while the sample position is set at 27 cm. The sample is far enough from the energetic species of the plasma discharge and thus interacts with a much less damaging environment. Still, three different reactive species (plasma-generated N atoms, N₂(A) metastable species and N₂⁺) are present in significant quantities in the afterglow and can induce significant change of the graphene properties [20]. Their respective densities in the flowing afterglow region were previously determined by optical emission spectroscopy and Langmuir probe measurements [80]. The setup is presented in **Supplementray information S-I**.

RIMA Measurement

The setup is detailed elsewhere [18]. Briefly, a 3.25-W laser at 532 nm uniformly irradiates a 130×130 μm² area via a beam shaping device and a 100× objective. Resulting Raman emission is then spectrally separated using a volumetric Bragg tunable filter. Despite the beam shaping device, the absolute value mappings of Raman bands still show a large difference between the side and the center of the detector. The line-ratio are not affected but signal to noise varies. In the current study, to reduce the effect of a large variation of the signal-to-noise ratio between the center and the sides of the hyperspectral cube, 20-μm bands are cropped from each side resulting in a 90 × 90 μm² final probed area. The RIMA experiments can be time-consuming and thus a 3x3 binning is used in order to reduce by a factor 9 the length of each experimental run. Typical unfiltered spectra are presented in **Supplementray information S-II**.

Data preparation and processing

The core of the processing methods employed in this article is detailed elsewhere [18]. Noise removing algorithm and baseline subtraction were improved. The methods is inspired by the work of *Antonelli et al.* [81]. The following points detail each step.

PCA-based noise filtering

First data centering and normalization are carried out. PCA decomposition (centering) is then applied to extract the first 30 components maps of the measurements. A Gaussian unmixing is used to differentiate the 10 clusters core to this study. This is done to ensure that the following noise removal algorithm is able to properly remove the noise of the data of each cluster. Indeed, PCA is intrinsically biased by the intensity of each dimension and therefore mappings containing a low amount of highly distinguishable spectrum induce large error to the noise reduction of these outliers. Moreover, the number of components required to reconstruct all the data would be increased and could possibly reduce the quality of the noise reduction. Base on the work of *Antonelli et al.* [81], we thus try to remove a uniform simulated noise contribution for the data while ensuring that the noise is similar for all spectra and is of adequate amplitude. We must first estimate the intensity of the noise to be removed. We do so using the modified criteria proposed in another work [81] and do so for each cluster.

$$\text{Experimental noise criterium: } \frac{d^2 \text{err}_{\text{mean}}}{dN^2} < \text{median} \left(\frac{d^2 \text{err}_{\text{mean}}}{dN^2} \right)$$

This criterium is verified for each cluster in order to select the components up to the change in the slope of the average spectrum error. An extreme precision for this first evaluation of experimental noise is not mandatory as a correction of experimental noise is later assessed. We then perform a weighted average of the estimated experimental noise values. To converge towards a more precise value of the experimental noise, we then evaluate a minimum delta value for all clusters simultaneously (adjusting the root mean square of the error by the normalization factor of each cluster).

$$\text{Delta calculation: } \delta(N_T) = \frac{1}{N} \sum_{j=1}^N \left| (e_{\eta}(v_j)^2 - e_{rr}(v_j)^2) \right| \quad (\text{eq 26 from [79]})$$

This allows to obtain the corrected experimental noise value. Through delta minimisation again, we find the number of components in each cluster that allows to remove a constant noise of the appropriate amplitude. Filtered spectra are presented in **Supplementary information S-III**.

PCA assisted artefact subtraction

The nature of the artefact of the Raman Imager (RIMA) is yet unknown. Its main cause is believed to be the fluorescence of the system objectives. The shape of the artefact can drastically change from one position to another on the CCD. A measurement is taken on a clean substrate of SiO₂. Through PCA decomposition (centering, no normalization), 4 main components are extracted. A linear combination of those can be used to describe the behavior of all the artefacts on the CCD.

Spectrum fitting

It results that 4 parameters are fitted simultaneously to the band parameters to ensure proper baseline subtraction. The constraints imposed by the 4 core-artefacts enable better fitting of the baseline on the extreme regions of the spectra, i.e. regions where polynomial fitting tends to diverge and somewhat induces error on band fittings. The fitting method is least square fitting with centering, normalization and dynamic bounds. Line shapes are set to Lorentzian for all bands. Spectra fitting and artefact subtraction can be assessed for typical spectra presented in **Supplementary information S-III**.

7. Acknowledgments

This work was financially supported by the National Science and Engineering Research Council (NSERC), PRIMA-Québec, Plasmionique Inc., Photon Etc., the Fonds de Recherche du Québec - Nature et Technologies (FRQNT), and the Canada Research Chair (L. Stafford and R. Martel). The authors thank Carl Charpin for providing the CVD-grown graphene samples and Charlotte Allard for technical support with Raman imaging.

8. Author contributions

G.R.B performed all experimental measurements and the code for the analysis of RIMA data. X.G. and P.V. participated in the initial writing of the manuscript. All authors contributed to the design of experiments and data interpretation and manuscript revision. L.S. and R.M. contributed to the funding and the supervision of the study.

9. Competing financial interests

The authors declare no competing financial interests

10. References

- [1] S. Bae, H. Kim, Y. Lee, X. Xu, J.-S. Park, Y. Zheng, J. Balakrishnan, T. Lei, H. Ri Kim, Y. Il Song, Y.-J. Kim, K.S. Kim, B. Özyilmaz, J.-H. Ahn, B.H. Hong, S. Iijima, *Nat. Nanotechnol.* 5 (2010) 574–578.
- [2] O. V. Yazyev, S.G. Louie, *Nat. Mater.* 9 (2010) 806–809.
- [3] Z. Fei, A.S. Rodin, W. Gannett, S. Dai, W. Regan, M. Wagner, M.K. Liu, A.S. McLeod, G. Dominguez, M. Thiemens, A.H. Castro Neto, F. Keilmann, A. Zettl, R. Hillenbrand, M.M. Fogler, D.N. Basov, *Nat. Nanotechnol.* 8 (2013) 821–825.
- [4] Q. Yu, L.A. Jauregui, W. Wu, R. Colby, J. Tian, Z. Su, H. Cao, Z. Liu, D. Pandey, D. Wei, T.F. Chung, P. Peng, N.P. Guisinger, E.A. Stach, J. Bao, S.-S. Pei, Y.P. Chen, *Nat. Mater.* 10 (2011) 443–449.
- [5] R. Grantab, V.B. Shenoy, R.S. Ruoff, *Science* (80-.). 330 (2010) 946–948.
- [6] J. Červenka, M.I. Katsnelson, C.F.J. Flipse, *Nat. Phys.* 5 (2009) 840–844.
- [7] S. Malola, H. Häkkinen, P. Koskinen, *Phys. Rev. B* 81 (2010) 165447.
- [8] P. Yasaee, B. Kumar, R. Hantehzadeh, M. Kayyalha, A. Baskin, N. Repnin, C. Wang, R.F. Klie, Y.P. Chen, P. Král, A. Salehi-Khojin, *Nat. Commun.* 5 (2014) 4911.
- [9] R. Yang, L. Zhang, Y. Wang, Z. Shi, D. Shi, H. Gao, E. Wang, G. Zhang, *Adv. Mater.* 22 (2010) 4014–4019.
- [10] P. Nemes-Incze, G. Magda, K. Kamarás, L.P. Biró, *Nano Res.* 3 (2010) 110–116.
- [11] P. Vinchon, X. Glad, G. Robert Bigras, R. Martel, L. Stafford, *Nat. Mater.* (2020).
- [12] O. V. Yazyev, *Solid State Commun.* 152 (2012) 1431–1436.
- [13] A. Isacsson, A.W. Cummings, L. Colombo, L. Colombo, J.M. Kinaret, S. Roche, *2D Mater.* 4 (2016) 012002.
- [14] J. Dong, H. Wang, H. Peng, Z. Liu, K. Zhang, F. Ding, *Chem. Sci.* 8 (2017) 2209–2214.
- [15] L.P. Biró, P. Lambin, *New J. Phys.* 15 (2013) 035024.
- [16] C. Ophus, A. Shekhawat, H. Rasool, A. Zettl, *Phys. Rev. B* 92 (2015) 205402.
- [17] B. Wang, Y. Puzyrev, S.T. Pantelides, *Carbon N. Y.* 49 (2011) 3983–3988.
- [18] G. Robert Bigras, P. Vinchon, C. Allard, X. Glad, R. Martel, L. Stafford, *Rev. Sci. Instrum.* 91 (2020) 063903.

- [19] E. Gaufrès, S. Marcet, V. Aymong, N.Y.W. Tang, A. Favron, F. Thouin, C. Allard, D. Rioux, N. Cottenye, M. Verhaegen, R. Martel, J. Raman Spectrosc. 49 (2018) 174–182.
- [20] G. Robert Bigras, X. Glad, R. Martel, A. Sarkissian, L. Stafford, Plasma Sources Sci. Technol. 27 (2018) 124004.
- [21] G. Robert Bigras, X. Glad, L. Vandsburger, C. Charpin, P. Levesque, R. Martel, L. Stafford, Carbon N. Y. 144 (2019) 532–539.
- [22] S. Choubak, M. Biron, P.L. Levesque, R. Martel, P. Desjardins, J. Phys. Lett. 4 (2013) 1100–1103.
- [23] H.J. Jeong, H.Y. Kim, S.Y. Jeong, J.T. Han, K.-J. Baeg, J.Y. Hwang, G.-W. Lee, Carbon N. Y. 66 (2014) 612–618.
- [24] R. Beams, L. Gustavo Cançado, L. Novotny, J. Phys. Condens. Matter 27 (2015) 083002.
- [25] A. Vladar, M. Postek, Microsc. Microanal. 11 (2005) 764–765.
- [26] J. Ribeiro-Soares, M.E. Oliveros, C. Garin, M.V. David, L.G.P. Martins, C.A. Almeida, E.H. Martins-Ferreira, K. Takai, T. Enoki, R. Magalhães-Paniago, A. Malachias, A. Jorio, B.S. Archanjo, C.A. Achete, L.G. Cançado, Carbon N. Y. 95 (2015) 646–652.
- [27] H. PAQUETON, J. RUSTE, Tech. l'ingénieur. Anal. Caractérisation (2006).
- [28] N. Lisi, T. Dikonomos, F. Buonocore, M. Pittori, R. Mazzaro, R. Rizzoli, S. Marras, A. Capasso, Sci. Rep. 7 (2017) 1–11.
- [29] M.A. Bissett, W. Izumida, R. Saito, H. Ago, ACS Nano 6 (2012) 10229–10238.
- [30] J.E. Lee, G. Ahn, J. Shim, Y.S. Lee, S. Ryu, Nat. Commun. 3 (2012) 1024.
- [31] A.C. Ferrari, J. Robertson, Phys. Rev. B 61 (2000) 14095–14107.
- [32] L. Gustavo Cançado, M. Gomes da Silva, E.H. Martins Ferreira, F. Hof, K. Kampioti, K. Huang, A. Pénicaud, C. Alberto Achete, R.B. Capaz, A. Jorio, 2D Mater. 4 (2017) 025039.
- [33] A. Eckmann, A. Felten, A. Mishchenko, L. Britnell, R. Krupke, K.S. Novoselov, C. Casiraghi, Nano Lett. 12 (2012) 3925–3930.
- [34] A. Das, S. Pisana, B. Chakraborty, S. Piscanec, S.K. Saha, U. V Waghmare, K.S. Novoselov, H.R. Krishnamurthy, a K. Geim, A.C. Ferrari, A.K. Sood, Nat. Nanotechnol. 3 (2008) 210–215.
- [35] M. Bruna, A.K. Ott, M. Ijas, D. Yoon, U. Sassi, A.C. Ferrari, ACS Nano 8 (2014) 7432–7441.
- [36] K. Jia, Y. Su, Y. Chen, J. Luo, J. Yang, P. Lv, Z. Zhang, H. Zhu, C. Zhao, T. Ye, Vacuum 116 (2015) 90–95.
- [37] Y.-B.B. Zhou, Z.-M.M. Liao, Y.-F.F. Wang, G.S. Duesberg, J. Xu, Q. Fu, X.-S.S. Wu, D.-P.P. Yu, J. Chem. Phys. 133 (2010) 234703.
- [38] E.H. Martins Ferreira, M.V.O. Moutinho, F. Stavale, M.M. Lucchese, R.B. Capaz, C. a. Achete, A. Jorio, Phys. Rev. B 82 (2010) 125429.
- [39] M.S. Dresselhaus, A. Jorio, A.G. Souza Filho, R. Saito, Philos. Trans. R. Soc. A Math. Phys. Eng. Sci. 368 (2010) 5355–5377.
- [40] T. Lee, F.A. Mas’ud, M.J. Kim, H. Rho, Sci. Rep. 7 (2017) 16681.
- [41] A. Das, B. Chakraborty, A.K. Sood, Bull. Mater. Sci. 31 (2008) 579–584.
- [42] A. Eckmann, A. Felten, I. Verzhbitskiy, R. Davey, C. Casiraghi, Phys. Rev. B 88 (2013) 035426.
- [43] L. Zhao, R. He, A. Zabet-Khosousi, K.S. Kim, T. Schiros, M. Roth, P. Kim, G.W. Flynn, A. Pinczuk, A.N. Pasupathy, Nano Lett. 15 (2015) 1428–1436.
- [44] Y. Ahn, J. Kim, S. Ganorkar, Y.-H. Kim, S.-I. Kim, Mater. Express 6 (2016) 69–76.
- [45] S. Ryu, L. Liu, S. Berciaud, Y.-J. Yu, H. Liu, P. Kim, G.W. Flynn, L.E. Brus, Nano Lett. 10 (2010) 4944–4951.

- [46] Z. Zafar, Z.H. Ni, X. Wu, Z.X. Shi, H.Y. Nan, J. Bai, L.T. Sun, *Carbon N. Y.* 61 (2013) 57–62.
- [47] L.S. Panchakarla, K.S. Subrahmanyam, S.K. Saha, A. Govindaraj, H.R. Krishnamurthy, U. V. Waghmare, C.N.R. Rao, *Adv. Mater.* 21 (2009) 4726–4730.
- [48] F. Banhart, J. Kotakoski, A. V. Krasheninnikov, *ACS Nano* 5 (2011) 26–41.
- [49] A. Achour, S. Vizireanu, G. Dinescu, L. Le Brizoual, M.-A. Djouadi, M. Boujtita, *Appl. Surf. Sci.* 273 (2013) 49–57.
- [50] H. Estrade-Szwarcopf, *Carbon N. Y.* 42 (2004) 1713–1721.
- [51] M.. b Koinuma, H.. b Tateishi, K.. b Hatakeyama, S.. b Miyamoto, C.. b Ogata, A.. b Funatsu, T.. b Taniguchi, Y.. b Matsumoto, *Chem. Lett.* 42 (2013) 924–926.
- [52] A. Siokou, F. Ravani, S. Karakalos, O. Frank, M. Kalbac, C. Galiotis, *Appl. Surf. Sci.* 257 (2011) 9785–9790.
- [53] D. Yang, A. Velamakanni, G. Bozoklu, S. Park, M. Stoller, R.D. Piner, S. Stankovich, I. Jung, D.A. Field, C.A. Ventrice, R.S. Ruoff, *Carbon N. Y.* 47 (2009) 145–152.
- [54] T. Susi, T. Pichler, P. Ayala, *Beilstein J. Nanotechnol.* 6 (2015) 177–192.
- [55] N. Hellgren, R.T. Haasch, S. Schmidt, L. Hultman, I. Petrov, *Carbon N. Y.* 108 (2016) 242–252.
- [56] S.C. Hernández, F.J. Bezares, J.T. Robinson, J.D. Caldwell, S.G. Walton, *Carbon N. Y.* 60 (2013) 84–93.
- [57] I. Bertóti, M. Mohai, K. László, *Carbon N. Y.* 84 (2015) 185–196.
- [58] S. Kaciulis, *Surf. Interface Anal.* 44 (2012) 1155–1161.
- [59] V. Datsyuk, M. Kalyva, K. Papagelis, J. Parthenios, D. Tasis, A. Siokou, I. Kallitsis, C. Galiotis, *Carbon N. Y.* 46 (2008) 833–840.
- [60] C.D. Batich, D.S. Donald, *J. Am. Chem. Soc.* 106 (1984) 2758–2761.
- [61] J.R. Pels, F. Kapteijn, J.A. Moulijn, Q. Zhu, K.M. Thomas, *Carbon N. Y.* 33 (1995) 1641–1653.
- [62] X. Wang, X. Li, L. Zhang, Y. Yoon, P.K. Weber, H. Wang, J. Guo, H. Dai, *Science* (80-.). 324 (2009) 768–771.
- [63] M. Scardamaglia, B. Aleman, M. Amati, C. Ewels, P. Pochet, N. Reckinger, J.F. Colomer, T. Skaltsas, N. Tagmatarchis, R. Snyders, L. Gregoratti, C. Bittencourt, *Carbon N. Y.* 73 (2014) 371–381.
- [64] W. Ding, Z. Wei, S. Chen, X. Qi, T. Yang, J. Hu, D. Wang, L.J. Wan, S.F. Alvi, L. Li, *Angew. Chemie - Int. Ed.* 52 (2013) 11755–11759.
- [65] T. Schiros, D. Nordlund, L. Pálová, D. Prezzi, L. Zhao, K.S. Kim, U. Wurstbauer, C. Gutiérrez, D. Delongchamp, C. Jaye, D. Fischer, H. Ogasawara, L.G.M. Pettersson, D.R. Reichman, P. Kim, M.S. Hybertsen, A.N. Pasupathy, *Nano Lett.* 12 (2012) 4025–4031.
- [66] M. Rybin, A. Pereyaslavtsev, T. Vasilieva, V. Myasnikov, I. Sokolov, A. Pavlova, E. Obraztsova, A. Khomich, V. Ralchenko, E. Obraztsova, *Carbon N. Y.* 96 (2016) 196–202.
- [67] P. Vinchon, X. Glad, G. Robert-Bigras, R. Martel, A. Sarkissian, L. Stafford, *J. Appl. Phys.* 126 (2019) 233302.
- [68] F.R. Gilmore, *J. Quant. Spectrosc. Radiat. Transf.* 5 (1965) 369-IN3.
- [69] C.. Ewels, M.. Heggie, P.. Briddon, *Chem. Phys. Lett.* 351 (2002) 178–182.
- [70] Y. Zhang, Z. Li, P. Kim, L. Zhang, C. Zhou, *ACS Nano* 6 (2012) 126–132.
- [71] M. Seifert, J.E.B. Vargas, M. Bobinger, M. Sachsenhauser, A.W. Cummings, S. Roche, J.A. Garrido, *2D Mater.* 2 (2015) 024008.
- [72] L. Xie, L. Jiao, H. Dai, *J. Am. Chem. Soc.* 132 (2010) 14751–14753.
- [73] A. V. Krasheninnikov, K. Nordlund, *J. Appl. Phys.* 107 (2010) 071301.

- [74] L.F. Huang, M.Y. Ni, G.R. Zhang, W.H. Zhou, Y.G. Li, X.H. Zheng, Z. Zeng, *J. Chem. Phys.* 135 (2011) 064705.
- [75] J. Kotakoski, A. V. Krasheninnikov, Y. Ma, A.S. Foster, K. Nordlund, R.M. Nieminen, *Phys. Rev. B* 71 (2005) 205408.
- [76] N. Kang, M. Lee, A. Ricard, S. Oh, *Curr. Appl. Phys.* 12 (2012) 1448–1453.
- [77] H. Wang, T. Maiyalagan, X. Wang, *ACS Catal.* 2 (2012) 781–794.
- [78] M. Fan, Z. Feng, C. Zhu, X. Chen, C. Chen, J. Yang, D. Sun, *J. Mater. Sci.* 51 (2016) 10323–10349.
- [79] M. Inagaki, M. Toyoda, Y. Soneda, T. Morishita, *Carbon N. Y.* 132 (2018) 104–140.
- [80] J. Afonso Ferreira, L. Stafford, R. Leonelli, A. Ricard, *J. Appl. Phys.* 115 (2014) 163303.
- [81] P. Antonelli, H.E. Revercomb, L.A. Sromovsky, W.L. Smith, R.O. Knuteson, D.C. Tobin, R.K. Garcia, H.B. Howell, H.-L. Huang, F.A. Best, *J. Geophys. Res. Atmos.* 109 (2004) 1–22.

11. Supplementary Data

Additional data on the optical decoupling of strain and doping, XPS survey scans, energy uptake in the late afterglow, damage type assessment, experimental setup, unprocessed RIMA measurements, spectrum noise filtering and spectrum fitting are provided in **Annexe 5** of this thesis.

Chapitre 4 – Rôles respectifs des espèces actives de la post-décharge et modèle d'incorporation des atomes d'azote

4.1 Introduction

Le rôle des inhomogénéités de croissance du graphène, en particulier des joints de grains, sur (i) l'évolution des spectres Raman (mise en évidence de signatures spectrales distinctes), (ii) la dynamique de formation des défauts par irradiation ionique dans les plasmas d'argon (mise en évidence de l'auto-réparation préférentielle aux joints de grains), ainsi que (iii) la cinétique d'incorporation des atomes d'azote dans la post-décharge en flux (mise en évidence de l'incorporation sélective dans les domaines) ont été discutés au **Chapitre 3**. Cependant, le rôle exact de chacune des espèces actives de la post-décharge en flux sur l'interaction plasma-graphène n'a été que très peu abordée. Pour examiner ces aspects, nous avons sélectionné différentes conditions opératoires de la post-décharge en flux. Dans chacun des cas, la caractérisation par spectroscopie optique d'émission a été réalisée afin de sonder les densités des particules pertinentes à l'étude. Ceci inclut des mesures de titrage avec NO pour sonder les populations d'atomes d'azote [R95,96] mais aussi des mesures d'actinométrie pour analyser les concentrations de métastables N₂(A) et d'atomes d'oxygène [R97]. Pour la caractérisation du graphène, le montage XPS utilisé permet l'acquisition de mesures sur une zone de 500 µm. Bien qu'assez étroite, cette région est trop grande pour pouvoir distinguer le comportement des inhomogénéités sondées par imagerie Raman. Nous avons donc décidé de corrélérer la signature XPS à celle des régions les plus abondantes au RIMA : les domaines du graphène. De ce fait, les travaux de ce dernier chapitre sont consacrés uniquement à l'évolution des dommages et à l'incorporation des atomes d'azote dans les domaines de graphène.

La **Section 4.2** présente des traitements réalisés dans trois conditions particulières. En plus de la post-décharge lointaine à 6 Torr discutée dans les Chapitres 2 et 3, nous avons sélectionné une autre condition de la post-décharge lointaine à 6 Torr dans laquelle nous avons ajouté un tuyau de cuivre. Ce dernier est utilisé pour induire l'extinction partielle des atomes d'azote due à leur recombinaison sur la surface du cuivre tel que vérifié par spectroscopie d'émission optique. Les

espèces métastables N₂(A) et les hauts niveaux vibrationnels de l'azote se désexcitent peu sur une telle surface de sorte que leurs densités sont faiblement affectées. Ensuite, une condition à une plus basse pression de 1 Torr est étudiée. Pour celle-ci, il y a extinction de la post-décharge de sorte que les densités d'espèces excitées sont diminuées. On joue ainsi sur le ratio entre les densités d'atomes d'azote et de métastables N₂(A). En corrélant les signatures spectrales des dommages obtenues par RIMA avec les doses d'énergie apportée au graphène par les populations de N (recombinaison en surface libérant environ 5 eV) et les métastables N₂(A) (désexcitation en surface libérant environ 6 eV), nous avons pu confirmer que les deux espèces participent à la dynamique de formation de défauts. Dans les conditions opératoires étudiées, il s'avère que ces défauts sont surtout 0D. Quant à la cinétique d'incorporation des atomes d'azote, on observe que celle-ci n'est pas directement liée à la population des atomes d'azote dans la post-décharge en flux, suggérant que la formation des dommages joue également un rôle important. Un modèle d'incorporation considérant la formation de dommages, l'adsorption des atomes d'azote ainsi que l'incorporation des atomes d'azote dans un site de défaut est proposé. Cette section est présentée sous la forme d'un article soumis à *Nanoscale*. Les contributions sont comme suit : G. Robert Bigras – prise de mesures, traitement des données et rédaction, R. Martel et L. Stafford – supervision. Ensemble des auteurs – discussion et interprétation des résultats.

Inspiré des résultats présentés dans le précédent article, des mesures complémentaires ont été réalisées en présence d'espèce oxydantes. Les mesures et analyses sont présentées à la **Section 4.3**. On montre que le rôle des espèces oxydantes sur la production de dommages est inférieur à celui des N et N₂(A) pour toutes les conditions opératoires étudiées. De plus, il semble que ces espèces oxygénées ne jouent un rôle important sur la cinétique d'incorporation des atomes d'azote qu'uniquement après la transition du graphène vers l'amorphisation.

4.2 Rôle des azotes atomiques et des azotes moléculaires métastables

Incorporation-limiting mechanisms during nitrogenation of monolayer graphene films in nitrogen flowing afterglows

G. Robert Bigras¹, R. Martel², L. Stafford¹

¹Département de Physique, Université de Montréal, Montréal, Québec, CANADA.

²Département de Chimie, Université de Montréal, Montréal, Québec, CANADA.

Abstract

Monolayer graphene films are exposed to the flowing afterglow of a low-pressure microwave nitrogen plasma, characterized by the absence of ion irradiation and significant populations of N atoms and N₂(A) metastables. Hyperspectral Raman imaging of graphene domains reveals damage generation with a progressive rise of the D/G and D/2D band ratios following subsequent plasma treatments. Plasma-induced damage is mostly zero-dimensional and the graphene state remains in the pre-amorphous regime. Over the range of experimental conditions investigated, damage formation increases with the fluence of energy provided by heterogenous surface recombination of N atoms and deexcitation of N₂(A) metastable species. In such conditions, X-ray photoelectron spectroscopy reveals that the nitrogen incorporation (either as pyridine, pyrrole, or quaternary moieties) does not simply increase with the fluence of plasma-generated N atoms but is also linked to the damage generation. Based on these findings, a surface reaction model for monolayer graphene nitrogenation is proposed. It is shown that the nitrogen incorporation is first limited by the plasma-induced formation of defect sites at low damage and then by the adsorption of nitrogen atoms at high damage.

1. Introduction

Disordered states of the graphene lattice following the incorporation of a foreign atom, such as nitrogen, are widely studied due to their potential uses in many fields of applications [1,2], including biosensing [3–6], super-capacitors [7,8] and catalysts for oxygen reduction reactions [9,10]. Numerous studies have been done to better understand defective graphene structures

[11–16], the evolution of such structures in damaging environments [17,18], and the key roles of all species involved in damage formation [19–21]. Ion irradiation is routinely used for post-synthesis modification and incorporation of nitrogen species in graphene [22–27]. Controlling the nature of the nitrogen incorporation is a key challenge, as the different nitrogen moieties contribute differently to doping [28] and present different reactivities [8]. For example, low-energy nitrogen ion bombardment (\sim 25–100 eV) was found to create large multi-vacancies and thus both pyridine- and graphitic-like structures [29,30]. High-temperature annealing (\sim 900 – 1300K) can also be used to restructure the graphene lattice in ion-irradiated samples and/or to achieve better yields for nitrogen inclusions [29,30]. For conventional direct plasma treatments in which graphene is exposed to positive ions accelerated in a plasma sheath, graphitic inclusions can be achieved with ion bombardment energy as low as 5–35 eV [31]. These plasma processes face the same selectivity challenge as ion beam experiments. In such systems, selectivity and yield of the nitrogen inclusion is strongly dependent on the energy of the ions impinging onto the graphene surface as these species are the main vector for plasma-induced defect formation [32]. However, details on all factors driving the nitrogen incorporation dynamics remain unclear as some authors report rises of the nitrogen content with the plasma treatment time [32–34], while others show either saturation or loss with the dose of nitrogen species [8,35,36].

As reported by many authors, direct plasma treatments typically yield to significant damage in low-dimensional materials [4,37–40]. On the contrary, indirect plasma treatments based on flowing afterglows have shown low-damage modifications of materials and nanomaterials [31,41–43]. Such systems are characterized by extremely low ion populations such that ion irradiation phenomena play a negligible role in the plasma-material interaction. In the specific case of the flowing afterglow of microwave N₂ plasmas, the surface becomes mainly exposed to plasma-generated N atoms, N₂ vibrational species, and N₂ metastable species. While the probability of heterogenous surface deexcitation of N₂ vibrational states is very small [42,44–47], a significant energy transfer to the graphene lattice can arise due to heterogenous surface recombination of N atoms [42] and deexcitation of N₂(A) metastables [48].

This work examines damage formation and N incorporation in graphene films exposed to the flowing afterglow of a low-pressure microwave N₂ plasma. Through judicious controls of the

nature and flux of all species interacting with the graphene sample, it is shown that the nitrogen incorporation involves processes of both damage formation and nitrogen adsorption. In line with the experimental findings, a surface reaction model for the nitrogen incorporation is proposed.

2. Experimental details

Graphene films grown on copper substrates by chemical vapor deposition (CVD) [49] are first transferred to SiO₂/Si substrate using standard PMMA procedures [50,51]. The samples are then exposed to the flowing afterglow of a low-pressure N₂ plasma sustained by a microwave electromagnetic field [21,52]. In this work, the samples undergo four subsequent plasma treatments between each of which they are characterized by Raman Spectroscopy and X-Ray Photoelectron Spectroscopy (XPS). Raman analysis are performed using a Hyperspectral Raman IMager system (RIMATM, Photon Etc [53]) at an excitation wavelength of 532 nm. The same 90 x 90 μm² area (116 281 spectra, spatial resolution of 390 nm) of the graphene substrate is probed between each plasma treatment such that mean values and standard deviations of few selected Raman band parameters can be extracted. The processing method of the huge data set obtained from RIMA is detailed elsewhere [54]. As underlined below, the RIMA analysis is performed mainly from graphene domains (and not on graphene grain boundaries or any other surface disorders [54,55]). XPS analysis is realized on the same area probed by RIMA (spot size of about 400 microns). The setup is a Thermo Scientific K-Alpha (CAE detector, 180° double focusing hemispherical analyzer, 128 channel detector) operating with pass energies of 200 eV and 50 eV for survey and high-resolution scans, respectively. The step energy is 1 eV for the surveys and 0.1 eV for the high-resolution spectra. When needed, a flood gun is used to reduce charging shifts.

The plasma setup is detailed elsewhere [21,56]. In short, a gap-type wave launcher sustains a 2.45 GHz surface-wave plasma along a 8-mm outer diameter (6-mm inner diameter) fused silica tube and the flowing afterglow expands into a stainless-steel chamber where plasma-graphene interaction occurs [57]. The injected power is set at 30 W, the gas flow of high-purity (99.999%) nitrogen is fixed at 100 sccm and the working pressure is varied between 1 and 6 Torr. In such conditions, the nitrogen flowing afterglow is present [47]. This radiative region downstream of the main plasma column is due to N₂ vibrational-vibrational pumping. These energetic N₂

vibrational states can thus excite $N_2(A)$ and $N_2(a')$ metastable species (at 6 eV and 8.1 eV above ground state $N_2(X)$, respectively) by gas-phase collisions and can induce ion-electron pairs by associative ionization reactions [47]. A residual vacuum of 1.7×10^{-7} Torr is achieved between each subsequent plasma treatment and a gas purifier (SAES Pure Gas Inc Nitrogen MC1-920F) is used to minimize the effect from impurities [52]. In addition, to preserve the sample from adsorbed contaminants, the graphene samples are maintained between each plasma treatment, RIMA measurement, and XPS analysis in a reduced-pressure (~ 0.1 Torr) vacuum chamber.

3. Experimental Results

3.1 Plasma characterization

Figure 1 presents typical optical emission spectra of the first positive system of N_2 ($\Delta v = -4$) and the second positive system of N_2 ($\Delta v = -1$) at the sample position in the stainless-steel processing chamber for three treatment conditions. Detail on such optical emission spectroscopy measurements is provided elsewhere [21,56]. The preferential pumping of $N_2(B, v' = 11)$ state by gas-phase recombination of N atoms leading to the typical 580 nm emission of the late afterglow region of the microwave flowing afterglow [58] is strong for the 6 Torr condition. This is further confirmed by the vibrational energy distribution $N_2(B, v')$ presented in **Figure 2a**, which is characterized by a sharp rise at the vibrational number $v' = 11$. As the pressure decreases, a transition towards the early afterglow occurs [58]. In such cases, as demonstrated in **Figure 2a** for the 1 Torr condition, the vibrational energy distribution follows a typical Maxwellian energy distribution with a vibrational temperature of about 0.6 eV.

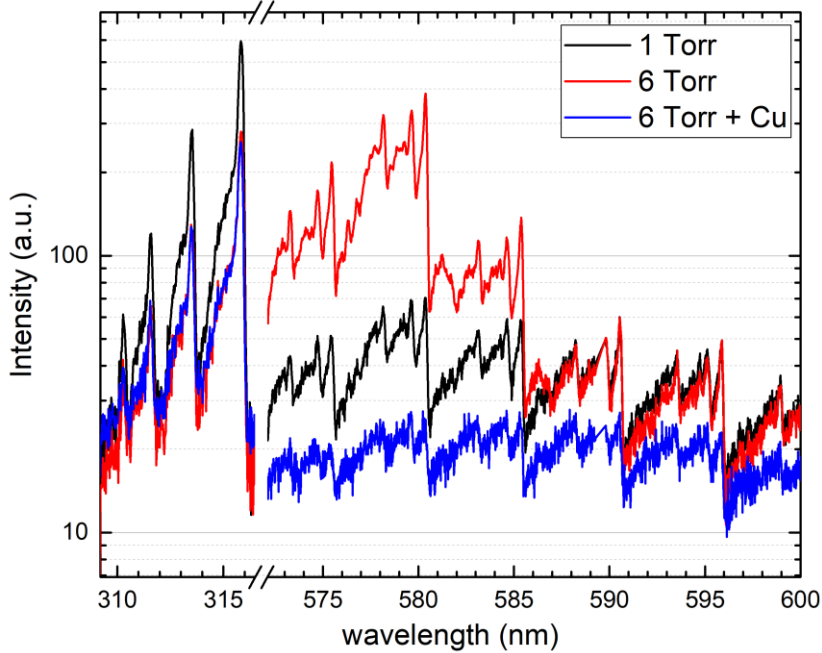


Figure 1 – Optical emission spectra of the second positive ($\Delta v = -1$) and first positive ($\Delta v = -4$) systems of N_2 in the flowing afterglow of microwave nitrogen plasmas in 1 Torr (black), 6 Torr (red) and 6 Torr + Cu (blue) conditions.

In the flowing afterglow of microwave N_2 plasmas, it is common to describe the vibrational energy distribution $N_2(B, v')$ as a linear function of early $N_2(B, v')_{\text{early}}$, and late $N_2(B, v')_{\text{late}}$ flowing afterglow contributions [58]:

$$N_2(X, v') = (1 - a) N_2(X, v')_{\text{early}} + a N_2(X, v')_{\text{late}} \quad (1)$$

where the so-called a coefficient is 0 in a nominally pure early afterglow and 1 in a nominally pure late afterglow. As shown in Figure 2b, the graphene sample mostly sees a late afterglow at 6 Torr and an early afterglow at 1 Torr. A third condition, identified as 6 Torr + Cu, is also presented in **Figure 1** and **Figure 2**. Here, the pressure is kept constant at 6 Torr, but a 2-cm long hollow copper tube is introduced on the chamber walls of the fused silica tube 3 cm before the sample position. Since the heterogeneous surface recombination coefficient of N atoms is much larger on Cu than on fused silica [59–61], this results in a significant decrease in the population of N atoms and thus

in a net loss of the optical signature of the late afterglow. In such cases, even if significant vibrational-vibrational pumping occurs, α becomes very small.

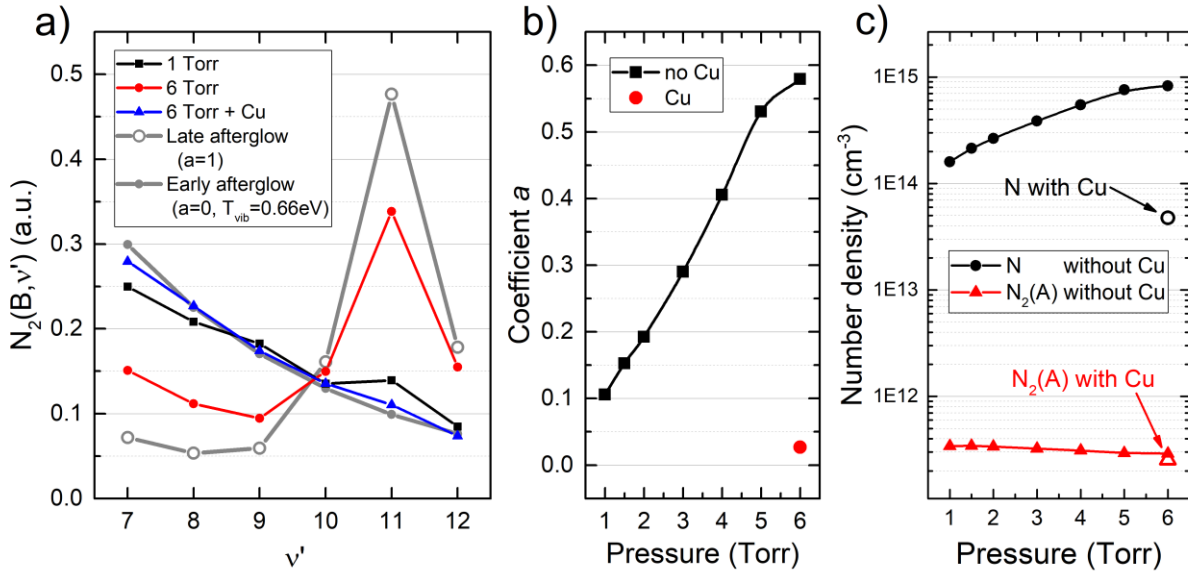


Figure 2 – (a) Evolution of the vibrational energy distribution of the first positive system of N_2 for the early and late afterglows with $\alpha = 0$ in the early afterglow and $\alpha = 1$ in the late afterglow and $T_{vib} = 0.66\text{ eV}$. The results obtained at 6 Torr with and without Cu, and the results obtained at 1 Torr are also shown. (b) Influence of pressure on the α coefficient. The α value in red obtained with Cu at 6 Torr is also shown for comparison. (c) Number density of atomic N (black) and metastable $N_2(A)$ (red) as a function of pressure. At 6 Torr, the results with Cu (open symbols) are also shown for comparison. Note that the lines are guides to the eye.

Figure 2c presents the evolution of the number density profiles for N atoms (black) and $N_2(A)$ metastable species (red) as a function of pressure. Here, the population of nitrogen atoms is obtained by a NO titration method [62,63] while the one of $N_2(A)$ is deduced from actinometry measurements using the emission from the first and second positive systems of N_2 [64]. All details on plasma diagnostics are presented in **Supplementary Data S1**. A significant increase of atomic nitrogen is observed as pressure increases from 1 Torr to 6 Torr, whereas the $N_2(A)$ remains more

or less constant. The addition of the hollow copper tube (open symbols) on the chamber walls only slightly alters the population of N₂(A) but drastically decreases the one of atomic nitrogen. This set of values is consistent with other sets of data obtained under comparable experimental conditions [21,56,58].

3.2 Assessment of plasma-induced damage

Raman imaging is used to characterize the modification to graphene [14,15,17,18,65,66] by the microwave N₂ plasma and the main results are presented in **Figure 3**. Untreated samples reveal graphene bands at: ~1580 cm⁻¹ (G) and ~2650 cm⁻¹ (2D), which generally gives 2D:G intensity ratios superior to 2, a characteristic of monolayer graphene [67]. In addition, two bands at 1350 cm⁻¹ (D) and 1600 cm⁻¹ (D') are used to construct images of the D:G intensity ratio, which is linked to defect density [12,15]. This D:G ratio allows to quantify the damage (e.g. pre-amorphization) induced by the plasma. **Figure 3a-c** and **3d-f** present the D:G mapping of the same regions probed for each sample before (untreated) and after 90 sec plasma treatments, respectively and according to the three conditions analyzed in **Section 3.1**. Initially, all untreated samples presents similar low (<0.1) D:G values. Localized regions of higher ratios (~0.3) indicate some inhomogeneities that are inherent to the growth conditions, which are probably due to the presence of diverse contaminations on the graphene surface [54,55]. Their evolution following plasma processing is detailed elsewhere [20,55] and here the discussion focuses on modifications within the graphene domains. The disorder at 1 Torr is much higher than the one at 6 Torr (D:G ~ 0.7 versus D:G ~ 0.3), while the condition with the hollow copper tube reveals very limited damage (D:G ~ 0.2 or less). A more in-depth characterisation method of graphene disorder was proposed by *Cancado et al.* [17] and consists of evaluating the areal D:G ratio multiplied by the energy of the laser at the forth power (ELaser4). **Figure 3g.** presents the energy-corrected D:G areal ratio for each sample for each treatment time as a function of the width of the G band (Γ_G). For reference, the gray lines show the expected behaviors for zero-dimensional (0D) and one-dimensional (1D) defects [17]. Although the amplitude of the change for a given treatment time is different, all treatment conditions reveal similar behavior following plasma-induced modification. More specifically, all samples show a small decrease of Γ_G for the initial treatments (typically linked to the removal of surface impurities) followed by a sharp rise of both D:G and Γ_G .

This trend in the D:G and Γ_G behavior suggests that the nature of the defects induced by the plasma treatments are the same in all cases. Over the range of experimental conditions investigated, using the framework developed by *Cancado et al.* [17], **Figure 3g** further indicates that the damage generation is mostly 0D with an average inter-defect distance (~ 4.5 nm for the later states), which is much lower than the size of nanocrystallites (~ 45 nm for the later states) [17]. This result also reveals that the damage generation is not limited to existing disordered regions as the latter is expected to produce 1D rather than 0D defects [17,68]. Finally, the change in the energy fluence for each condition delivered by plasma-generated species to the graphene lattice indicate different plasma-induced disorder levels. This important finding is further discussed below.

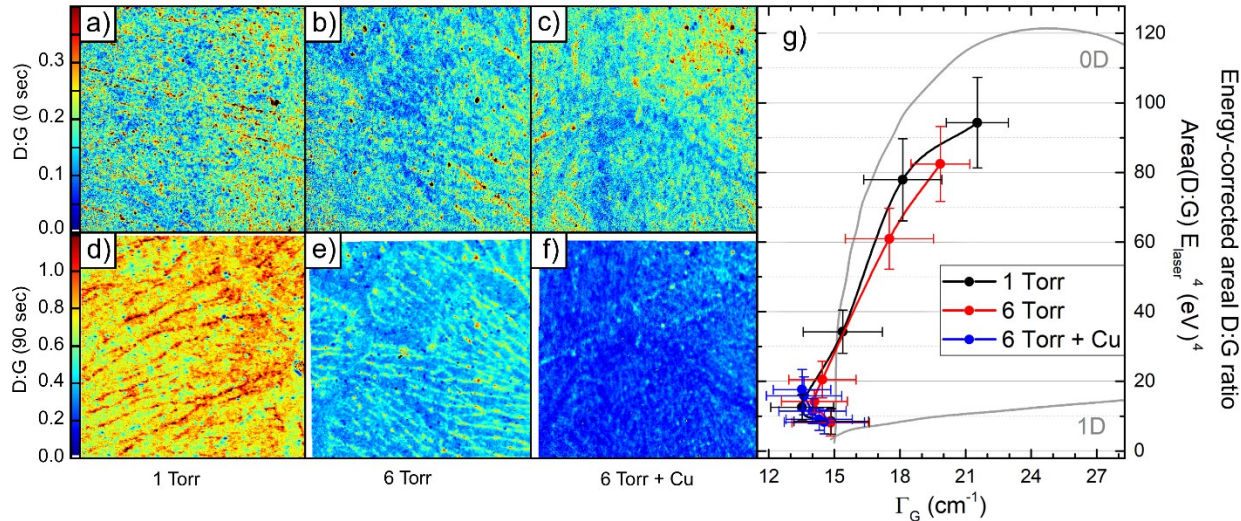


Figure 3 – Mappings of the D:G ratio for the untreated samples (a-c) and after 90 sec plasma treatments (d-f): 1 Torr (a,d), 6 Torr (b,e), and 6 Torr treatments in the presence of the copper tube (c,f). (g) Energy-corrected areal D:G ratio as a function of the width of the G band (Γ_G) for different treatment conditions and times. Lines are guides to the eyes. Error bars are one standard deviation as probed by RIMA measurements within the graphene domains

Based on the results presented in **Figure 2c**, the energy fluences provided to the graphene lattice by key species in the plasmas are calculated for each treatment condition. Two energy inputs for

damage formation are considered: heterogeneous surface recombination of nitrogen atoms (providing 5 eV per nitrogen atom) and heterogeneous surface deexcitation of metastable N₂(A) states (providing 6 eV per molecule of N₂(A)). In contrast to direct plasma treatments, the contribution of ion irradiation can be discarded here since the population of positive ions in the flowing afterglow is many orders of magnitude lower than the one of the metastables N₂(A) [21,56]. Surprisingly, the Raman results in **Figure 3** indicate significant damage introduced into the graphene samples by the species in the plasma while these are at relatively low energies (between 2 and 6 eV) compared to the energy thresholds for damage formation by ions and electrons, which are typically reported to be in the range between 18 and 22 eV [69,70]. Therefore, damage formation must involve low-energy surface deexcitation and recombination processes rather than simple knock-on collisions, but this mechanism remains to be understood. This could include defect creation through multi-steps processes, possibly involving Stone Wale defects characterized by a formation energy of ~5 eV [71–73]. It could also include “transitionary state of graphene” occurring as a result of electron excitation and subsequent energy dissipation through electron-phonon coupling [20,74–77].

As discussed previously [20,54,55], the band intensity ratio D:2D represents a key indicator of damage generation in graphene as it monotonously increases with damage and does not vary significantly with strain and doping [15]. **Figure 4a** and **4b** present the ratio D:2D as a function of the fluence of energy provided by either the heterogeneous surface recombination of nitrogen atoms or the heterogeneous surface deexcitation of metastable N₂(A) states, respectively. Here, as a first approximation, the probability of both processes is assumed to be equal to 1.

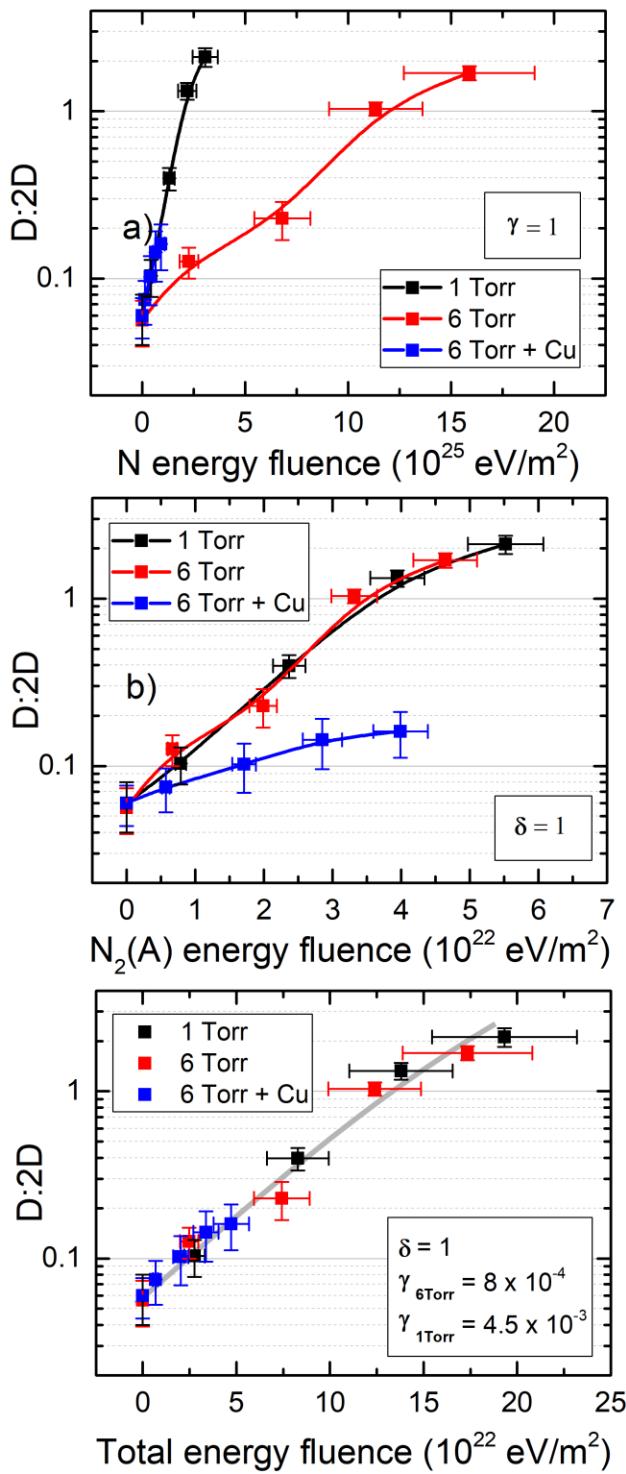


Figure 4 – Band ratio D:2D as a function of (a) N energy fluence, (b) $N_2(A)$ energy fluence and (c) $N + N_2(A)$ energy fluence. Lines are guides to the eyes.

Over the range of experimental conditions investigated, the energy fluence provided by N or $N_2(A)$ cannot explain the sharp growth in **Figure 4** of the D:2D ratio. In both cases, damage generation

exhibits different trends from one set of condition to the other. On one hand, the 1 Torr and 6 Torr with Cu show in **Figure 4a** similar behaviors while the 6 Torr condition without Cu is a way off. On the other hand, the 1 Torr and 6 Torr conditions in **Figure 4b** reveal similar behaviors but the 6 Torr with Cu is again a way off the trends. This complete set of data suggests that both mechanisms play an important role in damage formation. This aspect is examined in more details by considering a total energy fluence, E_{Total} , represented as a linear contribution of the ones due to surface recombination of N atoms, E_N , and to surface deexcitation of $N_2(A)$ states, E_{N2A} :

$$E_{Total} = \gamma E_N + \delta E_{N2A}, \quad (2)$$

where γ and δ are dimensionless parameters (between 0 and 1) that represent the probability for the recombination of N and for the deexcitation of $N_2(A)$ at the graphene surface, respectively. Assuming $\delta=1$ and treating γ as an adjustable parameter for the 1 Torr and 6 Torr data sets, we note a universal trend for all conditions explored (**Figure 4c**). Quantitatively, γ values obtained from the best fits are 4.5×10^{-3} at 1 Torr and 8×10^{-4} at 6 Torr. These values match extremely well the ones reported by other authors [59,60]. A decrease of the surface recombination of nitrogen atoms with increasing pressure has also been observed by a number of authors and is ascribed to a competition between nitrogen atoms and molecules for adsorption sites [60,78,79].

3.3 Analysis of the plasma-induced N incorporation

Figure 5 presents the XPS areal ratio N:C as a function of the fluence of plasma-generated nitrogen atoms provided to the graphene lattice. The survey spectra obtained from XPS analysis are presented in **Supplementary Data S2**. Here, the fluence is calculated from the number density of N atoms provided in **Figure 2c**. Only plasma-generated N atoms are considered since dissociative adsorption of N_2 is negligible for carbonaceous materials [80,81]. For short plasma treatment times, i.e. small fluences of nitrogen atoms, all conditions reveal similar nitrogen content. However, for longer plasma treatment times, and thus larger fluences, departures are observed between the conditions at 1 Torr and 6 Torr. In particular, the 1 Torr treatment systematically provides larger nitrogen incorporation levels for a given nitrogen dose. Based on **Figure 4a**, damage generation for comparable fluence of plasma-generated nitrogen atoms is more important at 1 Torr than at 6 Torr. The increased incorporation at 1 Torr thus seems to be enabled

by strongly disordered states. Over the range of experimental conditions, high-resolution XPS analysis further shows that all treatments reveal similar content of pyridine, pyrrole or quaternary moieties [41,82–84]. This finding is obtained from the N1s and C1s high-resolution spectra presented in **Supplementary Data S2**.

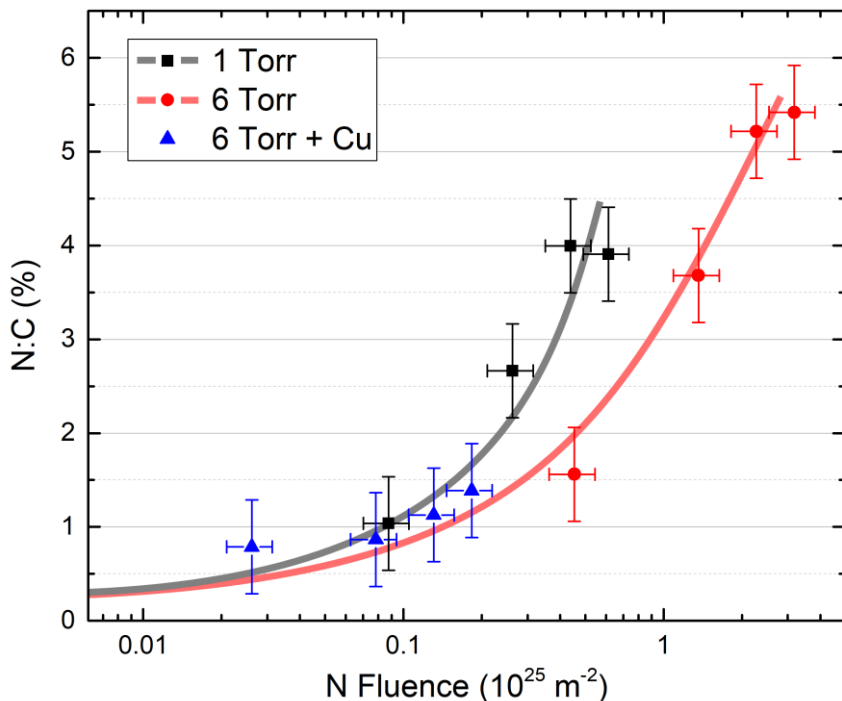


Figure 5 – XPS N:C areal ratio as a function of fluence of nitrogen atoms for treatment conditions at 1 and 6 Torr and at 6 Torr with Cu. Lines are guides to the eyes only.

The influence of surface disorders on the nitrogen incorporation is examined in more details by correlating the N:C values obtained from XPS with the Raman D:2D band ratios. The results are presented in **Figure 6**. For low damage levels, i.e. low D:2D band ratios, the XPS results reveal similar nitrogen content despite a significant difference in the fluence of the plasma-generated nitrogen atoms. For stronger lattice disorders, i.e. higher D:2D band ratios, a clear separation in the total N:C content is noted between 1 and 6 Torr conditions. More specifically, higher nitrogen contents are detected for comparable damage levels at 6 Torr than at 1 Torr. Because the

population of nitrogen atoms is higher at 6 Torr than at 1 Torr, see **Figure 2c**, these results indicate that the nitrogen incorporation depends on the fluence of the plasma-generated nitrogen atoms.

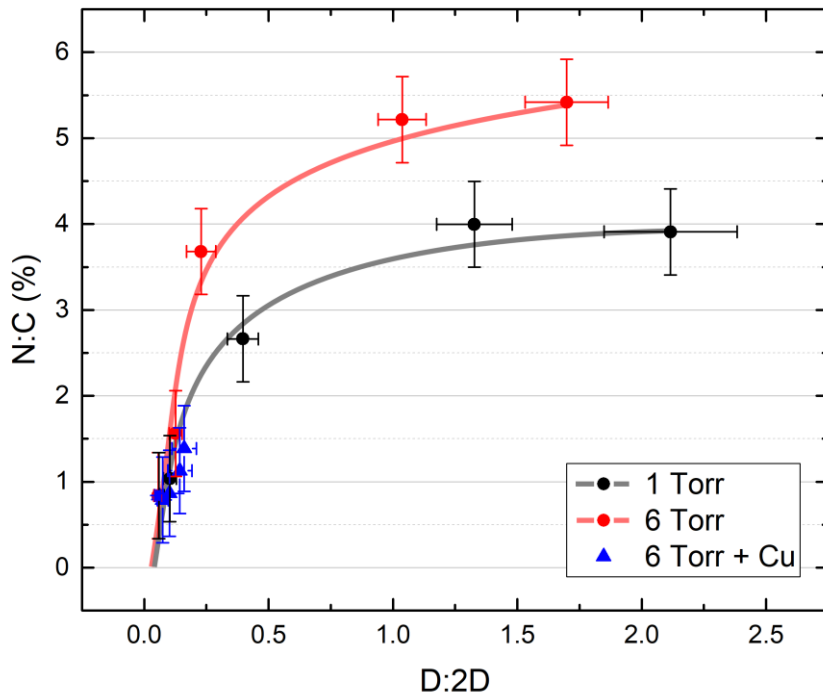
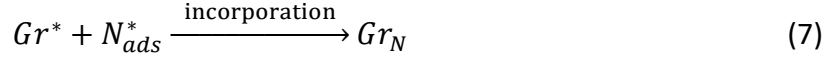


Figure 6 – XPS N:C areal ratio as a function of Raman D:2D band ratio for all treatment conditions. Lines are guides to the eyes.

In order to better understand the trends displayed in **Figure 6**, a surface reaction model for the nitrogen incorporation in monolayer graphene is proposed. This model includes: (i) 0D defect formation by heterogeneous surface recombination of N atoms and heterogeneous surface deexcitation of $N_2(A)$ metastable species, (ii) adsorption of the plasma-generated nitrogen atoms on a site of the graphene surface, (iii) migration of adsorbed nitrogen atoms from one site to the other on the graphene surface, (iv) surface recombination of the adsorbed nitrogen atoms leading to the desorption of $N_2(X)$ from the graphene surface, and (v) incorporation of adsorbed nitrogen atoms in the graphene lattice at a native or a plasma-induced defect site:





where Gr is a surface site of the graphene, Gr^* is a 0D defect site, and Gr_N is a nitrogen incorporation site leading to either pyridine, pyrrole or quaternary moieties. In Equations (4)-(7), N_{ads} is a nitrogen atom adsorbed on graphene and N_{ads}^* is a nitrogen atom adsorbed at a defect site in the graphene lattice. In this framework, the rate for adsorption (v_{ads} , Equation (4)) and desorption (v_{des} , which includes the recombination, v_{rec} , in Equation (6) and the incorporation, v_{inc} , in Equation (7)) processes can be written as [85]:

$$v_{ads} = \Gamma_N S_N (1 - \theta_N) n_0 \quad (8)$$

$$v_{des} = v_{rec} + v_{inc} = \Gamma_{rec} \theta_N n_0 + k_{inc} n_{Gr^*} \theta_N n_0 \quad (9)$$

where Γ_N is the flux of nitrogen atoms impinging onto the graphene sample ($m^{-2} s^{-1}$); S_N is the adsorption probability (*i.e.* a dimensionless parameter between 0 and 1) of nitrogen atoms; θ_N is the fraction of graphene sites covered by the adsorbed nitrogen atoms (*i.e.* a dimensionless parameter between 0 and 1); n_0 is the surface density of adsorption sites on the graphene lattice (m^{-2}); n_{Gr^*} is the surface density of defect sites in the graphene lattice (m^{-2}); Γ_{rec} is the flux of nitrogen atoms desorbing from the graphene sample due to heterogeneous surface recombination (in $m^{-2} s^{-1}$; this parameter is linked to the surface recombination coefficient γ [86]); k_{inc} is the reaction frequency for incorporating an absorbed nitrogen atoms into a graphene defect site (s^{-1}). At steady-state, $v_{ads} = v_{des}$ such that θ_N can be written as:

$$\theta_N = \left(1 + \frac{\Gamma_{rec} + k_{inc} n_{Gr^*}}{\Gamma_N S_N} \right)^{-1}. \quad (10)$$

Since the nitrogenation of the graphene film is proportional to the incorporation rate provided by Equation (7), the nitrogen content, as probed by XPS, can be written as:

$$\frac{N}{C} \propto k_{inc} n_{Gr^*} \theta_N n_0 = \frac{k_{inc} n_{Gr^*} n_0}{\left(1 + \frac{\Gamma_{rec} + k_{inc} n_{Gr^*}}{\Gamma_N S_N}\right)}. \quad (11)$$

From Equation (11), the model predicts that the nitrogen incorporation should increase linearly with the number density of defect sites and its slope is independent of the population of plasma-generated nitrogen atoms. This corresponds to a defect-limited nitrogen incorporation regime, which is in good agreement with the experimental data presented in Figure 6 at low damage levels. Beyond that point when the damage level is very high, both the defect density and the fluence of plasma-generated atoms drive the nitrogen incorporation. Finally, when damage levels is very large, the nitrogen incorporation becomes independent of the defect concentration, which corresponds to an adsorption-limited incorporation regime. This is in good agreement with the experimental data presented in Figure 6 at high damage levels.

In line with the good agreement between the model and experimental findings, one can probably better understand the different trends reported in literature. Some reports indicate a rise of the nitrogen content with the plasma treatment time [32–34], while others show either a saturation or even a loss behavior with the dose of plasma-generated nitrogen species [8,35,36]. These different trends thus seem to be linked to either the adsorption- or defect-limited incorporation regime.

4. Conclusion

A detailed characterisation of the flowing afterglow of a microwave nitrogen plasma at reduced pressure and of CVD-grown graphene samples treated in such plasma was used to highlight the roles of each plasma-generated species in the nitrogenation of graphene films. Both the heterogenous surface recombination of nitrogen atoms and the heterogeneous surface deexcitation of metastable N₂ species were found to play an important role in damage formation. As for the nitrogen incorporation, it first rises with plasma-induced damage according to a behavior that is independent of the flux of plasma-generated nitrogen atoms. For larger damage levels, both the defect density and the population of nitrogen atoms influence the incorporation. A comprehensive surface reaction model is proposed to highlight a defect-limited incorporation regime at low disorder and an adsorption-limited incorporation regime at higher disorder.

5. Acknowledgments

This work was financially supported by the National Science and Engineering Research Council (NSERC), PRIMA-Québec, Plasmionique inc., Photon Etc., and the Fonds de Recherche du Québec – Nature et Technologies (FRQNT). L.S. and R.M. acknowledge support from the Canada Research Chair and from the Canadian Foundation of Innovation.

6. Author contributions

Germain Robert Bigras performed all experimental measurements and data treatment. All authors contributed to the design of the experiments, the data interpretation and the manuscript revision. Luc Stafford and Richard Martel contributed to the funding acquisition and the supervision of the study.

7. Competing interests

The authors declare that there are no competing interests.

8. Data availability statement

The data that support the findings of this study are available from the corresponding author upon request.

9. References

- [1] A.C. Ferrari, F. Bonaccorso, V. Fal’ko, K.S. Novoselov, *Nanoscale* 7 (2015) 4598–4810.
- [2] Q. Tang, Z. Zhou, Z. Chen, *Nanoscale* 5 (2013) 4541.
- [3] S.K. Vashist, J.H.T. Luong, *Carbon N. Y.* 84 (2015) 519–550.
- [4] M. Baraket, R. Stine, W.K. Lee, J.T. Robinson, C.R. Tamanaha, P.E. Sheehan, S.G. Walton, *Appl. Phys. Lett.* 100 (2012) 233123.
- [5] N.G. Shang, P. Papakonstantinou, M. McMullan, M. Chu, A. Stamboulis, A. Potenza, S.S. Dhesi, H. Marchetto, *Adv. Funct. Mater.* 18 (2008) 3506–3514.
- [6] H. Tian, Z. Sofer, M. Pumera, A. Bonanni, *Nanoscale* 9 (2017) 3530–3536.
- [7] R. Narayanan, H. Yamada, M. Karakaya, R. Podila, A.M. Rao, P.R. Bandaru, *Nano Lett.* 15 (2015) 3067–3072.
- [8] H.M. Jeong, J.W. Lee, W.H. Shin, Y.J. Choi, H.J. Shin, J.K. Kang, J.W. Choi, *Nano Lett.* 11 (2011) 2472–2477.
- [9] C.N.R. Rao, K. Gopalakrishnan, A. Govindaraj, *Nano Today* 9 (2014) 324–343.

- [10] T. Xing, Y. Zheng, L.H. Li, B.C.C. Cowie, D. Gunzelmann, S.Z. Qiao, S. Huang, Y. Chen, *ACS Nano* 8 (2014) 6856–6862.
- [11] F. Banhart, J. Kotakoski, A. V. Krasheninnikov, *ACS Nano* 5 (2011) 26–41.
- [12] M.M. Lucchese, F. Stavale, E.H.M. Ferreira, C. Vilani, M.V.O. Moutinho, R.B. Capaz, C. a. Achete, A. Jorio, *Carbon N. Y.* 48 (2010) 1592–1597.
- [13] A.C. Ferrari, J. Robertson, *Phys. Rev. B* 61 (2000) 14095–14107.
- [14] J.E. Lee, G. Ahn, J. Shim, Y.S. Lee, S. Ryu, *Nat. Commun.* 3 (2012) 1024.
- [15] M. Bruna, A.K. Ott, M. Ijäs, D. Yoon, U. Sassi, A.C. Ferrari, *ACS Nano* 8 (2014) 7432–7441.
- [16] K.S. Mali, J. Greenwood, J. Adisoejoso, R. Phillipson, S. De Feyter, *Nanoscale* 7 (2015) 1566–1585.
- [17] L. Gustavo Cançado, M. Gomes da Silva, E.H. Martins Ferreira, F. Hof, K. Kampioti, K. Huang, A. Pénicaud, C. Alberto Achete, R.B. Capaz, A. Jorio, *2D Mater.* 4 (2017) 025039.
- [18] A. Eckmann, A. Felten, I. Verzhbitskiy, R. Davey, C. Casiraghi, *Phys. Rev. B* 88 (2013) 035426.
- [19] P. Vinchon, X. Glad, G. Robert-Bigras, R. Martel, A. Sarkissian, L. Stafford, *J. Appl. Phys.* 126 (2019) 233302.
- [20] P. Vinchon, X. Glad, G. Robert Bigras, R. Martel, L. Stafford, *Nat. Mater.* (2020).
- [21] G. Robert Bigras, X. Glad, R. Martel, A. Sarkissian, L. Stafford, *Plasma Sources Sci. Technol.* 27 (2018) 124004.
- [22] A. V. Krasheninnikov, K. Nordlund, *J. Appl. Phys.* 107 (2010) 071301.
- [23] O. Lehtinen, J. Kotakoski, A. V. Krasheninnikov, A. Tolvanen, K. Nordlund, J. Keinonen, *Phys. Rev. B* 81 (2010) 153401.
- [24] O. Lehtinen, J. Kotakoski, a V Krasheninnikov, J. Keinonen, *Nanotechnology* 22 (2011) 175306.
- [25] G. Gawlik, P. Ciepielewski, J. Jagielski, J. Baranowski, *Nucl. Instruments Methods Phys. Res. Sect. B Beam Interact. with Mater. Atoms* 406 (2017) 683–688.
- [26] C. Wang, Y. Zhou, L. He, T.-W. Ng, G. Hong, Q.-H. Wu, F. Gao, C.-S. Lee, W. Zhang, *Nanoscale* 5 (2013) 600–605.
- [27] X. Xie, D. Su, J. Zhang, S. Chen, A.K. Mondal, G. Wang, *Nanoscale* 7 (2015) 3164–3172.
- [28] T. Schiros, D. Nordlund, L. Pálová, D. Prezzi, L. Zhao, K.S. Kim, U. Wurstbauer, C. Gutiérrez, D. Delongchamp, C. Jaye, D. Fischer, H. Ogasawara, L.G.M. Pettersson, D.R. Reichman, P. Kim, M.S. Hybertsen, A.N. Pasupathy, *Nano Lett.* 12 (2012) 4025–4031.
- [29] W. Zhao, O. Höfert, K. Gotterbarm, J.F. Zhu, C. Papp, H.-P. Steinrück, *J. Phys. Chem. C* 116 (2012) 5062–5066.
- [30] M. Telychko, P. Mutombo, M. Ondráček, P. Hapala, F.C. Bocquet, J. Kolorenč, M. Vondráček, P. Jelínek, M. Švec, *ACS Nano* 8 (2014) 7318–7324.
- [31] Y.P. Lin, Y. Ksari, J. Prakash, L. Giovanelli, J.C. Valmalette, J.M. Themlin, *Carbon N. Y.* 73 (2014) 216–224.
- [32] I. Bertóti, M. Mohai, K. László, *Carbon N. Y.* 84 (2015) 185–196.
- [33] M. Rybin, A. Pereyaslavtsev, T. Vasilieva, V. Myasnikov, I. Sokolov, A. Pavlova, E. Obraztsova, A. Khomich, V. Ralchenko, E. Obraztsova, *Carbon N. Y.* 96 (2016) 196–202.
- [34] F. Orlando, P. Lacovicig, M. Dalmiglio, A. Baraldi, R. Larciprete, S. Lizzit, *Surf. Sci.* 643 (2015) 214–221.
- [35] B. Liu, C.-M. Yang, Z. Liu, C.-S. Lai, *Nanomaterials* 7 (2017) 302.

- [36] N. M. Santhosh, G. Filipič, E. Kovacevic, A. Jagodar, J. Berndt, T. Strunskus, H. Kondo, M. Hori, E. Tatarova, U. Cvelbar, *Nano-Micro Lett.* 12 (2020) 53.
- [37] A. Dias, N. Bundaleski, E. Tatarova, F.M. Dias, M. Abrashev, U. Cvelbar, O.M.N.D. Teodoro, J. Henriques, *J. Phys. D. Appl. Phys.* 49 (2016) 055307.
- [38] N. Bundaleska, N. Bundaleski, A. Dias, F.M. Dias, M. Abrashev, G. Filipič, U. Cvelbar, Z. Rakočević, Z. Kissovski, J. Henriques, E. Tatarova, *Mater. Res. Express* 5 (2018) 095605.
- [39] L.G. Cançado, A. Jorio, E.H.M. Ferreira, F. Stavale, C. a. Achete, R.B. Capaz, M.V.O. Moutinho, A. Lombardo, T.S. Kulmala, a. C. Ferrari, *Nano Lett.* 11 (2011) 3190–3196.
- [40] A. Eckmann, A. Felten, A. Mishchenko, L. Britnell, R. Krupke, K.S. Novoselov, C. Casiraghi, *Nano Lett.* 12 (2012) 3925–3930.
- [41] J.B. McManus, A. Hennessy, C.P. Cullen, T. Hallam, N. McEvoy, G.S. Duesberg, *Phys. Status Solidi* 1700214 (2017) 1700214.
- [42] L. Lefèvre, T. Belmonte, H. Michel, *J. Appl. Phys.* 87 (2000) 7497–7507.
- [43] T. Czerwic, H. Michel, E. Bergmann, *Surf. Coatings Technol.* 108–109 (1998) 182–190.
- [44] Z.L. Petrovic, V.L. Markovic, M.M. Pejovic, S.R. Gocic, *J. Phys. D. Appl. Phys.* 34 (2001) 1756–1768.
- [45] M.P. Fewell, S.C. Haydon, *J. Phys. D. Appl. Phys.* 30 (1997) 1778–1782.
- [46] M.. Fewell, S.. Haydon, A.. Ernest, *Chem. Phys.* 206 (1996) 257–267.
- [47] V. Guerra, P.A. Sá, J. Loureiro, *J. Phys. Conf. Ser.* 63 (2007) 012007.
- [48] J.A. Ferreira, H.P.T. Nguyen, Z. Mi, R. Leonelli, L. Stafford, *Nanotechnology* 25 (2014) 435606.
- [49] S. Choubak, M. Biron, P.L. Levesque, R. Martel, P. Desjardins, *J. Phys. Lett.* 4 (2013) 1100–1103.
- [50] H.J. Jeong, H.Y. Kim, S.Y. Jeong, J.T. Han, K.-J. Baeg, J.Y. Hwang, G.-W. Lee, *Carbon N. Y.* 66 (2014) 612–618.
- [51] F. Qing, Y. Zhang, Y. Niu, R. Stehle, Y. Chen, X. Li, *Nanoscale* 12 (2020) 10890–10911.
- [52] G. Robert Bigras, X. Glad, L. Vandsburger, C. Charpin, P. Levesque, R. Martel, L. Stafford, *Carbon N. Y.* 144 (2019) 532–539.
- [53] E. Gaufrès, S. Marcket, V. Aymong, N.Y.W. Tang, A. Favron, F. Thouin, C. Allard, D. Rioux, N. Cottenye, M. Verhaegen, R. Martel, *J. Raman Spectrosc.* 49 (2018) 174–182.
- [54] G. Robert Bigras, P. Vinchon, C. Allard, X. Glad, R. Martel, L. Stafford, *Rev. Sci. Instrum.* 91 (2020) 063903.
- [55] G. Robert Bigras, X. Glad, P. Vinchon, R. Martel, L. Stafford, Submitt. to *NPJ 2D Mater. Appl.* (2020).
- [56] J. Afonso Ferreira, L. Stafford, R. Leonelli, A. Ricard, *J. Appl. Phys.* 115 (2014) 163303.
- [57] M. Moisan, Z. Zakrzewski, R. Pantel, *J. Phys. D. Appl. Phys.* 12 (1979) 219–237.
- [58] H. Zerrouki, A. Ricard, J.P. Sarrette, *Contrib. to Plasma Phys.* 54 (2014) 827–837.
- [59] Y.C. Kim, M. Boudart, *Langmuir* 7 (1991) 2999–3005.
- [60] J.-P. Sarrette, B. Rouffet, A. Ricard, *Plasma Process. Polym.* 3 (2006) 120–126.
- [61] J. Guha, R. Khare, L. Stafford, V.M. Donnelly, S. Sirard, E.A. Hudson, *J. Appl. Phys.* 105 (2009) 113309.
- [62] P. Vasina, V. Kudrle, A. Tálský, P. Boto, M. Mrázková, M. Me ko, *Plasma Sources Sci. Technol.* 13 (2004) 668–674.
- [63] A. Ricard, M.M.S. Moreau, 34 (2001) 1203–1212.

- [64] A. Ricard, S. Oh, V. Guerra, *Plasma Sources Sci. Technol.* 22 (2013) 035009.
- [65] A. Das, S. Pisana, B. Chakraborty, S. Piscanec, S.K. Saha, U. V Waghmare, K.S. Novoselov, H.R. Krishnamurthy, a K. Geim, A.C. Ferrari, A.K. Sood, *Nat. Nanotechnol.* 3 (2008) 210–215.
- [66] R. Beams, L. Gustavo Cançado, L. Novotny, *J. Phys. Condens. Matter* 27 (2015) 083002.
- [67] A.C. Ferrari, J.C. Meyer, V. Scardaci, C. Casiraghi, M. Lazzeri, F. Mauri, S. Piscanec, D. Jiang, K.S. Novoselov, S. Roth, A.K. Geim, *Phys. Rev. Lett.* 97 (2006) 187401.
- [68] M. Seifert, J.E.B. Vargas, M. Bobinger, M. Sachsenhauser, A.W. Cummings, S. Roche, J.A. Garrido, *2D Mater.* 2 (2015) 024008.
- [69] F. Banhart, *Reports Prog. Phys.* 62 (1999) 1181.
- [70] B.W. Smith, D.E. Luzzi, *J. Appl. Phys.* 90 (2001) 3509–3515.
- [71] J. Kotakoski, A. V. Krasheninnikov, U. Kaiser, J.C. Meyer, *Phys. Rev. Lett.* 106 (2011) 105505.
- [72] L. Li, S. Reich, J. Robertson, *Phys. Rev. B* 72 (2005) 184109.
- [73] J. Ma, D. Alfè, A. Michaelides, E. Wang, *Phys. Rev. B* 80 (2009) 033407.
- [74] A. Tomadin, D. Brida, G. Cerullo, A.C. Ferrari, M. Polini, *Phys. Rev. B* 88 (2013) 035430.
- [75] M. Lazzeri, S. Piscanec, F. Mauri, A.C. Ferrari, J. Robertson, *Phys. Rev. Lett.* 95 (2005) 236802.
- [76] C. Su, M. Tripathi, Q.-B. Yan, Z. Wang, Z. Zhang, C. Hofer, H. Wang, L. Basile, G. Su, M. Dong, J.C. Meyer, J. Kotakoski, J. Kong, J.-C. Idrobo, T. Susi, J. Li, *Sci. Adv.* 5 (2019) eaav2252.
- [77] S. Butscher, F. Milde, M. Hirtschulz, E. Malić, A. Knorr, *Appl. Phys. Lett.* 91 (2007) 203103.
- [78] D. V Lopaev, E.M. Malykhin, S.M. Zyryanov, *J. Phys. D. Appl. Phys.* 44 (2011) 015201.
- [79] V.M. Donnelly, J. Guha, L. Stafford, *J. Vac. Sci. Technol. A Vacuum, Surfaces, Film.* 29 (2011) 010801.
- [80] A. Allouche, Y. Ferro, *Carbon N. Y.* 44 (2006) 3320–3327.
- [81] Y.-J. Xu, J.-Q. Li, *Chem. Phys. Lett.* 406 (2005) 249–253.
- [82] N. Hellgren, R.T. Haasch, S. Schmidt, L. Hultman, I. Petrov, *Carbon N. Y.* 108 (2016) 242–252.
- [83] M. Scardamaglia, T. Susi, C. Struzzi, R. Snyders, G. Di Santo, L. Petaccia, C. Bittencourt, *Sci. Rep.* 7 (2017) 7960.
- [84] C.D. Batich, D.S. Donald, *J. Am. Chem. Soc.* 106 (1984) 2758–2761.
- [85] M.A. Lieberman, A.J. Lichtenberg, in:, Wiley-Interscience (Ed.), 1, Second Edi, A John Wiley & Sons, 2005, pp. 311–320.
- [86] P.J. Chantry, *J. Appl. Phys.* 62 (1987) 1141–1148.

10. Supplementary Data

Additional data on the NO titration, actinometry and XPS HR N1s data are provided in **Annexe 6** of this thesis.

4.3 Rôle des espèces oxydantes

Tel que discuté dans la **Section 4.2**, la recombinaison d'azote atomique ainsi que la désexcitation de métastables de l'azote moléculaire en surface du graphène jouent un rôle crucial dans la formation de dommages. Nous nous intéressons dans cette section au rôle que pourraient avoir les espèces oxydantes sur les propriétés du graphène lors d'expositions dans la post-décharge en flux d'azote. Dans ce contexte, nous discutons de traitements réalisés dans la post-décharge lointaine du plasma d'azote dans trois conditions opératoires différentes : traitement en azote ultra haute pureté avec purificateur de gaz, en azote haute pureté sans purificateur de gaz et en azote haute pureté avec ajout de 0.25% d'oxygène. Dans tous les cas, la pureté de la bonbonne d'azote est de 99.999% et le vide résiduel dans le réacteur à plasma est de 2×10^{-7} Torr. Trois purges de la chambre du réacteur et de toutes les lignes sont effectuées avec tout traitement ou séance de caractérisation par spectroscopie optique d'émission. Le purificateur *SAES Pure Gas Inc Nitrogen MC1-902F* permet d'amener les impuretés gazeuses sous les 100 parties-par-trillion.

Tel que décrit au **Chapitre 1**, on pourrait s'attendre à une plus forte production de défauts dans les plasmas à base d'oxygène. En effet, que ce soit pour les traitements directs ou indirects, avec ou sans chauffage de l'échantillon, plusieurs auteurs ont rapporté des gravures partielles ou complètes du graphène [R42,52,98]. Ainsi, les études de graphène fonctionnalisé par traitement avec des plasmas à base d'oxygène sont typiquement réalisées pour de très courts temps de traitement : 1 à 3 sec. Pour les recuits thermiques (**Section 1.1.3**) en atmosphère d'oxygène, la gravure n'a lieu que pour des température d'environ 500 K [R32] et sur des échelle de temps de la dizaine de minutes.

Sur un autre sujet, la présence de traces d'oxygène dans la post-décharge en flux de plasmas d'azote à pression réduite s'est vue attirer un intérêt particulier pour la stérilisation d'objets médicaux ainsi que pour le traitement de matériaux ligno-cellulosiques comme le bois [R81,99,100]. En particulier, elle favorise la présence d'espèces excitées (notamment NO) qui sont responsables de l'émission de photons de faible longueur d'onde (200-300 nm). Elle assure également la présence d'atomes d'oxygène permettant la gravure de matériaux polymériques. Pour une faible concentration d'oxygène (< 0.25 %), la densité d'azote atomique augmente

typiquement d'environ un facteur 2-3. Après ce maximum, la concentration diminue progressivement. Quant à la densité d'oxygène atomique, elle augmente de manière monotone avec l'ajout d'oxygène dans la post-décharge en flux du plasma d'azote [R81].

La **Figure 24** présente les spectres d'émission optique de la post-décharge en flux pour les trois conditions opératoires choisies. On note les bandes du second système positif (SPS) de l'azote à 316 nm et la bande NO_β à 320 nm. Avec l'ajout du purificateur de gaz, on distingue une baisse marquée de l'émission de NO. Pour les conditions de pression étudiées (6 Torr dans le réacteur versus un vide résiduel de 2×10^{-7} Torr), il semble donc que la contamination d'impuretés dans la phase gazeuse provenant de la bouteille est suffisante pour altérer substantiellement la post-décharge en flux. L'ajout de l'impureté contrôlée de 0.25% d'oxygène transforme énormément l'allure du spectre. Le SPS de l'azote est peu reconnaissable et noyé dans d'autres émissions.

Au **Tableau 1** sont présentées les densités de l'azote atomique, de l'oxygène atomique et des métastables N₂(A) pour les trois conditions opératoires choisies. Alors que la densité de métastables reste sensiblement constante pour toutes les conditions, la densité d'atomes d'azote augmente d'environ un facteur 4 entre la condition la plus pure et celle comportant le plus d'oxygène. Ces données sont conformes avec celles de la littérature [R81]. L'oxygène, pour sa part, montre une augmentation assez marquée d'un peu moins d'un facteur 100 entre les deux conditions.

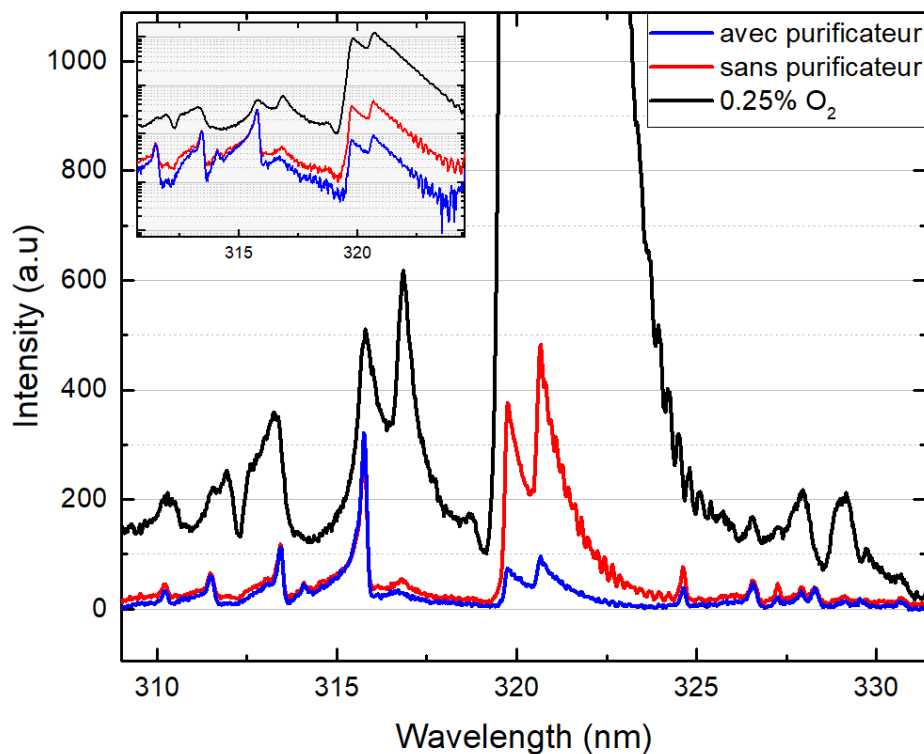


Figure 24 : Spectres des trois conditions étudiées pour cibler le rôle des espèces oxydantes. On distingue le second système positif de l'azote (~316 nm) et l'émission de la NO_β à 320 nm.

Densité (m ⁻³)	Purificateur	Sans purificateur	0.25% O ₂
N	1.14 x 10 ²¹	1.50 x 10 ²¹	5.41 x 10 ²¹
N ₂ (A)	3.66 x 10 ¹⁷	3.24 x 10 ¹⁷	3.68 x 10 ¹⁷
O	2.74 x 10 ¹⁹	1.93 x 10 ²⁰	2.43 x 10 ²¹

Tableau 1 : Densités d'espèces dans la post-décharge en flux pour trois conditions de pureté du gaz principal.

Pour chacune des conditions, une zone est sélectionnée au microscope optique sur l'échantillon de graphène. Celle-ci est prise afin d'être suffisamment éloignée des bords de l'échantillon et loin de défauts apparents en surface du graphène reliés à la croissance ou au transfert. Ces mêmes régions sont sondées par imagerie Raman (**RIMA Section 3.2**) avant et après chaque traitement subséquent de 60 secondes. La même région est caractérisée par XPS. Des régions de nature similaire sont identifiées par la méthode de regroupement de la **Section 3.4**. Seuls les domaines

du graphène sont considérés pour la suite des résultats, puisque ceux-ci représentent la forte majorité de la surface (~70%).

La **Figure 25a** montre l'évolution de ratio d'aire des pics D et G (corrigé en énergie) en fonction de la largeur à mi-hauteur de la bande G. En gris sont présentés les profils attendus pour une production de dommages purement 0D et 1D [R101]. L'ensemble des conditions étudiées suit une même courbe de progression de dommages. Toutefois, l'amplitude des dommages est beaucoup plus prononcée pour les traitements en présence d'oxygène. Dans l'ensemble, l'évolution des dommages reportée est principalement 0D. La baisse du signal D:G suivant un certain degré de désordre est signe d'une transition graduelle du graphène vers un état amorphe; *Régime 1* – pré-amorphisation et le *Régime 2* – amorphisation [R101–103]. En vue de s'affranchir de la dépendance de D:G sur le dopage, D:2D est typiquement choisi comme critère de désordre monotone [R104]. L'axe des abscisses a donc été remplacé par D:2D à la **Figure 25b**. On note la transition du Régime 1 vers le Régime 2 pour des valeurs de D:2D d'environ 3. À noter que l'échantillon traité dans la post-décharge lointaine à 6 Torr (sans le tube de cuivre) et discuté à la **Section 4.2** est également présenté. Notons que des variations sur l'effet des traitements peuvent être attendues puisque l'échantillon provient d'une autre croissance de graphène et que de légères variations entre croissances peuvent avoir lieu (propreté de la chambre de croissance, pureté du polymère PMMA utilisé dans le transfert). Dans tous les cas, un accord entre l'ensemble des données est observé, ce qui suggère que ces variations sont assez minimales, en particulier à la **Figure 25b** sur laquelle l'accord est assez remarquable.

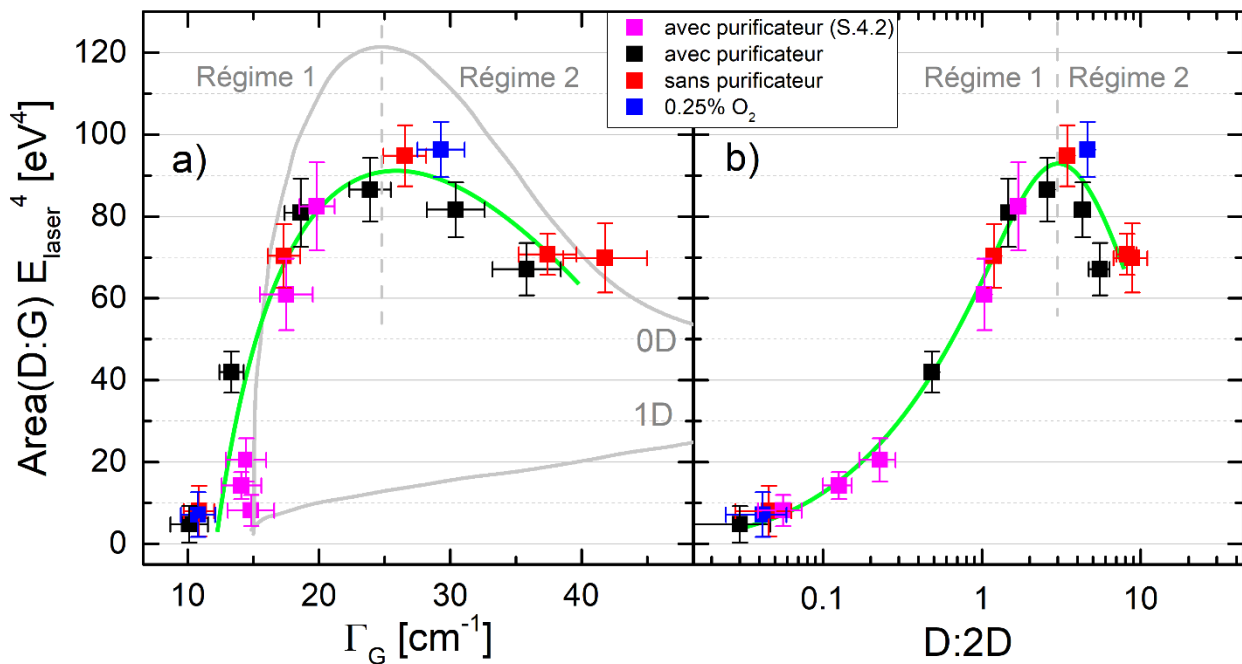


Figure 25 : Évolution du ratio d'aire $D:G$ corrigé en énergie en fonction de la largeur à mi-hauteur de la bande G . Les deux courbes en gris représentent le comportement attendu pour des défauts purement 0D ou 1D. La ligne verte est pour guider l'œil seulement.

Tel que discuté dans l'article présenté à la **Section 4.2**, pour une condition de pression donnée, la cinétique de formation de dommages suit la fluence totale d'énergie fournie par la recombinaison en surface des atomes d'azotes et la désexcitation en surface des métastables $N_2(A)$. La **Figure 26** présente la fluence totale d'énergie pour ces mêmes réactions pour toutes les conditions de pureté d'oxygène étudiées ainsi que pour la courbe de post-décharge lointaine avec purificateur présentée dans l'article de la **Section 4.2**. Les coefficients de probabilité de dépôt d'énergie déterminés à la **Section 4.2** sont utilisés. On constate qu'en considérant l'erreur assez importante des méthodes de caractérisation, les courbes suivent un comportement très similaire. On conclut ainsi que, pour toutes les conditions étudiées, le rôle de l'oxygène atomique dans la dynamique de formation des dommages est négligeable face aux autres mécanismes inhérents à la post-décharge en flux du plasma d'azote. Si l'oxygène atomique avait joué un rôle dans la production de défauts, on s'attendrait à un écart considérable entre les valeurs de $D:2D$ sur la

vaste gamme de fluences rapportées à la **Figure 26**. Ainsi, la présence de l'oxygène dans la post-décharge en flux d'azote ne joue qu'indirectement sur la production de défauts : elle ne fait qu'augmenter la population de N.

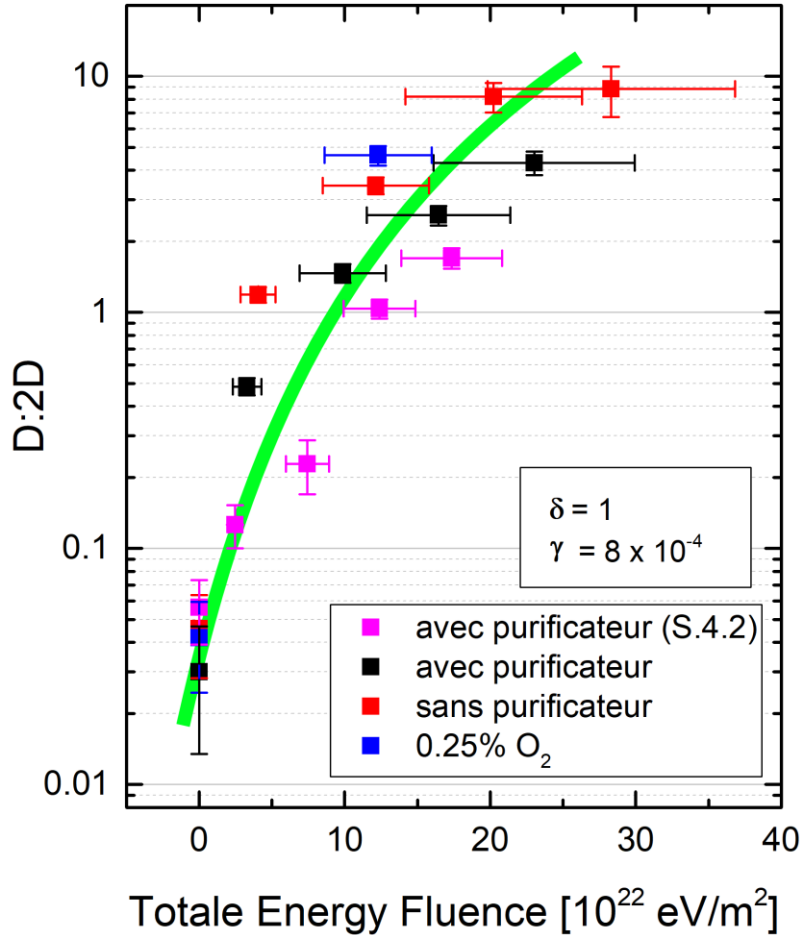


Figure 26 : Évolution du ratio D:2D en fonction de la fluence totale de recombinaison des N et de la désexcitation des métastables N₂(A) en surface. La ligne est pour guider l'œil uniquement.

Inspirée des analyses de l'article de la **Section 4.2**, la **Figure 27** présente le ratio N:C obtenu des survols XPS en fonction du ratio D:2D obtenu par RIMA pour les trois présences d'espèces oxydantes étudiées. Avant que le graphène n'entre dans la transition vers l'amorphisation (D:2D < 3), le comportement dans la post-décharge, avec et sans purificateur, est similaire. Pour un degré de désordre donné, l'incorporation est de même amplitude. À noter également que les spectres haute résolution de l'azote (non présenté ici) ne présentent aucune différence dans la

proportion des différents types d'incorporation (pyrole, pyridine et graphitique). Le fort dommage engendré par le premier traitement à 0.25% d'O₂ ne nous permet pas de conclure sur la génération de dommages pré-amorphisation pour cette condition. Au-delà du seuil de la transition vers l'amorphisation, on constate que l'incorporation est plus importante pour la condition avec purificateur. Le rôle de l'oxygène dans cette baisse de l'incorporation est incertain. Il est probable que l'amorphisation du graphène (et donc le passage du régime 1 vers le régime 2) change la cinétique d'incorporation des atomes d'azote, en particulier la mobilité des atomes d'azote adsorbés à la surface de l'échantillon au cours de leur recherche d'un site de défaut pour l'incorporation. Dans ce contexte, il devient plus probable que la cinétique d'incorporation entre en compétition avec un processus de recombinaison en surface avec des atomes d'oxygène menant à la production de NO, et donc à une perte d'azote mesurée par XPS. Ces aspects de compétition entre les divers processus de surface ont notamment été observés pour le traitement du bois dans ce même type de plasma [R99]. Cette perte d'incorporation d'azote peut potentiellement expliquer le faible ratio N:C obtenu pour la condition à 0.25% O₂.

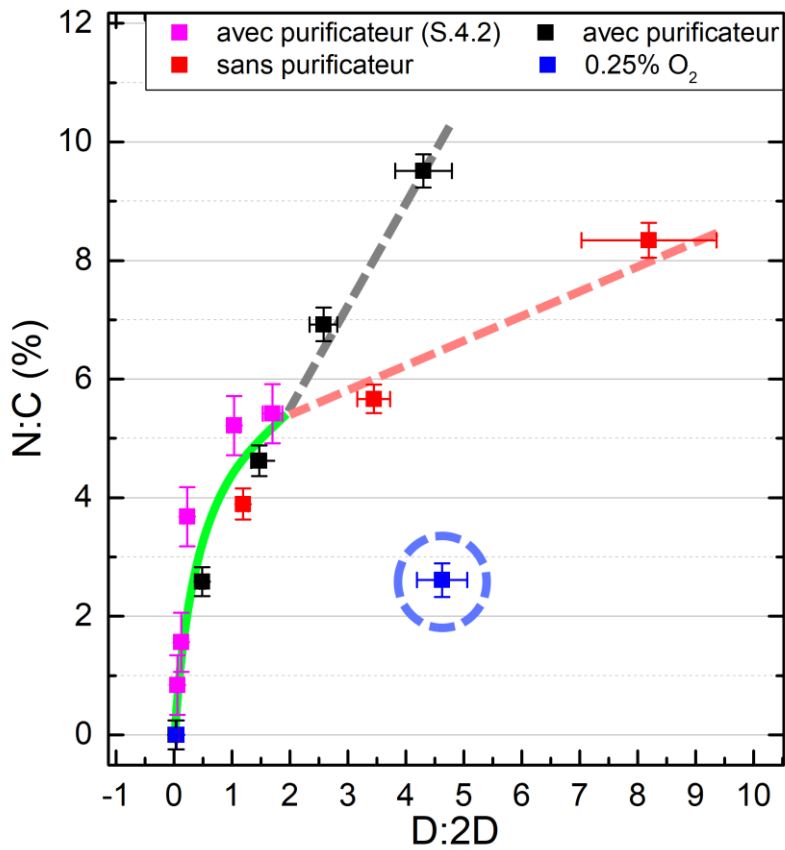


Figure 27 : Ratio XPS – N:C en fonction du ratio RS – D:2D pour trois conditions de traitement dans la post-décharge lointaine avec présence d'espèces oxydantes. Les lignes sont pour guider l'œil et pour matière à discussion seulement.

Conclusion

Les travaux de recherche réalisés dans le cadre de cette thèse de doctorat avaient pour objectif principal de jeter les bases physiques et chimiques de la modification post-croissance de films de graphène dans la post-décharge en flux de plasmas micro-ondes d'azote à pression réduite. La caractérisation du plasma jumelée à la caractérisation du graphène ont permis d'établir des liens essentiels pour une meilleure compréhension des mécanismes physiques et chimiques mis en jeu à l'interface plasma-graphène. Une meilleure maîtrise de ces mécanismes est impérative à la sélection judicieuse de conditions opératoires de traitements visant à atteindre les propriétés optimales du graphène selon l'application envisagée.

La post-décharge en flux d'azote a été montrée très versatile pour le traitement post-croissance du graphène. La nature des dommages et des incorporations se sont révélés fortement dépendants de la position des traitements dans la post-décharge. Deux positions de traitements ont été étudiées, la post-décharge proche et la post-décharge lointaine. La post-décharge proche présente des densités d'espèces métastables d'azote et ioniques fortement supérieures à celles de la lointaine. L'incorporation d'azote et la production de dommages augmentent de façon monotone pour les traitements dans la post-décharge lointaine. L'incorporation peut atteindre des niveaux extrêmement élevés ($(N1s/(C1s+N1s+O1s))$ de 18%) pour des dommages extrêmement faibles ($D:G < 0.3$). Un tel niveau d'incorporation est associé à la fonctionnalisation de contaminants d'hydrocarbure en surface issus de l'exposition à l'air ambiant. L'incorporation est limitée par les défauts de surface; les dommages sont limités par la présence de l'hydrocarbure qui joue le rôle de barrière protectrice. Seules les inclusions graphitiques d'azote dans le graphène révèlent ainsi une saturation. On distingue également la présence d'inhomogénéités en surface reliées à l'oxydation du cuivre sous l'échantillon. La production de dommages est rapide et sature rapidement à ces sites, alors que l'amplitude du désordre augmente progressivement dans les domaines avoisinants. Cette différence dans le profil de formation de défauts s'explique par la variation de l'interaction avec le substrat et la hausse de contraintes de traction à ces régions. Les traitements dans la post-décharge proche engendrent beaucoup plus d'incorporations ($(N1s/(C1s+N1s+O1s))$ de 49%) et de désordres ($D:G = 1.3$).

L'apport supérieur d'énergie à la surface engendre ultimement l'amorphisation du graphène. Il y a alors formation de lacunes multiples et d'un complexe amorphe graphène-hydrocarbure en surface. Le transfert vers un substrat de SiO₂ du graphène révèle qu'une forte proportion (80%) des atomes d'azote sont faiblement liés au graphène. L'énergie de liaison sondée par XPS pour ces inclusions est toutefois identique à celle d'inclusions purement aromatiques fortement liées. Le rôle des différentes inhomogénéités et des contaminants est majeur dans le traitement du graphène. L'importance d'un protocole précis dans l'entreposage, la croissance et le traitement de ces matériaux bidimensionnels fragiles est essentielle au contrôle et à la reproductibilité des traitements. De plus, l'étude de ces inhomogénéités peut s'avérer bénéfique à l'identification de certains mécanismes de modification en surface des matériaux.

Le développement d'une nouvelle méthode de traitement de mesures basée sur un nouveau montage a été mise au point pour s'affranchir des contraintes imposées par les méthodes de caractérisation de spectroscopie Raman conventionnelle (*inVia Renisha*). En effet, le montage d'imagerie Raman RIMA (*Raman IMAge*r) de *Photon Etc.* a été favorisé pour sa rapidité et sa meilleure résolution spatiale. L'acquisition de 10⁵ à 10⁶ spectres sur une région de 130 µm x 130 µm a permis de cartographier le comportement de certaines bandes Raman avec une résolution de 130 nm en cellules 1x1 (ou 490 nm en cellules 3x3). Une méthode adaptée de déconvolution de spectres et de filtrage de bruits de fond basée sur l'analyse de composantes principales (PCA) a été développée pour maximiser l'information extraite des mesures. La méthode a permis d'identifier différents processus ayant lieu au niveau d'inhomogénéités de surface du graphène. On note un processus d'auto-réparation des joints de grains du graphène pour une série de traitements par plasmas d'argon. Cet environnement inerte permet d'identifier le rôle des atomes de carbone dans la "résistance" apparente des joints de grains. La migration supérieure des adatomes de carbone face aux lacunes simples leur permet, lorsque l'échantillon n'a pas commencé sa transition vers l'amorphisation, de s'accumuler aux joints de grains. Cette accumulation aux joints de grains est induite par la migration préférentielle des adatomes le long de ceux-ci. Il s'en suit un mécanisme d'émission d'adatomes responsable de la réparation de lacunes simples dans le voisinage des joints de grains. Par le biais d'un découplage optique Raman de contraintes de surface et de dopages dans différentes régions du graphène, un mécanisme

similaire a été démontré pour les traitements dans la post-décharge en flux du plasma d'azote. En raison de la plus faible énergie de migration des adatomes de carbone, un déséquilibre analogue dans la distribution en surface des adatomes de carbone est responsable de l'auto-réparation de lacunes en proximité de joints de grains et, de ce fait même, d'un dopage d'azote localisé aux domaines du graphène. Ce dopage sélectif des domaines s'estompe néanmoins lorsque l'échantillon débute sa transition vers l'amorphisation. En effet, l'amorphisation entrave le transport des adatomes de carbone aux joints de grains et, conséquemment, l'accumulation essentielle au processus d'auto-réparation.

Finalement, deux séries de mesures ont été réalisées afin de cibler le rôle précis d'espèces particulières dans la modification des propriétés du graphène. Pour une pression donnée, l'ajout d'un tube de cuivre comme surface de recombinaison dans la post-décharge lointaine permet de diminuer fortement la densité d'azote atomique au niveau de l'échantillon, sans jouer fortement sur les densités d'azote moléculaire métastable et des hauts niveaux vibrationnels. Pour ces deux conditions, la fluence totale d'énergie délivrée par les recombinaisons en surface d'azote atomique et la désexcitation en surface de métastables dictent l'état de désordre de la surface. On en conclut que leur probabilité de dépôt d'énergie est similaire et que les niveaux vibrationnels de N₂ jouent peu sur la formation de dommages sur le graphène. Pour une pression plus basse, la densité d'azote diminue faiblement alors que les métastables N₂(A) maintiennent une densité conséquente. Toutefois, pour une pression de traitement plus basse, un processus moins efficace de dissipation d'énergie relié à un plus faible flux de neutre à l'état fondamental à la surface entraîne la formation de dommages plus importants pour un même dépôt d'énergie. Cette condition s'avère toutefois moins propice à l'incorporation d'azote dans le graphène. En effet, pour un niveau de désordre similaire (D:2D = 1.5), les traitements à 1 Torr engendrent un taux de N:C de 4.0% contre un taux de 5.5% pour les traitements à 6 Torr. Un mécanisme d'incorporation des atomes d'azote est aussi proposé. Finalement, le rôle d'espèces oxydantes dans le plasma sur le traitement du graphène est exploré par l'utilisation de trois conditions différentes : des traitements avec et sans purificateur de gaz ainsi qu'avec 0.25% d'oxygène. Les traces d'oxygène induisent une augmentation des densités d'azote dissocié dans la post-décharge lointaine. Les densités de métastables sont essentiellement constantes alors que les densités

d'oxygène augmentent d'un ou de deux ordres de grandeur. Malgré ces variations, la dynamique de formation de défauts et la nature de ceux-ci sont partagés par ces conditions. Malgré la présence des atomes d'oxygène, la fluence d'énergie de la recombinaison en surface des N et la désexcitation en surface des N₂(A) gouvernent la formation de dommages. Dans le régime 1 de l'amorphisation, le taux d'incorporation pour un degré de désordre est indépendant de la présence d'impuretés. Le rôle de l'oxygène devient apparent seulement pour des désordres importants dans le régime 2. On observe alors une baisse de l'incorporation d'azote lorsque l'oxygène a des densités considérables dans la post-décharge. On en déduit qu'il existe une compétition entre les processus d'incorporation des atomes d'azote et de recombinaison des atomes d'azote avec des atomes d'oxygène.

Évidemment, l'ensemble des études pertinentes sur les interactions plasma-graphène dans la post-décharge en flux de plasmas d'azote à pression réduite n'ont pas pu être réalisées en totalité. Des inconnus persistent dans l'identification du rôle précis des espèces dans la modification du graphène et la nature précise des mécanismes en surface. Plusieurs aspects mériteraient un travail additionnel afin d'explorer les pistes explorées dans le cadre du présent projet.

Plus précisément, malgré le lien réalisé entre la fluence d'énergie des N et des N₂(A) et la production de dommages liée au rapport D:2D, le mécanisme précis de formation de dommages demeure inconnu. Un modèle complet incluant les dépôts d'énergie vers les électrons du graphène et les transferts d'énergie de ces électrons de haute énergie vers les phonons serait requis pour réellement identifier l'ensemble des étapes mises en jeu. Le rôle de l'activation de la surface graphénique par l'apport d'énergie constante sur les barrières d'activation de formation de désordre ou d'incorporation demeure également indéterminé. Notamment, le lien entre les deux dynamiques de formation de défauts pour les mesures à deux pressions différentes reste à explorer. Plus précisément, le rôle des collisions des neutres à l'état fondamental sur la relaxation de l'état excité du graphène et l'influence de cet état hors équilibre sur les taux de formation de dommages mériteraient une meilleure compréhension.

Alors que le potentiel de la post-décharge en flux a été exploré pour lier dommages et incorporation d'atomes d'azote, un contrôle précis sur la nature des incorporations (pyrole, pyridine, graphitique) est parfois nécessaire selon l'application envisagée. Et bien qu'une certaine sélectivité se soit avérée présente pour les incorporations graphitiques dans la post-décharge lointaine, aucune condition n'a été identifiée pour permettre des incorporations totales de l'azote dans une seule et unique configuration. En effet, les incorporations d'azote étaient typiquement dominées par la présence de pyrole et de pyridine tandis que la contribution graphitique était toujours plus faible.

Malgré l'éventail des propriétés physico-chimiques du graphène obtenu pour les nombreuses conditions de traitement par plasma étudiées, l'utilisation de ce graphène pour le développement d'applications précises n'a pas été explorée. Alors que les traitements en post-décharge dans leur état actuel semble manquer de sélectivité dans le type d'inclusions d'azote obtenues, un fin contrôle des dommages est facilement envisageable. Le rôle du graphène fonctionnalisé par l'azote s'est vu associé un fort potentiel pour révolutionner plusieurs industries sans toutefois, à notre connaissance, engendrer de véritables applications à grande échelle. On peut supposer qu'une meilleure compréhension des mécanismes de dépôt d'énergie en surface entraînerait un meilleur contrôle des propriétés des monocouches de graphène fonctionnalisé. Le tout favoriserait le développement de graphène avec des propriétés distinctes à celles obtenues par les méthodes courantes. On peut également supposer que le savoir-faire développé dans le cadre de cette thèse pour le traitement de matériaux de faible dimension serait bénéfique à l'avancement de futurs projets de recherche sur des matériaux aux propriétés similaires ou connexes, notamment le phosphore noir ou les couches de disulfure de molybdène.

Références bibliographiques

- [R1] K.S. Novoselov, Science (80-.). 306 (2004) 666–669.
- [R2] D.R. Cooper, B. D’Anjou, N. Ghattamaneni, B. Harack, M. Hilke, A. Horth, N. Majlis, M. Massicotte, L. Vandsburger, E. Whiteway, V. Yu, ISRN Condens. Matter Phys. 2012 (2012) 1–56.
- [R3] K. Thiagarajan, B. Saravanakumar, S.-J. Kim, ACS Appl. Mater. Interfaces 7 (2015) 2171–2177.
- [R4] W. Zhao, Y. Wang, Z. Wu, W. Wang, K. Bi, Z. Liang, J. Yang, Y. Chen, Z. Xu, Z. Ni, Sci. Rep. 5 (2015) 11962.
- [R5] A.C. Ferrari, Solid State Commun. 143 (2007) 47–57.
- [R6] L.G. Cançado, A. Jorio, E.H.M. Ferreira, F. Stavale, C. a. Achete, R.B. Capaz, M.V.O. Moutinho, A. Lombardo, T.S. Kulmala, a. C. Ferrari, Nano Lett. 11 (2011) 3190–3196.
- [R7] R. Beams, L. Gustavo Cançado, L. Novotny, J. Phys. Condens. Matter 27 (2015) 083002.
- [R8] A. Eckmann, A. Felten, A. Mishchenko, L. Britnell, R. Krupke, K.S. Novoselov, C. Casiraghi, Nano Lett. 12 (2012) 3925–3930.
- [R9] J.E. Lee, G. Ahn, J. Shim, Y.S. Lee, S. Ryu, Nat. Commun. 3 (2012) 1024.
- [R10] A. Criado, M. Melchionna, S. Marchesan, M. Prato, Angew. Chemie - Int. Ed. 54 (2015) 10734–10750.
- [R11] M. Fan, Z. Feng, C. Zhu, X. Chen, C. Chen, J. Yang, D. Sun, J. Mater. Sci. 51 (2016) 10323–10349.
- [R12] R. Muñoz, C. Gómez-Aleixandre, Chem. Vap. Depos. 19 (2013) 297–322.
- [R13] J.D. Wood, S.W. Schmucker, A.S. Lyons, E. Pop, J.W. Lyding, Nano Lett. 11 (2011) 4547–4554.
- [R14] Y. Zhang, L. Zhang, C. Zhou, Acc. Chem. Res. 46 (2013) 2329–2339.
- [R15] N. Soin, S. Sinha Roy, S. Roy, K.S. Hazra, D.S. Misra, T.H. Lim, C.J. Hetherington, J.A. McLaughlin, J. Phys. Chem. C 115 (2011) 5366–5372.
- [R16] O. Lehtinen, J. Kotakoski, A. V. Krasheninnikov, A. Tolvanen, K. Nordlund, J. Keinonen, Phys. Rev. B 81 (2010) 153401.
- [R17] M.M. Lucchese, F. Stavale, E.H.M. Ferreira, C. Vilani, M.V.O. Moutinho, R.B. Capaz, C. a. Achete, A. Jorio, Carbon N. Y. 48 (2010) 1592–1597.
- [R18] A.C. Ferrari, J. Robertson, Phys. Rev. B 61 (2000) 14095–14107.
- [R19] E.H. Martins Ferreira, M.V.O. Moutinho, F. Stavale, M.M. Lucchese, R.B. Capaz, C. a. Achete, A. Jorio, Phys. Rev. B 82 (2010) 125429.
- [R20] F. Tuinstra, J.L. Koenig, J. Chem. Phys. 53 (1970) 1126–1130.
- [R21] D.C. Bell, M.C. Lemme, L. a Stern, J.R. Williams, C.M. Marcus, Nanotechnology 20 (2009) 455301.
- [R22] M.C. Lemme, D.C. Bell, J.R. Williams, L.A. Stern, B.W.H. Baugher, P. Jarillo-Herrero, C.M. Marcus, ACS Nano 3 (2009) 2674–2676.
- [R23] S. Zhu, Y. Song, X. Zhao, J. Shao, J. Zhang, B. Yang, Nano Res. 8 (2015) 355–381.
- [R24] G. Compagnini, F. Giannazzo, S. Sonde, V. Rainieri, E. Rimini, Carbon N. Y. 47 (2009) 3201–3207.
- [R25] B. Guo, Q. Liu, E. Chen, H. Zhu, L. Fang, J.R. Gong, Nano Lett. 10 (2010) 4975–4980.

- [R26] K. Kim, S. Yang, Y. Park, M. Lee, B. Kim, H. Lee, *J. Phys. Chem. C* 117 (2013) 2129–2134.
- [R27] W. Zhao, O. Höfert, K. Gotterbarm, J.F. Zhu, C. Papp, H.-P. Steinrück, *J. Phys. Chem. C* 116 (2012) 5062–5066.
- [R28] M. Telychko, P. Mutombo, M. Ondráček, P. Hapala, F.C. Bocquet, J. Kolorenč, M. Vondráček, P. Jelínek, M. Švec, *ACS Nano* 8 (2014) 7318–7324.
- [R29] D.E. Rosner, *Dep. Eng. Appl. Sci. Yale Univ.* (1972) 573–602.
- [R30] J. Moser, A. Barreiro, A. Bachtold, *Appl. Phys. Lett.* 91 (2007) 163513.
- [R31] X. Wang, X. Li, L. Zhang, Y. Yoon, P.K. Weber, H. Wang, J. Guo, H. Dai, *Science* (80-). 324 (2009) 768–771.
- [R32] Y. Yamada, K. Murota, R. Fujita, J. Kim, A. Watanabe, M. Nakamura, S. Sato, K. Hata, P. Ercius, J. Ciston, C.Y. Song, K. Kim, W. Regan, W. Gannett, A. Zettl, *J. Am. Chem. Soc.* 136 (2014) 2232–2235.
- [R33] B. Westenfelder, J.C. Meyer, J. Biskupek, S. Kurasch, F. Scholz, C.E. Krill, U. Kaiser, *Nano Lett.* 11 (2011) 5123–5127.
- [R34] V. Georgakilas, M. Otyepka, A.B. Bourlinos, V. Chandra, N. Kim, K.C. Kemp, P. Hobza, R. Zboril, K.S. Kim, *Chem. Rev.* 112 (2012) 6156–6214.
- [R35] P. Chabert, N. Braithwaite, *Physics of Radio-Frequency Plasmas*, First Edit, United Kingdom at the University press, Cambridge, 2011.
- [R36] M.A. Lieberman, A.J. Lichtenberg, *Principles of Plasma Discharges and Materials Processing*, Second Edi, 2005.
- [R37] K. Nakada, A. Ishii, *Solid State Commun.* 151 (2011) 13–16.
- [R38] W. Sesselmann, H. Conrad, G. Ertl, J. Küppers, B. Woratschek, *Phys. Rev. Lett.* 50 (1983) 446–450.
- [R39] G. Zhou, C. Cen, S. Wang, M. Deng, O. V. Prezhdo, *J. Phys. Chem. Lett.* 10 (2019) 7179–7187.
- [R40] J.C.W. Song, M.Y. Reizer, L.S. Levitov, *Phys. Rev. Lett.* 109 (2012) 106602.
- [R41] K. Oura, V.G. Lifshits, A. Saranin, A.V. Zotov, M. Katayama, *Adv. Texts Phys.* (2003).
- [R42] R. Rozada, P. Solís-Fernández, J.I. Paredes, A. Martínez-Alonso, H. Ago, J.M.D. Tascón, *Carbon N. Y.* 79 (2014) 664–669.
- [R43] V. Dusek, J. Musil, *Czech. J. Phys.* 40 (1990) 1185.
- [R44] B. Eren, W. Fu, L. Marot, M. Calame, R. Steiner, E. Meyer, *Appl. Phys. Lett.* 106 (2015) 011904.
- [R45] D.C. Elias, R.R. Nair, T.M.G. Mohiuddin, S. V. Morozov, P. Blake, M.P. Halsall, A.C. Ferrari, D.W. Boukvalov, M.I. Katsnelson, A.K. Geim, K.S. Novoselov, *Science* (80-). 323 (2009) 610–614.
- [R46] Z. Luo, T. Yu, K.J. Kim, Z. Ni, Y. You, S. Lim, Z. Shen, S. Wang, J. Lin, *ACS Nano* 3 (2009) 1781–1788.
- [R47] G. Diankov, M. Neumann, D. Goldhaber-Gordon, *ACS Nano* 7 (2013) 1324–1332.
- [R48] R. Yang, L. Zhang, Y. Wang, Z. Shi, D. Shi, H. Gao, E. Wang, G. Zhang, *Adv. Mater.* 22 (2010) 4014–4019.
- [R49] L. Xie, L. Jiao, H. Dai, *J. Am. Chem. Soc.* 132 (2010) 14751–14753.
- [R50] M. Seifert, J.E.B. Vargas, M. Bobinger, M. Sachsenhauser, A.W. Cummings, S. Roche, J.A. Garrido, *2D Mater.* 2 (2015) 024008.
- [R51] J. Roth, C. Garcia-Rosales, *Nucl. Fusion* 36 (1996) 1647–1659.

- [R52] M.Y. Han, B. ??zyilmaz, Y. Zhang, P. Kim, *Phys. Rev. Lett.* 98 (2007) 1–4.
- [R53] K. Kim, H.J. Park, B.-C. Woo, K.J. Kim, G.T. Kim, W.S. Yun, *Nano Lett.* 8 (2008) 3092–3096.
- [R54] K. Choi, J. Lim, J.R. Rani, H. Seo Yoon, J. Oh, T. Hong, T. Ha, B. Cheol Park, K. Ik Sim, S. Chan Jun, J. Hoon Kim, *Appl. Phys. Lett.* 102 (2013) 131901.
- [R55] H. Mao, R. Wang, J. Zhong, S. Zhong, W. Chen, *Carbon N. Y.* 76 (2014) 212–219.
- [R56] N. McEvoy, H. Nolan, N. Ashok Kumar, T. Hallam, G.S. Duesberg, *Carbon N. Y.* 54 (2013) 283–290.
- [R57] A. Nourbakhsh, M. Cantoro, T. Vosch, G. Pourtois, F. Clemente, M.H. van der Veen, J. Hofkens, M.M. Heyns, S. De Gendt, B.F. Sels, *Nanotechnology* 21 (2010) 435203.
- [R58] A. Nourbakhsh, M. Cantoro, A. V. Klekachev, G. Pourtois, T. Vosch, J. Hofkens, M.H. van der Veen, M.M. Heyns, S. De Gendt, B.F. Sels, *J. Phys. Chem. C* 115 (2011) 16619–16624.
- [R59] D.C. Kim, D.-Y. Jeon, H.-J. Chung, Y. Woo, J.K. Shin, S. Seo, *Nanotechnology* 20 (2009) 375703.
- [R60] V.M. Pereira, J. Nilsson, A.H. Castro Neto, *Phys. Rev. Lett.* 99 (2007) 166802.
- [R61] J. Jiang, R. Pachter, A.E. Islam, B. Maruyama, J.J. Boeckl, *Chem. Phys. Lett.* 663 (2016) 79–83.
- [R62] T. Schiros, D. Nordlund, L. Pálová, D. Prezzi, L. Zhao, K.S. Kim, U. Wurstbauer, C. Gutiérrez, D. Delongchamp, C. Jaye, D. Fischer, H. Ogasawara, L.G.M. Pettersson, D.R. Reichman, P. Kim, M.S. Hybertsen, A.N. Pasupathy, *Nano Lett.* 12 (2012) 4025–4031.
- [R63] J.J. Zeng, Y.J. Lin, *Appl. Phys. Lett.* 104 (2014) 233103.
- [R64] F. Joucken, Y. Tison, J. Lagoute, J. Dumont, D. Cabosart, B. Zheng, V. Repain, C. Chacon, Y. Girard, A.R. Botello-Méndez, S. Rousset, R. Sporken, J.-C. Charlier, L. Henrard, *Phys. Rev. B* 85 (2012) 161408.
- [R65] Y.P. Lin, Y. Ksari, J. Prakash, L. Giovanelli, J.C. Valmalette, J.M. Themlin, *Carbon N. Y.* 73 (2014) 216–224.
- [R66] C.N.R. Rao, K. Gopalakrishnan, A. Govindaraj, *Nano Today* 9 (2014) 324–343.
- [R67] I. Bertóti, M. Mohai, K. László, *Carbon N. Y.* 84 (2015) 185–196.
- [R68] F. Orlando, P. Lacovic, M. Dalmiglio, A. Baraldi, R. Larciprete, S. Lizzit, *Surf. Sci.* 643 (2015) 214–221.
- [R69] S.H. Park, J. Chae, M.-H. Cho, J.W.J.H. Kim, K.-H. Yoo, S.W. Cho, T.G. Kim, J.W.J.H. Kim, *J. Mater. Chem. C* 2 (2014) 933–939.
- [R70] J. Moon, J. An, U. Sim, S.-P. Cho, J.H. Kang, C. Chung, J.-H. Seo, J. Lee, K.T. Nam, B.H. Hong, *Adv. Mater.* 26 (2014) 3501–3505.
- [R71] U. Sim, T.-Y. Yang, J. Moon, J. An, J. Hwang, J.-H. Seo, J. Lee, K.Y. Kim, J. Lee, S. Han, B.H. Hong, K.T. Nam, *Energy Environ. Sci.* 6 (2013) 3658.
- [R72] Y. Shao, S. Zhang, M.H. Engelhard, G. Li, G. Shao, Y. Wang, J. Liu, I.A. Aksay, Y. Lin, *J. Mater. Chem.* 20 (2010) 7491.
- [R73] H.M. Jeong, J.W. Lee, W.H. Shin, Y.J. Choi, H.J. Shin, J.K. Kang, J.W. Choi, *Nano Lett.* 11 (2011) 2472–2477.
- [R74] N.A. Kumar, H. Nolan, N. McEvoy, E. Rezvani, R.L. Doyle, M.E.G. Lyons, G.S. Duesberg, *J. Mater. Chem. A* 1 (2013) 4431.
- [R75] M.J. Kim, Y. Jeong, S. Sohn, S.Y. Lee, Y.J. Kim, K. Lee, Y.H. Kahng, J.-H. Jang, *AIP Adv.* 3 (2013) 012117.
- [R76] M. Rybin, A. Pereyaslavtsev, T. Vasilieva, V. Myasnikov, I. Sokolov, A. Pavlova, E.

- Obraztsova, A. Khomich, V. Ralchenko, E. Obraztsova, Carbon N. Y. 96 (2016) 196–202.
- [R77] B. Wang, L. Tsetseris, S.T. Pantelides, J. Mater. Chem. A 1 (2013) 14927.
- [R78] Y.-C. Lin, C.-Y. Lin, P.-W. Chiu, Appl. Phys. Lett. 96 (2010) 133110.
- [R79] J.A. Ferreira, H.P.T. Nguyen, Z. Mi, R. Leonelli, L. Stafford, Nanotechnology 25 (2014) 435606.
- [R80] V. Guerra, P.A. Sá, J. Loureiro, J. Phys. Conf. Ser. 63 (2007) 012007.
- [R81] M.K. Boudam, B. Saoudi, M. Moisan, A. Ricard, J. Phys. D. Appl. Phys. 40 (2007) 1694–1711.
- [R82] O. Frank, J. Vejpravova, V. Holy, L. Kavan, M. Kalbac, Carbon N. Y. 68 (2014) 440–451.
- [R83] C.-H. Huang, H.-Y. Lin, C.-W. Huang, Y.-M. Liu, F.-Y. Shih, W.-H. Wang, H.-C. Chui, Nanoscale Res. Lett. 9 (2014) 64.
- [R84] S. Berciaud, S. Ryu, L.E. Brus, T.F. Heinz, Nano Lett. 9 (2009) 346–352.
- [R85] R. He, L. Zhao, N. Petrone, K.S. Kim, M. Roth, J. Hone, P. Kim, A. Pasupathy, A. Pinczuk, Nano Lett. 12 (2012) 2408–2413.
- [R86] J. Čermák, T. Yamada, K. Ganzerová, B. Rezek, Adv. Mater. Interfaces 3 (2016) 1600166.
- [R87] B. Wang, Y. Puzyrev, S.T. Pantelides, Carbon N. Y. 49 (2011) 3983–3988.
- [R88] Y.-C. Lin, C.-C. Lu, C.-H. Yeh, C. Jin, K. Suenaga, P.-W. Chiu, Nano Lett. 12 (2012) 414–419.
- [R89] N. Lisi, T. Dikonomos, F. Buonocore, M. Pittori, R. Mazzaro, R. Rizzoli, S. Marras, A. Capasso, Sci. Rep. 7 (2017) 1–11.
- [R90] G. Robert Bigras, X. Glad, L. Vandsburger, C. Charpin, P. Levesque, R. Martel, L. Stafford, Carbon N. Y. 144 (2019) 532–539.
- [R91] P. Vinchon, X. Glad, G. Robert Bigras, R. Martel, L. Stafford, Nat. Mater. (2020).
- [R92] L. Gustavo Cançado, M. Gomes da Silva, E.H. Martins Ferreira, F. Hof, K. Kampioti, K. Huang, A. Pénicaud, C. Alberto Achete, R.B. Capaz, A. Jorio, 2D Mater. 4 (2017) 025039.
- [R93] F. Banhart, J. Kotakoski, A. V. Krasheninnikov, ACS Nano 5 (2011) 26–41.
- [R94] L.F. Huang, M.Y. Ni, G.R. Zhang, W.H. Zhou, Y.G. Li, X.H. Zheng, Z. Zeng, J. Chem. Phys. 135 (2011) 064705.
- [R95] H. Zerrouki, A. Ricard, J.P. Sarrette, Contrib. to Plasma Phys. 54 (2014) 827–837.
- [R96] P. Vasina, V. Kudrle, A. Tálský, P. Boto, M. Mrázková, M. Me ko, Plasma Sources Sci. Technol. 13 (2004) 668–674.
- [R97] A. Ricard, S. Oh, V. Guerra, Plasma Sources Sci. Technol. 22 (2013) 035009.
- [R98] A. Nourbakhsh, M. Cantoro, T. Vosch, G. Pourtois, F. Clemente, M.H. van der Veen, J. Hofkens, M.M. Heyns, S. De Gendt, B.F. Sels, Nanotechnology 21 (2010) 435203.
- [R99] J. Prégent, G. Robert-Bigras, L. Stafford, Plasma Process. Polym. 15 (2018) e1800035.
- [R100] V. Mazánková, F. Krčma, Chem. List. 102 (2008) 1388–1393.
- [R101] L. Gustavo Cançado, M. Gomes da Silva, E.H. Martins Ferreira, F. Hof, K. Kampioti, K. Huang, A. Pénicaud, C. Alberto Achete, R.B. Capaz, A. Jorio, 2D Mater. 4 (2017) 025039.
- [R102] A.C. Ferrari, J. Robertson, Ann. Mag. Nat. Hist. 16 (1845) 131–135.
- [R103] A. Eckmann, A. Felten, I. Verzhbitskiy, R. Davey, C. Casiraghi, Phys. Rev. B 88 (2013) 035426.
- [R104] M. Bruna, A.K. Ott, M. Ijas, D. Yoon, U. Sassi, A.C. Ferrari, ACS Nano 8 (2014) 7432–7441.

Annexe

Annexe 1 : Données supplémentaires pour l'article PSST_2018

Treatment of graphene films in the early and late afterglows of N₂ plasmas: comparison of the defect generation and N-incorporation dynamics

Germain Robert Bigras¹, Xavier Glad¹, Richard Martel², Andranik Sarkissian³, Luc Stafford¹

¹ Département de Physique, Université de Montréal, Montréal, Québec, CANADA

² Département de Chimie, Université de Montréal, Montréal, Québec, CANADA

³ Plasmionique Inc., Varennes, Québec, CANADA

SUPPLEMENTARY DATA

S1. Raman baselines

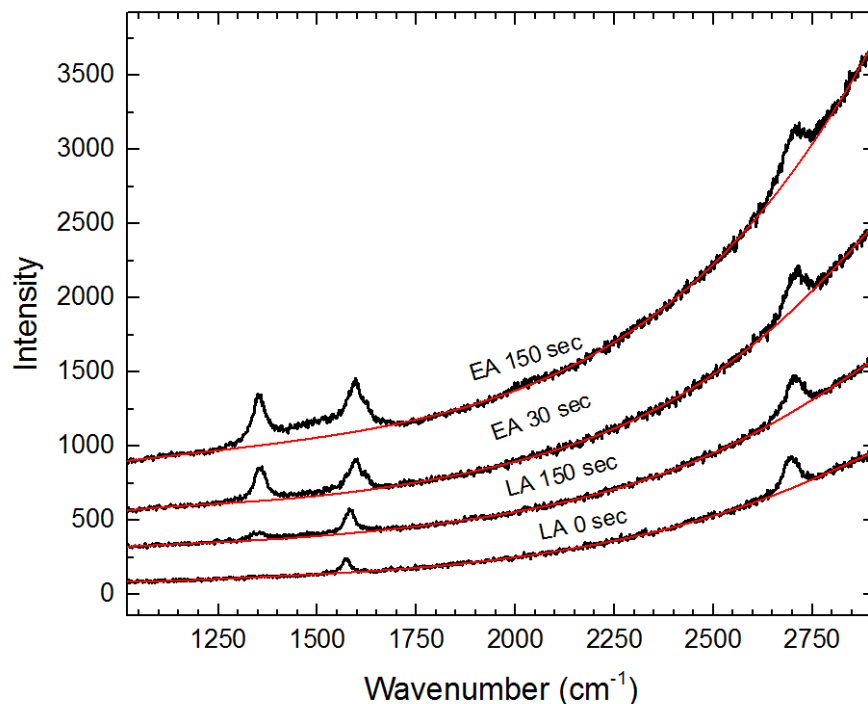


Fig. S1 –Raman raw spectra for early afterglow (EA) treatments for $t = 30$ and $t = 150$ s and for late afterglow (LA) treatments for $t = 0$ s and $t = 150$ s.

The red curve corresponds to the selected baseline for each spectrum. An offset is added to clearly distinguish the spectra. What appears to be an increase of luminescence for EA treated sample supports the formation of large vacancies that decreases the screening of the substrate emission by the graphene. The normalized background spectra only slightly differ; supporting that the luminescence comes mainly from the substrate.

S2. XPS Survey spectra

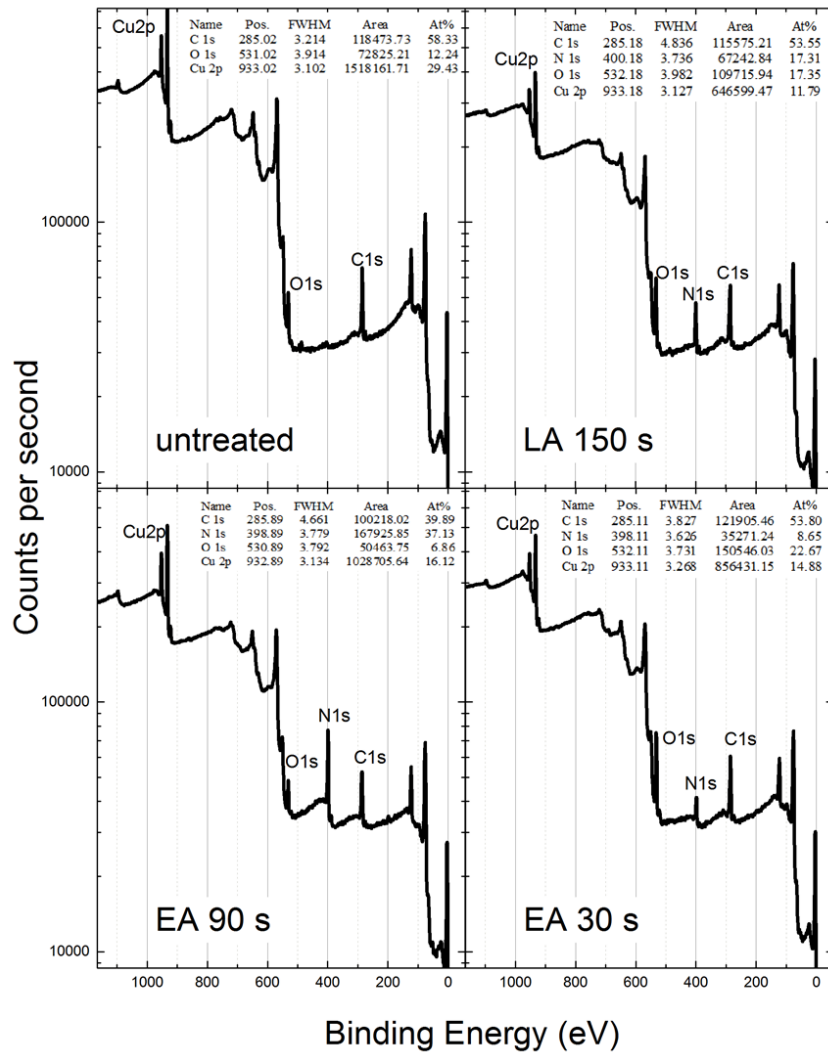


Fig. S2 –XPS survey for untreated, late afterglow (LA)-treated samples at $t = 150$ s and EA-treated sample at $t = 30$ and 90 s. Position, FWHM, area and at% are given for every element.

S3. XPS high-resolution Cu 2p spectra

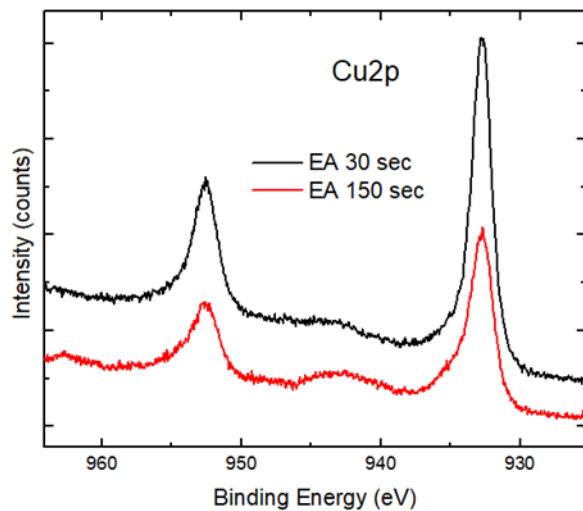


Fig. S3 –XPS high-resolution Cu 2p spectra for EA-treated sample at $t = 30$ and 150 s. This figure reveals a strong increase of the copper oxide contribution with treatment time for EA. As described in the manuscript, the presence of large multi-vacancies sites after treatment in the EA would obviously promote O bonding to the copper sample and increase the XPS response of the now uncovered copper oxide.

Annexe 2 : Données supplémentaires pour l'article Carbon_2019

Low-damage nitrogen incorporation in graphene films by nitrogen plasma treatment: effect of airborne contaminants

Germain Robert Bigras¹, Xavier Glad¹, Leron Vandsburger¹, Carl Charpin²,
Pierre Levesque², Richard Martel², Luc Stafford¹

¹ Département de Physique, Université de Montréal, Montréal, Québec, CANADA

² Département de Chimie, Université de Montréal, Montréal, Québec, CANADA

S1. SOURCES OF OXYGEN IMPURITIES

Oxygen impurities during low-pressure plasma treatments can come from residual vacuum or impurities in the feed gas. A base pressure of at least 2×10^{-7} Torr is achieved in the chamber before each treatment resulting in a maximum O₂ impurity concentration of 9×10^9 at/cm³ (using $P = n kb T$, with $T = 300$ K). Considering the impurities of the 99.999% N₂ high purity gas and the working pressure of 6 Torr, the oxygen impurity could go up to ($0.001\% * 6000$ mTorr * 3×10^{13} at/cm³-mTorr) 1.8×10^{12} at/cm³. Assuming a maximum O₂ fragmentation level of 10% in the microwave plasma, this yields a maximum population of reactive O atoms of 1.8×10^{11} at/cm³. Over the range of experimental conditions examined, the populations of O and O₂ is thus at least a decade lower than the population of plasma-generated N atoms (around $1 \times 10^{13} - 1 \times 10^{14}$ at/cm³ [1]). The addition of a gas purifier reduces to < 100 ppt (versus 10 ppm without the purifier) the oxygen contamination emanating from the N₂ feed gas, therefore eradicating the competition between nitrogen and oxygen functionalization in the late-afterglow treatment. Treatments with and without the purifier confirms that the purifier significantly reduces the oxygen incorporation.

Oxygen and water molecules physisorbed on graphene films upon exposure to ambient air could also be released in the low-pressure plasma environment and thus contribute to the plasma chemistry and plasma-surface interaction. However, those impurities are not present upstream (i.e. in the microwave plasma zone) such that only a minuscule fraction may be dissociated in the

late-afterglow region (the density and average energy of the electrons in the late afterglow are much lower than in the main plasma zone) and thus extensively contribute to the incorporation dynamics of oxygen atoms. Besides, in presence of significant nitrogen incorporation (as observed after treatment to the late afterglow of microwave N₂ plasmas), the energy barriers for dissociative adsorption of O₂ on carbon nanostructures (carbon nanotubes, graphene) decrease significantly [2]. The unavoidable physisorption of O₂ and humidity could therefore induce a number of phenomena on graphene films, including chemical etching by reactive oxygen atoms, carbon-oxygen functionalization or C_xN_yO_z surface polymerization. Such phenomena can occur in both ambient air and after the release of physisorbed species in the low-pressure plasma.

S2. RAMAN SPECTROSCOPY AND COPPER OXIDE

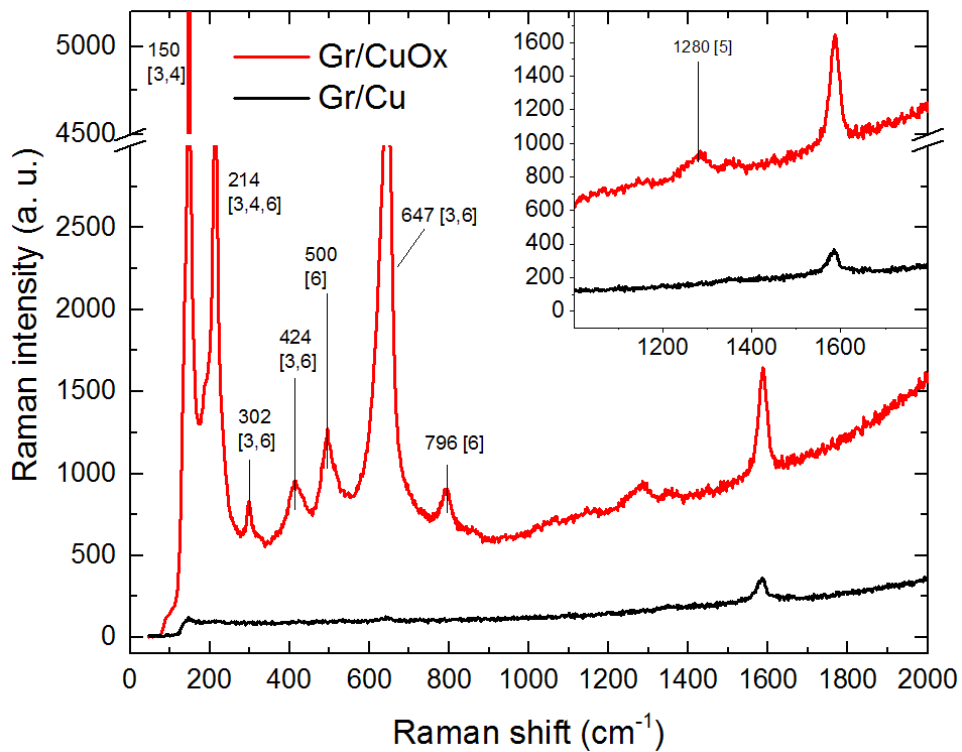


Fig. S2 – Raman Spectra for graphene on Cu or CuO_x. As can be seen, many additional bands linked to oxidized copper appear at lower Raman shifts for graphene samples on CuO_x [3–6].

S3. X-RAY PHOTOELECTRON SPECTROSCOPY AND COPPER OXIDE

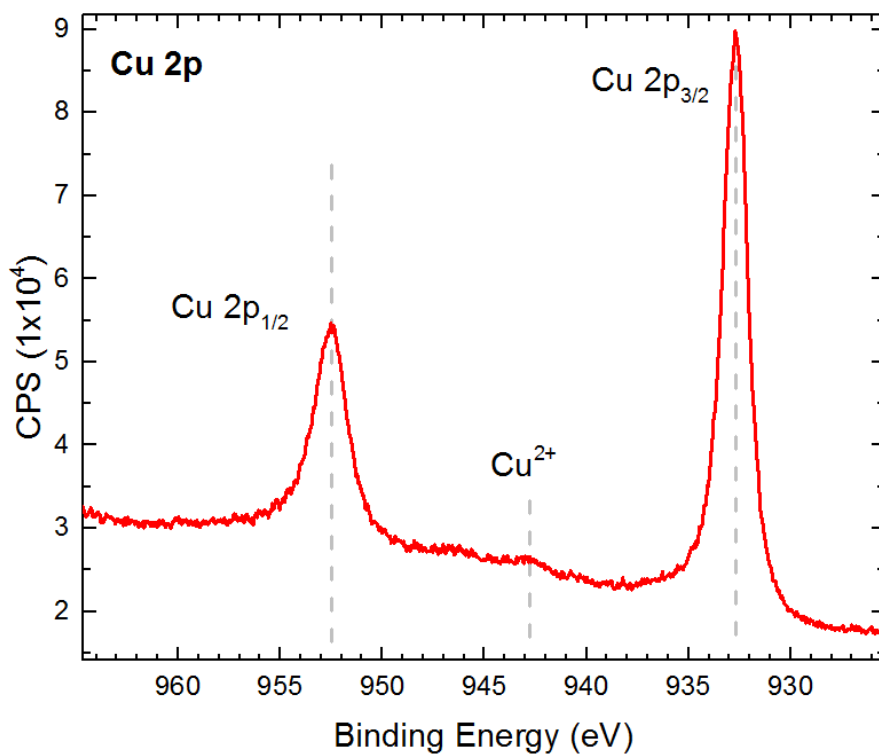


Fig. S2 – X-Ray photoelectron spectroscopy spectra of Cu 2p. The small Cu²⁺ peak around 947 eV binding energy show the surface-averaged weak oxidation of the graphene samples on copper.

S4. STATIC WATER CONTACT ANGLE

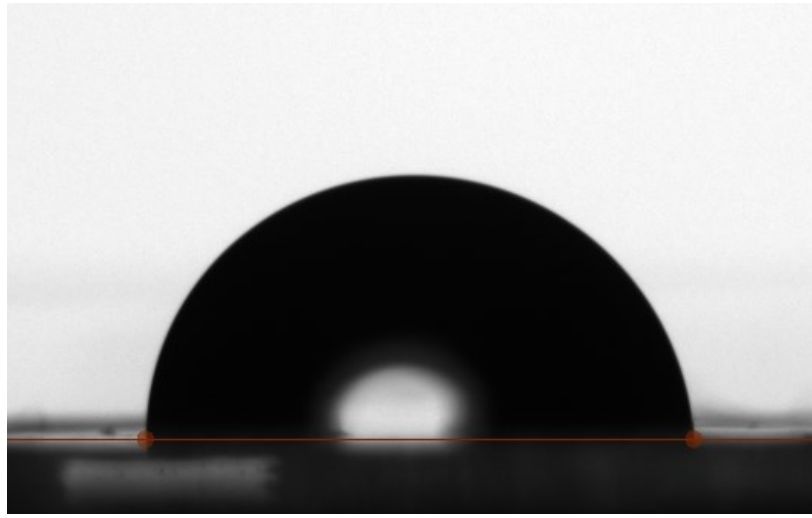


Fig. S4 – Static Contact Angle measured using a Biolin Scientific – Attension Theta setup. Three sets of images (each 200+ images) are taken. The average value of $93 \pm 7^\circ$ is obtained.

S5. RAMAN SPOT SIZE VERIFIED ON AMORPHOUS CARBON

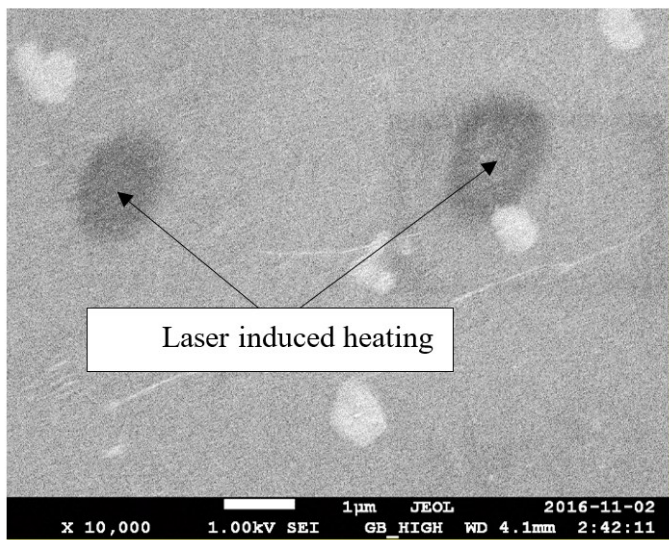


Fig. S3 – Scanning Electron Microscopy of laser induced heating resulting from previous Raman spectroscopy measurement on amorphous carbon. The setup used is a JEOL JSM-7600F at an acceleration voltage of 1 kV in the secondary electron mode (gentle-beam).

S6. IDENTIFICATION OF TOPOGRAPHY PROBED

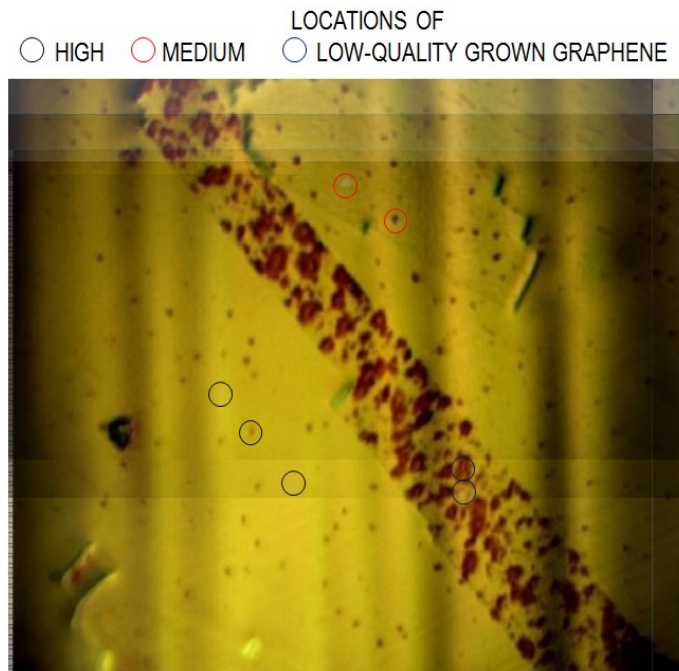


Fig. S4 – Superposition of the optical microscopy image used to target the precise regions of interest in this study. Seven different points were taken : 2 high-quality graphene for Cu, 1 high quality graphene for CuO_x , 1 medium and 1 low-quality graphene for both Cu and CuO_x .

S7. SURVEY ATOMIC PERCENT RATIO

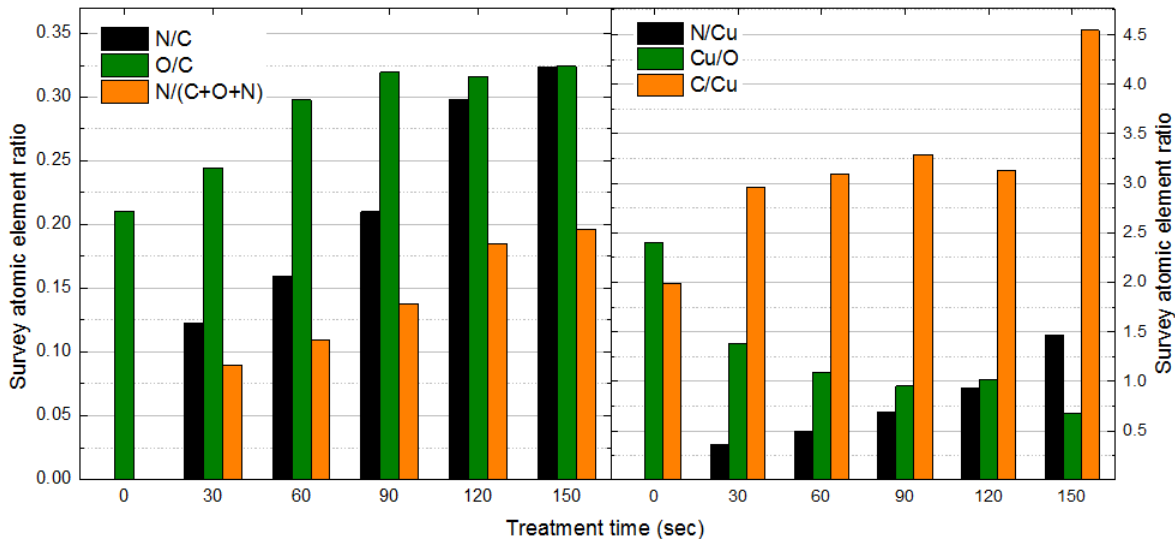


Fig. S5 – Various X-Ray photoelectron spectroscopy (XPS) band ratios. N/C and O/C saturates around 33%. C/Cu and N/Cu increases with treatment time. Cu/O decreases towards a minimal value around 60%.

S8. INDIVIDUAL SPECTRA

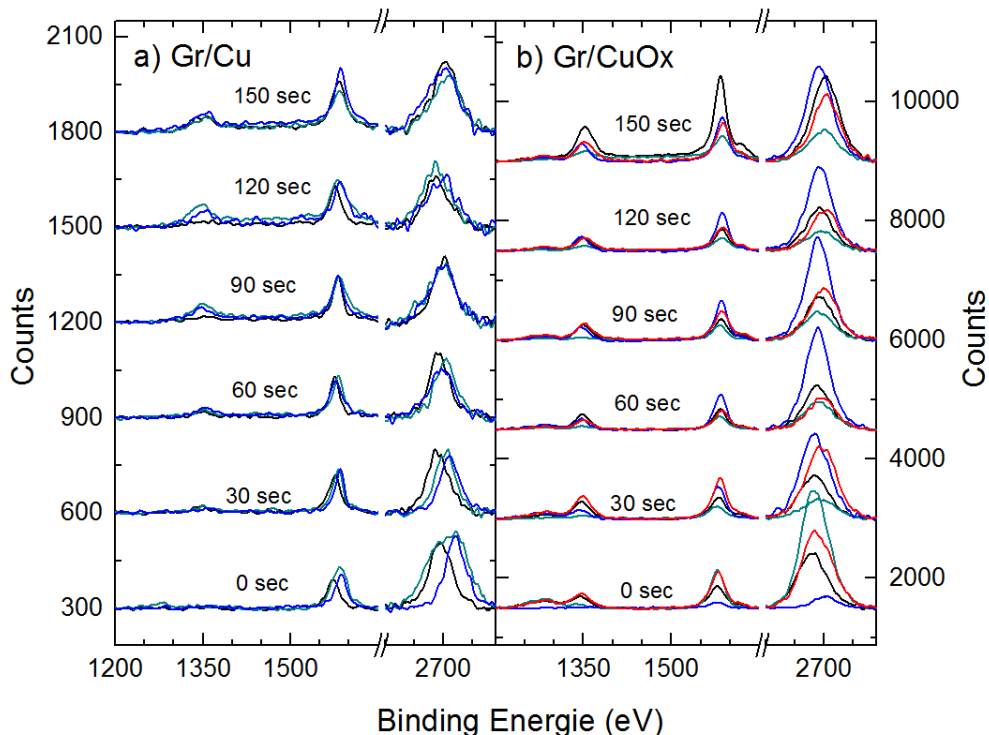


Fig. S6 – Raman spectroscopy spectra (non-normalized) for both regions on Cu (a) and CuOx (b) for numerous treatment times.

S9. SURVEY ATOMIC PERCENT RATIO

XPS analysis was performed before and after PMMA deposition/removal on graphene on copper samples. XPS results are presented below. Overall, {C,O} contamination is found present and linked to residual PMMA after the cleaning. The main C1s sp₂ C-C bonding remains largely dominant therefore excluding the possibility of large surface contamination with this transfer process. The O1s:C1s ratio indeed only rises from 14% to 17%.

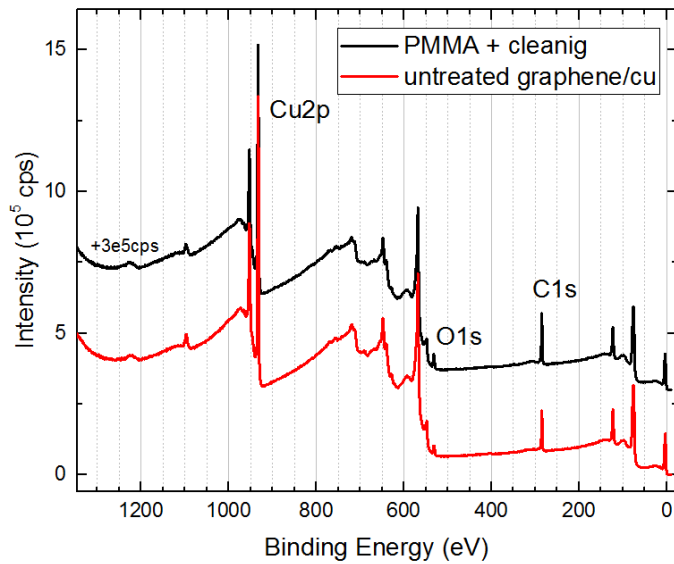


Fig. S9.1 – XPS Survey for untreated graphene on copper and the same sample after PMMA deposition, and PMMA removal (same procedure as in transfer)

G23a - untreated gr/Cu				G22c - PMMA + cleaning			
POINTS	C	O	Cu	POINTS	C	O	Cu
p1	56.23	7.71	36.05	p1	65.23	14.09	20.68
p2	55.06	7.65	37.29	p2	61.52	8.55	29.93
p3	54.06	7.04	38.9	p3	61.63	9.59	28.79
average	55.1	7.5	37.4	average	62.8	10.7	26.5
error	0.7	0.3	1.0	error	1.6	2.2	3.9
C:Cu		1.47	0.06	C:Cu		2.37	0.41
O:C		0.14	0.01	O:C		0.17	0.04

Table S9.1 – XPS at% for untreated graphene on copper and the same sample after PMMA deposition, and PMMA removal (same procedure as in transfer). For each sample, three points (beam size 400μm) were taken. The average values and standard deviation are presented. C:Cu and C:O ratios show both a slight increase with the polymer deposition and removal process.

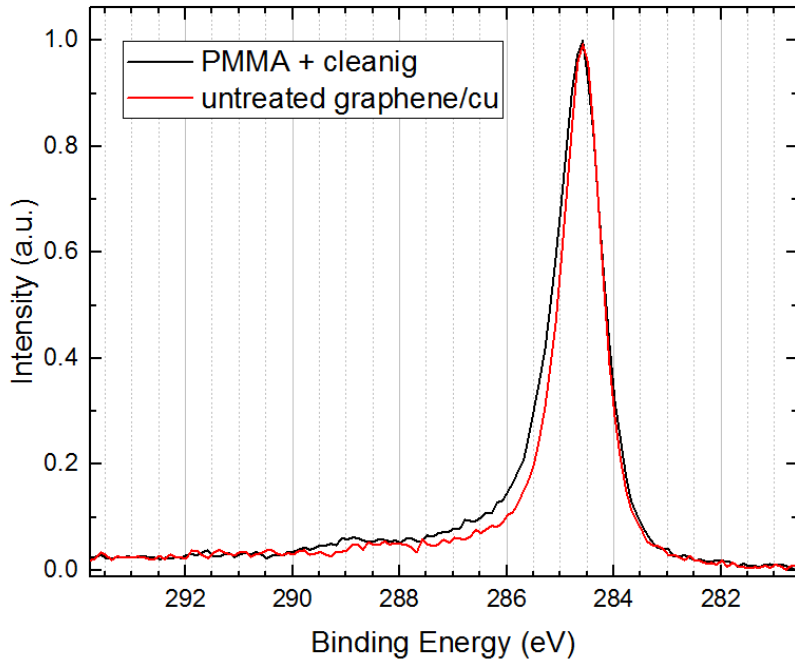


Fig. S9.2 – High resolution XPS C1s spectra for untreated graphene on copper and the same sample after PMMA deposition, and PMMA removal (same procedure as in transfer). Normalization is done according to maximum of C1s peak. Slight broadening of the band is associated to PMMA residue (various {C,O} bonding). Overall the sp² C-C remains dominant.

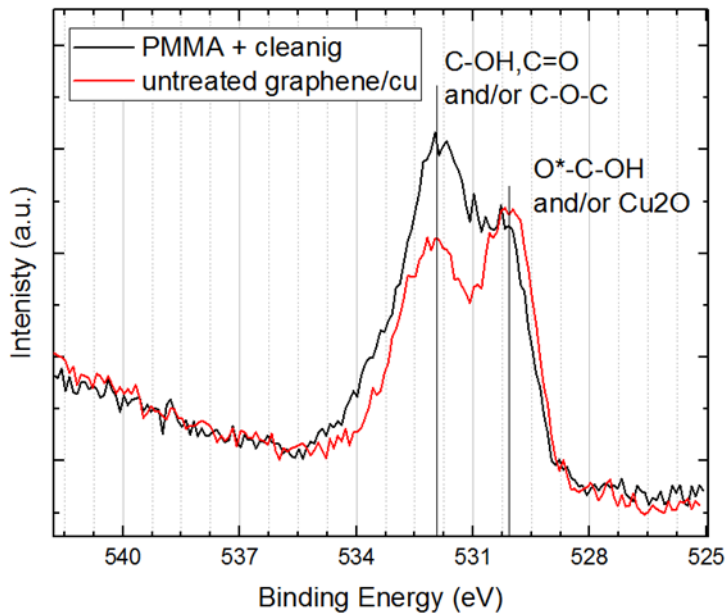


Fig. S9.3 – High resolution XPS O1s spectra for untreated graphene on copper and the same sample after PMMA deposition, and PMMA removal (same

procedure as in transfer). Peak normalization was done according to maximum of C1s peak. PMMA residue appear as an increase of the band at 532 eV.

SUPPLEMENTARY REFERENCES

- [1] J. Afonso Ferreira, L. Stafford, R. Leonelli, A. Ricard, *J. Appl. Phys.* 115 (2014) 163303.
- [2] S. Ni, Z. Li, J. Yang, *Nanoscale* 4 (2012) 1184–1189.
- [3] R. Hawaldar, P. Merino, M.R. Correia, I. Bdikin, J. Grácio, J. Méndez, J.A. Martín-Gago, M.K. Singh, *Sci. Rep.* 2 (2012) 682.
- [4] Y. Wang, J. Ghanbaja, F. Soldera, S. Migot, P. Boulet, D. Horwat, F. Mücklich, J.F. Pierson, *Appl. Surf. Sci.* 335 (2015) 85–91.
- [5] J. Cermak, T. Yamada, K. Ganzerova, B. Rezek, *Adv. Mater. Interfaces* 3 (2016) 1–7.
- [6] S. Chen, L. Brown, M. Levendorf, W. Cai, S.Y. Ju, J. Edgeworth, X. Li, C.W. Magnuson, A. Velamakanni, R.D. Piner, J. Kang, J. Park, R.S. Ruoff, *ACS Nano* 5 (2011) 1321–1327.

Annexe 3 : Effet de régénérescence aux joints de grains

PREFERENTIAL SELF-HEALING AT GRAIN BOUNDARIES IN PLASMA-TREATED GRAPHENE

P. Vinchon^{1†}, X. Glad^{1†}, G. Robert Bigras¹, R. Martel², L. Stafford¹

¹Département de Physique, Université de Montréal, Montréal, Québec, CANADA.

²Département de Chimie, Université de Montréal, Montréal, Québec, CANADA.

[†]Co-authors sharing the same contribution to this work

ABSTRACT

Engineering of defects located in-grain or at grain boundary is central to the development of functional materials. While there is a recent surge of interest in the formation, migration, and annihilation of defects during ion and plasma irradiation of bulk (3D) materials, the fundamental processes are rarely assessed in low-dimensional materials and remain mostly unexplored spectroscopically at the micrometer scale due to experimental limitations. A new hyperspectral Raman imaging scheme providing high selectivity and diffraction-limited spatial resolution is here adapted to examine plasma-induced damage in a polycrystalline graphene film. Spatially resolved Raman conducted before and after each plasma treatment shows defect generation in graphene exposed to very low-energy (11-13eV) ion bombardment following a 0D defect curve, while the domain boundaries tend to develop as 1D defects. Surprisingly and contrary to common expectations of plasma-surface interactions, damage generation at grain boundaries is slower than within the grains, a behavior ascribed to preferential self-healing. These evidences of local defect migration and structural recovery in graphene shed new light on the complexity of chemical and physical processes at the grain boundaries of 2D materials.

INTRODUCTION

The outstanding properties of graphene makes this 2D materials attractive for many applications [1]. Large-area graphene grown by chemical vapor deposition (CVD) is interesting for flexible

electronics, but the method produces polycrystalline films in which the graphene grains are attached together by covalent carbon bonds in various configurations. Beyond 1 nm grain size, grain boundaries (GBs) limit the electronic properties of graphene [2] and hence, significant efforts have been invested towards increasing the grain size. Theoretically, GBs are not only limiting electronic transport [3], but can also, depending on their atomic arrangement, exhibit distinct mechanical [4], magnetic [5], and chemical [6] properties. Adjusting the gas flows during CVD [7,8] can tailor geometric aspects of the grains (tilt misorientation and edge type [3,9]), but the influence of GBs are difficult to avoid completely.

Post-growth modification, either by ion bombardment or by plasma treatment, are used to engineer graphene [1,10,11]. While high-energy ions lead to a sputtering of both the 2D materials and the substrate below, low-energy ions (typically below the displacement threshold energy of 18–22eV [12]) can be used for damage generation within the honeycomb lattice [13–15]. However, the formation, migration, and annihilation of defects have been difficult to probe experimentally [16–18]. Graphene damage evolution at GBs have been studied using transmission electron microscopy, but the material is unstable, even below 80kV [19,20]. The vibrational modes of graphene are sensitive to disorders and lattice perturbations [21] such that Raman spectroscopy is a relevant technique to study damage in graphene [22,23]. Highlighting different types of defects has, however, been difficult due to the low sensitivity and restrained spatial resolution of conventional Raman systems – mapping Raman is slow and the laser diameter (\sim 1 nm) is much larger than the defect size (e.g. 2.8nm for GBs [24]). Such resolution limitations can be overcome by Tip Enhanced Raman Spectroscopy [25] (TERS), which enables nano-scale studies of graphene.

In this work, the advantages of the new RIMATM system (Raman IMAge from Photon Etc.) are used to study plasma-induced damage in graphene. Hyperspectral Raman imaging with RIMATM provides global Raman mapping (130 \times 130 μm^2) with improved sensitivity and tremendous statistics (10^5 - 10^6 spectra over the probed area), while maintaining diffraction-limited spatial resolution [26]. RIMATM measurements have been performed between each of the 12 subsequent plasma treatments and Raman band parameters were extracted and analyzed. It is demonstrated that graphene domains develop ion-induced 0D defects while pixels containing

GBs reveal a greater density of 1D type defects. RIMATM analysis further highlights a surprising resilience of GBs under very-low-energy ion irradiation. Such advances in non-destructive monitoring and plasma-induced modification of grain defects and grain boundaries in 2D materials can significantly benefit applications. This includes the ability to control CVD growth over very-large-area substrates as well as the doping and band gap tuning by ion or plasma irradiation.

RESULTS

Raman mappings with RIMA™ were performed at a laser wavelength of 532nm (2.33eV) on a CVD-grown polycrystalline monolayer graphene film transferred on SiO₂ substrate, from t=0s (pristine) to a total cumulated treatment time of t=1005s in a pulsed, inductively-coupled argon plasma (see section S-I of the supplementary information). Plasma-graphene interaction in such plasmas involves not only argon ions accelerated in the sheath surrounding the graphene sample, but also metastable argon atoms and photons. Over the range of experimental conditions examined, the contribution for each species to the total energy fluence is 43% by ions, 16% by metastable (and resonant) species, and 41% by photons (see section S-II). Finally, for a duty cycle of 10%, incident ions impinge on the graphene sample with 11-13eV of kinetic energy for 10% of the total treatment time (plasma on) and 1eV for the other 90% (plasma off).

Raman imaging was carried out after each subsequent treatment, giving 13 measurements over the same 130×130-um² area of the graphene sample with 3·10⁵ points each. Raman spectrum of pristine, single-layer graphene contains mainly 2 features: G (~1580cm⁻¹) and 2D (~2690cm⁻¹) bands. Disorder in graphene induces the D band (~1350cm⁻¹). The expected behavior of the G, 2D and D band parameters (position ω , full-width at half maximum Γ , peak intensity I, and peak area A) with damage, strain (tensile and compressive), number of layers in ABAB-stacking, and p- and n-doping are summarized in Section S-III.

The relevant Raman band parameters –thoroughly extracted according to section S-IV– were plotted in a Cançado-like graph [23]. The results for pristine and plasma-treated graphene are displayed in Figure 1. One notices that weak but distinct steps in the damage generation were obtained due to chosen plasma irradiation conditions. Results show a slow but constantly

increasing evolution towards amorphization following the 0D defect type curve (top green curve). The *amorphization trajectory* is usually defined in stage 1 when progressing from undisturbed graphene to nanocrystalline graphene, and in stage 2 progressing towards amorphous carbon [27,28]. The delimitation between the two stages occurs at the maximum of I_D/I_G and A_D/A_G . Interestingly, the statistically meaningful $3 \cdot 10^5$ -point distribution reveals a tail at higher Γ_G for $t=0$ (black arrow) progressively switching to a lower A_D/A_G tail at $t=340\text{s}$ (i.e. $0.25\text{J}\cdot\text{cm}^{-2}$; red arrow). This induces a notable distribution broadening from the pristine state to 340s of cumulative plasma treatment. The distribution narrows down afterwards.

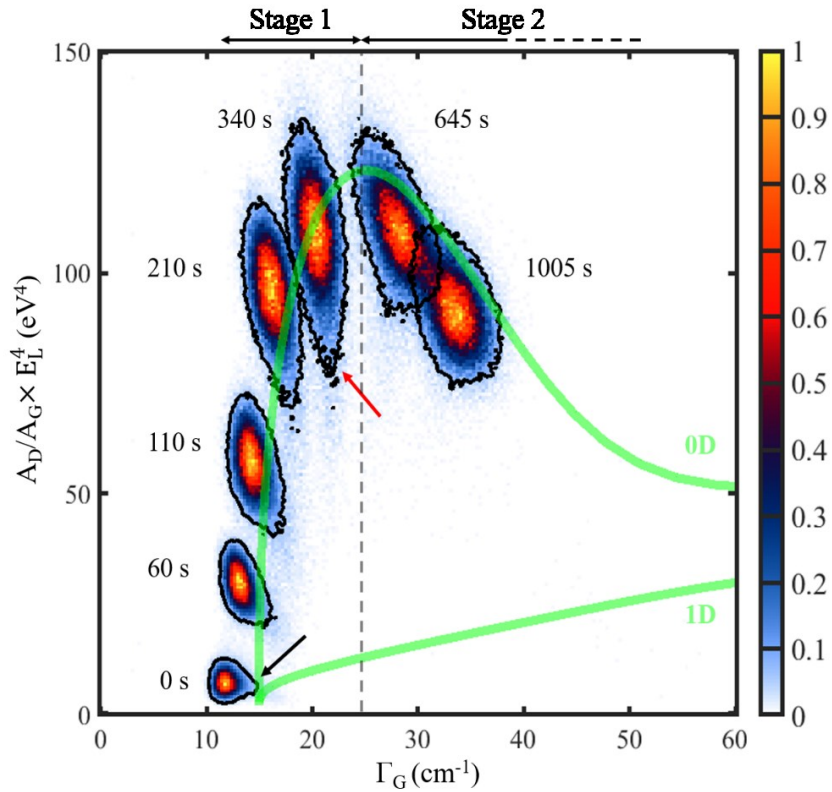


Figure 1. Subsequent graphene treatments plotted in a Cançado-like graph: evolution of $A_D/A_G \times E_L^4$ versus Γ_G . The colored scale is density-normalized. Green lines delimit the 0D and 1D defect-type evolutions. For clarity, black outlines highlight the 7 different sets of data. The gray dashed line delimits the 2 commonly reported stages of the amorphization trajectory.

A deeper understanding of this broadening in the statistics calls for spatially-resolved analysis. To do so, an image registration algorithm has been carried out to align together subsequent RIMATM

mappings. Figure 2 presents the laser-corrected AD/AG ratio (vertical scale of **Fig. 2**) for 3 cumulative times: $t=0$, 60 and 425s (i.e. 0, 4.5×10^{-2} , and $0.32 \text{J} \cdot \text{cm}^{-2}$, respectively). Subfigure 2(a) displays a great homogeneity with only local and randomly spread discrepancies exhibiting higher values; this demonstrates a good quality of CVD-grown graphene. However, subfigures 2(b) and 2(c) highlight continuous lines of notably lower values. This implies areas richer in 1D-type defects matching with graphene grain boundaries (GBs) [23]. This aspect was further confirmed by optical microscopy: linear discrepancies observed in RIMATM perfectly matched with GBs (see section S-IV).

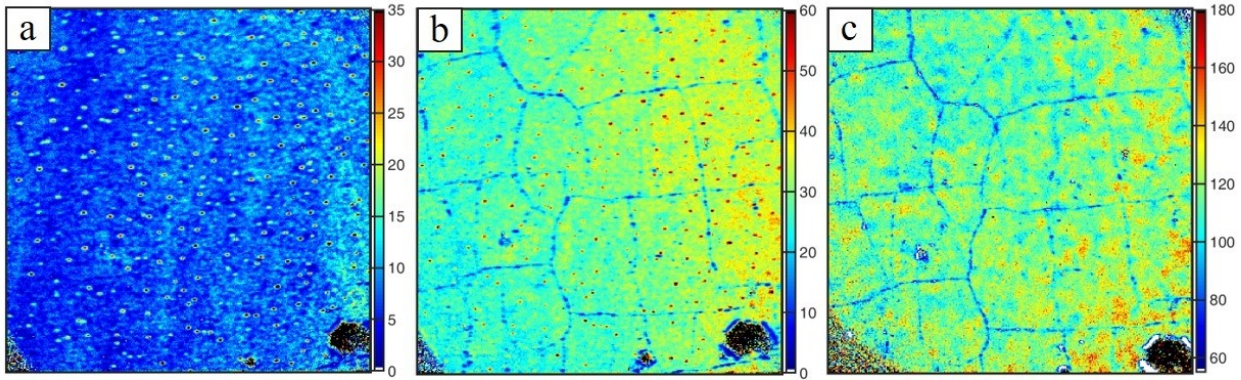


Figure 2. $130 \times 130 \mu\text{m}^2$ $A_D/A_G \times E_L^4$ mappings of (a) pristine, (b) 60s and (c) 425s plasma-treated graphene. Note the color scale difference for each map.

Figure 3 displays a color map of the horizontal scale of **Fig. 1** for the same area and same cumulative treatment times. **Fig. 3a** highlights areas of greater Γ_G values and thus displays a higher density of lattice disorder [23,29], especially from 1D-type defects. At $t=0$ (**Fig. 3a**), GBs are discernible from graphene grains (GRs) with average values of $\Gamma_{G,GB}=15 \text{cm}^{-1}$ and $\Gamma_{G,GR}=12 \text{cm}^{-1}$; these are typical values for slightly-doped graphene [30]. Results are similar for $t=60\text{s}$ (**Fig. 3b**) with values of $\Gamma_{G,GB}=16.5 \text{ cm}^{-1}$ and $\Gamma_{G,GR}=13.5 \text{ cm}^{-1}$ for GBs and GRs, respectively. However, **Fig. 3c** ($t=425\text{s}$) presents different look since the continuous lines no longer stand out and Γ_G has become rather homogeneous throughout the whole area probed by RIMATM with an average value of 25 cm^{-1} . This value coincides with maxima of I_D/I_G and A_D/A_G , which is often marked as the onset of graphite/graphene amorphization (**Fig. 1**) [27,28].

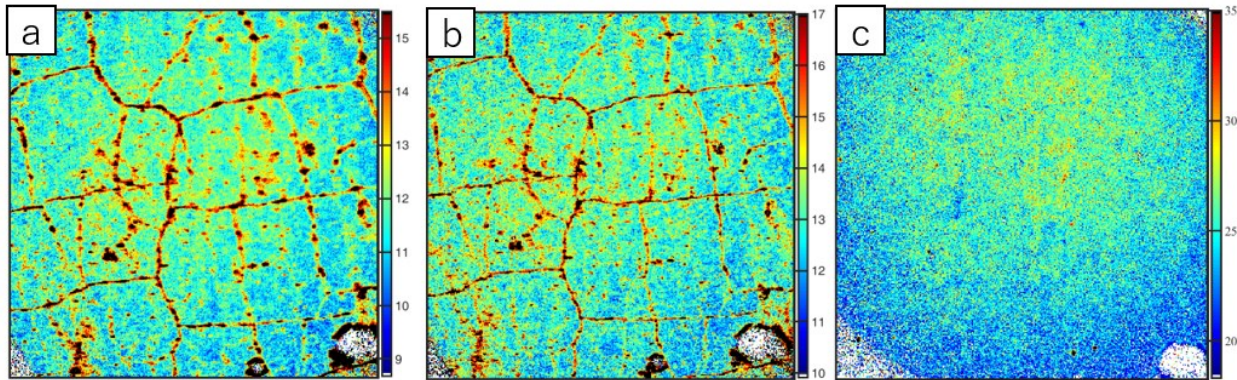


Figure 3. $130 \times 130 \mu\text{m}^2$ Γ_G mappings of (a) pristine, (b) 60s and (c) 425s plasma-treated graphene. Note the color scale difference for each map.

From these results, it can be seen that GBs exhibit more 1D-like defect properties than GRs, which follow exactly the 0D-type defect line. Hence, the local difference on the GBs seems linked to the broadening observed in the distribution of **Fig. 1**. This behavior is most likely related to the facts that graphene on SiO_2 is generally p-doped due to water-oxygen redox doping [31]: this influences both AD/AG [30] and Γ_G [32] (see Section S-III). Γ_G has also been shown to increase in CVD-grown polycrystalline graphene due to tensile or compressive strain [33,34].

To discriminate defect signals from doping and strain, the intensity ratio I_D/I_{2D} , has been evaluated because this parameter depends strongly on the damage generation [29] and only weakly on p- or n-doping of damaged graphene [32]. Figure 4 presents the values of I_D/I_{2D} of the same $130 \times 130 \mu\text{m}^2$ area at $t=0$ (a), 60s (b) and 425s (c). Maps in 4(a) and 4(b) indicate good homogeneity of the graphene surface even after tenfold increase of I_D/I_{2D} values after 60s of plasma treatment. Nevertheless, the discrepancy between GBs and GRs is noticeable for $t=425\text{s}$ as the former have a mean value of ~ 3 while the latter average at ~ 5 . This implies that the GBs are more resilient than the rest of the graphene to the damage generation in such mild, pulsed argon plasma conditions.

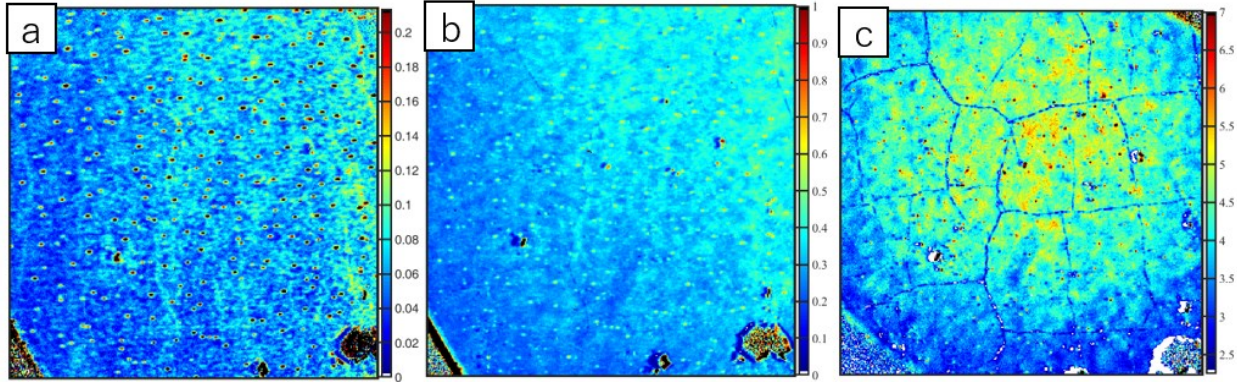


Figure 4. $130 \times 130 \mu\text{m}^2$ I_D/I_{2D} mappings of (a) pristine, (b) 60s and (c) 425s plasma-treated graphene. Note the color scale difference for each map.

Taking advantage of the characteristic Raman signatures at the GBs (Figs. 2-4), a method to extract the spectra associated with GB-pixels was developed (see section S-IV). From the set of data displayed in Figure 1, subfigure 5(a) presents the chosen GB-pixels whose spectroscopic data lead to the encircled points in **Fig. 5b**. When taking all 13 measurements into consideration, a spatially-resolved representation of the defect generation dynamics is obtained. Figure 5b reveals the strong difference between GBs and GRs to match the distribution broadening observed in **Fig. 1**: data from GRs follow almost perfectly the 0D-type defect line while those at GBs are shifted towards the 1D line. Note that the RIMATM pixel size is 400nm while GBs have a characteristic width of about 2-3nm only [24]. This size difference allegedly reduces the discrepancies between both curves since one can estimate that, within a GB-pixel, a maximum of 5% of the probed atoms might be included or affected by the boundary. The distinction between GBs and GRs is no longer observable after 1005s, which means that the damaged graphene has become more homogeneous due to amorphization over the whole sample surface. It is worth mentioning that the observed GRs and GBs evolution cannot be explained by the pure geometrical superposition of 0D defects over GBs (see section S-V); another mechanism must be considered.

Figure 5. (a) $92 \times 92 \mu\text{m}^2$ area map of Fig. 2c highlighting in red the locations of the selected GB spectra used to distinguish GBs from the rest of the graphene. (b) the *Cançado-like* graph extracted from Fig. 3. The dashed ellipse highlights the 425-sec plasma treated data.

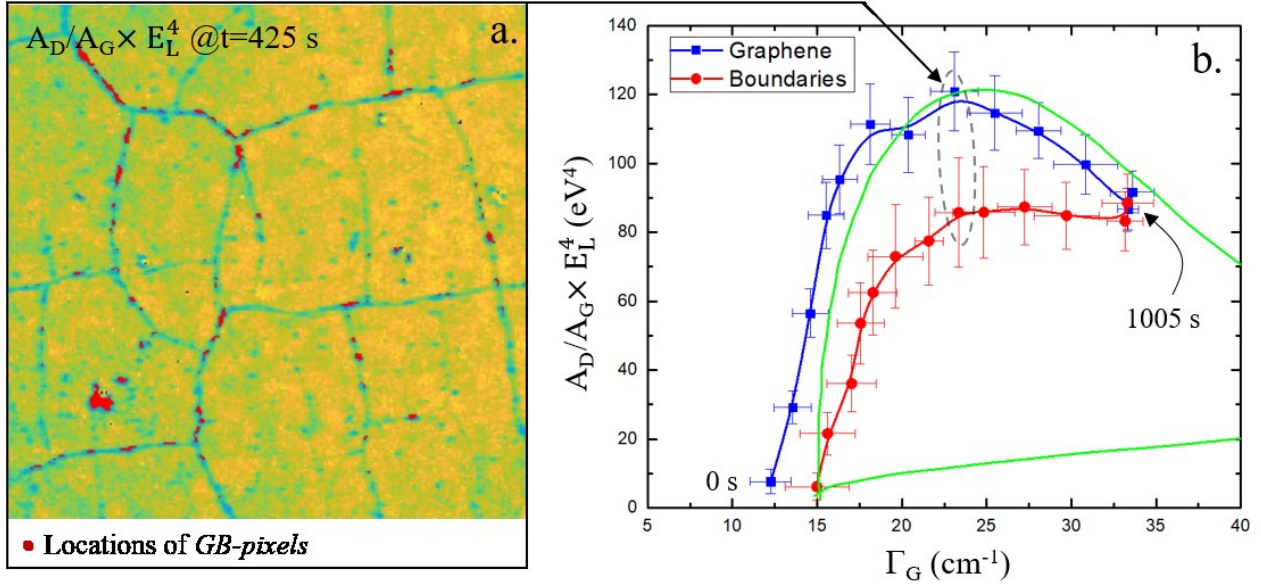


Figure 5. (a) $92 \times 92 \mu\text{m}^2$ area map of Fig. 2c highlighting in red the locations of the selected GB spectra used to distinguish GBs from the rest of the graphene. (b) the *Cançado-like* graph extracted from Fig. 3. The dashed ellipse highlights the 425-sec plasma treated data.

The aforementioned method was used to examine the evolution of other band parameters, namely I_{2D}/I_G , I_B/I_{2D} , Γ_{2D} , Γ_G , ω_G and ω_{2D} . Values for I_{2D}/I_G and I_B/I_{2D} are shown in Figure 6 as a function of the total energy fluence, from $t=60\text{s}$ ($0.03\text{J}\cdot\text{cm}^{-2}$) to $t=1005\text{s}$ ($0.75\text{J}\cdot\text{cm}^{-2}$). As a reference, values obtained on pristine graphene are given as horizontal dashed lines with the associated blue (GR) or red (GB) color. Additionally, the behaviors of Γ_{2D} , Γ_G , ω_G and ω_{2D} are detailed in Section S-VI. These parameters are influenced by different lattice perturbations (see Section S-III), but all are associated with graphene disorder [23,29]. Focusing on their pristine values, each parameter initially reports a greater defect density and/or a different defect-type for GBs versus GRs. In Fig. 6a, the initially high I_{2D}/I_G ratios, which is relatively lower at GBs, is also consistent with morphological differences between GB and GR regions. Indeed, a lower I_{2D}/I_G value at GBs is characteristic of structural defects, such as wrinkles and defective boundaries (see

section S-VI). To avoid interdependencies and focus solely on defect formation, **Fig. 6b** displays the evolution of I_D/I_{2D} [29,32]. With rising energy fluence, both signals at the GRs and GBs show a monotonous increase of I_D/I_{2D} due to rising density of defects. Yet, GBs show a different behavior characterized with a weaker slope. A definite distinction is further seen between total energy fluences of 0.16 and $0.57\text{J}\cdot\text{cm}^{-2}$, which is just before convergence of I_D/I_{2D} at $0.66\text{J}\cdot\text{cm}^{-2}$. This behavior before reaching a homogeneous density of defects throughout the whole analyzed area (amorphization) is consistent with a lower rate of damage generation at GBs with respect to the rest of the graphene film.

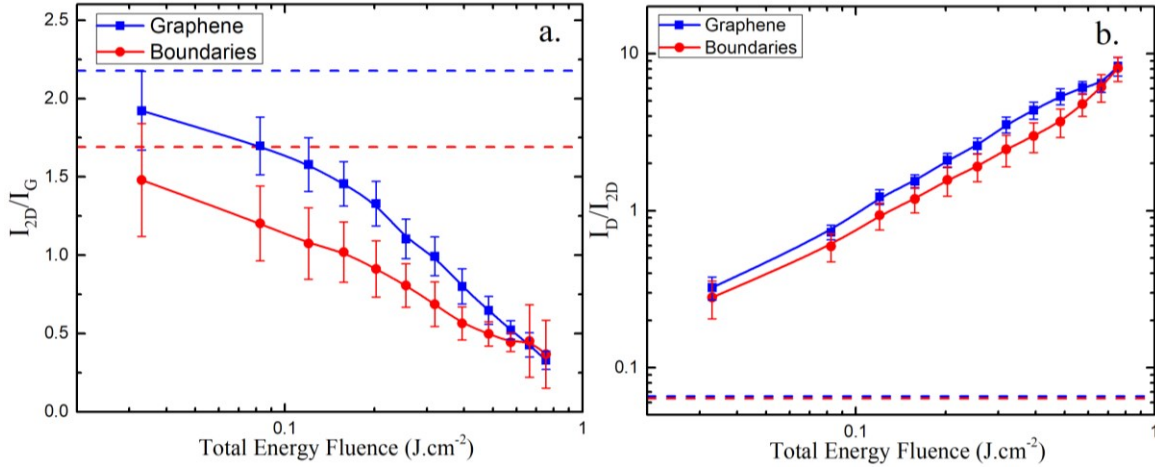


Figure 6. Relevant Raman parameters highlighting the discrepancies between graphene grain and grain boundaries. All parameters are plotted versus the total energy fluence during the subsequent plasma treatments ($60\text{s} \leftrightarrow 0.03\text{J}\cdot\text{cm}^{-2}$, $1005\text{s} \leftrightarrow 0.75\text{J}\cdot\text{cm}^{-2}$). The extracted Raman band parameters are: (a) I_{2D}/I_G and (b) I_D/I_{2D} . Values for pristine graphene are displayed as horizontal dashed lines. Pristine values are similar in (b).

DISCUSSION

After plasma treatment, the evolution of all Raman features –especially I_D/I_{2D} – demonstrates different damage formation/annihilation dynamics between GBs and GRs. More specifically, limited damage is observed at GBs compared with GRs. Due to their positive enthalpy as compared with GRs [35], GBs have been shown to be highly sensitive to irradiation processes, especially by reactive atoms [36,37] or high-energy electrons [19]. Under ion irradiation (between 1 eV and 1 keV), a preferential etching of GBs has been suggested [13,38], which is clearly

inconsistent with the results. This statement holds considering that GBs are not flat. In such conditions, lower binding energies and thus enhanced defect production rates are expected [39]. Therefore, a preferential adatoms-vacancies recombination at GBs, as illustrated in Figure 7, appears as key to explain their resilience.

Considering the 11-13eV argon ion flux and additional energy uptakes provided by plasma-generated species (for example, the surface recombination of argon ions and the surface deexcitation of argon metastable species that represents an instantaneous energy release of 15.8 and 11.5 eV, respectively), the plasma treatment yields to significant damage in the graphene lattice, including carbon adatom/vacancy pairs (Frenkel pairs). The current level of knowledge on the physics driving such damage formation by very-low energy ion irradiation is summarized in Section S-VII[12,13,15]. While a single vacancy requires ~1.3 eV for migration on a graphene surface, a carbon adatom only needs 0.4 eV to diffuse[12]. Thus, carbon adatoms on graphene are considered as mobile species under plasma irradiation and can adopt different migration paths that should eventually cross 0D or 1D type defects. In a first case scenario, annihilation can naturally occur at a 0D defect site [40]. Upon contact with grain boundaries (1D defects), carbon adatoms become highly mobile alongside the boundary [41,42], triggering an anisotropic transport responsible of an imbalance in the spatial distribution of carbon adatoms.[43] Hence, a second scenario can be inferred in which an accumulation or excess of carbon adatoms at the GBs enhances the annihilation probability at defects/vacancies near the GBs. Locally, the interstitial emission from this imbalance of adatom population in the zone of potential repair further contributes to the healing of vacancies near GBs [18]. The GB processes illustrated in Figure 7, which are supported by both calculations [44,45] and experiments [42,46,47], provide the main conditions to explain a preferential self-healing reported here at GBs.

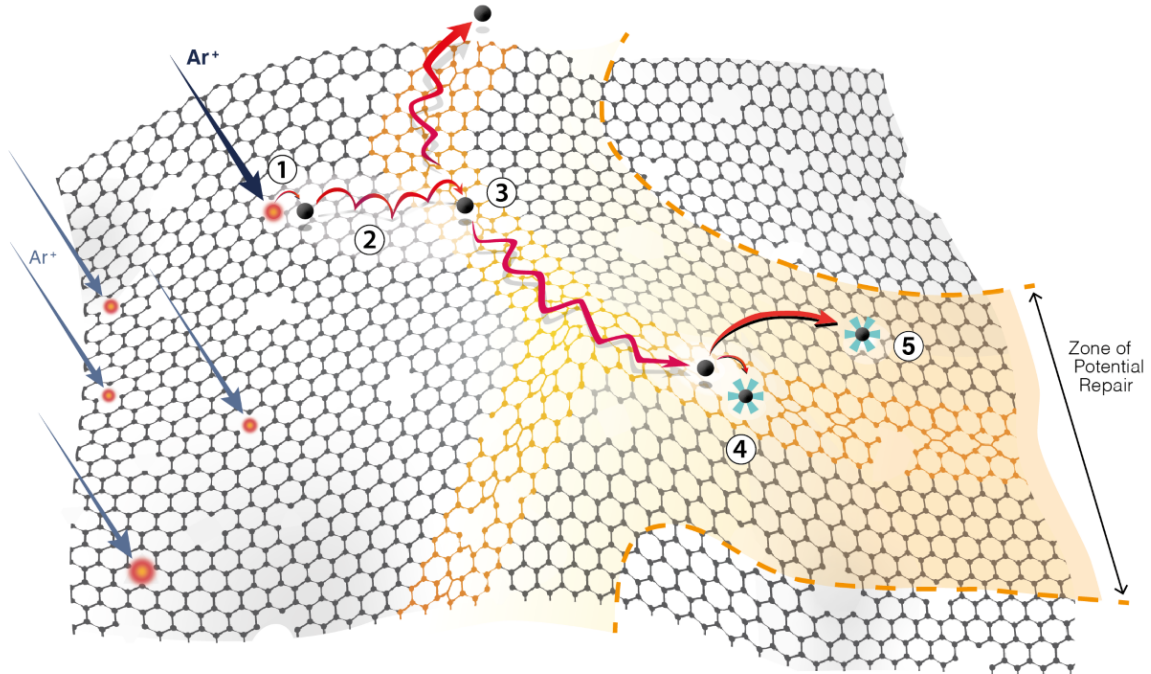


Figure 7. Schematics of preferential self-healing at GBs in plasma-treated graphene involving: (1) Formation of carbon adatoms-vacancies by plasma-generated species; (2) Preferential migration of carbon adatoms on the graphene surface; (3) Anisotropic transport of carbon adatoms along grain boundaries; (4) Defect healing at GBs; (5) Carbon adatom emission from GBs leading to defect healing in the zone of potential repair.

Preferential self-healing of radiation damage at GBs was first theorized by Bai et al. on Cu [18] and predicted to have a pronounced effect on graphene [42]. To the best of our knowledge, this is the first experimental demonstration of the resilience of GBs during damage generation in low-dimensional materials. A similar signature was observed on highly oriented pyrolytic graphite (HOPG) in very similar argon plasma etching conditions where hexagonal graphite pyramids were reported to form preferentially along GBs [48]. Their formation mechanism was ascribed to a greater etching rate at the GBs, suggesting preferential erosion at GBs as compared with graphene grains. Since domain boundaries are generally of the same type (i.e. 5-7 ring chains) in HOPG [49], the results presented in this study reveal, however, a completely different explanation to this behavior.

CONCLUSION

Because of their positive enthalpies with respect to the undisturbed honeycomb lattice, grain boundaries found in graphite or graphene were often assumed to be subject to faster and stronger lattice disorder under plasma irradiation. The five-order-of-magnitude size difference between grains and grain boundaries has made difficult, however, the experimental assessment of such difference during CVD growth and post-growth modifications of graphene films. Capitalizing on the highly innovative nature of the RIMATM system, damage generation induced by 12 subsequent plasma treatments in well-controlled conditions was analyzed. While a synergetic plasma effect is present due to the simultaneous energy input by ions, metastable species, and VUV photons, the main contribution to the damage generation is the 11-13eV ion flux. Thorough the analyses of 8 different Raman features related to the D, G and 2D bands, plasma-induced defect generation in graphene grains and grain boundaries were compared. In accordance with recent literature, a lattice reconstruction mechanism occurring preferentially at domain boundaries and induced by preferential atom migration and adatoms-vacancies recombination was revealed. This is, to our knowledge, the first experimental report of such preferential self-healing at grain boundaries in plasma processing of materials as well as in radiation damage studies of 2D materials.

Advances in Raman monitoring of plasma-graphene interactions together with the peculiar evolution of graphene grains and grain boundaries during ion and plasma irradiation open a new window for fundamental and applied studies on the structure, properties, and control of grains and grain boundaries. This includes detailed analysis of CVD-growth processes of graphene films over large area substrates as well as ion- and plasma-assisted processes for doping, band gap tuning, and layer-by-layer etching of low-dimensional materials. This study further suggests revisiting the mechanism for the formation of chemically doped graphene film under mild plasma treatments using argon mixed with either traces of N- or B-bearing gases, especially the latter since B-adatoms have a migration barrier on graphene far below that of C-adatoms [50]. More generally, these new results provide insights on the future of the design and engineering of 2D materials and call for a better integration of an important but too often marginalized feature of polycrystalline materials: the grain boundaries.

ACKNOWLEDGMENTS

This work was financially supported by the National Science and Engineering Research Council (NSERC), PRIMA-Québec, Plasmionique Inc., Photon Etc., the Fonds de Recherche du Québec - Nature et Technologies (FRQNT), and the Canada Research Chair program (L. Stafford and R. Martel). The authors thank Carl Charpin for providing the CVD-grown graphene samples and Charlotte Allard for technical support with RIMATM measurements.

REFERENCES

- [1] A. Zurutuza, C. Marinelli, *Nat. Nanotechnol.* 9 (2014) 730–734.
- [2] K. Balasubramanian, T. Biswas, P. Ghosh, S. Suran, A. Mishra, R. Mishra, R. Sachan, M. Jain, M. Varma, R. Pratap, S. Raghavan, *Nat. Commun.* 10 (2019) 1–9.
- [3] O. V. Yazyev, S.G. Louie, *Nat. Mater.* 9 (2010) 806–809.
- [4] R. Grantab, V.B. Shenoy, R.S. Ruoff, *Science* (80-.). 330 (2010) 946–948.
- [5] J. Červenka, M.I. Katsnelson, C.F.J. Flipse, *Nat. Phys.* 5 (2009) 840–844.
- [6] S. Malola, H. Häkkinen, P. Koskinen, *Phys. Rev. B - Condens. Matter Mater. Phys.* 81 (2010) 1–6.
- [7] A.W. Tsen, L. Brown, R.W. Havener, J. Park, *Acc. Chem. Res.* 46 (2013) 2286–2296.
- [8] A.W. Tsen, P.Y. Huang, R.W. Havener, C.S. Ruiz-Vargas, D.A. Muller, L. Brown, M.P. Levendorf, J. Park, F. Ghahari, P. Kim, *Science* (80-.). 336 (2012) 1143–1146.
- [9] K.W. Clark, X.G. Zhang, I. V. Vlassiouk, G. He, R.M. Feenstra, A.P. Li, *ACS Nano* 7 (2013) 7956–7966.
- [10] V. Georgakilas, J.N. Tiwari, K.C. Kemp, J.A. Perman, A.B. Bourlinos, K.S. Kim, R. Zboril, *Chem. Rev.* 116 (2016) 5464–5519.
- [11] Z. Xiang, Q. Dai, J.F. Chen, L. Dai, *Adv. Mater.* (2016) 6253–6261.
- [12] F. Banhart, J. Kotakoski, A. V. Krasheninnikov, *ACS Nano* 5 (2011) 26–41.
- [13] P. Ahlberg, F.O.L. Johansson, Z.B. Zhang, U. Jansson, S.L. Zhang, A. Lindblad, T. Nyberg, *APL Mater.* 4 (2016).
- [14] P. Vinchon, X. Glad, G. Robert-Bigras, R. Martel, A. Sarkissian, L. Stafford, *J. Appl. Phys.* 126 (2019) 233302.
- [15] A. V. Krasheninnikov, F. Banhart, *Nat. Mater.* 6 (2007) 723–733.
- [16] X. Zhang, K. Hattar, Y. Chen, L. Shao, J. Li, C. Sun, K. Yu, N. Li, M.L. Taheri, H. Wang, J. Wang, M. Nastasi, *Prog. Mater. Sci.* 96 (2018) 217–321.
- [17] K. Nordlund, S.J. Zinkle, A.E. Sand, F. Granberg, R.S. Averback, R.E. Stoller, T. Suzudo, L. Malerba, F. Banhart, W.J. Weber, F. Willaime, S.L. Dudarev, D. Simeone, *J. Nucl. Mater.* 512 (2018) 450–479.
- [18] X.M. Bai, A.F. Voter, R.G. Hoagland, M. Nastasi, B.P. Uberuaga, *Science* (80-.). 327 (2010) 1631–1634.
- [19] S. Kurasch, J. Kotakoski, O. Lehtinen, V. Skákalová, J. Smet, C.E. Krill, A. V. Krasheninnikov, U. Kaiser, *Nano Lett.* 12 (2012) 3168–3173.
- [20] J. Kotakoski, C. Mangler, J.C. Meyer, *Nat. Commun.* 5 (2014) 2–6.

- [21] R. Beams, L.G. Cançado, L. Novotny, *J. Phys. Condens. Matter* 27 (2015) 083002.
- [22] M.M. Lucchese, F. Stavale, E.H.M. Ferreira, C. Vilani, M.V.O. Moutinho, R.B. Capaz, C. a. Achete, A. Jorio, *Carbon N. Y.* 48 (2010) 1592–1597.
- [23] L. Gustavo Cançado, M. Gomes da Silva, E.H. Martins Ferreira, F. Hof, K. Kampioti, K. Huang, A. Pénicaud, C. Alberto Achete, R.B. Capaz, A. Jorio, *2D Mater.* 4 (2017) 025039.
- [24] J. Ribeiro-Soares, M.E. Oliveros, C. Garin, M.V. David, L.G.P. Martins, C.A. Almeida, E.H. Martins-Ferreira, K. Takai, T. Enoki, R. Magalhães-Paniago, A. Malachias, A. Jorio, B.S. Archanjo, C.A. Achete, L.G. Cançado, *Carbon N. Y.* 95 (2015) 646–652.
- [25] R. Beams, *J. Raman Spectrosc.* 49 (2018) 157–167.
- [26] E. Gaufrès, S. Marcket, V. Aymong, N.Y.W. Tang, A. Favron, F. Thouin, C. Allard, D. Rioux, N. Cottenye, M. Verhaegen, R. Martel, *J. Raman Spectrosc.* 49 (2018) 174–182.
- [27] A.C. Ferrari, J. Robertson, *Philosophical Trans. Math. Phys. Eng. Sci.* 363 (2004) 2477–2512.
- [28] A. Eckmann, A. Felten, A. Mishchenko, L. Britnell, R. Krupke, K.S. Novoselov, C. Casiraghi, *Nano Lett.* 12 (2012) 3925–3930.
- [29] Y.-B.B. Zhou, Z.-M.M. Liao, Y.-F.F. Wang, G.S. Duesberg, J. Xu, Q. Fu, X.-S.S. Wu, D.-P.P. Yu, *J. Chem. Phys.* 133 (2010) 234703.
- [30] A. Das, S. Pisana, B. Chakraborty, S. Piscanec, S.K. Saha, U. V Waghmare, K.S. Novoselov, H.R. Krishnamurthy, a. K. Geim, A.C. Ferrari, A.K. Sood, *Nat. Nanotechnol.* 3 (2008) 210–215.
- [31] P.L. Levesque, S.S. Sabri, C.M. Aguirre, J. Guillemette, M. Siaj, P. Desjardins, T. Szkopek, R. Martel, *Nano Lett.* 11 (2011) 132–137.
- [32] M. Bruna, A.K. Ott, M. Ijäs, D. Yoon, U. Sassi, A.C. Ferrari, *ACS Nano* 8 (2014) 7432–7441.
- [33] M.A. Bissett, W. Izumida, R. Saito, H. Ago, *ACS Nano* 6 (2012) 10229–10238.
- [34] Y. Wang, Y. Wang, C. Xu, X. Zhang, L. Mei, M. Wang, Y. Xia, P. Zhao, H. Wang, *Carbon N. Y.* 134 (2018) 37–42.
- [35] C. Ophus, A. Shekhawat, H. Rasool, A. Zettl, *Phys. Rev. B - Condens. Matter Mater. Phys.* 92 (2015).
- [36] R. Yang, L. Zhang, Y. Wang, Z. Shi, D. Shi, H. Gao, E. Wang, G. Zhang, *Adv. Mater.* 22 (2010) 4014–4019.
- [37] G. Diankov, M. Neumann, D. Goldhaber-Gordon, *ACS Nano* 7 (2013) 1324–1332.
- [38] T. Larionova, T. Koltsova, E. Bobrynnina, A. Smirnov, I. Eliseyev, V. Davydov, O. Tolochko, *Diam. Relat. Mater.* 76 (2017) 14–20.
- [39] M. Kabir, K.J. Van Vliet, *J. Phys. Chem. C* 120 (2016) 1989–1993.
- [40] J. Chen, T. Shi, T. Cai, T. Xu, L. Sun, X. Wu, D. Yu, *Appl. Phys. Lett.* 102 (2013).
- [41] L.F. Huang, M.Y. Ni, G.R. Zhang, W.H. Zhou, Y.G. Li, X.H. Zheng, Z. Zeng, *J. Chem. Phys.* 135 (2011).
- [42] B. Wang, Y. Puzyrev, S.T. Pantelides, *Carbon N. Y.* 49 (2011) 3983–3988.
- [43] A. Hashimoto, K. Suenaga, A. Gloter, K. Urita, S. Iijima, *Nature* 430 (2004) 870–873.
- [44] L.J. Zhou, Z.F. Hou, L.M. Wu, Y.F. Zhang, *J. Phys. Chem. C* 118 (2014) 28055–28062.
- [45] T. Botari, R. Paupitz, P. Alves Da Silva Autreto, D.S. Galvao, *Carbon N. Y.* 99 (2016) 302–309.
- [46] T.H. Liu, G. Gajewski, C.W. Pao, C.C. Chang, *Carbon N. Y.* 49 (2011) 2306–2317.
- [47] S.U. Yu, B. Park, Y. Cho, S. Hyun, J.K. Kim, K.S. Kim, *ACS Nano* 8 (2014) 8662–8668.
- [48] X. Glad, L. de Poucques, J. Bougdira, *J. Phys. D. Appl. Phys.* 48 (2015) 495304.
- [49] P. Simonis, C. Goffaux, P.A. Thiry, L.P. Biro, P. Lambin, V. Meunier, *Surf. Sci.* 511 (2002) 319–322.

[50] J. Kotakoski, A. V. Krasheninnikov, Y. Ma, A.S. Foster, K. Nordlund, R.M. Nieminen, Phys. Rev. B 71 (2005) 205408.

SUPPLEMENTARY DATA

S-I. MATERIALS & METHODS

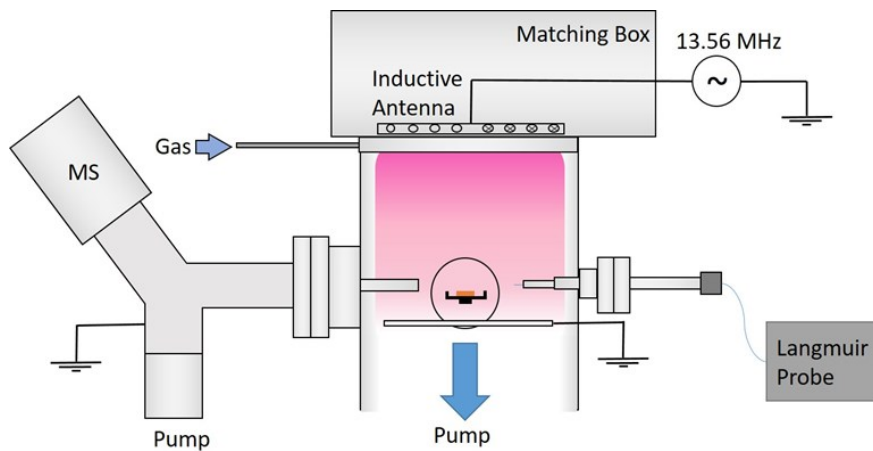


Figure S1. Sketch of the plasma apparatus.

The ICP reactor from Plasmionique Inc. used in this study has been extensively described in a previous study [1]. A detailed schematic is shown in Figure S1 of the supplementary data. Briefly, a 13.56 MHz RF power supply (R601, from Seren IPS Inc.), operating in continuous or pulsed mode, is coupled with an automatic matching box to ensure minimal reflected power via impedance matching. The RF current then goes through a planar spiral-shaped antenna which inductively couples the input RF power to produce a high-density argon plasma (plasma density, $n_i = 10^9\text{-}10^{11}\text{ cm}^{-3}$). The reactor walls are a 30 cm-high 16 cm-wide hollow stainless-steel cylinder terminated on its upper edge by a quartz window located just below the antenna. The pumping system encircles the bottom of the chamber and ensures a base pressure of 5×10^{-8} Torr (6.7×10^{-6} Pa) to limit the presence of traces of contaminants during the plasma treatments. Ultra-high-purity (99.999%) argon gas flux is controlled via a solenoid valve to reach the desired pressure before plasma ignition. Prior to any treatment, a degassing of graphene sample in the reactor is carried out until residual pressure decreases below 1×10^{-7} Torr. The sample is then conserved and

protected in the load lock during the reactor chamber conditioning. To avoid desorption of adsorbed species from the reactor walls and eventual deposition on the graphene films during plasma exposure, a 30-min argon plasma conditioning is systematically carried out before sample insertion with the exact same conditions used for plasma treatment of graphene films. Thanks to the conditioning procedure to minimize contamination aspects during plasma processing, excellent reproducibility was achieved over many plasma treatments of comparable graphene films. During plasma exposure, graphene films are placed on an isolated substrate-holder, which is inserted in the plasma chamber using a load lock. The graphene film is then positioned 20 cm below the antenna (in the diffused plasma region) and at the very center of the plasma reactor.

Plasma electrical parameters were measured by a cylindrical rf-compensated Langmuir Probe (LP) from Scientific Systems Ltd. The latter was placed at about 2 cm above the substrate holder. Time-resolved measurements were taken in sequential mode triggered directly by a pulse generator synchronized with the pulse from the power supply. The probe bias voltage ranged from -60 to 30 V every 20 μ s to obtain the current-voltage characteristics from which we extracted the electron temperature T_e , the ion density n_i (or electron density assuming quasi-neutrality), and the plasma and floating potentials, V_p and V_f , respectively.

Optical absorption spectroscopy (OAS) was performed to determine argon metastable (Ar^m : $1s^3$ and $1s^5$ at \sim 11.6 eV above the fundamental state Ar^0) and argon resonant (Ar^* : $1s^2$ and $1s^4$ at \sim 11.7 eV above Ar^0) state densities. The setup used is described in details in [2]. In this case, however, the argon lamp is powered by a continuous tension generator up to 4 kV in order to avoid alternating current perturbations during measurements in a pulsed argon plasma. Optical spectra were taken with a Princeton Instruments Isoplane spectrometer with a 300 gr \cdot mm $^{-1}$ grating. The spectrometer was temporally synchronized with the power supply using a pulse generator to trigger data collection 40 μ s before the input power pulse. Measurements were then taken every microsecond and each spectrum is averaged over 500 accumulations to ensure reproducibility. Coupling these results with the ones from the LP analysis, we can extract the total energy fluence, i.e. the maximum transferable energy (in $J\cdot cm^{-2}$) by argon ions, metastable neutrals, and VUV photons (emitted by resonant states). Over the range of experimental conditions examined in this study, the total energy fluence mostly results from very-low-energy

ion irradiation. Note that the ion energy distribution function is assumed as monoenergetic within the approximation $E_{\text{ion}} = e \cdot (V_p - V_f)$, e being the elementary charge. This aspect was confirmed by plasma sampling mass spectrometry analysis of the ion energy distribution function. Extensive details about this procedure are given in a previous work [1].

The graphene film was synthesized on a 25- μm -thick polycrystalline copper foil by CVD in a controlled CH_4/H_2 environment [3]. The technique is well-mastered, reproducible and lead to high-quality polycrystalline monolayer graphene films. Then, the film is transferred using the standard PMMA transfer method from the Cu foil to a SiO_2/Si substrate [4]. The sample underwent 12 subsequent treatments in fixed plasma conditions that were adequately chosen to provide a mild 2-step physical etching of CVD-grown polycrystalline graphene films. These are detailed in the next section.

Damage generation within the lattice was assessed for pristine graphene and after each subsequent plasma treatment by hyperspectral Raman spectroscopy using the RIMA (Raman IMAgEr) system [5,6]. In short, a uniform laser illumination ($\lambda_{\text{laser}} = 532 \text{ nm}$) of the graphene film induces a global Raman response over a wide area ($130 \times 130 \mu\text{m}^2$). The reemitted light is then directed to a volume Bragg grating in order to discriminate and select a specific range of wavelengths to be projected onto a CCD camera. Following the acquisition, data is then reconstructed as to obtain a cube (3D matrix) containing information on the spectral evolution of the whole probed area. Each collected spectrum has a spectral step of 3 cm^{-1} . Binning on the CCD camera ensures a spatial resolution of 400 nm, which corresponds to the size of a pixel in the Raman mappings. From the resulting Raman spectra, meaningful data is extracted through a process presented in detail in a previous paper [6]. Briefly, a noise filtering method based on Principal Component Analysis (PCA) is used to decorrelate Raman peaks from (i) the noise and (ii) the spatially non-uniform artefact inherent to the RIMA setup. This allows for a correct fitting of all Raman bands and produces mappings of various parameters, such as position (ω), full width at half maximum (Γ), peak intensity (I) and peak area (A).

S-II. PLASMA CHARACTERIZATION

A previous study [1] showed that argon plasmas can easily generate tremendous damage on CVD-grown polycrystalline graphene films despite a very-low ion energy and short-time treatment. Indeed, the high population of charged species in inductive mode (H-mode) of a low-pressure argon plasma induces elevated ion flux ($10^{17} \text{ cm}^{-2} \cdot \text{s}^{-1}$) and thus very high ion fluences compared to ion bombardment with typical ion guns ($10^{11}\text{-}10^{15} \text{ cm}^{-2}$) [7]. Aiming at thoroughly studying the defect formation dynamics in graphene films, intermediate treatment steps were required. Thus, it was needed to find plasma conditions leading to a weaker damage generation (smaller energy fluence) while ensuring a minimal contribution from argon metastable species to the total energy flux as their deexcitation on the surface of graphene can have a strong influence on the graphene defect formation dynamics [1].

To circumvent this issue, the energy fluence provided to the graphene films is reduced by first lowering pressure and RF input power as much as possible while keeping the power coupling in the inductive mode. This is primordial as it has been shown that the metastable states dominates the energy flux in capacitive mode (arising at very low RF input power and/or higher pressure) [1]. Thus, conditions with a pressure of 5 mTorr at 100 W were selected. Additionally, to decrease the energy fluence even further, the discharge was ignited in pulsed mode. The mildest conditions were found for a frequency of 1 kHz (period $T = 1 \text{ ms}$) with a duty cycle DC = 10%, i.e. a pulse duration $\tau = 100 \mu\text{s}$ ($10\% \times T$).

In these pulsed argon plasma conditions, Figure S2 of the supplementary data presents the temporal evolution of (a) T_e and $(V_p - V_f)$, as well as (b) n_i , $n(\text{Ar}^m)$ and $n(\text{Ar}^*)$ over a period T . At the beginning of the RF power pulse, a sharp increase of T_e and $(V_p - V_f)$ up to respectively 3.5 eV and 12 V is observed. Both parameters slowly decrease within the duration of the pulse down to 2.9 eV and 10 V, respectively. These values are close to the ones observed in continuous mode [1]. The sharp T_e increase is due to an imbalance between electron energy gains and losses before reaching a quasi-steady-state regime [8]. The same behavior is observed for $(V_p - V_f)$ as this parameter is expected to be proportional to T_e in low-pressure argon plasmas [9]. Immediately after switching off the RF power, T_e and $(V_p - V_f)$ values decrease rapidly and then stabilise during

the rest of the period at around 0.5 eV and 1 V, respectively. Non-null values can only be explained by the presence of a temporal afterglow (post-discharge) [10]. This is confirmed by the results presented in **Fig. S2b** of the supplementary data, as n_i , $n(\text{Ar}^m)$ and $n(\text{Ar}^*)$ maintain significant proportion of their plasma-on values during the post-discharge [11]. Metastable density is barely affected by the pulse and stays at around $1 \times 10^{10} \text{ cm}^{-3}$ for the whole period. The slight increase observed is related to Ar^m sources greater than losses during plasma on phase, while the balance changes in the afterglow; the steady decrease is due to deexcitation by electron quenching [11] and diffusion to the walls. Regarding the ion density, it rises sharply from $8 \times 10^8 \text{ cm}^{-3}$ to $3 \times 10^9 \text{ cm}^{-3}$ and then reaches a plateau. At the pulse end in the absence of a creation mechanism, the plasma monotonously declines back to its previous value due to losses by diffusion to the walls [12]. The population of resonant species is greatly affected by the power pulse since it increases rapidly up to $2 \times 10^9 \text{ cm}^{-3}$ at plasma on before quickly dropping down to about $3 \times 10^8 \text{ cm}^{-3}$ in the post-discharge. Such behavior is explained by the very low-pressure conditions, which prevent VUV to be absorbed and reemitted by the gas phase, their mean-free-path being rather large at such a low pressure [13]. Note that the increasing noise seen at plasma off is due to the detection limit of the OAS method.

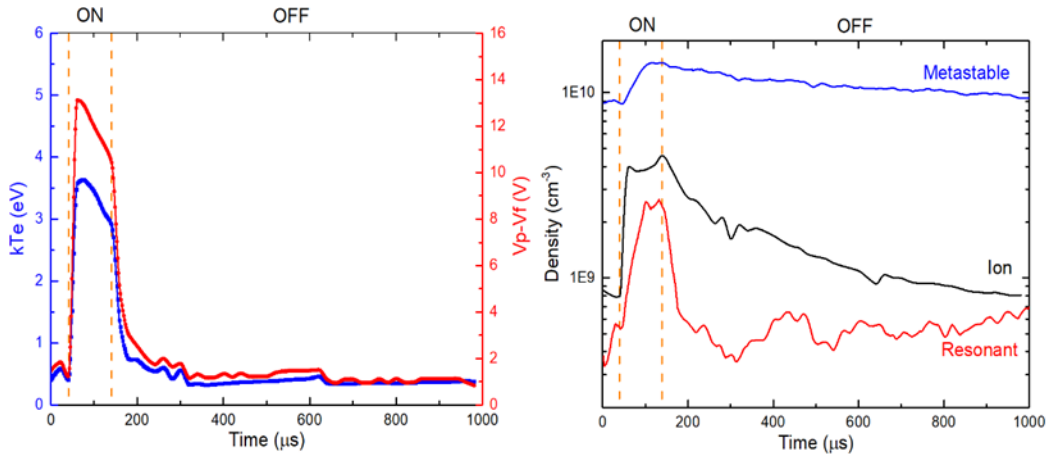


Figure S2. (a) Electron temperature kT_e (in eV, blue) and $V_p - V_f$ (in V, red) derived from cylindrical LP measurements. The ion energy E_{ion} may be approximated to $(V_p - V_f)$. (b) Argon ion, metastable and resonant densities extracted from LP measurements for ions and OAS measurements otherwise.

Based on the data presented in **Fig. S2** of the supplementary data, the contribution of each species in the total power fluxes can be obtained. The results are shown in **Fig. S3** of the supplementary data for different pulsed conditions as compared with the continuous (DC = 100) plasma used in [1]. While VUV photons take a greater part of the total power flux, the ratio between the ion and metastable contributions has not changed between 5mTorr-500W-DC100 and 5mTorr-100W-1KHz-DC10. Between these two conditions, however, the power density drastically drops by about 3 orders of magnitude. This lower power density in pulsed argon plasma conditions allows a much more progressive study of the damage formation dynamics in graphene films since longer plasma treatment times (~ 80 s for each of the 12 subsequent treatments leading to a total treatment time of 1005 s) can be used to achieve comparable energy fluence as in continuous plasma conditions (single treatment of 15 s). Note that the total fluence is of the same order as the ablation threshold of graphene [14].

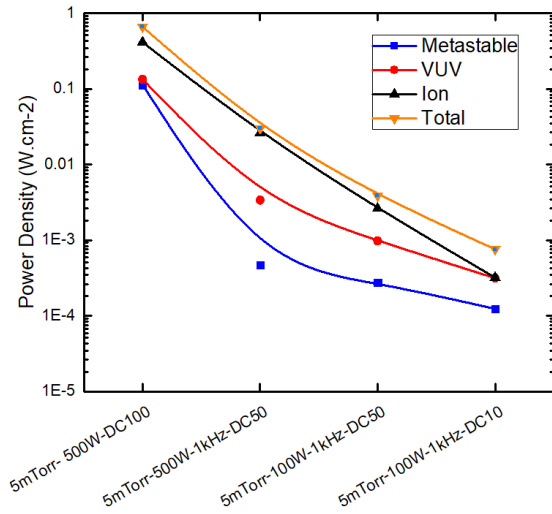


Figure S3. Evolution of the power density measured in the plasma reactor at the substrate location for 4 different conditions, labelled on the x-axis. Lines are guides to the eyes highlighting the net drop in power density.

S-III. EVOLUTION OF SELECTED RAMAN BAND PARAMETERS

Band	Doping		Strain ϵ		Damage	# of layers (Bernal stackings)
	p	n	<0 (compr.)	>0 (tensile)		
G	ω_G	[15,16]	↑ [15,16]	↑ [17,18]*	↓ [17–20]	↑ [21,22]
	Γ_G	[16]	↓ [16]	↑ [23]	↑ [19]	↑ [22,24]
D	ω_D			↑ [17,18]	↓ [17,18]	
	Γ_D					↑ [24,25]
D/ G	A_D/A_G	[15]	↓ [15]			↑ then ↓ [21,22]
2D	ω_{2D}	[16]	↑ then ↓ [16]	↑↑ [17,18]	↓↓ [17–20]	↑ [26,27]
	Γ_{2D}			↑ [23]	↑ [19,28]	↑ [26,27]
2D/ G	I_{2D}/I_G	[16]	↓ [16]			↓ [24,25] ↓ [26,27]
D/ 2D	I_D/I_2	[15]	= [15]			↑↑ [24,25]
	A_D/A_{2D}	[15]	= [15]			↑↑ [29]

*A different behavior has been observed for grain boundaries, *i.e.* nanocrystalline CVD-grown graphene as compared with exfoliated graphene [23].

Table 1. Summary of the effects arising from the increase of different graphene lattice defects on the parameters of D, G and 2D bands. Data are taken from exfoliated and/or CVD-grown polycrystalline graphene films.

S-IV. DISTINGUISHING GRAIN BOUNDARIES FROM GRAPHENE DOMAINS

To efficiently process the sheer number of spectra obtained via the RIMA system, an improved method based on Principal Component Analysis (PCA) filtering has been carried out [6]. It allows for the subtraction of intrinsic RIMA baseline (polynomial fit) and artefacts for the 3×105 spectra. This number of spectra is roughly 3-order of magnitude improvement from previous data obtained by conventional confocal Raman microscopy [1].

As a mean to study the local dynamics of the defect generation, a method aimed at thoroughly distinguishing the local spectra obtained at GBs from those at graphene domains was developed. Figs. 2-4 of the main manuscript and Fig S4 the supplementary data show that GBs are easily distinguishable depending on the selected Raman band parameters. By scanning the mappings of chosen Raman band parameters and isolating pixels presenting local non-uniformity, the so-called GB-pixels for all 12 plasma treatment times were extracted. Note that the number of GB-pixels necessarily vary depending on the chosen Raman band parameter but at least 1000 pixels attributed to GBs were selected within the central $92 \times 92 \mu\text{m}^2$ area from the previous figures. The error bars shown are statistical values defined by the interval of two standard deviations (i.e. 68.2% of the distribution of all the extracted values).

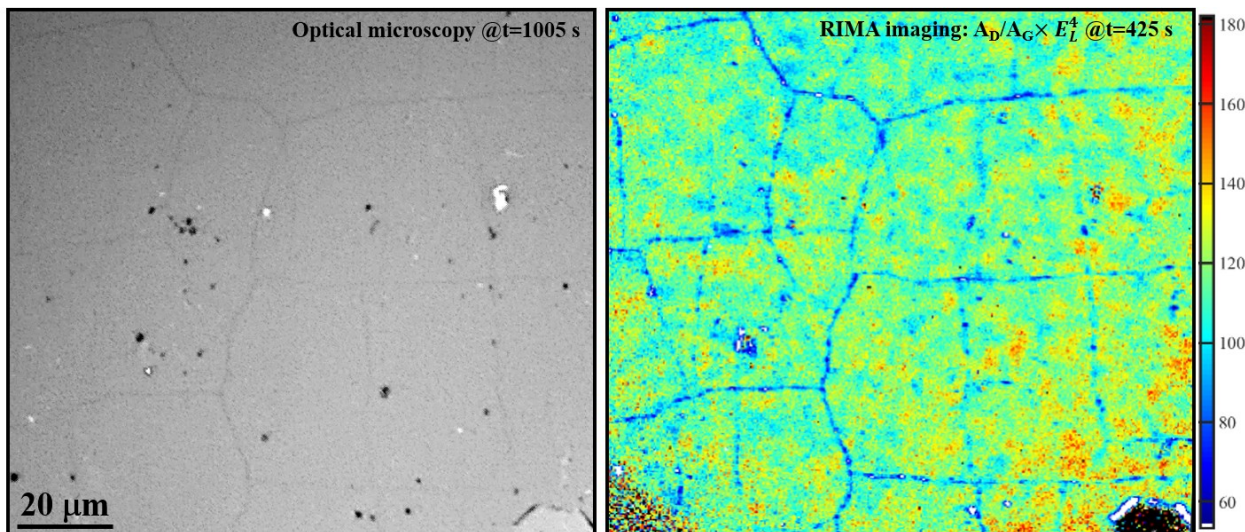


Figure S4. Comparison between optical microscopy (left, after 1005 s of plasma treatment) and D/G area ratio extracted from RIMA imaging (right, 425 s).

Optical microscopy was further performed using an OMAX microscope at a $\times 600$ magnification. As can be seen in Figure S4 of the supplementary data, the linear discrepancies observed in the Raman mappings perfectly match the grain boundaries (GBs) discernable on the optical micrograph. The sharpen process in imageJ [30] was applied in the picture to highlight GBs.

S-V. GEOMETRIC CONSIDERATIONS ON GRAPHENE RAMAN SIGNATURE

In this section, the expected Raman signature of GBs during 0D defect generation is examined. The model proposed by *Cançado et al.*[31] explicitly takes into account the case of a point defect falling into a 1D line. Indeed, in appendix C of the corresponding article, the determination of $(A_D/A_G) \times E_L^4$ is proposed to be the sum of three contributions (C.1) :

$$\left(\frac{A_D}{A_G}\right) E_L^4 = \left(\frac{A_D}{A_G}\right)_{0D}^{(S)} + \left(\frac{A_D}{A_G}\right)_{1D}^{(S)} + \left(\frac{A_D}{A_G}\right)_{0D,1D}^{(A)} \quad (\text{C.1})$$

where $(A_D/A_G)_{0D}^{(S)}$ is the contribution term from structural deformation of 0D defects, $(A_D/A_G)_{1D}^{(S)}$ is the term from structural deformation of 1D defects, and $(A_D/A_G)_{0D,1D}^{(A)}$ is the term from the activated region around both 0D and 1D defects.

In this framework, *Cançado et al.* indicate that the loss of surface area of defective 1D defects (A_B) over the total surface (A_T) is detailed by the rate equation (C.6):

$$\frac{dA_B}{dN} = -\pi r_s^2 \frac{A_B}{A_T} \quad (\text{C.6})$$

where N is the number of 0D defects and r_s is the radius of the structurally damaged area. *Cançado et al.* carry out this geometrical consideration over the calculation of the total contribution of the defective area of the 1D defects. In the end, contribution by 1D line defects is estimated as the following (see equation C.9):

$$\left(\frac{A_D}{A_G}\right)_{1D}^{(S)} = C_S^{1D} \frac{4l_S(L_a-l_S)}{L_a^2} e^{-\pi r_s^2 \sigma} \quad (\text{C.9})$$

where C_S^{1D} is the Raman response from 1D defects, l_S is the width of the 1D line, L_a is the crystallite size and σ is the surface density of 0D defects. The term $e^{-\pi r_s^2 \sigma}$ arises from the integration of equation C.6. This term decreases the contribution of the 1D-type defects in the total Raman response as the surface density of point defects increases.

It is worth noting that the way these mechanisms are considered, the structurally damage area of 0D defects has precedence over the defective 1D area. Since the Raman response of

$(A_D/A_G) \times E_L^4$ is higher for 0D defects (51 eV^4 versus 30.3 eV^4 – table 1 of the same article, values fitted from experimental data), 0D defects consequently lead to a higher value of $(A_D/A_G) \times E_L^4$.

Cançado et al. used the same considerations for the term of the activated area (third term of C.1.). Indeed, the equation C.14 in ref.[31] depends on the covering of structurally damaged 1D defects ($f_{S,1D}$).

Therefore, the creation of point defects (0D) in the vicinity of grain boundaries (1D) would quickly favor a typical 0D-type signature. Thus, when 0D defects are created in a location where there is already a 1D defect (the grain boundary), spectral change towards a 0D-type defect signature will be observed in the Raman response of RIMA.

Regarding the possibility of a point defect arising within –or *on top*– of a GB, it is taken into account by the model and should increase the contributions of 0D defects –greatly increasing A_D/A_G – and should decrease the ones of 1D defects –which are responsible for a significantly milder increase of A_D/A_G . Therefore, the 0D defects do *overwrite* 1D defects and thus cause an increase of the A_D/A_G ratio.

S-VI. HINTS ON THE NATURE OF THE GRAIN BOUNDARIES

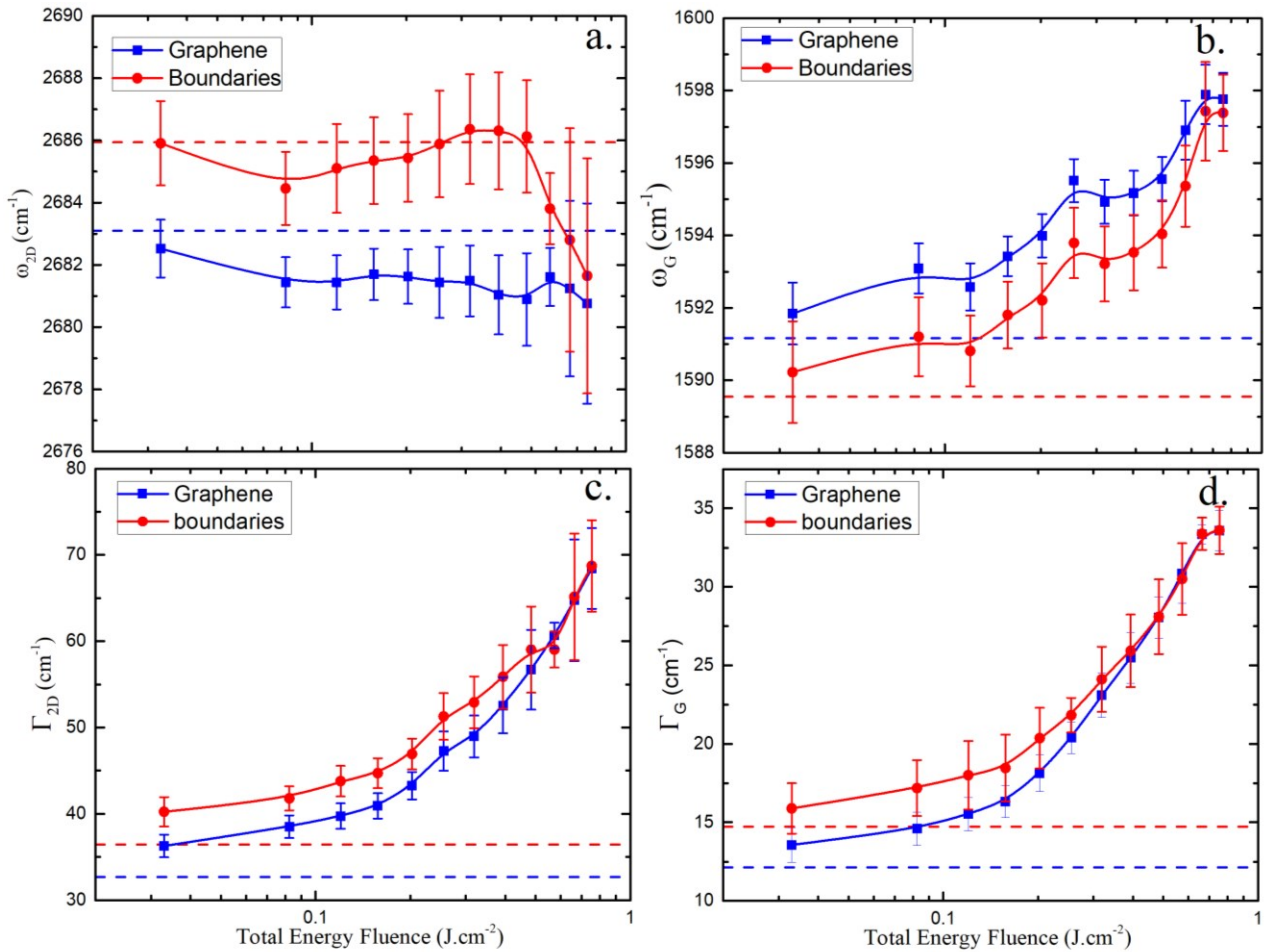


Figure S5. Evolution of (a) ω_{2D} , (b) ω_G , (c) Γ_{2D} and (d) Γ_G highlighting the discrepancies between GBs and graphene grains. All parameters are plotted versus the total energy fluence accumulated during the subsequent plasma treatments ($60\text{ s} \leftrightarrow 0.03\text{ J}\cdot\text{cm}^{-2}$, $1005\text{ s} \leftrightarrow 0.75\text{ J}\cdot\text{cm}^{-2}$). Values for pristine graphene are displayed as horizontal dashed lines.

Figure S5 presents the evolution of the 2D and G bands positions. Regarding graphene in its pristine state, ω_{2D} value at GBs is at least 3 cm⁻¹ greater than at the grains. Knowing that this parameter is strongly linked with compressive ($\epsilon < 0$) or tensile ($\epsilon > 0$) strains in graphene (see Table S1) [17,19,32], it shows therefore that GBs are subject to a compressive strain. Indeed, CVD-grown graphene on copper exhibits a compressive strain after cooling due to a difference in thermal expansion between graphene and Cu [33]. Such effect may even be enhanced after transfer to SiO₂ [34] and expected to be contained within the GBs [35]. The pristine value of Γ_G is

smaller within GBs (1589 cm^{-1}) than within GR (1591 cm^{-1}) which is expected for CVD-graphene GBs under compressive strain or Stone-Wales defects [23,36]. Moreover, overlapping layers or wrinkles (found at the domain boundaries) are also known to induce a blueshift of the 2D band [26,37,38]. Such results are the definitive proof that the method carried out here is capable of disentangling signals at graphene domains from that at their boundaries. Note that local doping could also explain a shift in the G and 2D peaks position, but n- and p-doping would only lead to an increase of Γ_G . Significant differences between GBs and GR can also be seen for Γ_{2D} and Γ_G . For example, $\Gamma_{2D,GB}$ is about 4cm^{-1} wider than $\Gamma_{2D,GR}$. This results from the difference in morphology at the boundary of two graphene domains: overlapping layers, wrinkles or defective boundaries such as 5-7 ring chains [26,36,37] (see also discussion related to Figure S5).

When comparing the evolution of both ω_G and ω_{2D} , graphene domains and their boundaries present similar behaviors, which are constant $\Delta\omega_G$ and $\Delta\omega_{2D}$ –i.e. a constant strain difference—up until $t = 765\text{ s}$ ($0.57\text{ J}\cdot\text{cm}^{-2}$). This sudden gap reduction in the data might coincide with strain relaxation in GBs, possibly due to the high defect density evidenced by the monotonous increase of ω_G within the whole probed area [21,22]. Note that the position of the 2D band is seen to slightly increase within the GBs between 160 and 525 s (0.12 to $0.39\text{ J}\cdot\text{cm}^{-2}$) of cumulative plasma treatments which could be associated with an increase of compressive strain due to adatoms incorporation, such as in inverse Stone-Wales defects [39].

A supplementary proof of GBs nature as defective 1D lines stitched grains can be found by a careful look at the results in Figure S5a. Indeed, a high 2D/G intensity ratio is typically obtained with high-quality monolayer graphene whereas increasing disorder [24] and number of layers (ABAB-stacking) reduces this ratio [40]. Furthermore, due to the irregular graphene growth by CVD process on polycrystalline copper substrates [41], each grain is formed with a specific orientation, which may lead to overlapping layers at GBs. However, this angular shift within the basal plane leads to higher I_{2D}/I_G values [37,40]. Hence, the smaller value of I_{2D}/I_G at GBs (**Fig. S5b**) rules out bilayer stacking as one of the main morphological differences. A lower I_{2D}/I_G value at GBs is therefore characteristic of structural defects, such as wrinkles and defective boundaries [42].

S-VII. DAMAGE FORMATION BY VERY LOW-ENERGY ARGON IONS

The different contributions from the energetic plasma species have been detailed previously in section S-II. Metastable species only represent 16% of the total energy fluence provided to the graphene sample compared to ions and VUV photons (43 and 41%, respectively). Among those, the Ar⁺ species (11-13 eV at plasma on and 1 eV during the post-discharge of the pulsed argon plasma) impinge the surface at normal incidence due to the potential drop in the sheath surrounding the graphene sample and, thus, transfer a significant part of the energy. Regarding VUV photons, the graphene photo-absorption at 11.7 eV is expected to be very weak [43]. Additionally, the results presented in **Fig. 5b** confirm that the 11-13-eV ions are the main energy input responsible for the damage generation since the defects observed by Raman are mainly 0D [22].

Considering the 11-13eV argon ion flux, each incident ion transfers a maximum of 8-10 eV to the graphene lattice during the plasma-on time. Theoretical first-principles estimates of Td, the minimum energy that needs to be transferred to a carbon atom to leave its lattice position without immediate recombination with the vacancy, is 18-22 eV,[44] whereas electron-beam experiments reveals 18-20 eV.[45,46] Over the range of experimental conditions investigated, despite clear evidences of 0D defect formation by Raman spectroscopy, the energy of argon ions seems too small to produce any significant damage by ballistic ejection of carbon atoms. However, during ion irradiation of graphene, in addition to knock-on collisions, additional energy transfer processes linked to surface recombination of positive ions also needs to be considered. For instance, a significant rise of the D:G ratio was observed in graphene exposed to a beam of very-low-energy argon ions (1-2 eV range, both single (15.8 eV) and double ionization (43.4 eV)).[47] This aspect is even more complex in far-from equilibrium plasma environments due to the simultaneous impingement of a collection of energetic particles characterized by various energy transfer time scales. This so-called plasma synergetic effect[48,49] includes, for example, the surface recombination of argon ions as in ion beam experiments but also the surface deexcitation of metastable argon atoms.[50] While recombination and deexcitation surface

processes leading to electron excitation in the graphene lattice are extremely fast (\sim fs),[51,52] electron energy relaxation phenomena (for example, through electron-phonon coupling) are much slower (\sim ps).[53,54]

In this context, Molecular Dynamics simulations were realized to examine the damage formation dynamics by very-low-energy argon ions. In order to simulate additional energy uptakes by plasma species (for example, the surface recombination of argon ions and the deexcitation of argon metastable species that represents an instantaneous energy release of 15.8 and 11.5 eV, respectively), simulations were performed at various surface temperatures in the 300-3000K range. It is worth highlighting that this is not an “actual temperature” of the graphene substrate but rather represents a “transitionary state of graphene” as a result of additional energy uptake and subsequent energy dissipation phenomena. Since the knock-on collision occurs at the fs time scale and energy relaxation at the ps time scale,[51–54] a fixed “graphene temperature” seems reasonable at the time scale of MD simulations.

More precisely, simulations were carried out with the open-source code LAMMPS. A three-body ZBL/Tersoff potential was used for the pristine graphene lattice [55–58] whereas a Lennard-Jones potential [56,58] was used to describe the argon-carbon interaction. As in comparable MD studies reported in literature, the system consisted of suspended graphene with 8530 carbon atoms ($22 \times 22 \text{ nm}^2$). Graphene was first minimised and then heated up to 300 K during 10ps in a N-P-T (constant Number-Pressure-Temperature) environment. Since energy transfers due to surface recombination of argon ions cannot be considered in LAMMPS (the system only considers argon-carbon collisions), the system was manually heated up to a given temperature. Hence, for each simulation, graphene obtained at 300 K was progressively heated for 50ps in a N-P-T environment to attain the desired temperature. The graphene was subsequently relaxed for another 50 ps at this temperature. Each simulation consisted of a random introduction of one argon atom (with a fixed kinetic energy, E_{ion}) close to the center of the simulation domain in order to avoid any edge effects. Every simulation lasted for 1ps and were produced in an N-V-E (constant Number-Volume and Energy) environment. To obtain statistics in a reasonable time, 200 collisions were simulated for each set of conditions. From each simulation image, the damage probability was assessed as follows. The difference in the z direction of each carbon atom with respect to its closest neighbors

was compared with the mean position of all carbon atoms in the graphene lattice. If the difference for the suspected carbon adatom generated by the knock-on collision is higher than the mean value plus six times the standard deviation, it is confirmed as a carbon adatom. Therefore, in such simulations, the probability for damage formation is linked to the formation of carbon adatoms/vacancy pairs (Frenkel pairs), and not to simple bond rotations (Stones Wales defects).

Figure S6 presents the probability for defect formation on graphene as a function of “graphene temperature” for various values of the energy transferred to the graphene lattice through argon-carbon collisions $T = 4 m_C m_{Ar} E_{ion} / (m_C + m_{Ar})^2$, where m_C and m_A are the masses of carbon and argon atoms, respectively. While more or less temperature-independent behavior is observed at 22.5 eV (i.e. above $T_d=18-22$ eV[39,44–46]), a significant rise with temperature is observed for 17.8 and 15.5 eV (i.e. below $T_d=18-22$ eV[39,44–46]). In the latter conditions, damage formation can therefore appear at energies below T_d , in very good agreement with the study of Ahlberg *et al.*[47] as well as our experimental data obtained in both pulsed and continuous plasma conditions.

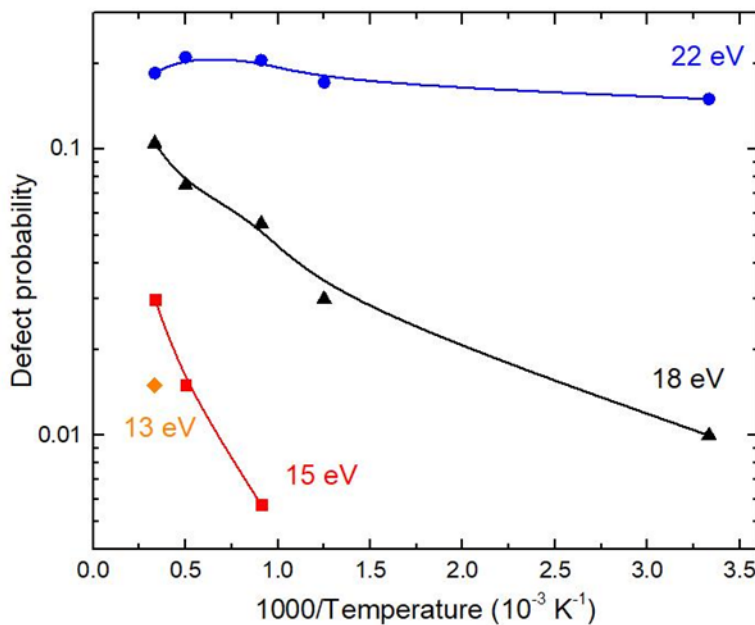


Figure S6. Defect probability obtained from MD simulations as a function of “graphene temperature” for various of the energy transferred to the graphene lattice through argon-carbon collisions.

Figure S6 further reveals that damage formation at energies below T_d is thermally-activated (Arrhenius plot), with an activation energy that decreases with increasing value of T (linked to the energy of argon atoms). A similar behavior was observed for temperature-dependent radiation-enhanced diffusion in ion-irradiated solids.[59]

It is worth highlighting that the probability for defect formation for $T < T_d$ and reasonable “graphene temperatures” (below 1000K)[51–54] remains very small (~1%). Such low probability is important to prevent graphene amorphization. Considering a fluence of positive ions of 9×10^{15} part.cm⁻² for 60s and 1.5×10^{17} part.cm⁻² for 1005s, this corresponds to a defect concentration of 9×10^{13} part.cm⁻² for 60s and 1.5×10^{15} part.cm⁻² for 1005s. While the former is much lower than the surface atomic density of carbon atoms in the graphene lattice ($\sim 3.8 \times 10^{15}$ part.cm⁻²), the latter becomes much closer, in very good agreement with the expected transition from stage 1 (from undisturbed graphene to nanocrystalline graphene) to stage 2 (progression towards amorphous carbon) with increasing plasma treatment time.[60,61]

The results presented in Figure X are also in very good agreement with a study of electron-graphene collisions by Kotakosky and co-workers recently published in Scientific Reports[62]. The authors have shown that the minimum energy that needs to be transferred to a carbon atom to leave its lattice position without immediate recombination with the vacancy is not an absolute value but rather present an energy distribution function [62]. In addition, this broadening rises with increasing graphene temperature due to the corresponding increase in the vibration dynamics of carbon atoms in the graphene lattice.

S-VIII. PREFERENTIAL MIGRATION OF CARBON ADATOMS

The formation and migration energies of various defects are of critical importance in radiation-damage studies of graphene. An extensive review of those values is presented by *Banhart et al* [39]. It is commonly accepted that the threshold energy for carbon adatoms ejection from created defects is $T_d = 18\text{--}20$ eV [39]. Even though argon ions can only transfer 8 eV to carbon atoms by knock-on collisions, these positively charged species can also neutralise on the surface, transmitting a potential energy of 15.8 eV to the graphene lattice. Furthermore, argon metastable and VUV photon can deliver around 11.5 eV to the surface. All those potential energies lead to a

reduction of the threshold energy for defect formation, referenced as the plasma synergetic effect inherent to plasma processing.

Considering argon ions as initiator for defect formation in low-pressure argon plasmas, the creation of Stone-Wales defects ($E_F(SW) = 6.4\text{--}7.9$ eV)[63–65] appears the most probable, involving only bond rotation and no ballistic ejection of carbon atoms. A subsequent argon ion impinging the same location can produce a carbon adatom due to the already fragile structure. On the other hand, considering the plasma synergetic effect lowering the various energy thresholds, it is possible to consider Frenkel pair formation ($E_F(FP) = 14$ eV) as a possible outcome (see S-VII). This adatom-vacancy pair is stable unless some energy is provided.

While single vacancy requires ~ 1.3 eV for migration on graphene surfaces, a carbons adatom only needs 0.4 eV to diffuse [39]. As for a Stones-Wales defect, it demands 10 eV to move [41], which makes such defect essentially immobile with respect to other species. Hence, carbon adatoms and single vacancies are the species with the highest probability to diffuse on the graphene surface. The energy necessary for such migration is provided locally in both time and space by the non-equilibrium plasma through ions, metastable and VUV photons. In this framework, jump frequencies can be estimated through an Arrhenius equation $f = A \exp(-E_a/(k_B T))$, [66] where A is a pre-factor depending of the studied species, E_a is the activation energy, and $k_B T$ is the thermal energy. In the case of carbon adatoms, the pre-factor for surface diffusion on graphene can be estimated at 3.7×10^{12} s $^{-1}$ [67]. Since the pre-factor for the displacement of single vacancies is of the same order of magnitude (1.2×10^{12} s $^{-1}$)[66], the jump frequency of carbon adatoms and single vacancies become mostly linked to the corresponding values of E_a . Since carbon adatoms on graphene have a much lower activation energy (0.4 eV) compared to single vacancies (1.5 eV), it results in a higher mobility for carbon adatoms than single vacancies. For example, at room temperature ($T = 300$ K), the jump frequency for carbon adatoms and vacancies can be estimated as 7.6×10^5 s $^{-1}$ and 7.9×10^{-14} s $^{-1}$, respectively.

SUPPLEMENTARY REFERENCES

- [1] P. Vinchon, X. Glad, G. Robert-Bigras, R. Martel, A. Sarkissian, L. Stafford, J. Appl. Phys. 126 (2019) 233302.
- [2] L. Maaloul, S. Morel, L. Stafford, J. Vac. Sci. Technol. A Vacuum, Surfaces Film. 30 (2012).

- [3] S. Choubak, P.L. Levesque, E. Gaufres, M. Biron, P. Desjardins, R. Martel, *J. Phys. Chem. C* 118 (2014) 21532–21540.
- [4] Y.-C. Lin, C.-C. Lu, C.-H. Yeh, C. Jin, K. Suenaga, P.-W. Chiu, (2011).
- [5] E. Gaufrès, S. Marcket, V. Aymong, N.Y.W. Tang, A. Favron, F. Thouin, C. Allard, D. Rioux, N. Cottenye, M. Verhaegen, R. Martel, *J. Raman Spectrosc.* 49 (2018) 174–182.
- [6] P. Vinchon, G. Robert Bigras, X. Glad, C. Allard, R. Martel, L. Stafford, Submitt. to *Rev. Sci. Instruments* (2019).
- [7] E.H. Martins Ferreira, M.V.O. Moutinho, F. Stavale, M.M. Lucchese, R.B. Capaz, C. a. Achete, A. Jorio, *Phys. Rev. B - Condens. Matter Mater. Phys.* 82 (2010).
- [8] M.A. Lieberman, A.J. Lichtenberg, *Principles of Plasma Discharges and Materials Processing: Second Edition*, 2005.
- [9] D. Barton, D.J. Heason, R.D. Short, J.W. Bradley, *Meas. Sci. Technol.* 11 (2000) 1726.
- [10] X. Tang, D.M. Manos, *Plasma Sources Sci. Technol.* 8 (1999) 594–602.
- [11] V. Sushkov, H.T. Do, M. Cada, Z. Hubicka, R. Hippler, *Plasma Sources Sci. Technol.* 22 (2013) 015002.
- [12] Y. Celik, T. V. Tsankov, M. Aramaki, S. Yoshimura, D. Luggenhölscher, U. Czarnetzki, *Phys. Rev. E - Stat. Nonlinear, Soft Matter Phys.* 85 (2012) 1–12.
- [13] Y. Golubovskii, S. Gorchakov, D. Uhrlandt, *Plasma Sources Sci. Technol.* 22 (2013).
- [14] W. Zhang, L. Li, Z.B. Wang, A.A. Pena, D.J. Whitehead, M.L. Zhong, Z. Lin, H.W. Zhu, *Appl. Phys. A Mater. Sci. Process.* 109 (2012) 291–297.
- [15] M. Bruna, A.K. Ott, M. Ijäs, D. Yoon, U. Sassi, A.C. Ferrari, *ACS Nano* 8 (2014) 7432–7441.
- [16] A. Das, S. Pisana, B. Chakraborty, S. Piscanec, S.K. Saha, U. V Waghmare, K.S. Novoselov, H.R. Krishnamurthy, a K. Geim, A.C. Ferrari, A.K. Sood, *Nat. Nanotechnol.* 3 (2008) 210–215.
- [17] J. Zabel, R.R. Nair, A. Ott, T. Georgiou, A.K. Geim, K.S. Novoselov, C. Casiraghi, *Nano Lett.* 12 (2012) 617–621.
- [18] J.E. Lee, G. Ahn, J. Shim, Y.S. Lee, S. Ryu, *Nat. Commun.* 3 (2012) 1024.
- [19] Y. Wang, Y. Wang, C. Xu, X. Zhang, L. Mei, M. Wang, Y. Xia, P. Zhao, H. Wang, *Carbon N. Y.* 134 (2018) 37–42.
- [20] Z.H. Ni, T. Yu, Y.H. Lu, Y.Y. Wang, Y.P. Feng, Z.X. Shen, *ACS Nano* 2 (2008) 2301–2305.
- [21] A.C. Ferrari, J. Robertson, *Phys. Rev. B* 61 (2000) 14095–14107.
- [22] L. Gustavo Cançado, M. Gomes da Silva, E.H. Martins Ferreira, F. Hof, K. Kampioti, K. Huang, A. Pénicaud, C. Alberto Achete, R.B. Capaz, A. Jorio, *2D Mater.* 4 (2017) 025039.
- [23] M.A. Bissell, W. Izumida, R. Saito, H. Ago, *ACS Nano* 6 (2012) 10229–10238.
- [24] Y.-B.B. Zhou, Z.-M.M. Liao, Y.-F.F. Wang, G.S. Duesberg, J. Xu, Q. Fu, X.-S.S. Wu, D.-P.P. Yu, *J. Chem. Phys.* 133 (2010) 234703.
- [25] K. Jia, Y. Su, Y. Chen, J. Luo, J. Yang, P. Lv, Z. Zhang, H. Zhu, C. Zhao, T. Ye, *Vacuum* 116 (2015) 90–95.
- [26] A.C. Ferrari, J.C. Meyer, V. Scardaci, C. Casiraghi, M. Lazzeri, F. Mauri, S. Piscanec, D. Jiang, K.S. Novoselov, S. Roth, A.K. Geim, *Phys. Rev. Lett.* 97 (2006) 187401.
- [27] L.M. Malard, M. a. Pimenta, G. Dresselhaus, M.S. Dresselhaus, *Phys. Rep.* 473 (2009) 51–87.
- [28] O. Frank, M. Mohr, J. Maultzsch, C. Thomsen, I. Riaz, R. Jalil, K.S. Novoselov, G. Tsoukleri, J. Parthenios, K. Papagelis, L. Kavan, C. Galiotis, *ACS Nano* 5 (2011) 2231–2239.
- [29] P. Venezuela, M. Lazzeri, F. Mauri, *Phys. Rev. B - Condens. Matter Mater. Phys.* 84 (2011) 1–25.

- [30] W. Rasband, Natl. Institutes Heal. (2019).
- [31] L.G. Cançado, M. Gomes de Silva, E.H.M. Ferreira, F. Hof, 2D Mater. 4 (2017) 025039.
- [32] J.U. Lee, D. Yoon, H. Cheong, Nano Lett. 12 (2012) 4444–4448.
- [33] Y. Zhang, T. Gao, Y. Gao, S. Xie, Q. Ji, K. Yan, H. Peng, Z. Liu, ACS Nano 5 (2011) 4014–4022.
- [34] M.B.B.S. Larsen, D.M.A. Mackenzie, J.M. Caridad, P. Bøggild, T.J. Booth, Microelectron. Eng. 121 (2014) 113–117.
- [35] B. Wang, Y. Puzyrev, S.T. Pantelides, Carbon N. Y. 49 (2011) 3983–3988.
- [36] S.N. Shirodkar, U. V. Waghmare, Phys. Rev. B - Condens. Matter Mater. Phys. 86 (2012) 1–10.
- [37] K.D. Park, M.B. Raschke, J.M. Atkin, Y.H. Lee, M.S. Jeong, Adv. Mater. 29 (2017) 1–6.
- [38] K. Kim, S. Coh, L.Z. Tan, W. Regan, J.M. Yuk, E. Chatterjee, M.F. Crommie, M.L. Cohen, S.G. Louie, A. Zettl, Phys. Rev. Lett. 108 (2012) 246103.
- [39] F. Banhart, J. Kotakoski, A. V. Krasheninnikov, ACS Nano 5 (2011) 26–41.
- [40] Z. Ni, Y. Wang, T. Yu, Z. Shen, Nano Res. 1 (2008) 273–291.
- [41] S. Nie, J.M. Wofford, N.C. Bartelt, O.D. Dubon, K.F. McCarty, Phys. Rev. B - Condens. Matter Mater. Phys. 84 (2011) 1–7.
- [42] Y. Ogawa, K. Komatsu, K. Kawahara, M. Tsuji, K. Tsukagoshi, H. Ago, Nanoscale 6 (2014) 7288–7294.
- [43] P.E. Trevisanutto, M. Holzmann, M. Côté, V. Olevano, Phys. Rev. B - Condens. Matter Mater. Phys. 81 (2010) 3–6.
- [44] O. V. Yazyev, I. Tavernelli, U. Rothlisberger, L. Helm, Phys. Rev. B 75 (2007) 115418.
- [45] F. Banhart, Reports Prog. Phys. 62 (1999) 1181.
- [46] B.W. Smith, D.E. Luzzi, J. Appl. Phys. 90 (2001) 3509–3515.
- [47] P. Ahlberg, F.O.L. Johansson, Z.B. Zhang, U. Jansson, S.L. Zhang, A. Lindblad, T. Nyberg, APL Mater. 4 (2016).
- [48] B. Rousseau, H. Estrade-Szwarckopf, A.-L. Thomann, P. Brault, Appl. Phys. A Mater. Sci. Process. 77 (2003) 591.
- [49] J.P. Allain, A. Shetty, J. Phys. D. Appl. Phys. 50 (2017) 283002.
- [50] A. Bard, J. Vac. Sci. Technol. B Microelectron. Nanom. Struct. 15 (1997) 1805.
- [51] A. Tomadin, D. Brida, G. Cerullo, A.C. Ferrari, M. Polini, Phys. Rev. B 88 (2013) 035430.
- [52] C. Su, M. Tripathi, Q.-B. Yan, Z. Wang, Z. Zhang, C. Hofer, H. Wang, L. Basile, G. Su, M. Dong, J.C. Meyer, J. Kotakoski, J. Kong, J.-C. Idrobo, T. Susi, J. Li, Sci. Adv. 5 (2019) eaav2252.
- [53] M. Lazzeri, S. Piscanec, F. Mauri, A.C. Ferrari, J. Robertson, Phys. Rev. Lett. 95 (2005) 236802.
- [54] S. Butscher, F. Milde, M. Hirtschulz, E. Malić, A. Knorr, Appl. Phys. Lett. 91 (2007) 203103.
- [55] E.P. Bellido, J.M. Seminario, J. Phys. Chem. C 116 (2012) 4044–4049.
- [56] X.L. Wei, K.W. Zhang, R.Z. Wang, W.L. Liu, J.X. Zhong, J. Nanosci. Nanotechnol. 11 (2011) 10863–10867.
- [57] X. Wu, H. Zhao, H. Murakawa, J. Nanosci. Nanotechnol. 14 (2014) 5697–5702.
- [58] W. Li, L. Liang, S. Zhao, S. Zhang, J. Xue, J. Appl. Phys. 114 (2013).
- [59] D. Marton, J. Fine, G.P. Chambers, Phys. Rev. Lett. 61 (1988) 2697–2700.
- [60] A.C. Ferrari, J. Robertson, Philosophical Trans. Math. Phys. Eng. Sci. 363 (2004) 2477–2512.
- [61] A. Eckmann, A. Felten, A. Mishchenko, L. Britnell, R. Krupke, K.S. Novoselov, C. Casiraghi, Nano Lett. 12 (2012) 3925–3930.
- [62] A.I. Chirita Mihaila, T. Susi, J. Kotakoski, Sci. Rep. 9 (2019) 1–7.

- [63] L. Li, S. Reich, J. Robertson, Phys. Rev. B - Condens. Matter Mater. Phys. 72 (2005) 1–10.
- [64] J. Ma, D. Alfè, A. Michaelides, E. Wang, Phys. Rev. B - Condens. Matter Mater. Phys. 80 (2009) 1–4.
- [65] J. Kotakoski, A. V. Krasheninnikov, U. Kaiser, J.C. Meyer, Phys. Rev. Lett. 106 (2011) 105505.
- [66] J.D. Wadey, A. Markevich, A. Robertson, J. Warner, A. Kirkland, E. Besley, Chem. Phys. Lett. 648 (2016) 161–165.
- [67] A. V. Krasheninnikov, K. Nordlund, P.O. Lehtinen, A.S. Foster, A. Ayuela, R.M. Nieminen, Carbon N. Y. 42 (2004) 1021–1025.

Annexe 4 : Données supplémentaires pour l'article RSI_2020

Probing plasma-treated graphene using hyperspectral Raman

G. Robert Bigras ^{*1}, P. Vinchon ^{*1}, C. Allard ², X. Glad ¹, R. Martel ², L. Stafford ^{1**}

^{*} Equally credited authors ^{**} Corresponding author: luc.stafford@umontreal.ca

¹ Département de Physique, Université de Montréal, 1375 Avenue Thérèse-Lavoie-Roux,
Montréal, Québec, H2V 0B3, CANADA

² Département de Chimie, Université de Montréal, 5155 Chemin de la Rampe, Montréal, Québec,
H3T 1J4, CANADA

S-I. Plasma treatment conditions

Graphene was exposed to a planar-type Inductively Coupled Plasma (ICP) operated in nominally pure argon. The setup is described in detail elsewhere [1]. The residual pressure (1.5×10^{-7} Torr) was obtained with an association of rotary and turbomolecular pumps. The argon mass flow was fixed at 20 sccm and the operation pressure was maintained at 5 mTorr with an injected power of 500 W. A matchbox kept the reflected power at 0 W during the whole plasma treatment. Plasma characteristics were assessed by a combination of Langmuir probe and Plasma Sampling Mass spectroscopy such that a good control of the Ions Energy Distribution Function (IEDF) following the acceleration of positive ions in the plasma sheath was obtained. In the experimental conditions investigated, the IEDF was quite narrow (~ 1.2 eV) and centered at 15 eV. Furthermore, an ion fluence of 2.7×10^{17} part.cm⁻² was achieved using an ion density of $n_i = 1.1 \times 10^{11}$ cm⁻³, an ion Bohm velocity $v_b = 2.7 \times 10^5$ cm.s⁻¹ and a plasma exposure time of 15 s. Furthermore, Optical Absorption Spectroscopy (OAS) was used to probe metastable and resonant argon species in the plasma. Again, in the experimental conditions investigated, graphene-plasma interaction is dominated by very-low-energy ion irradiation [1].

S-II. PCA-Assisted Data Noise Filtering

Before the decomposition into principal component analysis, the mean spectrum is subtracted to all the spectra. Here are presented the mean spectra for the various measurements.

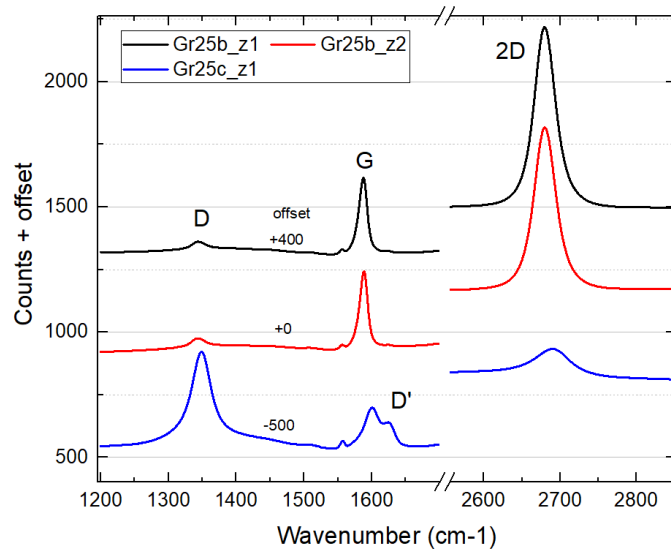


Figure S1. Mean spectra for the two regions before and after the plasma treatment process. The cubes of untreated graphene (black and red) and the cube for the treated graphene (blue) are presented.

A graphical confirmation of the number of components to consider is shown at Figure S2. Typically, the number of components retained should be higher than the change in curvature of the cumulative eigenvalues of the components. [2]

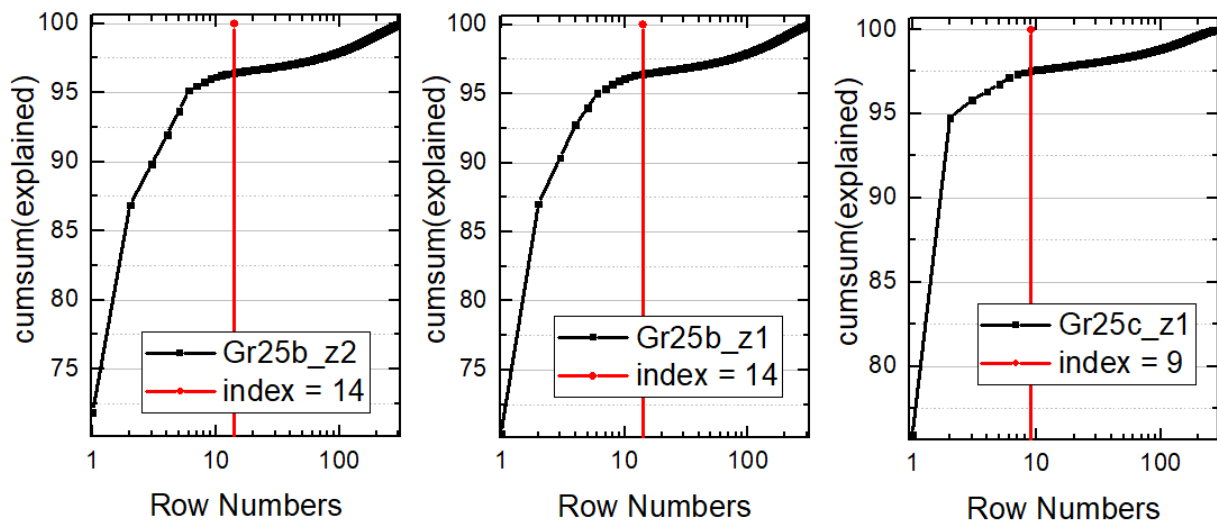


Figure S2. For each samples states is presented the cumulative eigenvalues of sorted principal components as a function of component index. The red line reveals the number of components retained for reconstruction as calculated from the criteria presented in the manuscript.

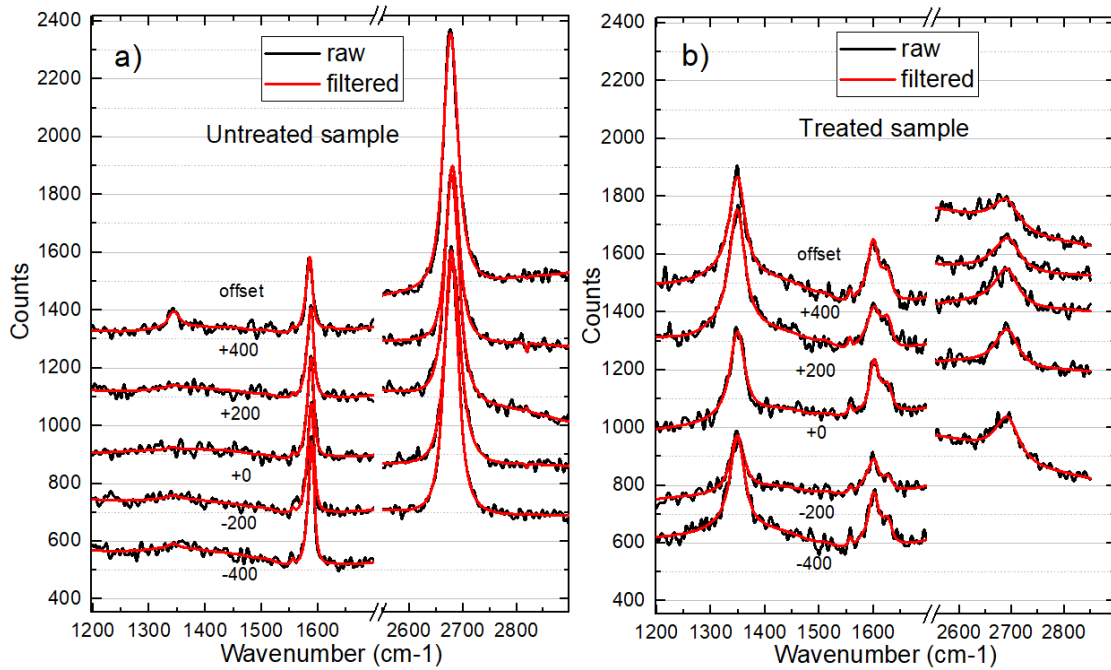


Figure S3. Small sample of spectra for both the untreated (a) and the treated (b) state of the graphene. Raw data (black) and filtered data (red) are shown.

S-III. Polynomial Baseline Subtraction

A key challenge for RIMA analysis is the subtraction of the artefact. Overfitting of the G/D' regions could induce large changes in the intensity, position, and width of the D' and G bands. To show the potential of the RIMA method without having to detail exhaustive processes, a commonly used method of baseline subtraction is chosen: polynomial fitting.

First, the fit is performed for increasing order of the polynomial baseline. Lower orders are automatically discarded when the fit becomes inadequate.

The shape of the artefact present at each band position varies drastically. Around the D band, a curve with a maximum around 1400 cm⁻¹ is present, while the baseline around the G and D' bands contains a minimum around 1600 cm⁻¹. The artefact at the 2D band reveals amuch less curvature. The expected order of the later is thus smaller.

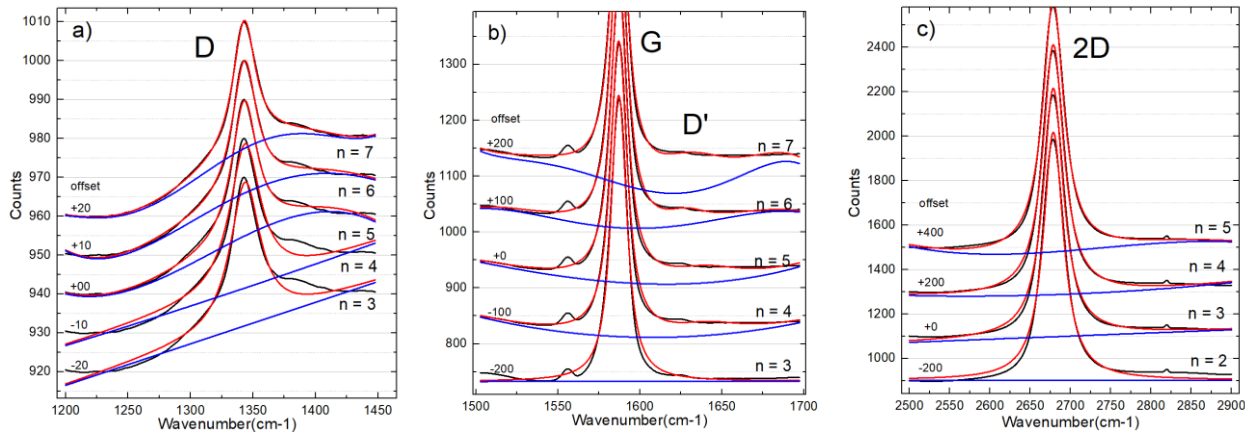


Figure S4. Example of various curve fit with different order of polynomial baseline for a point of the untreated graphene sample. Regions of the (a) D, (b) G and (c) 2D bands are shown.

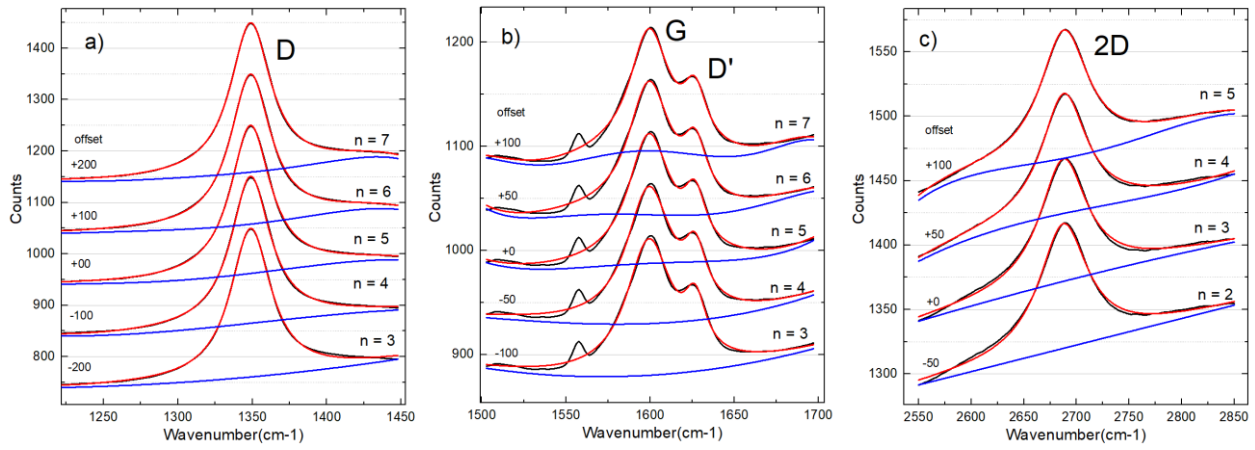


Figure S5. Example of various curve fit with different order of polynomial baseline for a point of the plasma-treated graphene sample. Regions of the (a) D, (b) G and (c) 2D bands are shown.

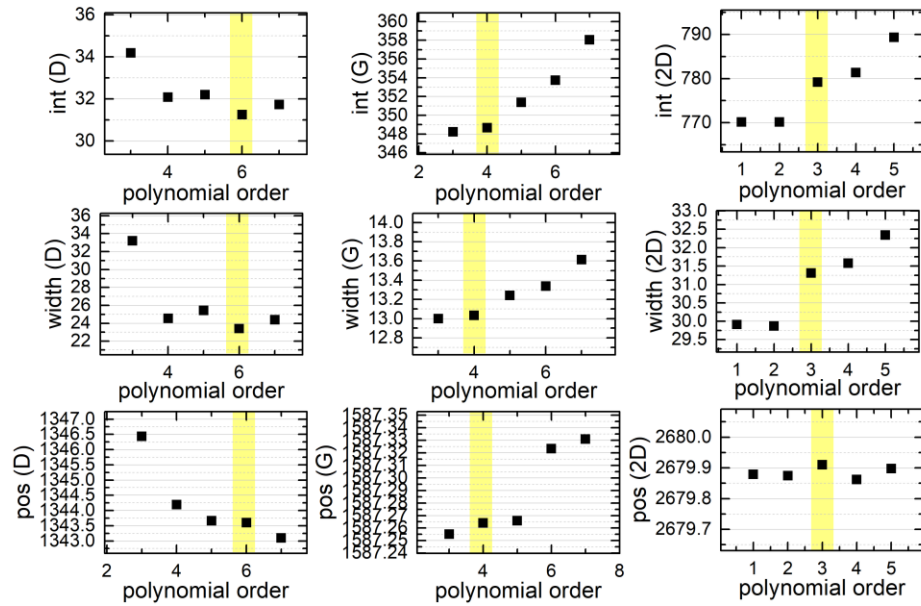


Figure S6. Mean values of peak parameters for various order of the polynomial baseline subtraction for the untreated sample. Chosen polynomial order are highlighted in yellow. D' values not shown since it is too small or irrelevant for undamaged graphene.

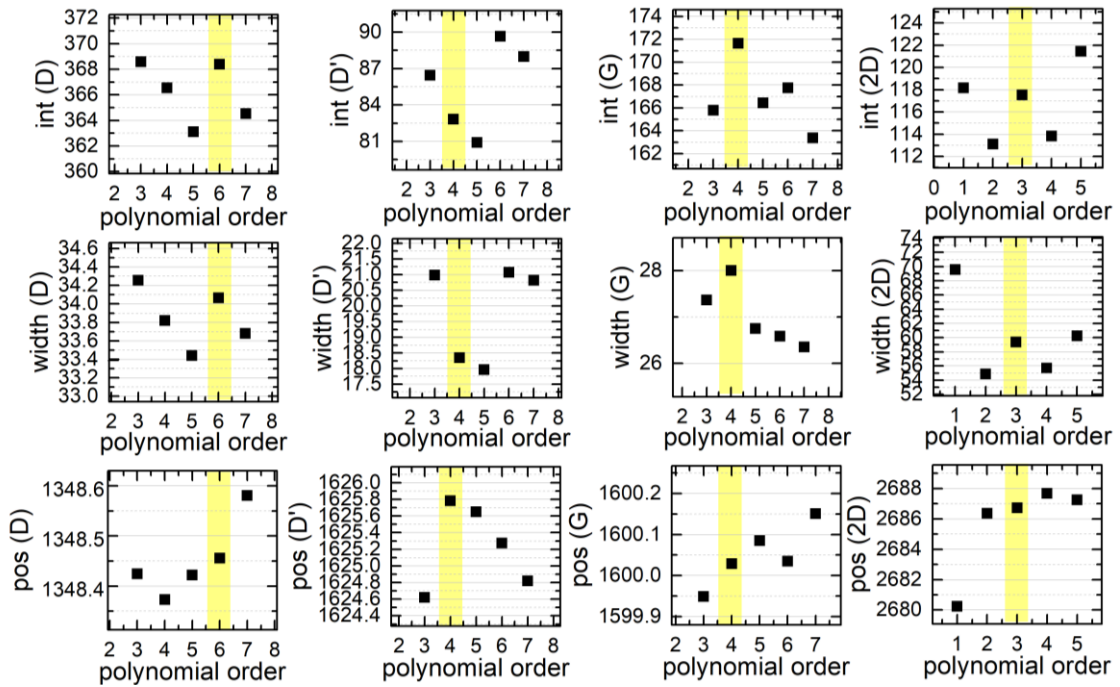


Figure S7. Mean values of peak parameters for various order of the polynomial baseline subtraction for the treated sample. Chosen polynomial order are highlighted in yellow.

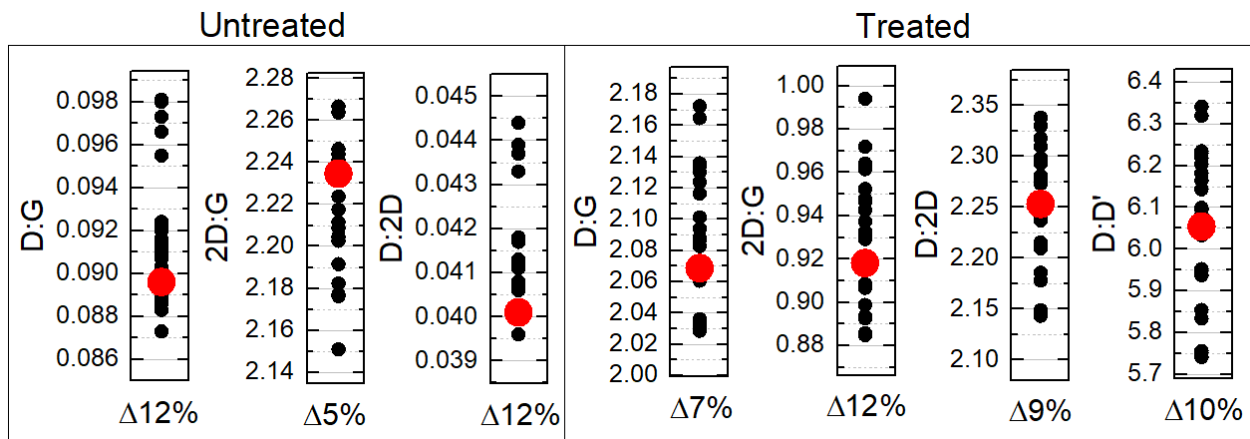


Figure S8. All different values of line ratio possible when considering the polynomial orders presented in Figure S6 and Figure S7. The ratio for the chosen order of polynomial baseline fitting is presented in red. Under each graph is presented the maximum value of deviation (max-min) over the value in red. These percent are shown very small; thus, the order of the polynomial does not impact considerably the data in the manuscript.

S-IV. Cube Registration



Figure S9 - Mean image for the image registration of an untreated zone and the same zone after plasma treatment. A criterion based on the G-band intensity is used to distinguish between specific zones within the graphene sample. Defects are therefore aligned so as to allow point by point analysis. Two mask of logical values are aligned. Points where both signal are 1 appear black; points where both signal are 0 appear white and points which values are opposite appear as grey.

S-V. Excitation Energy Correction

To properly compare inVia and the RIMA measurements, corrections must be applied to consider the different excitation energy (inVia : 514 nm (2.41 eV), RIMA : 532 nm (2.33 eV)).

The 2D band suffer a strong shift of 104 cm⁻¹/eV, the D band a 52 cm⁻¹/eV shift and the G band a 6 cm⁻¹/eV shift [3] with the excitation energy. The widths of the bands are not affected by the excitation energy; no correction is required. The line ratio D:G value is higher for low excitation energy and varies with the excitation energy at the power 4 [3]. Thus a factor of $(532/514)^4 =$

1.1476 is applied to the D:G extracted from the standard confocal setup at 514 nm. The D:D' band ratio depends on the defects nature [4,5]. Therefore, it could not be corrected without further assessments. To the knowledge of the authors, the correction for the 2D:G ratio is not discussed in the literature.

Expression	inVia not corrected		inVia corrected	
	Mean	STD	Mean	STD
2D:G	0.79	0.18	-	
D:G	1.65	0.31	1.89	0.36
D:D'	3.77	4.08	-	-
D:2D			-	-
Γ_G	23.69	3.28	23.69	3.28
Γ_{2D}	50.22	4.61	50.22	4.61
Γ_D	30.31	3.43	30.31	3.43
ω_G	1595.9	2.1	1596.4	2.1
ω_{2D}	2697.5	2.4	2705.8	2.4
ω_D	1350.8	1.3	1355.0	1.3

Table 1. – Raman spectroscopy comparison between standard confocal measurements (with inVia setup) and Rima measurements for the treated state and untreated state of the graphene.

References

- [1] P. Vinchon, X. Glad, G. Robert-Bigras, A. Sarkissian, R. Martel, L. Stafford, J. Vac. Sci. Technol. A (2019).
- [2] P. Antonelli, H.E. Revercomb, L.A. Sromovsky, W.L. Smith, R.O. Knuteson, D.C. Tobin, R.K. Garcia, H.B. Howell, H.L. Huang, F.A. Best, J. Geophys. Res. D Atmos. 109 (2004) 1–22.
- [3] L.G. Cançado, A. Jorio, E.H.M. Ferreira, F. Stavale, C. a. Achete, R.B. Capaz, M.V.O. Moutinho, A. Lombardo, T.S. Kulmala, a. C. Ferrari, Nano Lett. 11 (2011) 3190–3196.
- [4] P. Venezuela, M. Lazzeri, F. Mauri, Phys. Rev. B - Condens. Matter Mater. Phys. 84 (2011) 1–25.
- [5] A. Eckmann, A. Felten, I. Verzhbitskiy, R. Davey, C. Casiraghi, Phys. Rev. B 88 (2013) 035426.

Annexe 5 : Données supplémentaires pour l'article NPJ.2D_2020

Selective nitrogen doping of graphene domains due to preferential healing of plasma-generated defects near grain boundaries

G. Robert Bigras¹, X. Glad¹, P. Vinchon¹, R. Martel², L. Stafford¹

¹Département de Physique, Université de Montréal, Montréal, Québec, CANADA.

²Département de Chimie, Université de Montréal, Montréal, Québec, CANADA.

S-I : Experimental setup

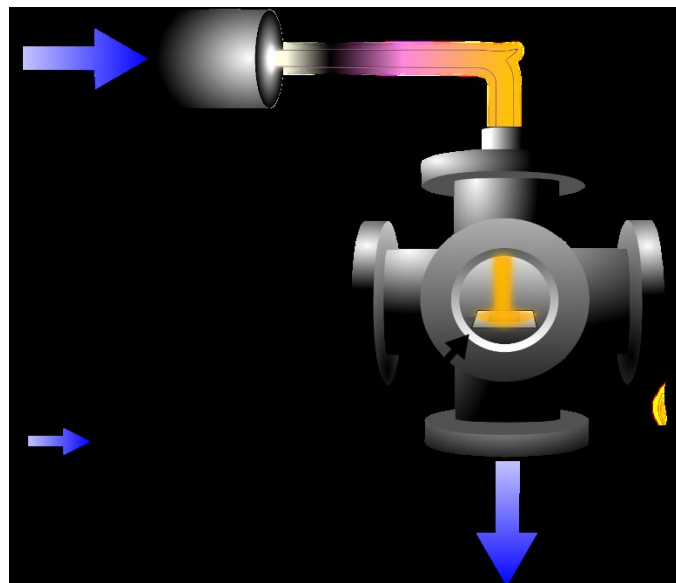


Figure S1. Schematic of the plasma system, where 1-4 refer to different zones of the discharge and 5 is the position of the graphene sample. The adequately-shaped knee in the discharge tube traps high-energy photons thus reducing photon energy flux at the sample surface placed in the flowing afterglow.

S-II: RIMA measurements

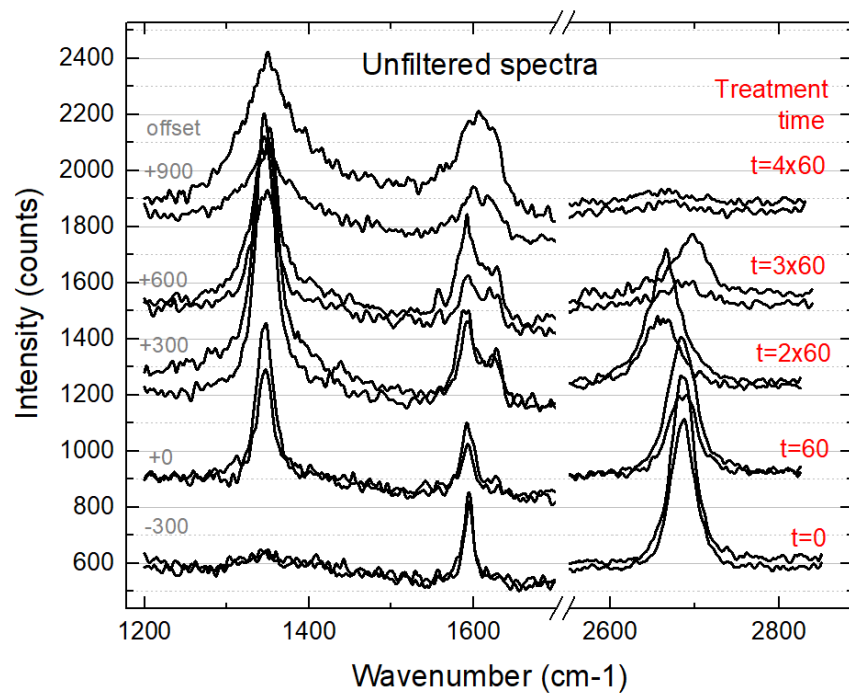


Figure S2. Random unfiltered spectra selected from the various state of the graphene. Offset to counts are identified.

S-VIII: Data preparation and processing

A) Filtering

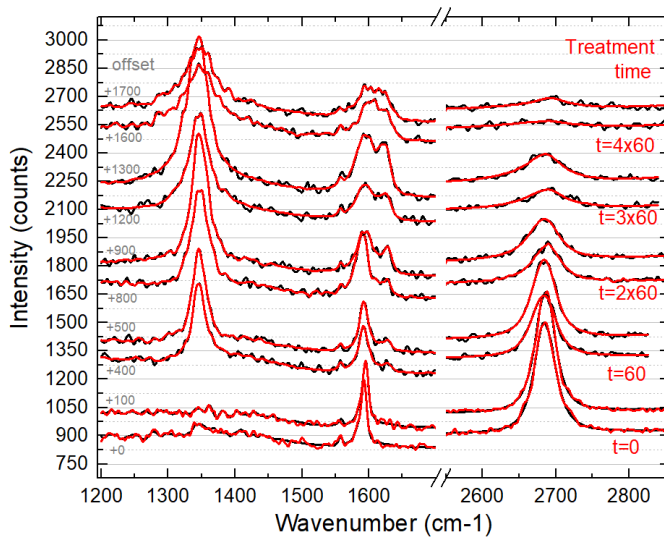


Figure S3. Filtering for random spectra for all the states of the graphene. Offsets and treatment times are identified on the figure.

B) Fitting

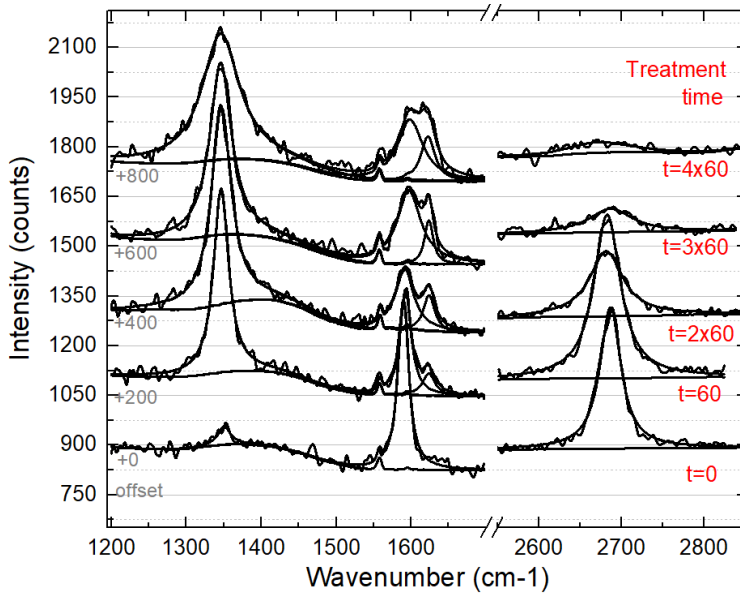


Figure S4. Typical fitted spectra for all the state of the graphene. Offsets and treatment times are identified on the figure.

S-IV: Optical Imaging of the whole area probed by RIMA

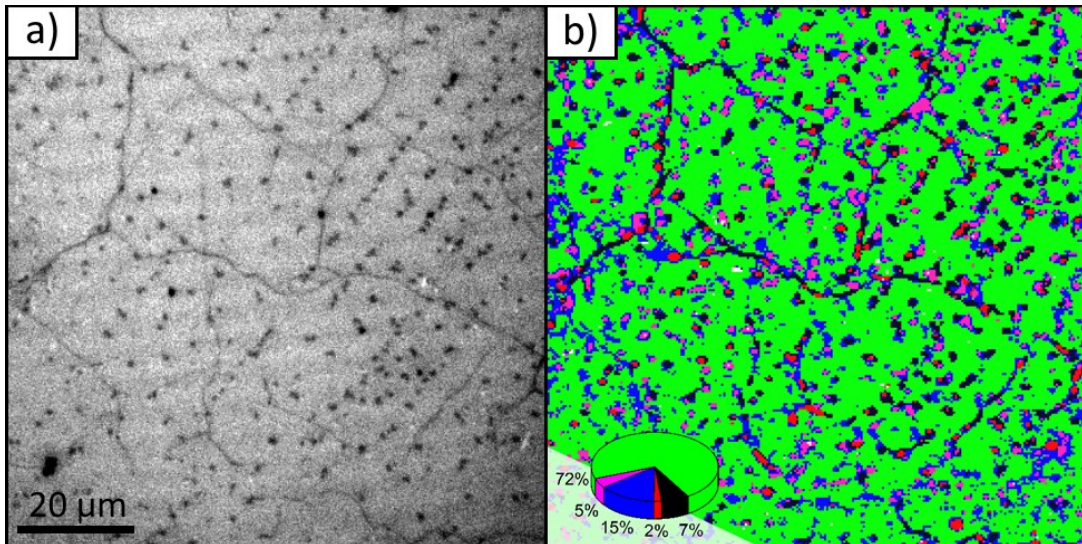


Figure S5. a) Optical microscopy picture of the whole area probed by RIMA in b). b) Cluster map, as defined for the untreated graphene film. Graphene domains (green) and various defect sites (blue, red, black, magenta) are distinguishable. A pie chart presents the coverage (normalized spectra counts) of the different clusters. Blue and magenta defects are mostly present at the center of graphene domains while red and black clusters match well with grain boundaries.

S-V: Energy-dispersive X-ray spectroscopy

Energy-Dispersive X-ray Spectroscopy (EDXS) analysis were performed along with SEM measurements to confirm the presence of SiO_x-based particles on the graphene/SiO₂ substrate. Here, the working distance was set at 14.3 mm and the beam energy and current was fixed to 2 keV and 10 nA, respectively. For such analysis, the Si EDXS signal is dominated by the substrate. However, a dip in EDXS scan is observed close to the SiO_x-based particles without any significant change in the carbon signal (see Figure S2). As presented in Figure S3, EDXS measurements further reveal a disbalance of carbon presence between graphene domains (GD), graphene boundaries (GB) and "dark circles". No significant change of the other elements is present. This indicates that the "dark circles" represent bilayer graphene domains, with a rise in the carbon EDXS signal by roughly a factor of two with respect to GDs.

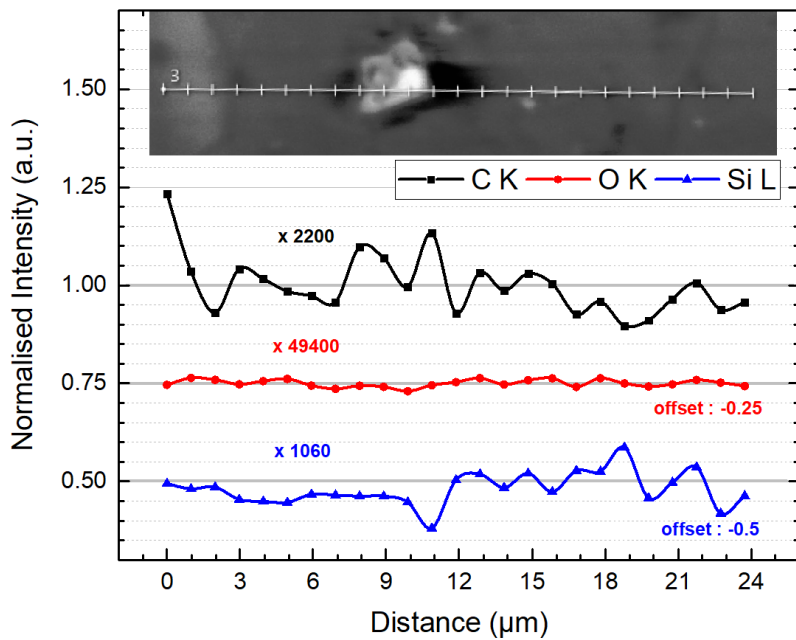


Figure S6. EDXS line profiles at graphene spots (GS) cluster S-I: Optical decoupling of strain and doping

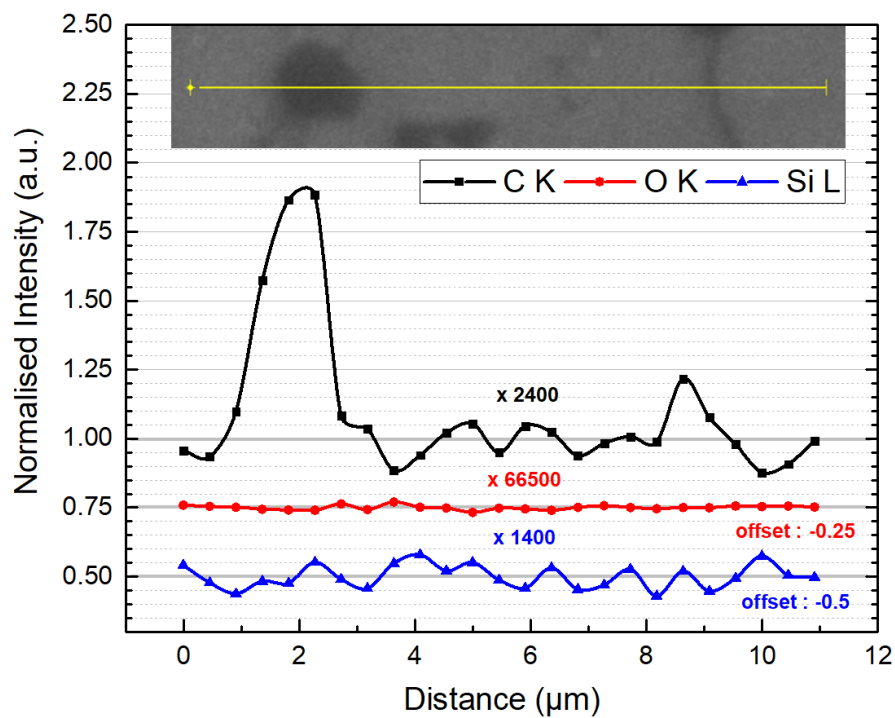


Figure S7. EDXS line profiles over a “dark circle” and over a grain boundary (GB).

S-VI: Raman band parameters

Raman band parameters for each plasma treatment and each cluster. Colors refer to the mapping of Figure 1. All values presented are mean of the distributions.

	GD				
	0 min	1 min	2 min	3 min	4 min
D:G	0.09	1.92	3.36	2.35	1.58
2D:G	1.83	1.60	0.98	0.32	0.20
D:D'	3.41	8.95	5.99	4.00	3.01
D:2D	0.05	1.20	3.44	7.58	8.39
ω_G (cm-1)	1593.9	1592.5	1592.2	1595.4	1599.8
ω_{2D} (cm-1)	2684.5	2684.1	2683.6	2682.1	2686.5
ω_D (cm-1)	1345.3	1346.6	1346.6	1345.0	1345.5
$\omega_{D'}$ (cm-1)	1628.8	1627.2	1626.5	1624.5	1624.9
Γ_G (cm-1)	11.0	17.3	24.9	36.6	42.1
Γ_D (cm-1)	31.5	38.0	48.7	70.3	73.3
Γ_{2D} (cm-1)	33.2	21.6	27.3	37.8	57.1
$\Gamma_{D'}$ (cm-1)	11.4	12.0	14.0	15.1	16.2
	GB				
	0 min	1 min	2 min	3 min	4 min
D:G	0.06	0.86	1.40	1.54	1.09
2D:G	0.86	0.89	0.58	0.41	0.31
D:D'	3.97	8.54	6.12	3.71	2.64
D:2D	0.06	0.97	2.47	4.28	4.30
ω_G (cm-1)	1589.2	1589.0	1588.8	1591.7	1594.1
ω_{2D} (cm-1)	2686.5	2687.1	2687.7	2689.5	2692.5
ω_D (cm-1)	1347.6	1346.9	1347.0	1345.7	1347.2
$\omega_{D'}$ (cm-1)	1630.2	1627.3	1626.1	1623.4	1623.3
Γ_G (cm-1)	16.2	18.3	20.0	27.3	28.4
Γ_D (cm-1)	35.9	40.6	48.1	57.5	54.5
Γ_{2D} (cm-1)	25.8	22.8	27.8	37.5	51.4
$\Gamma_{D'}$ (cm-1)	6.1	11.0	15.0	18.1	19.7
	GB				
	0 min	1 min	2 min	3 min	4 min
D:G	0.12	1.47	2.51	1.94	1.42
2D:G	1.92	1.68	1.21	0.62	0.54
D:D'	3.64	8.58	6.27	3.87	2.84
D:2D	0.06	0.90	2.20	3.57	3.23
ω_G (cm-1)	1591.6	1590.6	1590.3	1592.8	1595.5
ω_{2D} (cm-1)	2687.3	2687.7	2688.8	2690.5	2693.1
ω_D (cm-1)	1347.7	1346.9	1347.0	1345.9	1347.0

$\omega_{D'}$ (cm-1)	1629.3	1627.1	1626.3	1624.1	1624.2
Γ_G (cm-1)	15.2	18.7	22.7	30.5	33.5
Γ_D (cm-1)	35.8	39.6	45.4	51.5	48.4
Γ_{2D} (cm-1)	30.8	22.5	27.6	37.1	51.3
$\Gamma_{D'}$ (cm-1)	9.2	12.1	14.7	16.9	17.7
	GS				
	0 min	1 min	2 min	3 min	4 min
D:G	0.25	1.71	2.87	2.18	1.50
2D:G	1.75	1.45	0.94	0.39	0.25
D:D'	1.59	7.57	5.71	4.00	2.96
D:2D	0.15	1.20	3.14	6.21	7.17
ω_G (cm-1)	1593.9	1592.1	1592.3	1595.0	1598.4
ω_{2D} (cm-1)	2684.9	2684.4	2684.6	2684.5	2688.4
ω_D (cm-1)	1342.9	1346.5	1346.6	1345.6	1346.2
$\omega_{D'}$ (cm-1)	1624.5	1626.2	1626.2	1624.6	1624.7
Γ_G (cm-1)	18.1	20.9	28.6	36.6	43.5
Γ_D (cm-1)	34.5	39.7	49.3	66.5	70.1
Γ_{2D} (cm-1)	55.1	24.1	28.4	38.2	55.3
$\Gamma_{D'}$ (cm-1)	21.7	14.5	15.1	15.2	16.4
	GS				
	0 min	1 min	2 min	3 min	4 min
D:G	0.15	1.80	3.05	2.25	1.53
2D:G	1.86	1.53	0.95	0.36	0.24
D:D'	3.57	8.45	5.87	3.95	2.95
D:2D	0.08	1.18	3.24	6.70	7.20
ω_G (cm-1)	1592.9	1591.8	1591.6	1594.7	1598.7
ω_{2D} (cm-1)	2684.1	2684.2	2684.1	2683.9	2688.3
ω_D (cm-1)	1345.7	1346.4	1346.6	1345.0	1346.0
$\omega_{D'}$ (cm-1)	1627.3	1626.8	1626.2	1624.3	1624.8
Γ_G (cm-1)	13.5	18.6	25.4	35.8	41.2
Γ_D (cm-1)	33.1	39.0	49.1	67.3	68.9
Γ_{2D} (cm-1)	38.8	22.3	27.7	37.9	55.9
$\Gamma_{D'}$ (cm-1)	14.0	12.8	14.5	15.5	16.5

Table S1: Mean values of the Raman band parameters for all clusters and plasma treatment times.

S-VII: Optical decoupling of strain and doping

The method proposed by Lee et al. [1] was verified for very-low-disordered graphene sample. Figure S5 presents the comparison of the decoupling methods when applied to damaged graphene (Bruna et al. [2]) as opposed to untreated graphene (Das et al. [3]). The linear behavior highlighted by Lee et al. for p-type doping is presented (black) in Figure S5d. The same tendency is not present for damaged graphene (red). The different behavior is particularly apparent for n-type doping (Figure S5c). The corresponding relation between ω_{2D} and ω_G was used to decouple strain and doping in samples exposed to nitrogen-containing plasmas: $d\omega_G/dn = 10 \text{ cm}^{-1}/10^{13} \text{ cm}^{-2}$ and $d\omega_{2D}/dn = 5 \text{ cm}^{-1}/10^{13} \text{ cm}^{-2}$ or $(d\omega_{2D}/d\omega_G)n = 0.50 \pm 0.01$

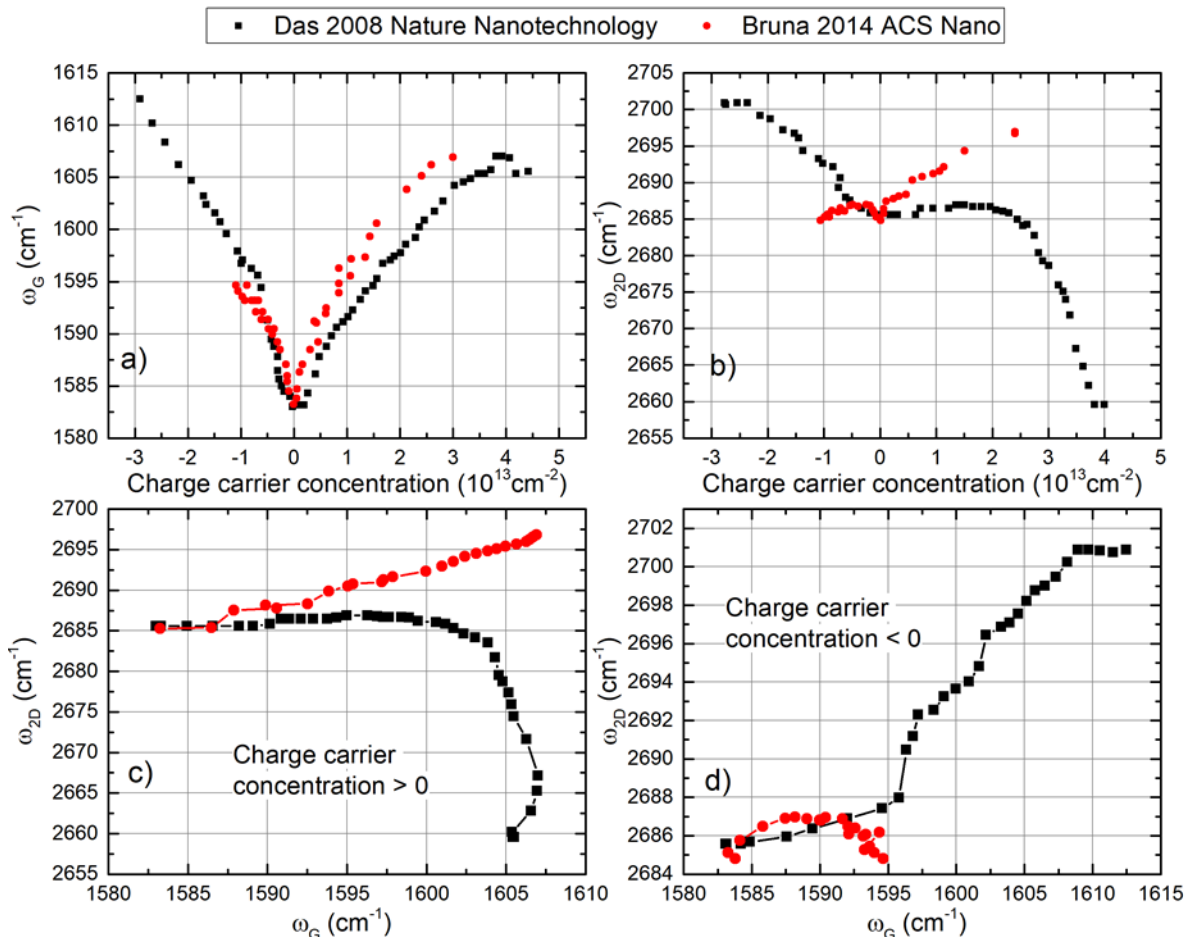


Figure S8. G band (a) and 2D band (b) frequencies as a function of charge carrier concentration. Points were extracted from the works of Bruna et al. [2] and Das et al. [3]. 2D band frequency as a function of G band frequency

for *n*-doping (*c*) and *p*-doping (*d*). The linear behavior of the measurements of Das et al. in ((*d*)-black dots) is used by Lee et al. [1] to decouple strain and doping for untreated graphene. Here, we highlight that the behavior is much more complex for damaged graphene.

S-VIII: XPS survey scans

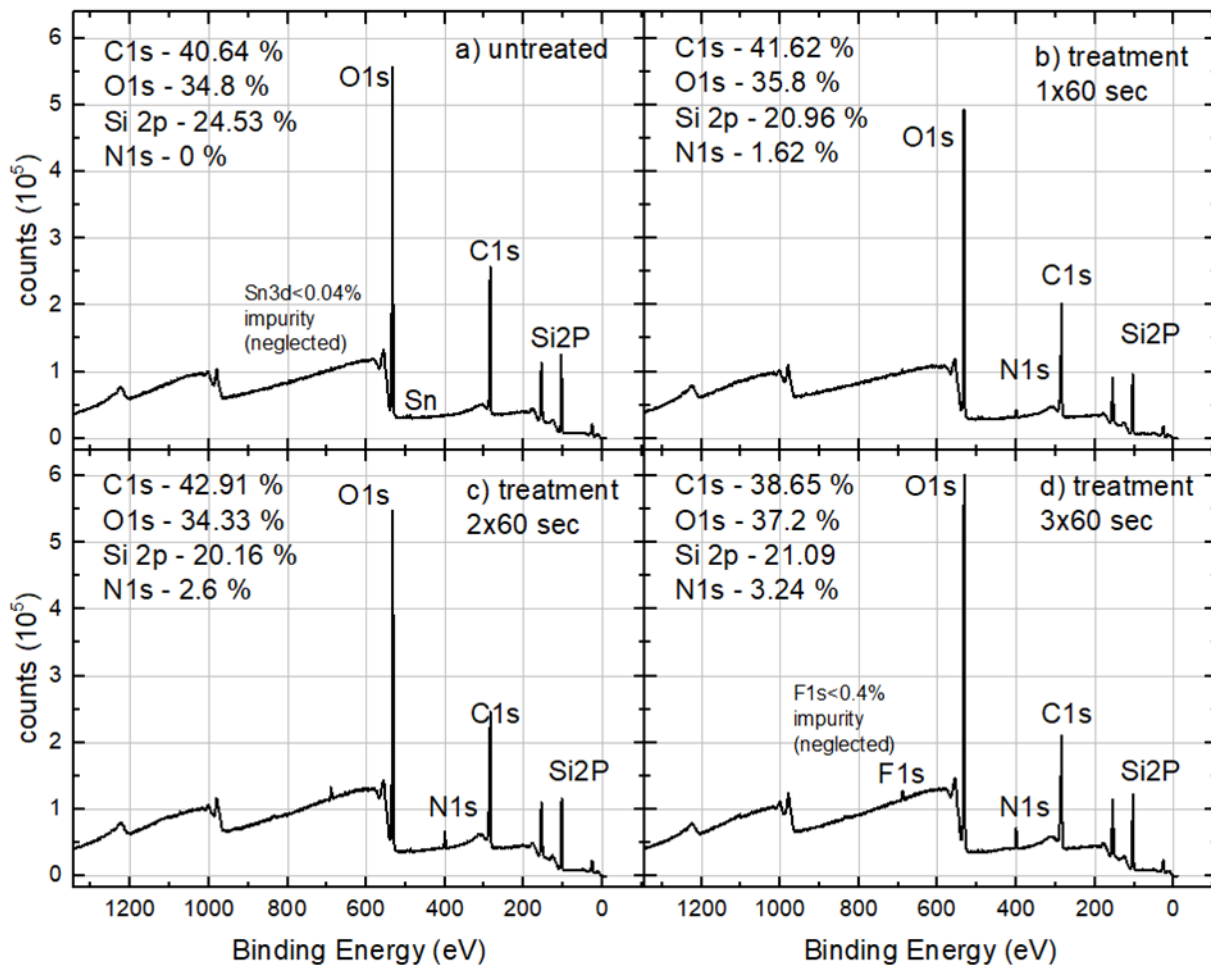


Figure S9. *a*) X-Ray Photoelectron Spectroscopy surveys of untreated (*a*), 1x60 sec (*b*), 2x60 sec (*c*) and 3x60 sec (*d*). Note that due to a contamination in the SEM chamber the last sample state is unavailable.

S-IX: Energy uptake in the Late afterglow

In the late afterglow, since the plasma potential is close to zero [4], the main source of ion acceleration is the local change in the density of ions along the gas flow lines. Assuming $n_i \gg n_e$ in the late afterglow, Poisson's law in 1D can be written as

$$\frac{dE}{dx} = \frac{en_i}{\epsilon_0}$$

where E is the space charge electric field along the gas flow line (x axis), e is the electron charge, ϵ_0 is the vacuum permittivity and n_i is the density of positive ions. The energy obtained by an ion over a distance Δx can thus be written as:

$$W = -\frac{e^2 n_i}{2\epsilon_0} \Delta x^2$$

The distance over which an ion can accelerate is limited by the ion-neutral mean free path via the polarization cross section of nitrogen species:

$$\sigma_{i-n} = \sqrt{\frac{7.5\pi a_0^3 e^2}{\epsilon_0 m_N}} \frac{1}{v_0}$$

where a_0 is the Bohr radius, m_N is the mass of the ion, and v_0 is the velocity of the ion. Since ions are thermalized in the late afterglow, the velocity is taken as the thermal velocity at 300 K : 744 m/s. The corresponding mean free path for ion-neutral collisions is thus:

$$l_{i-n} = 1/\sigma_{i-n} n_n = 6.16 \mu\text{m}$$

where n_n is the density of neutral gas species at 6 Torr. The typical ion density in the late afterglow is about $10^{13}\text{-}10^{15} \text{ m}^{-3}$. Here we take $n_i = 10^{16} \text{ m}^{-3}$ to estimate a higher limit to the ion bombardment energy [4–6]. Hence, for a n_i value of 10^{16} m^{-3} and a Δx value of $10 \cdot l_{(i-n)}$, $W = 0.35 \text{ eV}$. This value is obviously much lower than the one required for carbon displacement in graphene.

S-X: Damage type assessment

The ratio D:D' can be used to assess the type of defect generated by various irradiation conditions [7,8]. For each graphene state linked to a specific plasma treatment time, the value is similar for all the clusters. Thus, defects generated are of the same nature and their Raman response is expected to be the same.

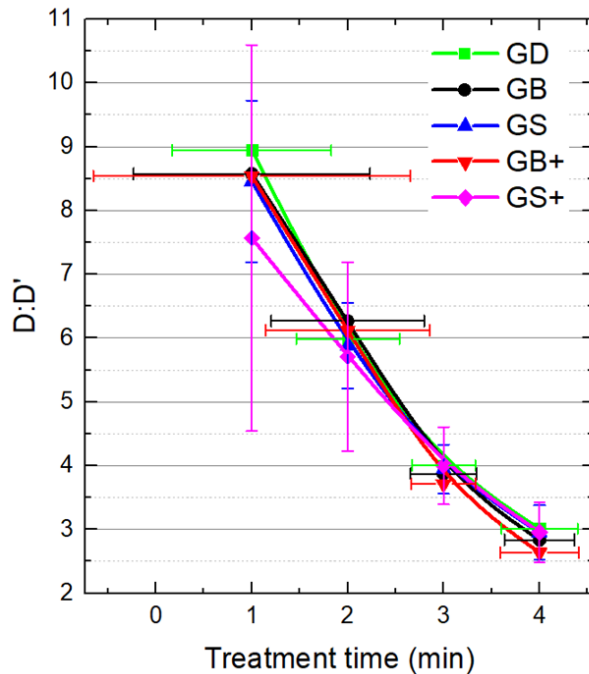


Figure S10. D:D' as a function of treatment time. The value is the mean of each cluster and the error bar is the standard deviation for each distribution. The value is constant among all clusters for each treatment step.

SUPPLEMENTARY REFERENCES

- [1] J.E. Lee, G. Ahn, J. Shim, Y.S. Lee, S. Ryu, *Nat. Commun.* 3 (2012) 1024.
- [2] M. Bruna, A.K. Ott, M. Ijas, D. Yoon, U. Sassi, A.C. Ferrari, *ACS Nano* 8 (2014) 7432–7441.
- [3] A. Das, S. Pisana, B. Chakraborty, S. Piscanec, S.K. Saha, U. V Waghmare, K.S. Novoselov, H.R. Krishnamurthy, a K. Geim, A.C. Ferrari, A.K. Sood, *Nat. Nanotechnol.* 3 (2008) 210–215.
- [4] J. Afonso Ferreira, L. Stafford, R. Leonelli, A. Ricard, *J. Appl. Phys.* 115 (2014) 163303.
- [5] G. Robert Bigras, X. Glad, L. Vandsburger, C. Charpin, P. Levesque, R. Martel, L. Stafford, *Carbon N. Y.* 144 (2019) 532–539.
- [6] G. Robert Bigras, X. Glad, R. Martel, A. Sarkissian, L. Stafford, *Plasma Sources Sci. Technol.* 27 (2018) 124004.
- [7] A. Eckmann, A. Felten, I. Verzhbitskiy, R. Davey, C. Casiraghi, *Phys. Rev. B* 88 (2013) 035426.
- [8] A. Eckmann, A. Felten, A. Mishchenko, L. Britnell, R. Krupke, K.S. Novoselov, C. Casiraghi, *Nano Lett.* 12 (2012) 3925–3930.

Annexe 6 : Données supplémentaires pour l'article Nanoscale_2020

Incorporation-limiting mechanisms during nitrogenation of monolayer graphene films in nitrogen flowing afterglows

G. Robert Bigras¹, R. Martel², L. Stafford¹

¹Département de Physique, Université de Montréal, Montréal, Québec, CANADA.

²Département de Chimie, Université de Montréal, Montréal, Québec, CANADA.

S1 – plasma diagnostics

Number densities of key species are extracted using NO titration and line-ratio of particular spectral bands. NO gas is added to the flowing afterglow and the emission intensity of the NO β band at 320 nm is followed. Extinction of the emission occurs when the density of N is equal to the density of NO (see **Figure S1**). The titration method allow for the calculation of a constant that can link the emission intensity of the 580 nm line to the number density of N atoms [1,2]:

$$\alpha I_{580} = k_{titration}[N]^2$$

where I_{580} is the emission intensity of the 580 nm line, $k_{titration}$ is a constant for a given geometry and exposure time of the acquisition, $[N]$ is the number density of atomic nitrogen and α is the coefficient that expresses the transition between the early afterglow and the late afterglow.

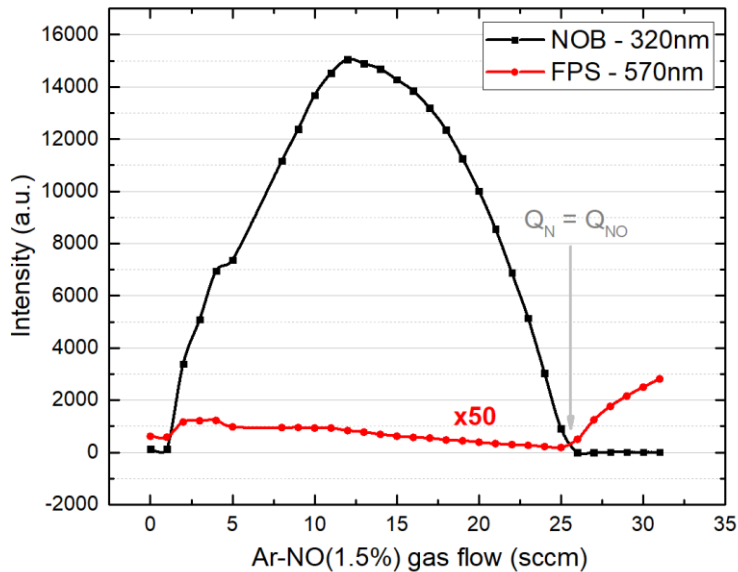


Figure S1 – NO titration. Intensity of the NO_{β} -320 nm as a function of Ar-NO gas flow. When the gas flow of NO (Q_{NO}) reaches the gas flow of atomic nitrogen Q_N , the loss of N is complete and the loss of N:O recombination results in the extinction of the NO_{β} emission.

A given set of experimental conditions with NO in the microwave nitrogen flowing afterglow is chosen as a calibration to obtain the vibrational energy distribution function of the early and late afterglow. As shown in Figure S1, by varying the NO concentration in the microwave nitrogen flowing afterglow, a full extinction of the late afterglow can be seen. From this set of data, constraint linear fitting of the distribution is done over the whole set of conditions. All coefficients are bound between 0 and 1, and the distribution are normalized. In addition, the distribution of the early afterglow is constrained to an exponential decay, with a vibrational temperature of 0.66 eV. The results are shown in Figure S2a for the vibrational energy distribution and in Figure S2b for the α coefficient as a function of the NO concentration.

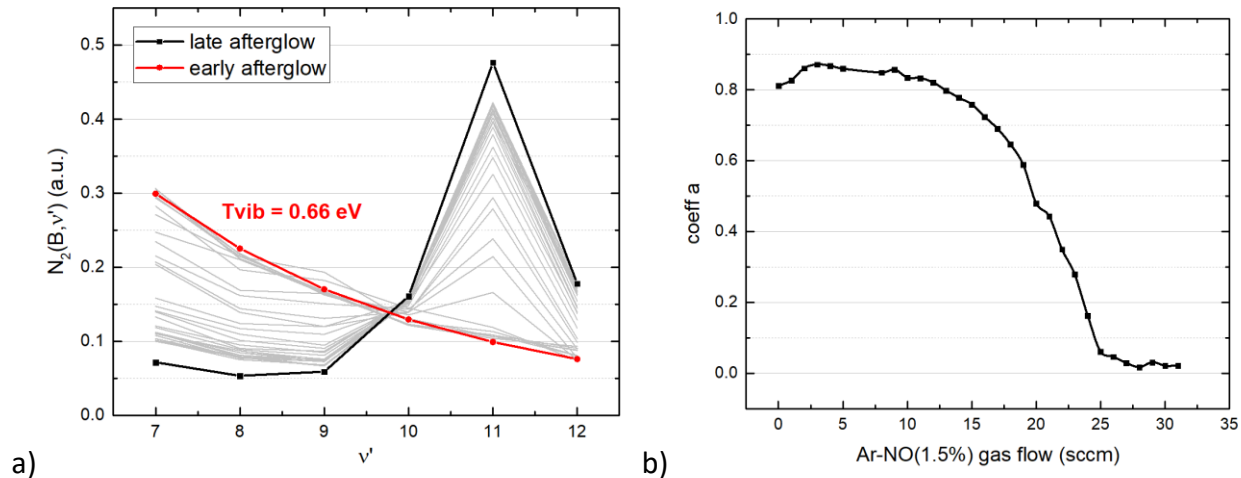


Figure S2 – (a) Evolution of the vibrational energy distribution of the first positive system of N₂ for various concentrations of NO leading to the extinction of the late afterglow. (b) Influence of the NO concentration on the a coefficient.

As for the population of N₂(A), it can be obtained from the band ratio [3]:

$$\frac{a I_{580}}{I_{316}} = \frac{A_{580} k_{01}[N_2][N]^2 / (v_{27} + k_{02}[N_2])}{A_{316} k_{03}[N_2(A)]^2 / (v_{30} + k_{26}[N_2])}$$

Reaction	Rate constant
N + N + N ₂ => N ₂ (B,v) + N ₂	k ₀₁ = 4.4e-34 ; cm ⁶ s ⁻¹
N ₂ (B) + N ₂ => N ₂ (A,X) + N ₂	k ₀₂ = 3e-11 ; cm ⁻³ s ⁻¹
N ₂ (A) + N ₂ (A) => N ₂ (C,1) + N ₂ (X)	k ₀₃ = 4.1e-11 ; cm ³ s ⁻¹
N ₂ (C,1) + N ₂ => products	k ₂₆ = 3e-11 ; cm ³ s ⁻¹
N ₂ (B,11) => N ₂ (A,v') + hν	v ₂₇ = 2e5 ; s ⁻¹
N ₂ (C,1) => N ₂ (B) + hν	v ₃₀ = 2.7e7 ; s ⁻¹

$$A_{580} = 7.8e4 ; s^{-1}$$

$$A_{316} = 1.3e7 ; s^{-1}$$

S2 – XPS ANALYSIS

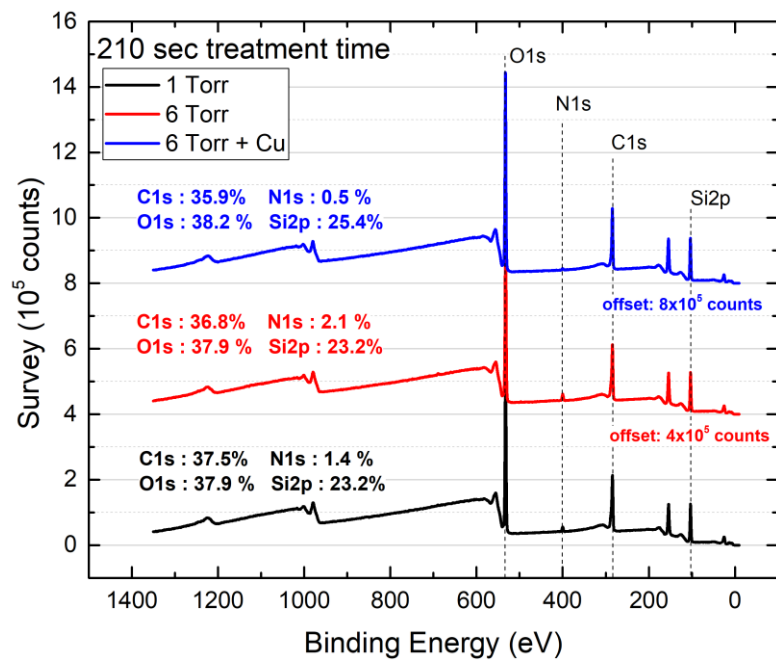


Figure S3 – Survey spectra for the 210-treatment time for all conditions

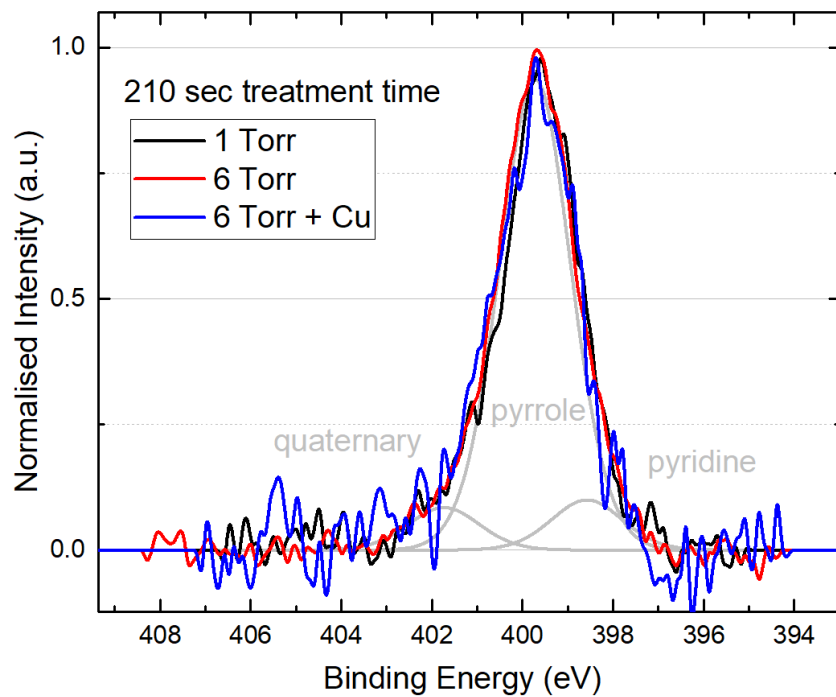


Figure S4 – Normalized high-resolution NIs XPS spectra for the 210 sec treatment time for all studied conditions.

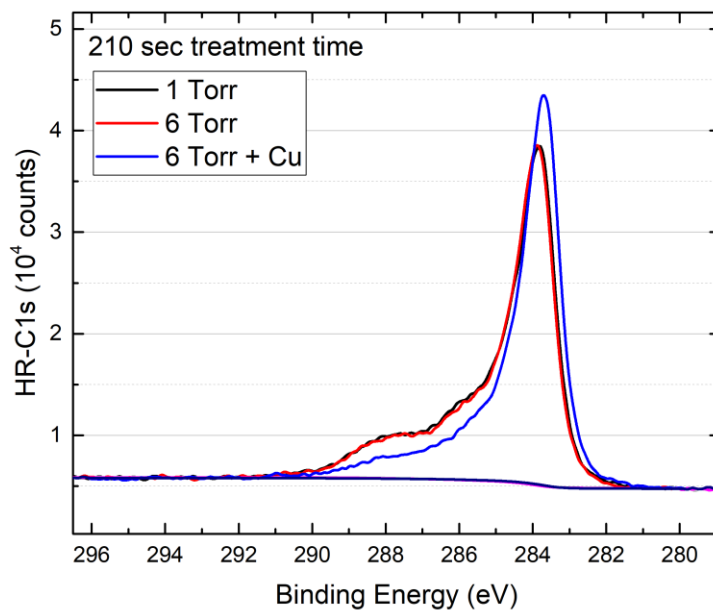


Figure S5 – High resolution C1s spectra for the 210-treatment time for all conditions.

Supplementary data references

- [1] H. Zerrouki, A. Ricard, J.P. Sarrette, Contrib. to Plasma Phys. 54 (2014) 827–837.
- [2] M.K. Boudam, B. Saoudi, M. Moisan, A. Ricard, J. Phys. D. Appl. Phys. 40 (2007) 1694–1711.
- [3] A. Ricard, S. Oh, V. Guerra, Plasma Sources Sci. Technol. 22 (2013) 035009.